

2008

A versatile imaging system for in vivo small animal research

Jianguo Qian

College of William & Mary - Arts & Sciences

Follow this and additional works at: <https://scholarworks.wm.edu/etd>



Part of the [Biomedical Engineering and Bioengineering Commons](#), [Biophysics Commons](#), and the [Investigative Techniques Commons](#)

Recommended Citation

Qian, Jianguo, "A versatile imaging system for in vivo small animal research" (2008). *Dissertations, Theses, and Masters Projects*. Paper 1539623532.
<https://dx.doi.org/doi:10.21220/s2-1rv1-ar33>

This Dissertation is brought to you for free and open access by the Theses, Dissertations, & Master Projects at W&M ScholarWorks. It has been accepted for inclusion in Dissertations, Theses, and Masters Projects by an authorized administrator of W&M ScholarWorks. For more information, please contact scholarworks@wm.edu.

A VERSATILE IMAGING SYSTEM FOR IN VIVO SMALL ANIMAL RESEARCH

Jianguo Qian

Yizheng, Jiangsu, China

M.S., Shanghai Jiao Tong University, 2000

B.S., Fudan University, 1997

A Dissertation presented to the Graduate Faculty
of the College of William and Mary in Candidacy for the Degree of
Doctor of Philosophy

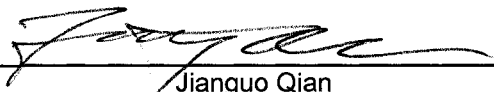
Applied Science / Medical Imaging

The College of William and Mary
August 2008

APPROVAL PAGE

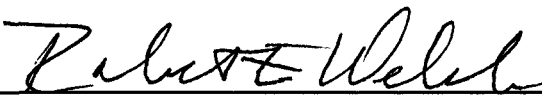
This dissertation is submitted in partial fulfillment of
the requirements for the degree of

Doctor of Philosophy

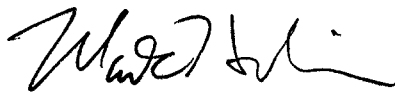


Jianguo Qian

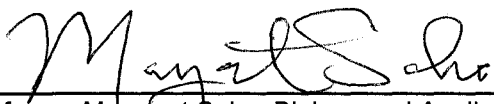
Approved by the Committee, May 2008



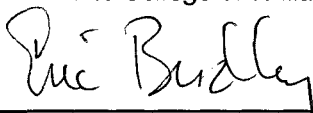
Committee Chair
Chancellor Professor Robert Welsh, Physics
The College of William and Mary



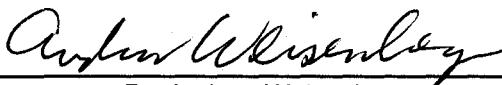
Professor Mark Hinders, Applied Science
The College of William and Mary



Professor Margaret Saha, Biology and Applied Science
The College of William and Mary



Professor Eric Bradley, Biology, Chair of Applied Science
The College of William and Mary



Dr. Andrew Weisenberger
Thomas Jefferson National Accelerator Facility

ABSTRACT PAGE

In vivo small animal imaging has become an essential technique for molecular biology studies. However, requirements of spatial resolution, sensitivity and image quality are quite challenging for the development of small-animal imaging systems. The capabilities of the system are also significant for carrying out small animal imaging in a wide range of biological studies. The goal of this dissertation is to develop a high-performance imaging system that can readily meet a wide range of requirements for a variety of small animal imaging applications. Several achievements have been made in order to fulfill this goal.

To supplement our system for parallel-hole single photon emission computed tomography (SPECT) based upon a 110 mm diameter circular detector, we have developed novel compact gamma cameras suitable for imaging an entire mouse. These gamma cameras facilitate multi-head (>2) parallel-hole SPECT with the mouse in close proximity to the detector face in order to preserve spatial resolution. Each compact gamma camera incorporates pixellated NaI(Tl) scintillators and a pair of Hamamatsu H8500 position sensitive photomultiplier tubes (PSPMTs). Two types of copper-beryllium parallel-hole collimators have been designed. These provide high-sensitivity imaging of I-125 or excellent spatial resolution over a range of object-detector distances. Both phantom and animal studies have demonstrated that these gamma cameras perform well for planar scintigraphy and parallel-hole SPECT of mice.

To further address the resolution limitations in parallel-hole SPECT and the sensitivity and limited field of view of single-pinhole SPECT, we have developed novel multipinhole helical SPECT based upon a 110 mm diameter circular detector equipped with a pixellated NaI(Tl) scintillator array. A brass collimator has been designed and produced containing five 1 mm diameter pinholes. Results obtained in SPECT studies of various phantoms show an enlarged field of view, very good resolution and improved sensitivity using this new imaging technique.

These studies in small-animal imaging have been applied to in vivo biological studies related to human health issues including studies of the thyroid and breast cancer. A re-evaluation study of potassium iodide blocking efficiency in radioiodine uptake in mice suggests that the FDA-recommended human dose of stable potassium iodide may not be sufficient to effectively protect the thyroid from radioiodine contamination. Another recent study has demonstrated that multipinhole helical SPECT can resolve the fine structure of the mouse thyroid using a relatively low dose (200 Ci). Another preclinical study has focused on breast tumor imaging using a compact gamma camera and an endogenous reporter gene. In that ongoing study, mammary tumors are imaged at different stages. Preliminary results indicate different functional patterns in the uptake of radiotracers and their potential relationship with other tumor parameters such as tumor size.

In summary, we have developed a versatile imaging system suitable for in vivo small animal research as evidenced by a variety of applications. The modular construction of this system will allow expansion and further development as new needs and new opportunities arise.

TABLE OF CONTENTS

	Page
Dedication	v
Acknowledgements	vi
List of Tables	vii
List of Figures	viii
1 Introduction	2
1.1 Motivation of this project	2
1.2 Project Overview	4
1.3 Scope of this dissertation	5
2 <i>In vivo</i> radionuclide imaging of small animals	7
2.1 <i>In vivo</i> small animal imaging	7
2.2 Radionuclide imaging for small animals	9
2.3 PET	10
2.3.1 Methodology	10
2.3.2 Detectors	12
2.3.3 PET system design.....	14
2.3.4 Image reconstruction	15
2.3.5 Reported PET systems for small animals	15
2.3.6 PET radiotracers and applications	16
2.3.7 Advantages and disadvantages of PET	17
2.4 Single photon imaging	18
2.4.1 Methodology	18
2.4.2 Detectors	19
2.4.3 SPECT system design.....	22
2.4.4 Image reconstruction	23
2.4.5 Reported SPECT systems for small animals	25
2.4.6 SPECT radiotracers and applications	29
2.5 Discussion of small animal radionuclide imaging	30
3 Evolution of our imaging system	33
3.1 X-ray/gamma-ray dual-modality planar imaging	33
3.1.1 Performance of gamma and X-ray imaging	35
3.1.2 Mouse bed and formation of the composite image of an entire mouse ...	37

3.1.3 Fusion of gamma-ray and X-ray images	38
3.1.4 Proof-of-concept studies	39
3.1.5 Conclusion	41
3.2 Simultaneous parallel-hole/pinhole gamma-ray imaging	42
3.2.1 Gamma cameras for parallel-hole and pinhole imaging	44
3.2.2 Setup of the imaging system	48
3.2.3 Image reconstruction for SPECT imaging	49
3.2.4 Simultaneous parallel-hole/pinhole planar imaging	49
3.2.5 Parallel-hole SPECT imaging - phantom study	50
3.2.5.1 Experiment I – snake phantom	51
3.2.5.2 Experiment II – thyroid phantom	53
3.2.6 Single-pinhole SPECT imaging – phantom study	55
3.2.7 Simultaneous parallel-hole/pinhole SPECT– animal study	56
3.2.8 Discussion and conclusion	58
3.3 Development of compact gamma cameras for biological imaging	59
3.3.1 Development of the first novel “mouse-sized” gamma camera	60
3.3.1.1 Summary of the first “mouse-sized” gamma camera	60
3.3.1.2 Calibration of the compact gamma camera	62
3.3.1.3 Characterization – efficiency and resolution	64
3.3.1.4 Planar and SPECT imaging – animal studies	66
3.3.2 Development of the second “mouse-sized” gamma camera	70
3.3.3 Conclusion	72
4 Development of multipinhole helical SPECT	73
4.1 System design	74
4.2 Gamma-ray detector for pinhole collimation	75
4.3 Design of a five-pinhole collimator	76
4.4 Step-and-shoot helical orbit	79
4.5 Image reconstruction program and validation	80
4.5.1 Simulation test	81
4.5.2 Phantom test	83
4.6 SPECT scans	85
4.7 Characterization comparison	85
4.7.1 Field of view	85
4.7.2 Efficiency	87
4.7.3 Resolution	89
4.8 SPECT imaging – phantom studies	91
4.9 Discussion and conclusion	95

5 <i>In vivo</i> gamma imaging in studies of the mouse thyroid	99
5.1 <i>In vivo</i> study of KI blocking efficiency in mice	100
5.1.1 Gamma-ray detector and imaging	101
5.1.2 Data analysis	102
5.1.3 Experiments and results	102
5.1.4 Discussion and conclusion	108
5.2 <i>In vivo</i> multipinhole helical SPECT imaging of a mouse thyroid	109
5.2.1 Multipinhole helical SPECT system and scans	112
5.2.2 Parallel-hole gamma-ray imaging	112
5.2.3 Phantom studies	113
5.2.3.1 Resolution	113
5.2.3.2 Sensitivity	115
5.2.3.3 Quantification	116
5.2.4 Mouse studies	118
5.2.4.1 <i>In vivo</i> multipinhole helical SPECT	118
5.2.4.2 Whole-mount immunohistochemistry and RT-PCR	121
5.2.5 Discussion and Conclusion	122
6 <i>In vivo</i> gamma imaging in a study of mammary tumors	125
6.1 Background	125
6.1.1 PET and breast cancer imaging	127
6.1.2 Scintimammography and breast cancer imaging	129
6.1.3 NIS and breast cancer imaging	132
6.2 Hypothesis and goals.....	133
6.3 Animals and tumor distribution	135
6.4 Whole-mount immunofluorescence methodology	137
6.5 <i>In vivo</i> gamma-ray imaging of MMTV tumors	137
6.5.1 Data acquisition	137
6.5.2 Data analysis	138
6.5.3 Correlation between gamma-ray imaging and immunohistochemistry	141
6.5.4 Results of gamma-ray imaging	145
6.5.4.1 Time for full-size distribution of iodine in MMTV tumors	146
6.5.4.2 Three patterns of ^{125}I distribution in MMTV tumors	148
6.5.4.3 Relationship among tumor patterns, size, and ^{125}I uptake	148
6.5.4.4 Difference plots	152
6.5.5 <i>In vivo</i> gamma-ray imaging and tumor development	153
6.6 Discussion and conclusion	154

7 Future directions and conclusion	159
7.1 Future directions	159
7.1.1 Development of a novel LaBr ₃ detector	159
7.1.2 Mouse monitoring system	162
7.1.3 Automated pattern recognition for tumor studies	163
7.2 Conclusion.....	164
Bibliography	165
Vita	180

Dedicated to my beloved

wife Qian Zhang

and

daughter Melody Qian

ACKNOWLEDGEMENTS

First and foremost, I would like to express my special thanks to my advisor Dr. Robert Welsh of Physics, a gracious, marvelous mentor to me not only in academia but also in life. Without his support and guidance this work would not have been possible. I truly appreciate his support and efforts to create every possible opportunity for me to make progress to complete this work. I thank him for his time spent on reviewing my writings, papers and dissertation, for his patience and encouragement, and for his invaluable advice, suggestions and help on a number of issues I have met in both this work and in life. I am particularly grateful for his invariable kindness, thoughtfulness and care to me and my family over these years.

I would like to thank my other advisors and collaborators, Dr. Margaret Saha and Dr. Eric Bradley of Biology for their in-depth advice over the years, careful and critical review of this work and countless suggestions for improvement. I will always benefit from their rigorous and professional approach to research. I particularly thank Dr. Bradley for his constant help in preparing phantoms and mice for imaging studies, for the fruitful discussions about many details in animal studies, and for his timely support and action to retain my legal status as a foreign student. I especially thank him for playing a vital role to coordinate our group spanning different disciplines and all that he has done to ensure my goal to be accomplished smoothly.

I wish to thank Dr. Mark Hinders of Applied Science for being a member of my committee and for reviewing my dissertation. I also owe special thanks to Dr. Andrew Weisenberger of Jefferson Lab for teaching me the essentials of many aspects of imaging system development, for reviewing my papers and dissertation, for answering a number of my questions regarding this work, and for constantly supporting and ardently helping me not only to complete this work but also to succeed in my future career.

I thank Dr. Mark Smith of University of Maryland School of Medicine for the invaluable reviews, discussions and suggestions regarding completion of this dissertation, and for making available his code for parts of the image reconstruction work. I thank our other Jefferson Lab collaborators, Dr. Stan Majewski whose research has played a major role in bringing medical and biological imaging to William and Mary. and Dr. Valadmir Popov for designing and building high-quality detectors for us. I thank Dr. Randy Wojcik for his skillful work in the design of our imaging gantry.

I would like to thank Eric R. Blue of Biology for providing supportive immunohistochemistry data for some imaging applications. I am also grateful to Stephen Schworer of Biology for providing reverse transcriptase polymerase chain reaction data as complementary materials. I sincerely thank Amir Yazdi, Jonathan Sutton, William Hammond, Kevin Smith, Julie Cella, Paul Brewer and Amoreena Rank of Physics for their contribution in data analysis and system development. I also would like to thank all my friends who generously contribute their help and encouragement to me and my family.

I wish to thank my parents Aihua Wu and Maoshun Qian and my sister Jianling Qian in China for their years of encouragement and faith in me. Here, I would like to express my great appreciation to my wife Qian Zhang who quit her doctoral program for taking care of this family. I thank her for her devotion, encouragement, optimism, endurance, and love. Finally, I want to thank our precious daughter Melody for bringing us the joy of life.

LIST OF TABLES

	Page
2.1 Properties of typical scintillators for PET	12
2.2 A summary of PET systems for small animal imaging	16
2.3 Properties of PET radioisotopes	17
2.4 Properties of typical scintillators for SPECT	22
2.5 Typical radioisotopes used in SPECT imaging.....	30
3.1 Imaging parameters for the experiments using the snake phantom	51
4.1 Total counts in the reconstructed images	84
4.2 Characterization comparison among various modes of SPECT.	86
6.1 Repeated imaging of a right thoracic tumor	154

LIST OF FIGURES

	Page
2.1 A diagram of a PET system	11
2.2 A diagram of conventional single-photon imaging system	19
3.1. Photograph of the imaging system incorporating both gamma- and X-ray modalities	34
3.2. A profile of the three hot spots in a one-hour gamma image.	35
3.3. A picture of the X-ray phantom made with CuBe and its X-ray image	36
3.4. Photograph of the mouse bed.	37
3.5. Examples of fusion of gamma-ray and X-ray images.....	39
3.6. Gamma images presenting the dynamic change of radioiodine distribution in unblocked and KI-blocked mice.....	41
3.7. Early photograph of the imaging system.....	43
3.8. Raw crystal map and crystal lookup table of the scintillator array.....	45
3.9. Normalized energy spectrum of ~ 35 keV gamma rays emitted by ^{125}I	46
3.10. Sample images of simultaneous parallel-hole/pinhole imaging.....	50
3.11. Photograph of the snake phantom containing ~ 20 μCi Na^{125}I	51
3.12. Reconstructed images of SPECT scans of the snake phantom using different imaging parameters.	52
3.13. Photographs of the plastic phantom simulating the thyroid and submaxillary glands of a mouse.	53
3.14. Six consecutive reconstructed images of the thyroid phantom.....	54
3.15. Single-pinhole SPECT of a three-capillary phantom.....	56
3.16. Parallel-pinhole SPECT of a mouse.....	57
3.17. Photograph of the detector and the collimator	61
3.18. The diagram of the inside view of the compact gamma camera	62
3.19. Raw crystal map and crystal lookup table of the scintillator array and a three-capillary image with uniformity corrected	63
3.20. A profile image of the three capillaries	64
3.21. Theoretical prediction and experimental measurement of the resolution as a function of the distance between source and detector.	65
3.22. One-hour parallel-hole planar image of a lactating mouse.....	66
3.23. A transaxial image (left) and its surface plot (right) of the thyroid region of a mouse	67
3.24. Transverse views of a mouse bearing a mammary tumor	69
3.25. Coronal views of the same mouse bearing a mammary tumor	69
3.26. Comparison of spatial resolution of two types of parallel-hole collimators.....	71
4.1. Photograph of current imaging system.....	74
4.2. Diagram of the 5-pinhole collimator	75
4.3. Pinholes with knife edge and channel edge.....	76
4.4. A projection simulation using the five-pinhole collimator.....	78
4.5. Photograph of the five-pinhole collimator	79

4.6. Photograph of the setup to accomplish step-and-shoot helical orbit.....	80
4.7. Pinhole SPECT of a simulated phantom.....	81
4.8. Longitudinal profile of the activity in the reconstructed digital tube	82
4.9. Predicted profile in a projection image of the reconstructed digital tube using the values in Fig. 4.7.....	83
4.10. Reconstructed images using Meikle's program and my program, respectively...	84
4.11. Reconstruction resolution (FWHM) as a function of ML-EM iteration number for various modes of pinhole circular or helical SPECT	88
4.12. Six sample profiles of the capillary in the transverse reconstructed slices for 1-, 3-, 5-pinhole helical SPECT and circular SPECT.....	90
4.13. Three-pinhole helical SPECT of a 54 μ Ci three-capillary phantom	91
4.14. Three-pinhole helical SPECT of a six-capillary phantom	92
4.15. Single, three-pinhole helical SPECT of a hot-rod phantom	94
5.1. The dynamic change of radioiodine uptake during the first hour after injection in thyroid, stomach, injection site, thorax and left leg.	104
5.2. Images which reflect KI blocking effects in different target tissues for five mice receiving KI blocking doses of 0, 1X, 3X, 5X, 10X the scaled human blocking dose.....	104
5.3. Evaluation of the retention of the 1X and 5X KI blocking efficiency	105
5.4. Evaluation of ^{125}I retention in thyroid, stomach and thorax.....	106
5.5. Urinary clearance as a function of equivalent human KI dose.....	107
5.6. Whole-body clearance as a function of equivalent human KI dose.....	107
5.7. Relationship between the reconstruction resolution (FWHM) and number of ML-EM iterations for two-pinhole helical SPECT	114
5.8. Two-pinhole helical SPECT of a two-capillary phantom.....	114
5.9. Two-pinhole helical SPECT of a hot-rod phantom.....	115
5.10. Diagram of the two-pinhole collimator and photo of the thyroid phantom.....	116
5.11. Two-pinhole helical SPECT of the thyroid phantom.....	118
5.12. Two-pinhole helical SPECT of the thyroid region of a mouse.....	119
5.13. <i>In vivo</i> two-pinhole helical SPECT of the thyroid region of a mouse.....	120
6.1. Tumor distribution in the MMTV mice.....	136
6.2. The ROIs of NMJs of two groups of C-57 mice bearing no tumors.....	143
6.3. Correlation between gamma image and immunohistochemistry.....	145
6.4. Distribution of times for ^{125}I to reach the maximum tumor size within one hour	146
6.5. Three typical patterns of ^{125}I distribution in MMTV tumors	147
6.6. Association/correlation among tumor patterns, size and ^{125}I uptake during 50- 55 minutes	149
6.7. Correlations between the ^{125}I uptake and different tumor sizes.....	150
6.8. Respective comparison of dynamic ^{125}I uptake and size between center-to- edge and multi-spot patterns.	151
6.9. Difference plots at beginning and ending periods of imaging	152
6.10. Presumed pathway for iodine transfer in a tumor with center-to-edge pattern	157
7.1. Photographs of the prototype $\text{LaBr}_3(\text{Ce})$ detector	162

A VERSATILE IMAGING SYSTEM FOR *IN VIVO*
SMALL ANIMAL RESEARCH

Chapter 1

Introduction

1. 1 Motivation of this project

The rapid development of imaging techniques such as computed tomography (CT), magnetic resonance imaging (MRI), ultrasound imaging, optical imaging and radionuclide imaging indicates that *in vivo* small animal imaging has become an essential tool for molecular biology studies. However, requirements of spatial resolution, sensitivity and image quality are quite challenging for the development of small-animal imaging systems. The capabilities of the system are also significant for carrying out small animal imaging in a wide range of biological studies. Developing a suitable imaging modality for a biological lab needs integrative consideration of imaging agents, system performance, economy, expandability and compactness. The goal of this work is to develop and to apply a high-performance imaging system that can meet different imaging requirements for a variety of *in vivo* small animal studies.

Radionuclide imaging includes single photon imaging (planar scintigraphy and SPECT) and positron emission tomography (PET). When compared to the instrumentation, sophisticated radiochemistry and relatively short half-lives of most radiotracers for PET imaging, single photon imaging based on collimated gamma cameras provides a complementary alternative with high performance. Different

collimators such as parallel-hole and pinhole collimators can be employed in a gamma camera, and each provides unique advantages. Parallel-hole collimation may provide high efficiency, acceptable resolution and better sampling completeness over a relatively large active area. Parallel-hole planar imaging is especially valuable for whole animal region of interest (ROI) quantitative analysis and distribution studies. Single pinhole collimator can have both high resolution and high sensitivity if the object is close to the pinhole aperture but with a reduced FOV. Multipinhole imaging has been demonstrated in several studies to be suitable for high-resolution (near or less than 1 mm) tomographic imaging with high sensitivity and enlarged field of view. According to individual imaging requirements for a specific preclinical study, researchers may require different modes of collimation. If the required mode is readily available, the inconvenience of changing collimators and frequently re-calibrating detectors will be dramatically reduced during biological studies.

As one of the radioisotopes for single photon imaging, ^{125}I is an excellent choice as a gamma imaging agent because of its low energy (~ 35 keV) for radiation safety and relatively long half-life (~ 60 days) for longitudinal studies. Hundreds of ligands tagged with ^{125}I are commercially available and readily meet the requirements of a variety of molecular imaging studies. However, the low energy photons emitted by ^{125}I can result in poor energy resolution for gamma cameras and raise a challenge for the imaging system to achieve high resolution. Because of the relatively long half-life of ^{125}I , the prolonged radiation exposure of tissues, particularly the thyroid, may require a relatively low administration dose. As a consequence, this may impose the need for high sensitivity from the imaging system in order to maintain image quality. Therefore, the performance

of the imaging system in both resolution and sensitivity becomes significant when a low dose of radiotracer is used in small animal studies.

1. 2 Project overview

This dissertation describes the development of a versatile compact gamma-ray imaging system incorporating multipinhole circular/helical SPECT, parallel-hole imaging (planar projection or tomography) and X-ray imaging as well. The system for *in vivo* small animal research using low doses of ^{125}I has been applied to preclinical studies of the mouse thyroid and mammary tumors, both of which potentially involve issues related to human health.

Novel compact gamma-ray cameras [1] with parallel-hole collimation, sized particularly for mouse imaging have been developed and utilized in this work. Both phantom and mouse studies have demonstrated that such a compact parallel-hole detector is particularly suitable for imaging an entire mouse with balanced resolution and efficiency. A second compact gamma camera has been constructed and incorporated into the system to form a dual-head imager to reduce imaging time. This dissertation deals particularly with an application study of gamma-ray imaging in detecting and characterizing mouse breast tumors *in vivo* with the sodium iodide symporter (NIS) as the reporter gene. In that study, one of the compact gamma cameras was employed in imaging breast tumors in mice infected with the mammary tumor virus (MMTV).

A novel high-resolution, high-sensitivity multipinhole helical SPECT system [2] has been used by incorporating a 110 mm diameter circular detector equipped with a multipinhole collimator designed specifically for imaging the mouse thyroid region. A translation rack supporting the mouse bed, driven by a stepping motor along the axis of

rotation (AOR) of the system, has been implemented so that a helical trajectory is accomplished in addition to the conventional circular orbit. Phantom studies indicate the potential for an enlarged field of view, good resolution and enhanced sensitivity while employing a relatively low dose of the radioisotope ^{125}I . Motivated by our earlier planar scintigraphy study of the blocking efficiency of potassium iodide in mice [2], a further study [3] has demonstrated the application of *in vivo* multipinhole helical SPECT in imaging the mouse thyroid using a moderate dose ($\sim 200 \mu\text{Ci}$) of ^{125}I . These results suggested potential applications in molecular imaging of other NIS-expressing tissues such as mammary tumors.

1.3 Scope of this dissertation

Since imaging system development is a collaborative work, I summarize the process made here with focus on the work I have carried out. Though some of this work is now seen in other systems, it will be described here as part of the evolution of our imaging system. In the section on application studies, details are given of the imaging performance of the system and image analysis. It is beyond the scope of this dissertation, however, to interpret the biological implications of the imaging results.

Following this introduction, Chapter 2 introduces the importance of *in vivo* small animal research and the role of radionuclide imaging in this field including single-photon imaging (planar scintigraphy and SPECT) and PET. Recent development of radionuclide imaging for small animal research is also reviewed in various aspects in Chapter 2. Chapter 3 describes those works in which I have taken part during the evolution of our imaging system with emphasis on my major responsibilities. The development of X-

ray/Gamma-ray dual-modality planar imaging is first described followed by a discussion of simultaneous gamma-ray imaging based on a pair of 110 mm diameter circular cameras equipped with parallel-hole and pinhole collimators respectively. The last part of Chapter 3 focuses on the development and characterization of novel mouse-sized compact gamma cameras. Instrumentation of multipinhole helical SPECT based on a 110 mm diameter circular detector is described in Chapter 4 with efficacy validated by results of proof-of-concept phantom studies. The application of this imaging system in a mouse thyroid study is described in Chapter 5 including a study of the efficiency of stable potassium iodide in blocking the uptake of radioiodine in the thyroid of a mouse and *in vivo* multipinhole helical SPECT imaging of the mouse thyroid. Presented in Chapter 6 is an imaging application of the system in the study of MMTV mammary tumors with preliminary results reported. Chapter 7 concludes the dissertation with a description of ongoing and prospective future work.

Chapter 2

***In vivo* radionuclide imaging of small animals**

This chapter introduces *in vivo* radionuclide imaging techniques for small animal research and reviews recent developments in this field. Section 2.1 describes the significance of *in vivo* small animal imaging. Section 2.2 is an overall introduction of radionuclide imaging techniques for small animals. Two major techniques for radionuclide imaging of small animals: positron emission tomography (PET) and single-photon imaging are reviewed in Section 2.3 and Section 2.4, respectively. This chapter is concluded with Section 2.5, a brief discussion of small animal radionuclide imaging.

2.1 *In vivo* small animal imaging

Small animals such as mice and rats are widely used in biomedical research and serve vital model systems for understanding organism development, determining gene functions, studying numerous human diseases, and developing new pharmaceuticals and therapies [4, 5]. Among the animal models, mice especially play a key role in biomedical studies with advantages of economy, rapid propagation and easy manipulation of the genome [6]. Genetically engineered mice mimicking human disorders are well-characterized models for the fundamental and therapeutic studies of diseases. Rats are also a favored animal model, especially in the field of neuroscience because the surgical manipulation of their brain is relatively easy along with the historically cumulative

knowledge base of the rat brain [6]. Small animals are essential for preclinical studies in translation to human application. However, the potential of small animal models in those studies is not yet fully realized. One significant limitation has been the requirement of sacrificing the animal to obtain desired information. Many natural or perturbed biomedical processes under study are unobservable *ex vivo*, which sequentially results in less-precise results [7]. Longitudinal studies in a single animal are barely possible in this case, leading to increased statistical variability due to the large number of sacrificed animals required by the molecular-biologic assays in order to achieve meaningful outcomes [5, 6]. At the molecular level, the *ex vivo* method makes it a formidable task to understand the function of numerous genes in the context of complex organisms [8, 9]. These intrinsic drawbacks of *ex vivo* methodology urge investigation of the biological, cellular and molecular processes in living animals.

With the increasing requirement to resolve such issues and the impressive development of imaging technologies, non-destructive *in vivo* imaging stands out as a powerful discovery tool and a substantial solution [10, 11]. Though many imaging techniques were initially designed for human studies, extension of those techniques to small animals makes it possible to acquire functional, quantitative and longitudinal data in addition to structural anatomic information *in vivo* [5]. The living animals can be studied non-invasively and thus repetitively. Therefore, the required number of animals can be dramatically decreased. The statistical variation brought by the inter-animal differences is reduced concurrently owing to the fact that each animal can serve as its own control [12]. Biomedical processes related to biochemistry, genetics and pharmacology are able to be revealed not only visually but also quantitatively and even

dynamically in more details [13, 14]. These outstanding advantages have made *in vivo* small animal imaging a very promising tool in drug discovery and development [5, 15], in human disease studies using animal models [4, 16], and in characterizing gene expression and protein function [9, 12, 17].

2.2 Radionuclide imaging for small animals

Major modern imaging techniques for *in vivo* small animal research include magnetic resonance imaging (MRI), ultrasound biomicroscopy (UBM), X-ray computed tomography (CT), optical imaging, and radionuclide imaging. Among these techniques, radionuclide imaging has shown great promise in small animal imaging for *in vivo* biomedical studies. Radionuclide imaging is a technique detecting gamma rays resulting from radiotracers injected and distributed in the body of a small animal. The radiotracer distribution may contain significant functional information at the molecular level such as gene expression and protein function. Therefore, radionuclide imaging is usually called *functional imaging* in order to distinguish it from other anatomical imaging techniques such as CT and MRI [18]. One may note that the recent development has extended MRI to functional imaging mainly in neuroscience, i.e. brain activity studies, by measuring cerebral blood flow/volume, blood oxygen level dependence or the level of manganese contrast agents associated with neuronal electrical activity [19]. However, non-manganese-enhanced functional MRI in brain activity studies is usually carried out under anesthesia while, in the manganese-enhanced case, the usage of manganese agents is limited to small animals due to the concerns about toxicity [19]. With hundreds of biologically targeting ligands labeled with a variety of radioisotopes, radionuclide

imaging has played a key role in functional imaging and offers numerous opportunities for preclinical studies related to human health such as drug discovery, disease diagnosis and therapy.

The production of gamma rays and the way to detect them divide radionuclide imaging into two categories: positron emission tomography (PET) and single-photon imaging. The latter can be further divided into two approaches: planar scintigraphy and single photon emission computed tomography (SPECT). Owing to the advances in detector instrumentation, imaging with both high resolution (< 1 mm) and high sensitivity is possible now for either PET or SPECT. However, the major drawback of functional radionuclide imaging obviously is lack of anatomical information, which could be compensated by an anatomical imaging modality.

Therefore, a combination of different modalities has been proved to be much more synergistic [20-22]. A typical example is to combine a functional imaging modality such as PET with another modality such as CT providing high-resolution structure information as reference for better interpretation of the molecular data. A variety of multi-modality imaging techniques for small animals has been developed or are under development including PET/CT, PET/MRI, PET/optical, SPECT/CT, SPECT/MRI, SPECT/optical, PET/SPECT/CT [10, 15, 23].

In the following sections, the methodology and recent development of radionuclide imaging for small animals will be introduced. This review will cover different aspects such as detectors, systems and applications.

2.3 PET

2.3.1 Methodology

PET imaging utilizes the gamma rays coming from annihilation of an electron and a positron emitted from radioisotopes such as ^{18}F and ^{11}C . The electron-positron annihilation results in a pair of 511 keV gamma rays emitted in opposite directions (approximately 180°), which are detected and paired by PET detectors (called a “coincidence event”). A line of response (LOR) can be formed making it possible to localize the source. When a PET detector has the response time of the order of picoseconds, it is possible to calculate the time of flight of the pair of gamma rays and to improve the accuracy in determining the source position along the LOR. All the coincidence events detected by a PET scan are grouped into projections which are sorted by view angles. Image reconstruction is then carried out based upon those projections.

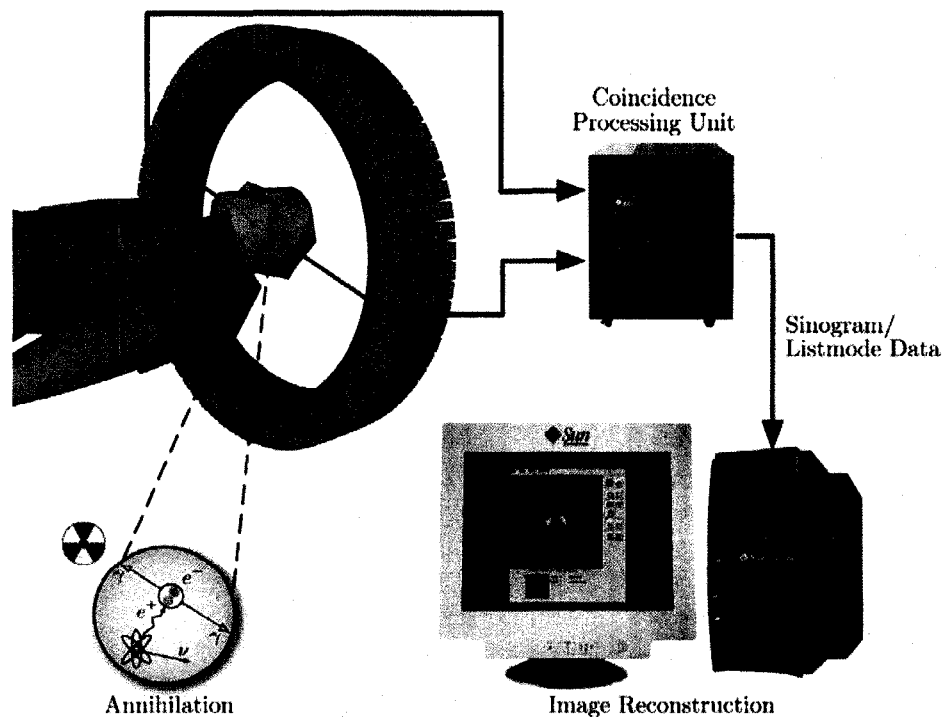


Fig. 2.1 A diagram of a PET system. Image courtesy of Jens Langner [24].

2.3.2 Detectors

Two types of detectors are usually employed for PET imaging: scintillation detectors and semiconductor detectors. Scintillation detectors contain scintillators and photodetectors such as photomultiplier tubes (PMTs) or solid-state photodiodes. The properties of scintillators mainly including high density, high light yield and short decay time are important for achieving PET imaging with high spatial, temporal and energy resolutions. One of the most commonly used scintillators is $\text{Bi}_4\text{Ge}_3\text{O}_{12}$ (BGO). However, the long decay time (~ 300 ns) and relatively low light yield (9000 photons/MeV) make it not an ideal material for new generations of PET imagers, especially for small animal imaging. Therefore, other state-of-the-art materials for PET imaging have been developed typically including $\text{Gd}_2\text{SiO}_5\text{:Ce}$ (GSO), $\text{Lu}_2\text{SiO}_5\text{:Ce}$ (LSO), $\text{LuAlO}_3\text{:Ce}$ (LuAP), YAP, $\text{Lu}_{1.8}\text{Y}_{0.2}\text{SiO}_5\text{:Ce}$ (LYSO, Saint Gobain Crystals), LFS (Zecotek Co.), and $\text{LaCl}_3\text{:Ce}$, etc [25, 26]. Listed in Table 2.1 are the properties of some typical scintillators for PET imaging with respect to density, light yield and decay time, etc.

	Density (g/cm^3)	Decay time (ns)	Light yield (% NaI)	Hygroscopic
NaI	3.67	230	100	Yes
BGO	7.13	300	15	No
GSO	6.71	30-60	25	No
LSO	7.4	40-43	75	No
LuAP	8.3	183800	32	No
$\text{LaCl}_3\text{:Ce}$	3.86	25	121	No
$\text{LaBr}_3\text{:Ce}$	5.3	23	160	No

Table 2.1 properties of typical scintillators for PET [25, 26]

As conventional photodetectors for PET imaging, PMTs, especially position sensitive PMTs (PSPMTs) continue to be widely used owing to their high performance in

spatial and timing resolution. The compactness and high quantum efficiency have made semiconductor photodetectors such as position sensitive avalanche photodiode (PSAPD) a promising alternative for developing high-resolution animal PET system. A variety of new PMTs and photodiodes is available now such as the Hamamatsu R9779 [27], Photonis XP20D0 [27], avalanche microchannel photodiode (AMPD) [28], micro-pixel avalanche photodiode (MAPD) [29], and the CMOS Geiger-mode avalanche photodiode (GPD) [30].

For a scintillation detector, the incident gamma rays are converted through scintillators to visible photons, which are measured by the photodetectors assembled with the scintillators. There are three ways to set up photodetectors with scintillators. The simplest configuration consists of a single plate of continuous scintillator and an array of photodetectors. In order to improve spatial resolution and reduce the cost per detector for PET imaging, the setup of a block detector has been developed by Jones *et al.* [31] which consists of an array of four single-channel PMTs and a scintillator empirically cut into elements with various lengths. A more effective configuration for high-resolution PET imaging of small animals is to employ the position sensitive photodetectors with an array of small individual scintillators (0.8 – 3 mm width and 5 to 20 mm length) [32].

With the advances of detector technology, semiconductor detectors based on silicon (Si) [33] or germanium (Ge) [34] have shown great promise for PET imaging of small animals. Unlike the scintillation detector with an interim conversion from gamma rays to visible photons, semiconductor detectors directly measure gamma rays by converting their photon energy into an electrical signal. Because Si and Ge detectors usually operate best at cryogenic temperatures, researchers recently have sought to

develop animal PET system using room-temperature compound semiconductor detector with high efficiency such as CdTe [35] and CdZnTe [36].

2.3.3 PET system design

A PET system usually incorporates a number of detectors to effectively detect the coincidence events. There are three basic geometries found in dedicated PET systems [18] including hexagonal geometry of large-size detectors, full-ring geometry of a number of detectors with discrete scintillators, and rotating partial-ring geometry with fewer detectors. Depending on whether the axial collimation is employed or not, data acquisition of a PET system can be determined as a 2-D or 3-D imaging mode. For the 2-D mode where axial collimation is applied, the LORs within each specific plane (direct plane) vertical to the axis of rotation (AOR) are considered. This mode results in the volume of the subject in each of those specific planes reconstructed individually. A stack of those reconstructed images forms the entire volume of the subject in the field of view (FOV). Since 3-D PET imaging uses no axial collimation, in addition to the direct planes, the LORs in other planes (oblique planes) in the system are also measured. This mode increases sensitivity and thus allows faster imaging. A disadvantage of this mode, however, is that more scattered events are detected after the removal of the axial collimation potentially degrading image quality. Also image reconstruction for 3-D PET becomes more computationally intensive owing to the larger size of the collected data in comparison with 2-D PET [37]. Development in software has helped to alleviate these issues [38, 39].

2.3.4 Image reconstruction

Image reconstruction for PET imaging can be divided into two types: analytic and iterative methods. The principle method for analytic image reconstruction is a Fourier transform-based backprojection algorithm. Image reconstruction algorithms based upon this principle have been developed for 2-D PET such as the filtered-backprojection (FBP) algorithm [40] and for 3-D PET such as the three-dimensional reprojection (3DRP) algorithm [41], respectively. The most widely used iterative methods for image reconstruction are based on expectation maximization (EM) algorithms [42] such as the maximum likelihood EM (ML-EM) algorithm and ordered subset EM (OSEM) algorithm. These methods, initially implemented in image reconstruction for 2-D PET, have been extended to 3-D PET [43]. Recent research related to image reconstruction focuses on developing faster algorithms such as rebinning algorithms [44] and the techniques for better modeling the statistical properties of the noise for 3-D PET. In addition, corrections of attenuation and scatter for PET imaging continue to be an interesting field to improve the quality and accuracy of reconstructed images for PET (see reviews in [18]).

2.3.5 Reported PET systems for small animals

The dramatic advances in both hardware and software for PET imaging have led to the development of a variety of PET systems with sufficient resolution (0.8 – 2 mm) and sensitivity (0.1% - 7%) for imaging small animals such as mice [35, 45-56]. Summarized in Table. 2.2 are the recent developed PET systems dedicated for small animal imaging. As shown in the table, the most recent development of a “Fine Structure

Imaging PET scanner” has achieved sub-millimeter resolution (0.8 mm) full-width at half maximum (FWHM) for the first practical semiconductor scanner [35]. One may also note the appearance of systems capable of multi-modality imaging including PET/CT [57], PET/SPECT [58], and PET-MRI [59].

Systems	Detector	Transaxial Resolution* (center of FOV, mm)	Sensitivity	notes
ratPET	BGO/PMT	2.3	1%	[47]
Sherbrooke PET	BGO/APD	2.1	0.51%	[51]
MMII PET	LSO/PMT	1.3	> 0.2%	[48]
ClearPET	LYSO+LuYAP/PMT	1.3	0.8-1.5%	[46]
YAP-PET	YAP/PMT	≤2.0	1.7%	[49]
TierPET	YAP/PMT	2	0.1%	[56]
MAD-PET II	LSO/APD	1.1	2.8%	[52]
MicroPET II	LSO/PMT	0.83	2.26%	[55]
MicroPET Focus 120	LSO/PSPMT	1.69	7.1%	[50]
Explore Vista DR	LGSO+GSO/PSPMT	1.6	4%	[54]
Mosaic	GSO/PMT	2.2	1.3%	[45]
quadHIDAC PET	HIDAC	1.0	1.8%	[53]
FSI-PET	CdTe	0.8	4.1%	[35]

* Transaxial resolution is defined as the reconstructed resolution measured in the transverse plane

Table 2.2. A summary of PET systems for small animal imaging

2.3.6 PET radiotracers and applications

Many positron radioisotopes have been implemented in PET imaging. The properties (half life and energy) of those typical radioisotopes are listed in Table 2.3. A number of positron isotope-labeled radiotracers have been developed to target different biological or clinical issues [60]. The advent of modern animal PET systems along with the development of these radiotracers has facilitated studying those health or biological issues using small animals [18]. These studies focus on measuring glucose metabolism in

the rat heart and brain, studying the dopaminergic system in rat brain, and imaging gene expression. Particularly, the advantages of PET in functional imaging have made it a promising technique for oncology applications such as breast cancer study [18]. More detail in this respect can be found in Chapter 6.

Radionuclide	Half-life	Energy (MeV)
^{11}C	20 min	0.97
^{13}N	9.9 min	1.2
^{15}O	122 sec	1.74
^{18}F	110 min	0.64
^{64}Cu	12.7 hr	0.66
^{68}Ga	68.3 min	1.9
^{124}I	4.15 day	2.1

Table 2.3. Properties of PET radioisotopes [60]

2.3.7 Advantages and disadvantages of PET

The most important advantage of PET is its exquisite sensitivity which can be as high as 7%. This easily facilitates researchers carrying out dynamic imaging studies by using PET scans of a few minutes. Short imaging time also reduces the problems resulting from other factors such as the animal's movement. Moreover, the available positron radioisotopes provide a variety of choices to develop ligands for different cellular targets. However, the properties of those positron isotopes also bring the disadvantages. Conjugation of positron isotopes to a wide range of molecules of interest may require sophisticated radiochemistry. Owing to the relatively short half-lives of most radioisotopes, preparation of radiotracers for PET imaging usually requires a nearby cyclotron and radiochemistry lab. Though ^{18}F labeled radiotracers can be produced commercially off site now, it is necessary to frequently recalibrate the remaining dose and to plan the experiments much more carefully owing to its half-life of 110 minutes.

From economical point of view, the cost of PET system and imaging is expensive in comparison with SPECT.

2.4 Single photon imaging

2.4.1 Methodology

Single photon imaging including planar scintigraphy and SPECT uses gamma cameras to detect the gamma rays emitted by radioisotopes such as ^{125}I and $^{99\text{m}}\text{Tc}$. After the radiotracer is injected into an animal, the intensity and position information delivered by detected gamma rays from the distributed radiotracer may convey the information of biological or pathological interest to researchers. When the gamma camera images an animal following injection of a radiotracer, one can achieve a planar gamma image (or “projection”) of the animal. This imaging method is called planar scintigraphy and is shown in the left panel of Fig. 2.2. Planar scintigraphy is useful for a number of studies such as determining the presence or localization of the radiotracers in some tissues (tumors, thyroid, etc.) or quantitative validation of the efficacy of some radiopharmaceuticals. However, since planar scintigraphy is a method of studying the 3-D subject in 2-D space, useful depth information in the animal is lost along the direction vertical to the detector. SPECT has been developed to address that issue. SPECT allows researchers to study the animal in 3-D space. Instead of holding the detector at a fixed position, conventional SPECT takes a set of projections of the animal at a variety of evenly distributed angular positions. The 3-D distribution of the radiotracer in the animal is then reconstructed from the set of planar images by using an appropriate algorithm of image reconstruction. Shown in the right panel of Fig. 2.2 is a diagram of a SPECT system.

2.4.2 Detectors

As with PET, SPECT detectors can be divided into conventional scintillation detectors and semiconductor detectors. The scintillation detector originates from the gamma detector first described by Anger [61]. The procedure of scintillation detection of gamma rays is shown in the left panel of Fig. 2.2. When incident gamma rays at right angles pass through the collimators and strike the scintillator, they induce visible photons which can be detected by photodetectors such as PSPMT or PSAPD. The spatial information and number of counts of the detected incident gamma photons are able to be computationally determined to form a 2-D projection. This imaging procedure is almost identical to PET imaging except that a collimator is employed between the incident gamma rays and scintillators. Therefore, a modern scintillation gamma camera contains three critical components: photodetectors (PSPMT, PSAPD or CCD), scintillators and collimators. Dramatic advances in gamma cameras have been achieved in each of these aspects.

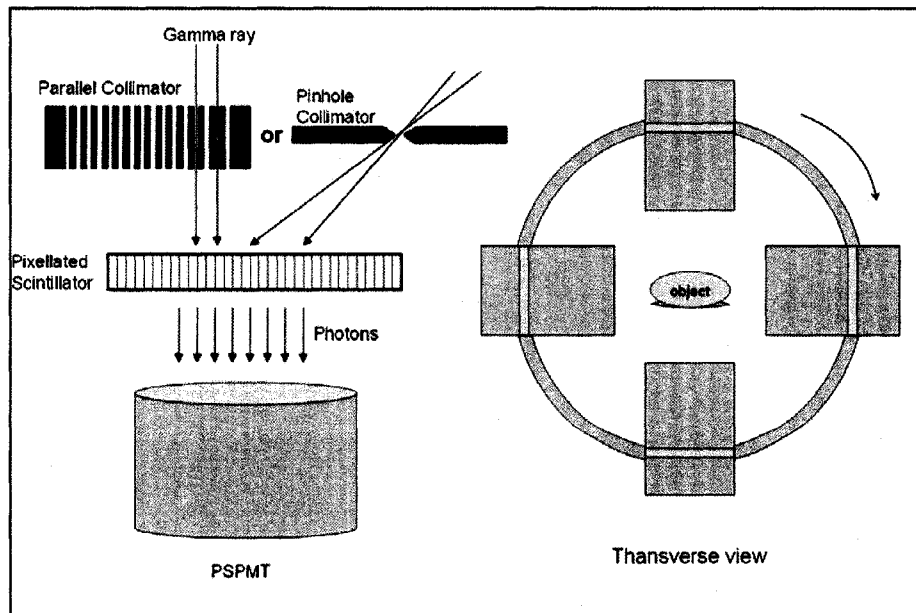


Fig. 2.2 A diagram of conventional single-photon imaging system

Owing to the need for a collimator, one may instantly note that the sensitivity of SPECT detectors dramatically decreases in comparison with PET detectors where only axial or even no collimators are employed. Nevertheless, high resolution and/or relatively high sensitivity for small animal imaging can readily be achieved using gamma cameras equipped with appropriately designed collimators. A variety of collimators have been designed and implemented for single-photon imaging of small animals. Most of the collimators used are parallel-hole or pinhole collimators as shown in Fig. 2.2. Parallel-hole collimators with square or hexagonal openings usually provide large FOV, high sensitivity and moderate resolution, which are sufficient for a number of studies. By incorporating a magnifying factor with a single pinhole collimator, one may achieve sub-millimeter spatial resolution using a gamma camera with intrinsic spatial resolution in the order of millimeters. The geometric sensitivity P_s and spatial resolution R_a of a pinhole collimator can be expressed as [62, 63]:

$$P_s = \frac{d_e \cos^3 \varphi}{16b^2} \quad (2.1)$$

$$R_a = \left[\frac{R_i^2}{M^2} + d_e^2 \left(\frac{M+1}{M} \right)^2 \right]^{1/2} \quad (2.2)$$

with the effective diameter d_e of the pinhole

$$d_e = \left(d^2 + \frac{2d}{\mu_c} \tan \frac{\omega}{2} \right)^{1/2} \quad (2.3)$$

Here, b is the distance between an object point and the collimator, φ is the incident angle of the photon, d is the diameter of the pinhole, ω is the opening angle of the pinhole, R_i is

the intrinsic resolution of the detector, M is the magnifying factor employed for the pinhole collimation, and μ_c is the linear absorption coefficient of the collimator material.

As indicated in the equation, the smaller the diameter of the pinhole, the higher the geometric resolution of the pinhole collimator. However, this resolution improvement is achieved at the expense of considerably reduced sensitivity. Recently, several groups have demonstrated that novel multipinhole collimation substantially improves sensitivity while retaining outstanding resolution [64-66]. This achievement significantly extends the capabilities of SPECT to image small-scale tissues containing fine structure such as pancreas, thyroid and brain. In the past few years, new “slit-slat” collimation has been proposed to combine the pinhole's magnification in the transaxial direction with parallel- or fan-beam's complete-sampling properties and large field of view in the axial dimension [67]. Such a collimation is especially suitable for imaging mice owing to its specific design.

Position-sensitive PMTs have been widely used in modern gamma cameras. Owing to their excellent performance, a variety of PSPMT modules has been developed, tested and implemented for single-photon imaging mainly including Hamamatsu R5900 [68], R2486 [69], R3292 [70], H8500 [1, 71], H9500 [72]. Recently, PSAPD modules have become promising photodetectors for developing scintillation gamma cameras. Several studies [73, 74] have been carried out to demonstrate the performance of PSAPD modules produced by Radiation Monitoring Device (RMD, www.rmdinc.com). Some other studies show that a CCD-based gamma camera can be another promising alternative for single-photon imaging with high performance [75, 76].

Common scintillators for single-photon imaging and their properties are listed in Table 2.4 [77]. The most widely used scintillator is NaI(Tl) which has an efficient light output (38000 photons/MeV). Since long decay time is of relatively less concern for SPECT in comparison with PET, CsI-based scintillators are also a good choice for SPECT imaging. While short decay time and high light output make LaBr₃ a promising scintillator for developing time-of-flight PET, this scintillator is also of great interest to researchers developing SPECT detectors because of its high energy resolution [77-79].

	Density (g/cm ³)	Decay time (ns)	Light yield (% NaI)	Hygroscopic
NaI(Tl)	3.67	230	100	Yes
CsI(Tl)	4.5	1000	45	No
CsI(Na)	4.51	630	85	No
LaBr ₃ (Ce)	5.3	23	160	No

Table 2.4. Properties of typical scintillators for SPECT [77]

As in applications to PET, room-temperature semiconductor detectors become promising and attractive as an alternative to conventional scintillation detectors because of their high energy resolution and compactness. Evaluation of detectors based on CdTe and CdZnTe (CZT) has been carried out [80, 81]. Results demonstrate the excellent performance of those semiconductor detectors suggesting their potential for small animal imaging.

2.4.3 SPECT system design

Unlike PET, there is no need to pair gamma cameras in SPECT. This results in a diversity of configuration for SPECT systems. The conventional configuration is a rotation system with single/multiple detectors in a circular orbit that is positioned perpendicular to the axis of rotation (AOR). Both parallel-hole and pinhole collimation

have been implemented in such systems [68]. Effected by incorporating the circular orbit with the displacement of the object under investigation along the AOR, a helical orbit (helical SPECT) has been introduced to address the issue of sampling completeness in pinhole circular SPECT [67]. In contrast to such a rotating system, a stationary system has been developed using no detector rotation. Instead, movement of the object under investigation is required. A simple stationary configuration similar to a circular rotation system can be effected by rotating the object instead of the detector(s) [82]. The appearance of novel collimator technology has advanced the development of modern stationary configurations. One new configuration translates the object through the FOV of single/multiple stationary multipinhole detectors and is referred to as Translatory SPECT (T-SPECT) [83]. Another configuration (mouseSPECT) requires no rotation of the object but the collimator rotates to achieve complete tomography with stationary large annular detectors [84]. Complete stationary systems (USPECT-I/II and FastSPECT II) requiring no movement of detectors and the object have been developed by implementing both multiple detectors and multipinhole collimators [64, 85].

2.4.4 Image reconstruction

As applied to PET imaging, the same principle algorithms i.e. analytic and iterative methods have been widely implemented in SPECT. Analytic methods have shown sufficient accuracy and efficiency for parallel-hole SPECT [86]. However, iterative methods gather more attention owing to both the complexity of implementing analytic methods in pinhole SPECT and the advent of fast computation including high-speed computers and accelerated algorithms such as OSEM [87].

A ML-EM algorithm for emission tomography (PET and SPECT) can be expressed as:

$$\lambda_i^{(n+1)} = \frac{\lambda_i^{(n)}}{\sum_{j=1}^d p_{ij}} \sum_{j=1}^d \frac{y_j p_{ij}}{\sum_{k=1}^s \lambda_k^{(n)} p_{kj}} \quad (2.4)$$

where, $i : 1, 2, \dots, s$; the labeling number of voxels in the object space for reconstruction

$j : 1, 2, \dots, d$; the labeling number of detectors.

$\lambda_i^{(n)}$: estimated radioactivity in i^{th} voxel in the object space after n iterations.

p_{ij} : probability that a photon emitted by i^{th} voxel is recorded by j^{th} detector

y_j : number of photons recorded by j^{th} detector

As indicated in this equation, the key to reconstruct the unknown object space λ_i is to determine the transition matrix p_{ij} . Li *et al.* has described in detail an analytic method to obtain each entry of this system matrix for pinhole SPECT imaging with a displaced center-of-rotation [88]. Siddon's ray-tracing technique has been implemented in that work in order to obtain the length of a ray in each voxel it intersects [89]. The experimental phantom tests have demonstrated that this method can effectively address the problems caused by misalignment of center-of-rotation. Corresponding to the analytic ways to determine system matrix p_{ij} , some groups have implemented more flexible numeric methods that can be easily adapted to complex pinhole shapes [66]. However, these numeric methods usually require higher computation resources.

2.4.5 Reported SPECT systems for small animals

Based upon advances in gamma-ray imaging technology, several groups have developed novel imaging systems with excellent performance for small animal research. These systems have been built with PSPMT or PSAPD-based scintillation detectors or semiconductor detectors equipped with a variety of collimators including parallel-hole, pinhole, slit and slit-slat. A review in this section indicates that SPECT imaging with good resolution and good sensitivity has been the goal of much research.

Parallel-hole SPECT continues to receive attention as a conventional imaging technology and a useful tool for biological studies. Kubo *et al.* have built a small animal SPECT system using CdTe semiconductor detectors equipped with a parallel-hole collimator. The achievement of high sensitivity and low scatter radiation by their system allows good quantitative analysis [90]. Owing to the increasing requirements of high resolution for small animal imaging, pinhole SPECT has received significant attention and development in the past several years.

Qi *et al.* have reported a desktop single-pinhole SPECT system for small animal imaging with a high resolution on the order of 1 mm [91]. The same technology has been used in commercial animal SPECT systems, X-SPECT and A-SPECT, from Gamma Medica Inc [92]. As mentioned above, high resolution with single-pinhole SPECT is achieved at the cost of poor sensitivity. Small animal studies may require a high level injection dose or a long imaging time when using single-pinhole SPECT. Therefore, great interest has been given to the development of multipinhole SPECT.

Several groups have demonstrated the feasibility of multipinhole SPECT in small animal imaging. Schramm et al [66, 93] presented multipinhole SPECT systems based on commercial gamma cameras and dedicated multipinhole collimators. They have carried out multipinhole imaging with high resolution as well as superior sensitivity based on commercial clinical equipment. In the recent report [93], they compared the performance of two multipinhole systems based on two commercial SPECT systems: a dual-headed Siemens ECAM and a triple-headed Trionix TRIAD. Both systems yield excellent performance in resolution and sensitivity. Lackas *et al.* developed a translatable SPECT system with two orthogonal and stationary multipinhole detectors, taking advantage of the movement of the relatively low-mass object instead of the more massive detectors [83]. They recently reported progress on the development of a proposed dual-modality SPECT/CT system specialized for rat brain studies [94]. Compact commercial gamma cameras equipped with multipinhole collimators were incorporated with a cone-beam CT system for better orientation in SPECT images. An additional 3D translation stage facilitated helical scan orbit for both modalities. Their initial studies achieved a resolution about 1.2 mm for SPECT and 300 μ m for CT. Bioscan Corporation is now providing commercial NanoSPECT/HiSPECT systems based on the work of the Schramm and Lackas group. Meikle *et al.* [65, 95] have reported a coded multipinhole SPECT system using detectors of their design based on Hamamatsu PSPMT modules. The performance has shown its suitability for certain high-resolution imaging applications in small animal studies. Using sixteen cameras, each of which was equipped with a single-pinhole collimator, Furenlid *et al.* developed a completely stationary SPECT system (FastSPECT II) presenting great potential for dynamic SPECT imaging [85]. Beekman *et al.* [64, 96]

proposed a novel stationary U-SPECT series incorporating multipinhole collimation without multiplexing. The U-SPECT-I system incorporating 75 gold pinholes and standard NaI detectors had demonstrated a combination of ultra-fast, ultra-sensitive and ultra-high resolution. Their U-SPECT-II/CT system is commercially available now with even better performance. Goertzen *et al.* [84] designed and constructed a multipinhole SPECT system (called “mouseSPECT”) with a stationary clinical scanner and a rotating collimator, which efficiently balances the resolution and sensitivity and has potential for dynamic imaging of small animals. Perterson *et al.* [97] reported the development of a multipinhole SPECT system equipped with silicon strip detectors. The results from their prototype system proved its feasibility for small field-of-view studies such as the mouse brain. Mok *et al.* [98] proposed a pinhole collimation system allowing flexible single- and multi-pinhole SPECT of small animals of different size and achieving optimum imaging in terms of their size. Hesterman *et al.* designed and built a novel multi-module, multi-resolution four-head SPECT system (M³R) for small animal imaging. This flexible system features interchangeable multipinhole plates for a variety of magnifications and pinhole configurations, which allows task-oriented system optimization for imaging applications [99]. Kim *et al.* developed the first full small-animal SPECT imager (SemiSPECT) based upon eight compact CZT detectors with high-intrinsic resolution. This achievement demonstrated the feasibility of simultaneous operation of multiple CZT detector arrays in a practical SPECT, which required solutions to issues including electronics, temperature control and mechanical assembly [100]. Funk *et al.* [101] designed a multipinhole SPECT system based on position sensitive avalanche photodiode

detectors (PSPADs). Their simulation results suggest submillimeter spatial resolution and potential for high throughput and low-dose SPECT imaging of small animals.

To solve the axial blurring of circular-orbit pinhole SPECT, Metzler *et al.* [67, 102-105] reported the application of the helical orbit conventionally used in transmission computed tomography (TCT) to imaging with SPECT. They compared the difference of sampling completeness and its dependence on radius of rotation between a circular orbit and a helical orbit. A laser alignment system was designed and incorporated into the setup of a helical SPECT system based on a clinical scanner. Phantom studies and molecular imaging of small animals were carried out to demonstrate the capability of helical SPECT in accomplishing high resolution and high sensitivity without sacrificing sampling completeness. Their recent study evaluated the effect of angular-dependent axial-shift correction on the axial resolution of pinhole SPECT. Patil and Metzler [106] also compared the improvement in axial resolution between helical SPECT systems with step-and-shoot motion and continuous motion. Sun *et al.* [107] have presented a helical SPECT scanner for small animals which features CZT detectors. Their initial results demonstrated improved axial spatial resolution and field of view (FOV).

Other developments in small animal SPECT systems include slit SPECT and slit-slat SPECT. Zeng *et al.* reported their development of SPECT imaging using a CZT strip detector equipped with a slit collimator [108]. Preliminary phantom studies indicated that this system outperformed pinhole SPECT imaging with a larger scintillation detector. Metzler *et al.* have recently re-evaluated the resolution and sensitivity of a slit-slat collimator [109]. Their results imply a possible niche for slit-slat collimation between

pinhole and parallel/fan beam collimation with improvements in sensitivity, resolution and sampling completeness [109].

To improve the accuracy in locating the radiotracer, dual-modality small animal imaging systems are also of interest. Hwang *et al.* [110] are building a dual-modality system incorporating X-ray CT and microSPECT for small animal imaging. Hong *et al.* have reported a SPECT/CT system suitable for functional imaging of small animals with high-resolution morphology information [111]. By combining a low-field MR imager and a small animal SPECT system, Goetz *et al.* [112] proposed a potential low-cost solution to achieve dual-modality imaging for preclinical studies.

2.4.6 SPECT radiotracers and applications

There is a range of radioisotopes used for SPECT imaging as listed in Table 2.5 along with their properties. As mentioned before, ^{125}I is of particular interest to the work carried out here because of its low emission energy, long half-life, and commercial availability of a large body of ^{125}I -tagged ligands. One disadvantage of ^{125}I , however, is that the applicable dose of ^{125}I should be kept as small as possible while its half life broadens the time window for imaging. In addition to ^{125}I -tagged radiotracers, a number of ligands labeled with other radiotracers such $^{99\text{m}}\text{Tc}$ and ^{131}I have also been developed. The large body of available ligands broadens the range of biological targets for SPECT imaging and provides a variety of opportunities to study biological or human health issues using small animals [86].

Isotope	Half-life	Energy (keV)
^{99m} Tc	6.02 hr	140
¹²⁵ I	60.2 day	30
¹²³ I	13.3 hr	159
¹³¹ I	8.2 day	364
¹¹¹ In	2.8 day	171 / 245

Table 2.5 Typical radioisotopes used in SPECT imaging [86]

Small animal SPECT has been applied in a number of such studies. A substantial portion of these studies focuses on brain [113] and myocardium [114]. Using a mouse model, studies of renal function and inflammatory bowel disease have been carried out with dedicated SPECT systems [115]. Thyroid function and small-animal tumors are two areas receiving considerable attention [116] and are also of interest to the work described in this dissertation. Details about specific studies carried out in this project can be found in Chapter 5 and Chapter 6 respectively, including a re-evaluation of potassium iodide blocking efficiency and visualization of sodium iodide symporter (NIS) in the mouse thyroid, and an imaging study of mouse mammary tumors.

2.5 Discussion of small animal radionuclide imaging

Among all the available imaging techniques, radionuclide imaging has been the most important one to achieve functional information. PET has shown exquisite advantage in sensitivity. Recent breakthroughs in spatial resolution to submillimeter dimensions makes PET a promising modality for a wider range of applications. However, the half-life window of PET radiotracers can limit its application in measuring slow biological processes such as cell division occurring over hours or days [86]. The cost of PET imaging is relatively high considering system instrumentation and radiotracer

preparation. As a complementary approach, SPECT has shown considerable promise to meet imaging requirements in a number of preclinical studies. SPECT has unique capabilities to probe endogenous ligand interactions, to measure slow kinetic processes and to simultaneously probe multiple molecular pathways [86].

A diversity of SPECT systems has been developed with different performance owing to recent advances. Trade-off always exists among those systems regarding the FOVs, sensitivities, resolutions and costs. Different studies can have different requirements in those aspects and require adjustment accordingly. However, the available small animal SPECT systems are much less flexible and some are unable to make such adjustment readily.

Recent development of multipinhole SPECT has provided new opportunities for high-resolution imaging of small animals with high sensitivity. The presence of the magnifying factor to improve spatial resolution, however, usually reduces the FOV of the detector. A helical orbit can extend the FOV along the AOR while improving sampling completeness of the pinhole collimator. Combination of multipinhole SPECT and a helical orbit thus provides a promising way to image large objects with high performance in resolution and sensitivity.

The following chapters describe the development and application of a compact gamma-ray imaging systems which can readily meet a wide variety of imaging requirements for resolution, sensitivity and FOV. This system is the first one incorporating multipinhole circular/helical SPECT, parallel-hole imaging (planar projection or tomography) and X-ray imaging. In addition to the development of novel detectors, unique multipinhole helical SPECT has been incorporated into the system. The

system has been evaluated based upon phantom studies. Applications of this system to several biological experiments have demonstrated the efficacy and versatility of this system for *in vivo* small animal research.

Chapter 3

Evolution of our imaging system

This chapter describes the development of our imaging system in which I have participated during the past several years. Section 3.1 presents a description of dual-modality imaging, which was achieved by incorporation of a small x-ray fluoroscope, followed by the development of simultaneous gamma-ray imaging with parallel-hole and pinhole collimation in Section 3.2. Section 3.3 details the calibration and performance evaluation of novel “mouse-sized” compact gamma cameras designed particularly for biological studies in the mouse model. Some results presented here have been published as journal articles [1, 117] or conference records [118, 119].

3.1 X-ray/gamma-ray dual-modality planar imaging

As discussed in Chapter 2, multi-modality imaging combining functional imaging with anatomical information can facilitate better interpretation of functional data with precise structural detail. This is especially useful in gamma imaging when evaluating the physiological or pathological response of a small animal to a given radiotracer. The additional anatomical information will enable one to determine the organs or tissues where the radioactive compound is distributed. Therefore, in the early stages of this work we enhanced our gamma imaging system by incorporating a fluoroscopic X-ray apparatus (see Fig. 3.1) in order to achieve dual-modality imaging [117]. We seek more

precisely to identify the distribution and location of ^{125}I -tagged compounds in the mouse through the fused image obtained by superimposing the anatomical X-ray image of a mouse with the gamma image. In order to validate the efficacy of this dual-modality planar imaging technique, we also carried out a proof-of-concept study of radioiodine uptake in mice blocked with stable potassium iodide (KI) in comparison with an unblocked control mouse. My major contribution to this work included data acquisition and performance evaluation of both gamma and X-ray imaging, design of the mouse bed, fusion of gamma and X-ray images, and their application in the proof-of-concept studies.

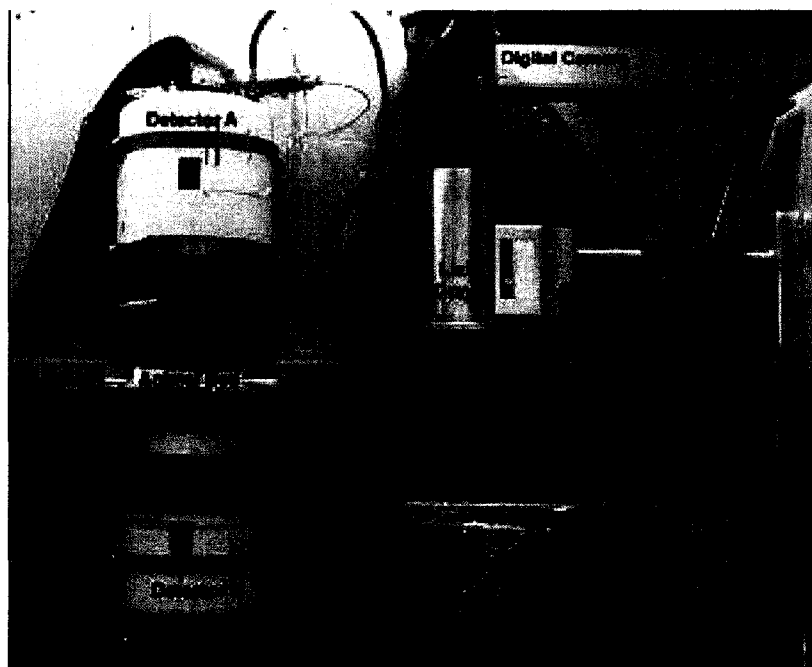


Fig. 3.1 Photograph of the imaging system incorporating both gamma- and X-ray modalities [117].

3.1.1 Performance of gamma and X-ray imaging

The gamma camera employed in this work had been developed previously and is described elsewhere in greater detail [69]. Briefly, the 110 mm diameter circular detector was based on a Hamamatsu R3292 PSPMT module air-coupled to an array of pixellated CsI(Tl) scintillators, in which each crystal measured $1 \times 1 \times 3 \text{ mm}^3$ with 0.2 mm separation between adjacent crystals. A 3 mm thick copper-beryllium parallel-hole collimator suitable for use with ^{125}I was employed in this work for high-resolution imaging. That collimator was fabricated of Cu-Be with 0.2 mm square holes separated by 0.05 mm walls. Programs developed with data acquisition software Kmax (Sparrow, Inc.) were implemented to obtain the raw data of gamma imaging. Those data were then analyzed using image analysis programs written in IDL language (Research Systems Inc.).

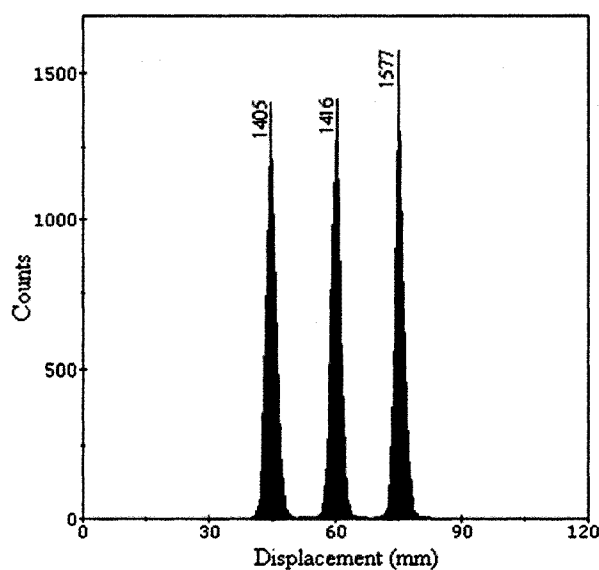


Fig. 3.2. A profile of the three hot spots in a one-hour gamma image. The phantom contained three spots with 15 mm spacing in a line. Each spot was loaded with $2 \mu\text{Ci}$ of ^{125}I [117].

We determined the resolution of the detector for ^{125}I imaging using a three-spot source. Three 1 mm deep, small depressions with 15 mm spacing were drilled in a line in

a plastic plate measuring $50 \times 50 \times 3 \text{ mm}^3$. Each spot was loaded with $2 \text{ } \mu\text{Ci}$ of ^{125}I . The three-spot source was placed 5 mm away from the collimator surface and imaged for one hour. Shown in Fig 3.2 is the profile of the three-spot source in the whole-hour image. A Gaussian fit to one of the peaks achieved a spatial resolution (FWHM) of just under 2 mm. The measured efficiency of the detector using the same phantom was $70 \pm 10 \text{ cpm}/\mu\text{Ci}$.

The small Lixi fluoroscopic X-ray apparatus [120] was employed for anatomical imaging of the mouse. This device has a 50 mm diameter effective view area. View area limitation necessitated making a composite view of the entire mouse with a series of X-ray images. On the other hand, the small size of the X-ray equipment made it an excellent choice for easy incorporation into the existing gamma imaging system and development of a compact dual-modality imaging system for biological research.

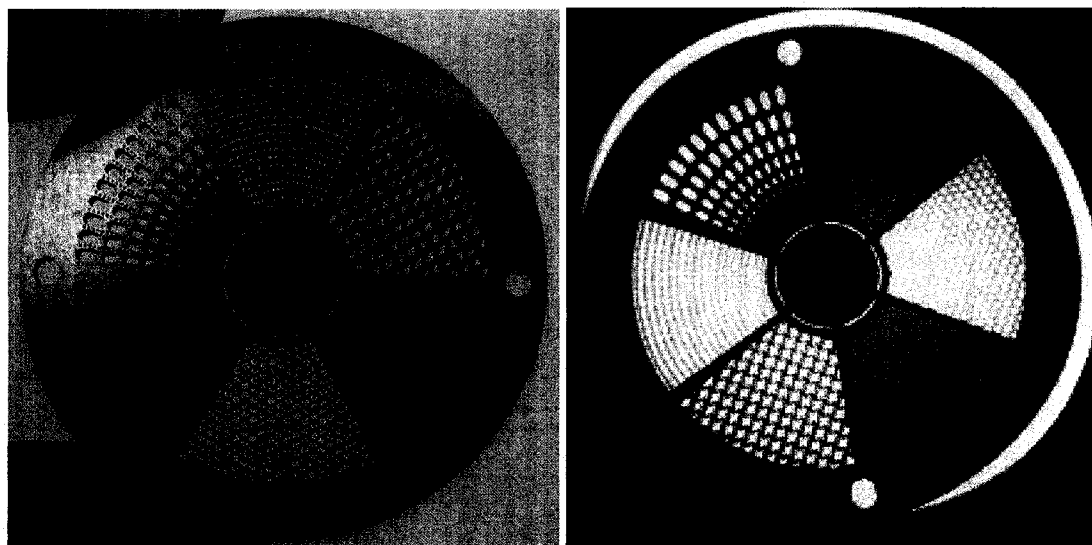


Fig. 3.3. A picture of the X-ray phantom made with CuBe and its X-ray image

The performance of the fluoroscope was assessed by using the X-ray device to image a small copper-beryllium disk shown in left panel of Fig. 3.3. This disk contained

etched holes with a variety of diameters. The smallest hole was 100 μm in diameter. As demonstrated by the right panel in Fig. 3.3, the smallest holes could be clearly resolved indicating that our fluoroscope could provide a spatial resolution of 0.1 mm with potential for better results.

3.1.2 Mouse bed and formation of the composite image of an entire mouse

Formation of a composite X-ray image of an entire mouse required a reference for alignment of the successive X-ray images of a part of the mouse body. A specially designed mouse bed served not only to support the mouse during imaging but also as a useful tool for formation of the composite image. Presented in Fig.3.3 is such a mouse bed made with balsa wood. Fine nichrome wire is imbedded and serves dual purposes as both a heater to keep the animal at appropriate body temperature during the imaging period and a reference for alignment when making the composite X-ray image. For more precise alignment, 1 mm diameter metal spheres were also imbedded in a line on each longitudinal side of the bed at 1 cm intervals. This design of the mouse bed ensured accurate, easy formation of the composite X-ray image of a mouse with negligible side-effects from the nichrome wire and metal spheres in gamma and X-ray imaging.

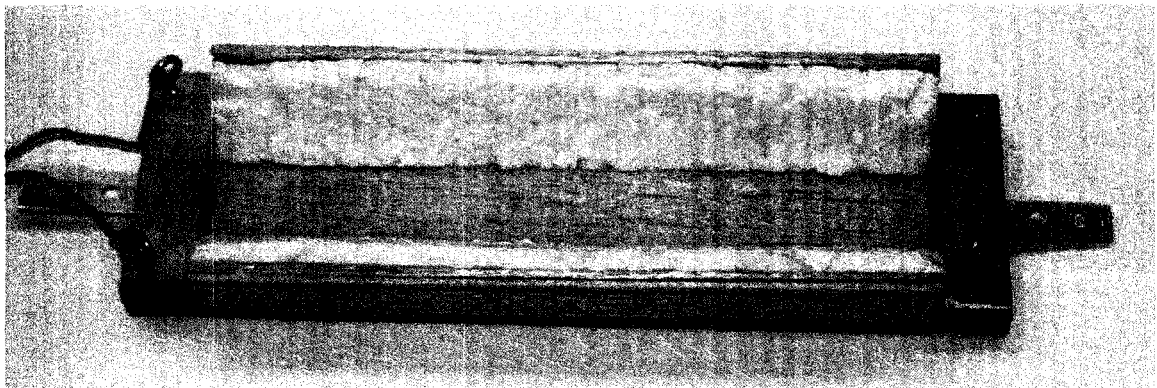


Fig. 3.4. Photograph of the mouse bed. Fine heating wires and 1-mm metal spheres were embedded for X-ray image alignment.

As Fig. 3.1 shows, the X-ray system positioned near the gamma cameras and the track supporting the mouse bed. When imaging, the anesthetized mouse placed on the mouse bed could be easily translated to an appropriate position for either gamma or X-ray imaging through the track. X-ray imaging was usually carried out immediately after gamma imaging of a mouse. A set of raw X-ray planar images from the Lixi fluoroscope was captured by a Canon G1 digital camera with the imaging window of the device focusing on 5 to 7 consecutive areas sufficient to cover the whole body of the mouse. The data were then transferred and stored in a Macintosh G4 computer for further image processing. Using the image processing software Photoshop, each of the X-ray images was cropped and corrected for distortion based on the image of a fine metal grid. Thereafter, the group of processed images was visually overlaid with opacity of each image set to 45% by referring to both the imbedded nichrome heating wires and metal spheres. Examples of the composite image of a mouse are shown in the bottom frames in Fig. 3.5.

3.1.3 Fusion of gamma-ray and X-ray images

Once a composite X-ray image of the entire mouse was produced, it could be fused with the gamma image acquired prior to the X-ray imaging to form the dual-modality gamma/X-ray image. However, such fusion requires reference points for co-registration of these two different types of images. Reference points were needed near the mouse to be visible in both gamma and X-ray imaging in order to facilitate overlaying the two images precisely. Metal toroids of 2 mm inside diameter into which ^{125}I has been loaded play the key role as a reference for fusion of gamma and X-ray images. These

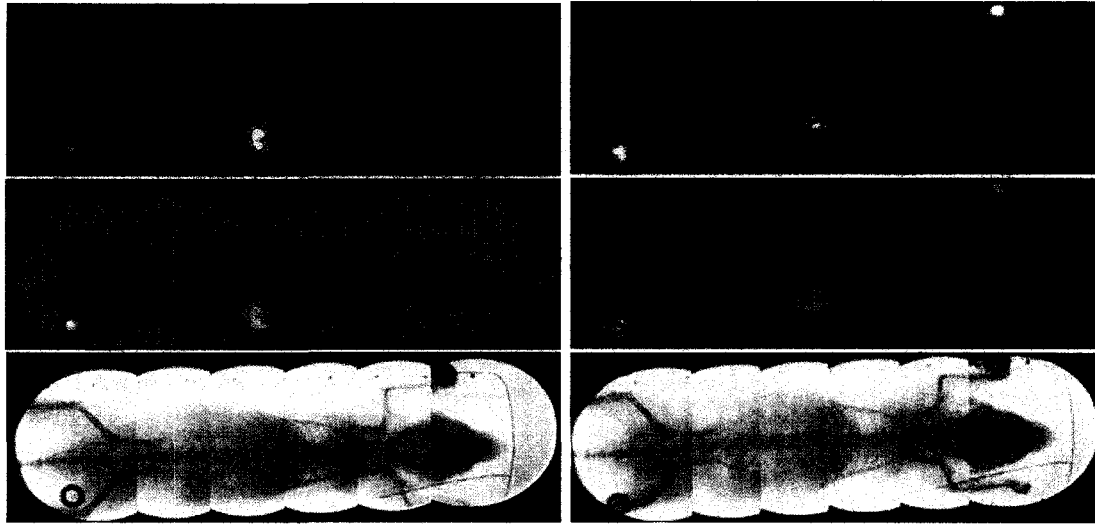


Fig. 3.5 Fusion of gamma-ray and X-ray images for unblocked (left) and KI-blocked cases (right), respectively. Each case contains a gamma image of the mouse on the top and a corresponding composite X-ray image at the bottom with their fused image presented in the middle [117].

fiducial marks were put in select positions of the mouse bed with negligible effect on the imaging and data analysis. Both the gamma camera and the X-ray device could readily observe these fiducial marks, which appeared as hot spots in gamma images and as dark rings in X-ray images (see Fig. 3.5). This allowed us to overlay gamma images on X-ray images easily and visually with opacity set to 30%-50%. The middle frames in Fig. 3.5 show an example of the fused gamma/X-ray images.

3.1.4 Proof-of-concept studies

Potassium iodide (KI) is an FDA-recommended agent to protect the thyroid from accumulating radioiodine in the event of accidental release of radioactive contamination. The blocking effects of KI have been reported and evaluated in a number of studies [121-123]]. In order to validate the efficacy and demonstrate the utility of dual-modality

gamma/X-ray imaging in biological research, we carried out *in vivo* proof-of-concept studies of radioiodine uptake in mice blocked with KI in comparison with control mice with no KI administered prior to radioiodine injection. A dose of 1% KI solution was administered orally to a mouse 60 minutes before the intramuscular injection of 4.8 μCi of radioiodine (as NaI) into the same mouse. Both the KI-blocked and control mice were imaged for 60 minutes immediately following the administration of radioiodine. The distribution of radioiodine in both KI-blocked and unblocked cases was analyzed and compared to assess the blocking effects of stable KI in mice and the advantages brought by incorporation of anatomical information in gamma images.

Presented in Fig. 3.5 are examples of unblocked (left in the figure) and KI-blocked (right in the figure) dual-modality images. Top frames in Fig. 3.5 are gamma images obtained during 40-50 minutes post radioiodine injection. Bottom frames are composite X-ray images of the entire mouse. Central frames are fused gamma/X-ray images. The integrated images precisely indicate that major radioiodine uptake is located in the thyroid and stomach regions of the mice. As expected, a KI-blocked mouse presented much less uptake of radioiodine in the thyroid than an unblocked mouse. A significant portion of radioiodine was accumulated in the stomach region in either case. Greater detail about the difference between the two cases can be revealed through region of interest analysis [117].

Shown in Fig. 3.6 are the dynamic changes of the distribution of radioactive iodine in KI blocked and unblocked mice over the first hour post injection. The three gamma images in each group in Fig. 3.6, from top to bottom, represent the radioiodine

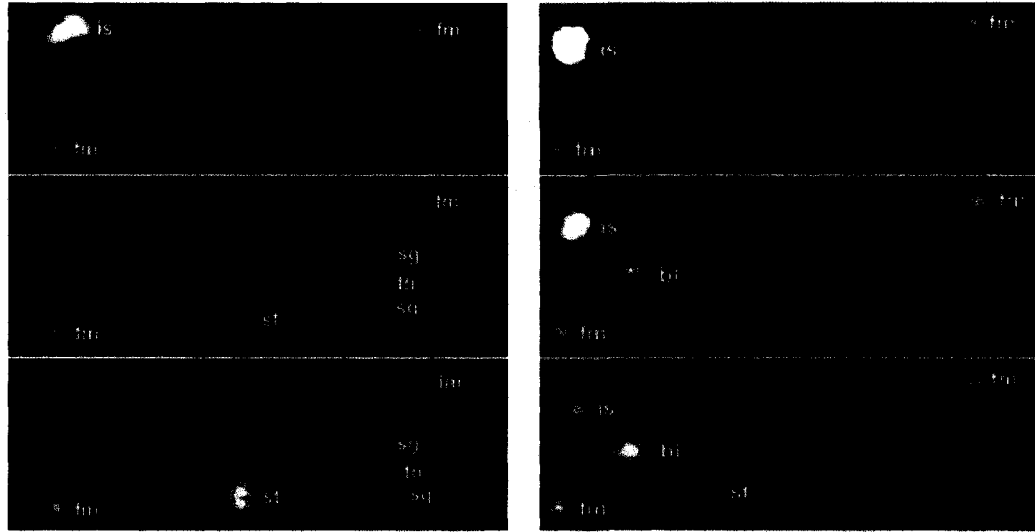


Fig. 3.6. Gamma images presenting the dynamic change of radioiodine distribution in unblocked (left) and KI-blocked (right) mice. The time period from top to bottom were 0-10 min, 20-30 min and 40-50 min post injection of $14 \mu\text{Ci Na}^{125}\text{I}$. Here, sg stands for salivary glands, th thyroid, st stomach, fm fiducial mark, is injection site, and bl bladder [117].

distribution during 0-10, 20-30, 40-50 min imaging periods, respectively. With the precise anatomical information provided by dual-modality images (see bottom frames in Fig. 3.5), ROI plots can readily determine that most radioiodine was accumulated in the thyroid and stomach regions for the unblocked mouse over the time. However, the KI-blocked mouse presented high quantity of radioiodine in the bladder and slow disappearance of radioiodine from the injection site as well as much less uptake in the thyroid.

3.1.5 Conclusion

By incorporating an X-ray imaging system into our gamma imager, we developed an imaging system capable of dual-modality planar imaging. The proof-of-concept studies validated the efficacy and demonstrated the advantages of dual-modality imaging

in biological research. This system allowed us to image temporal and spatial metabolic binding patterns *in vivo* of ^{125}I -tagged radiotracers accurately with precise structural information [117]. Moreover, this real-time gamma imaging system provides a novel approach to address the concerns of KI-blocking efficiency and safety in both animal and human studies [117], and has been presented in a recently published paper [2] (see also Chapter 5).

3.2 Simultaneous parallel-hole/pinhole gamma-ray imaging

As indicated in Chapter 2, gamma imaging of small animals has been a promising technique in nuclear medical imaging with the capability of providing valuable functional information and potential application in biomedical studies. The dual-modality imaging described above has demonstrated the utility of planar gamma imaging with parallel-hole collimation. Planar imaging can expose the distribution of radiotracer in the whole body of a mouse. However, details about the distribution of radiotracer in a specific organ or tissue may still remain unclear due to the resolution of parallel-hole imaging in the order of 2 mm. Such details may be useful in studying the physiology or pathology of organs or tissues such as thyroid or stomach. As one of the methods for collimation, pinhole collimation is well known for its suitability for high-resolution imaging. In addition to parallel-hole imaging to obtain whole-body information of a small animal, simultaneous pinhole imaging focusing on a specific organ or tissue can help researchers to obtain organ- or tissue-specific information with greater detail at the same time. Furthermore, though planar gamma imaging continues to present utility in numerous biological studies, gamma-ray computed tomography, i.e. SPECT is becoming an effective tool to determine

the biodistribution of radioactive ligands in three-dimensional space. Researchers will certainly benefit from the information from an additional dimension by overcoming the potential ambiguity brought by planar imaging. A further development of SPECT imaging can significantly expand the capability of the imager in achieving tomographic information without sacrificing the animal.

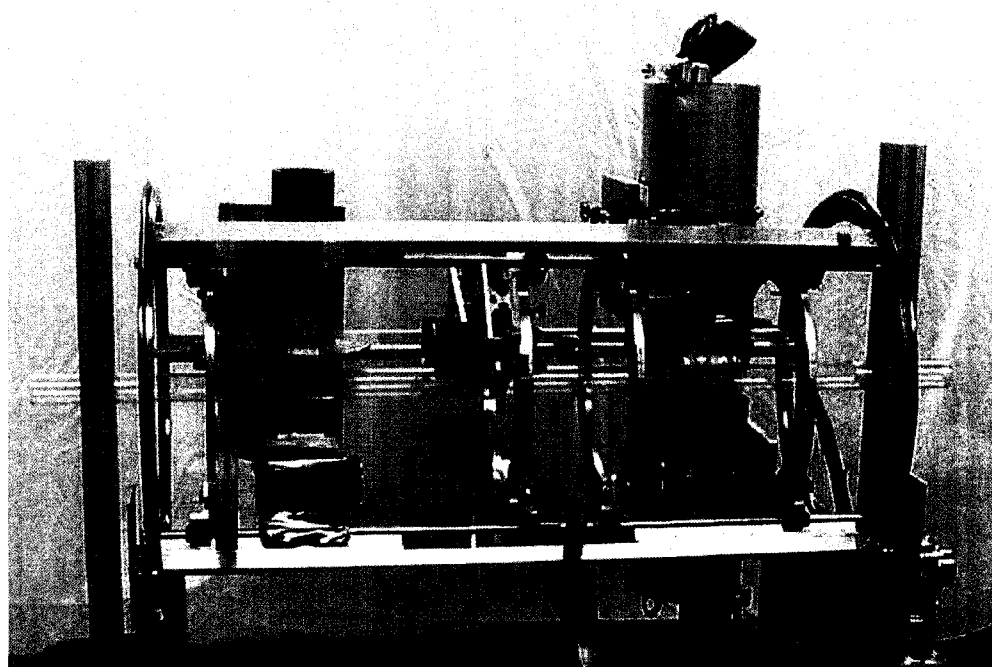


Fig. 3.7, Imaging system incorporating two 110 mm diameter circular gamma cameras and a fluoroscopic X-ray apparatus. The top gamma camera was equipped with pinhole collimator while the bottom camera with parallel-hole detector [118].

For these purposes, we sought to accomplish simultaneous gamma-ray imaging with parallel-hole and single-pinhole collimation by using a pair of 110 mm diameter circular detectors. Attempts to facilitate SPECT imaging were also carried out. Presented in Fig. 3.7 is the developed system incorporating two gamma cameras and a fluoroscopic X-ray apparatus. In this work, I have calibrated one of the gamma-ray detectors for

pinhole collimation equipped with a new pixellated NaI(Tl) scintillator, incorporated the detectors onto a cylindrical gantry for planar imaging or tomography, and carried out several proof-of-concept studies using this system.

3.2.1 Gamma cameras for parallel-hole and pinhole imaging

Both gamma cameras shown in Fig. 3.7 are 110 mm diameter circular detectors. The gamma camera for parallel-hole imaging has been described in subsection 3.1.1. In comparison with the parallel-hole gamma camera, the camera employed for pinhole imaging was also based on a Hamamatsu R3292 PSPMT module but was equipped with a crystal NaI(Tl) array of scintillators and a single-pinhole collimator. Described here is the calibration of the detector with the new scintillators employed. Detector calibration included three major steps: making the crystal lookup table, energy calibration and the uniformity correction.

The scintillators were a circular array with a diameter of 88 pixels. In this array, each crystal scintillator pixel measured $1 \times 1 \times 5 \text{ mm}^3$ with a pitch of 1.2 mm between two adjacent elements. Presented in the top panel of Fig. 3.8 is a raw crystal image, obtained by using high energy gamma rays ($\sim 660 \text{ keV}$) emitted from a point source of $\sim 15 \mu\text{Ci } ^{137}\text{Cs}$. The source was placed about 50 cm above the detector surface and imaged for two days. No collimator was employed during this imaging. With the high energy gamma rays, nearly each crystal element could readily be identified. A crystal lookup table (see Fig. 3.8, bottom panel) was then generated using a program developed with Kmax software and this raw crystal map. When this two-dimensional lookup table was

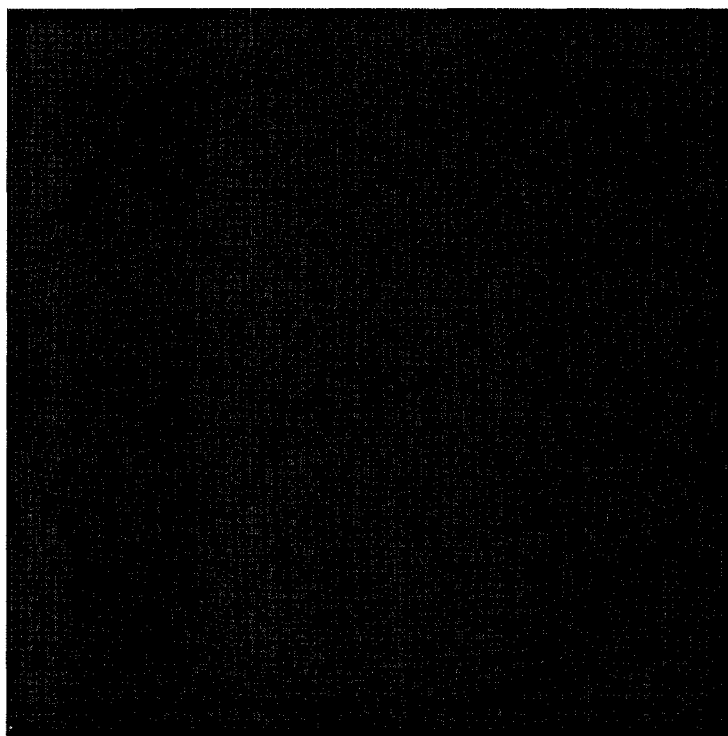
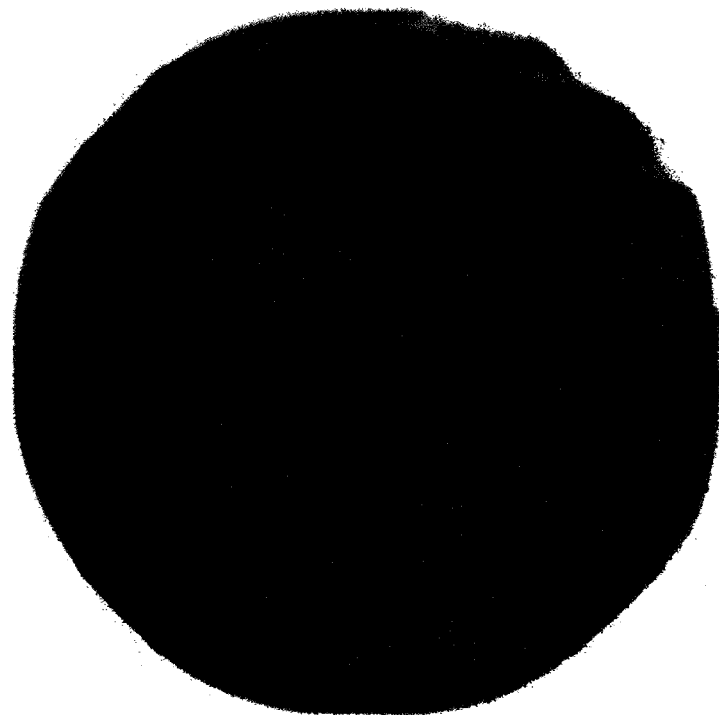


Fig. 3.8 Raw crystal map of the scintillator array (top) obtained with $\sim 15 \mu\text{Ci } ^{137}\text{Cs}$ (~ 662 keV) and crystal lookup table (bottom) based on this raw image.

implemented back into the data acquisition program, the exact crystal element that a detected gamma ray intersected could be determined by examining the position of that gamma ray. When each of the detected gamma rays was mapped to a two-dimensional image by referring to the crystal lookup table, we were able to achieve a gamma ray image representing the spatial distribution of the radioactive source.

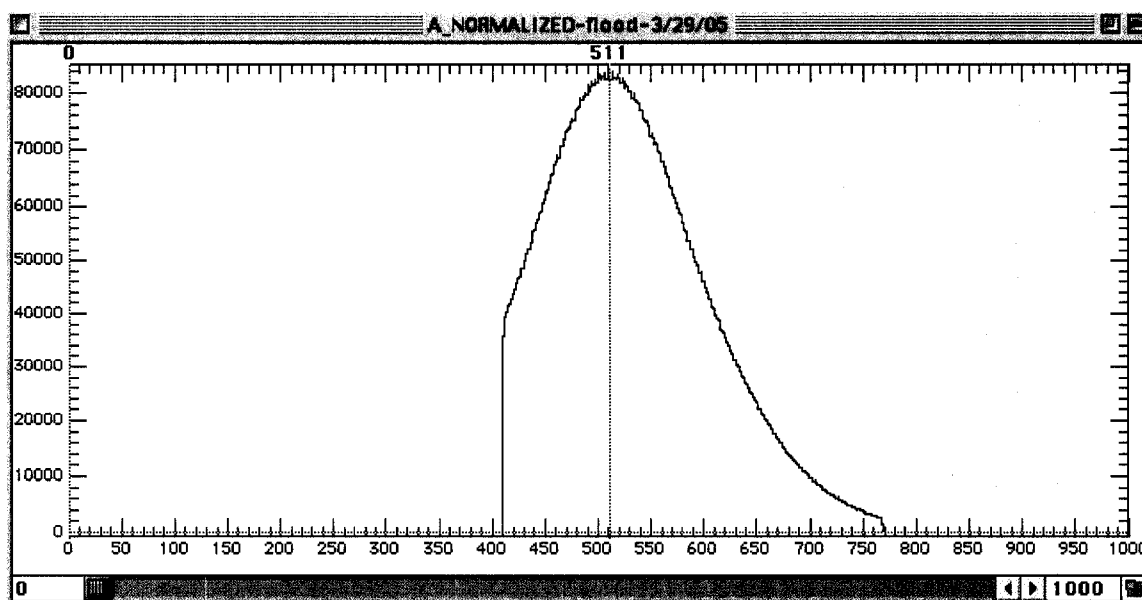


Fig. 3.9 Normalized energy spectrum of ~ 35 keV gamma rays emitted by ^{125}I . The truncation in the spectrum is because the energy window was set to accept only photons from 28 keV to 53 keV.

Since the crystal elements are not ideally identical and the response of the PSPMT not uniform, the energy response of the scintillators was not the same either. In order to obtain the best energy resolution of gamma imaging, an energy lookup table was necessary for energy calibration of individual scintillators. Because the energy response of the scintillators depends on the energy of gamma rays, the source selected for energy calibration should be the radioisotope, in our case ^{125}I , intended for use in the biological studies. A point source containing 200 μCi Na^{125}I was placed about 1 meter away from

the face of the detector with no collimator. The imaging lasted about 4 hours. Using a specific Kmax program for energy calibration, the energy spectrum of each crystal element was determined and the maximum value of that spectrum was recorded. The energy lookup table is the vector containing the maximum spectral values of individual crystals. The energy of each detected gamma ray was calibrated by referring to this lookup table implemented in the data acquisition program. Presented in Fig. 3.9 is the energy spectrum of 35 keV gamma rays of ^{125}I after the normalization.

After both crystal and energy lookup tables were implemented, a flood imaging with a uniform source of the target radioisotope is required for correction of non-uniformity of the detector. Unlike the case of parallel-hole collimation, the correction did not require the collimator to be employed for the case of pinhole collimation. The same point source for energy calibration (200 μCi Na^{125}I) was positioned 1 meter away from the surface of the detector and imaged 4 hours using the data acquisition program. The resulting image presented in the window "Image Full" was saved and implemented back into the data acquisition program for non-uniformity correction for future gamma imaging. This correction was automatically carried out by an embedded algorithm in the program.

After detector calibration, we designed and built an aluminum barrel which allowed us to install the 110 mm diameter detector in combination with a pinhole collimator with a select magnifying factor. A tungsten collimator was employed containing an array of pinholes. Only the central pinhole was used initially with others shielded with 1.5 mm lead sheet, which was sufficient to block the 35 keV gamma

photons from ^{125}I . The collimator was 6.5 cm away from the surface of the scintillator array.

3.2.2 Setup of the imaging system

The cylindrical rotating gantry employed for setting up the imaging system has been reported previously [118] and is presented in Fig.3.7. Briefly, it measures 45 cm in diameter and 110 cm in length. The gantry can hold a variety of detectors such as 25 mm square or 110 mm diameter circular detectors and a Lixi fluoroscopic x-ray system [120]. Space exists for incorporation of additional compact detectors such as the “mouse-sized” detectors we developed recently [1]. The gantry can be rotated by a stepping motor (200 steps per revolution) which can be controlled manually by a wired remote controller or automatically by a G3 Macintosh computer through the stepping motor driver Velmex NF90 (Velmex Inc.). The computer communicates with the driver via the RS232 interface.

Both parallel-hole and pinhole detectors are positioned onto the gantry face to face through mounting rings. The rings are easily be moved along the axis of the cylindrical gantry, which facilitates the easy focus of the pinhole detector on a specific region of interest of the mouse body while imaging the entire mouse with the parallel-hole detector. The distance from the axis of rotation to either detector was 25 mm for SPECT imaging. A magnifying factor of 2.6 was used for pinhole imaging.

A 120 mm long Lexan tube placed horizontally at the center of rotation and in the field of view of gamma cameras and X-ray fluoroscope facilitates the transfer of the animal among the various imaging devices while supporting a custom-made mouse bed. The support tube with ~1.5 mm thick walls absorbs only ~7% of the 35 keV photons

from ^{125}I . Its transparency allows easy positioning and visual monitoring of the animal. The tube can also serve a dual purpose of keeping the animal in stable condition with introduction of warmed, humidified air from one end and preventing contamination of the environment by exhaust of gases from the other end via a tube leading to a filtered exhaust system [118].

3.2.3 Image reconstruction for SPECT imaging

The approaches to image reconstruction were based on the iterative maximum likelihood-expectation maximization (ML-EM) algorithm. The modified EM algorithm by Green [124] which was translated from its original C code into the IDL programming language by Steven Meikle was adopted for image reconstruction of parallel-hole collimation. A program (in Fortran) written by a member¹ of our collaboration was used for image reconstruction of pinhole collimation. Siddon's ray tracing technique was implemented in both programs [89]. No attenuation correction was applied. The reconstruction used cubic voxels with edge length 1.2 mm.

3.2.4 Simultaneous parallel-hole/pinhole planar imaging

We carried out a proof-of-concept study to test this imaging method. An anesthetized mouse was imaged simultaneously with parallel-hole and pinhole collimation immediately following the injection of 14 μCi Na^{125}I . The pinhole detector was focused on the stomach region of the mouse. Shown in Fig. 3.10 are one-hour images from parallel-hole and pinhole detectors, respectively. The three hot spots in the parallel-

¹ The program was written by Mark Smith

hole image were fiducial marks. One may note the consistency between the parallel-hole and pinhole images in the same region of the mouse body. Additionally, the magnified pinhole image reveals a clearer boundary and shape of the hot region in the mouse stomach area than does the parallel-hole image.

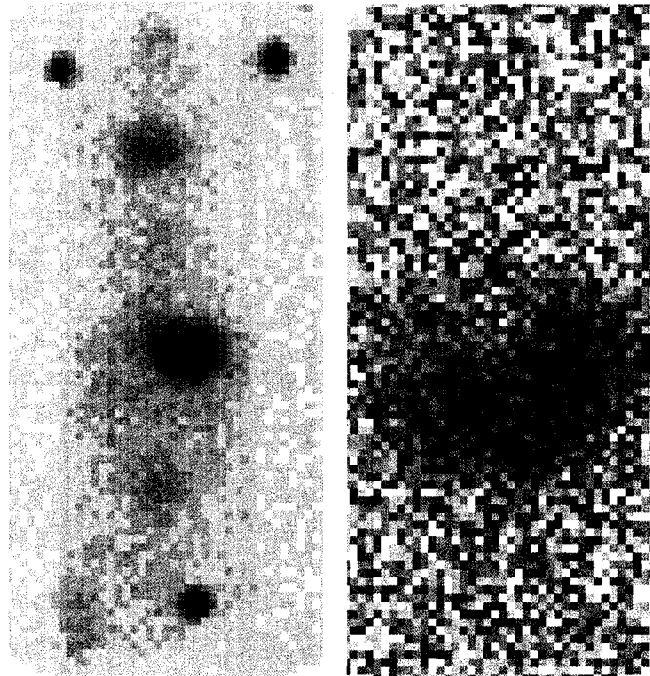


Fig. 3.10 (Left) one-hour parallel-hole image of the entire mouse injected with 14 μCi Na^{125}I . (Right) one-hour pinhole image of the stomach region of the same mouse obtained with a magnifying factor of 2.6. Both images were achieved simultaneously [118].

3.2.5 Parallel-hole SPECT imaging - phantom study

In order to verify the efficacy of our system for parallel-hole SPECT imaging, two studies were carried out with different phantoms. The two experiments were used to evaluate the trade-off between the imaging time and image quality, and the performance of parallel-hole SPECT for potential application to mouse thyroid imaging.

3.2.5.1 Experiment I – snake phantom

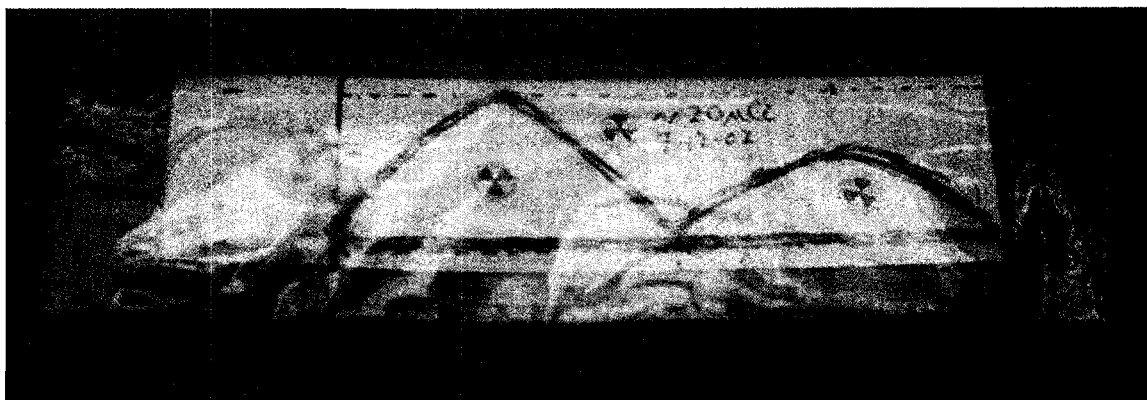


Fig.3.11 Photograph of the snake phantom containing $\sim 20 \mu\text{Ci Na}^{125}\text{I}$. The top peak is about 25 mm and the second peak is ~ 13 mm.

A series of SPECT tests has been carried out using a snake phantom illustrated in Fig. 3.11 to evaluate the interdependence between the imaging time and image quality for a fixed quantity of radioactivity. The phantom was made with a flexible plastic tube filled with $\sim 20 \mu\text{Ci } ^{125}\text{I}$ source. The series of experiments with this phantom could be roughly divided into three groups based on their total imaging time: long-term (> 2 hours), short-term (1-2 hours), and real-time (15 minutes). As listed in Table 3.1, the different imaging time resulted from the different combination of the angular increment around the AOR and the imaging time at each position. The results of four experiments are presented in Fig. 3.12. All the slices presented here are at the same location of the phantom.

Experiment	#1	#2	#3	#4
Angular increment (degree)	2	6	12	12
Imaging time at each position (mins)	8	5	2	30
Total imaging time (hours)	24	5	1	1/4

Table 3.1. Imaging parameters for the experiments using the snake phantom

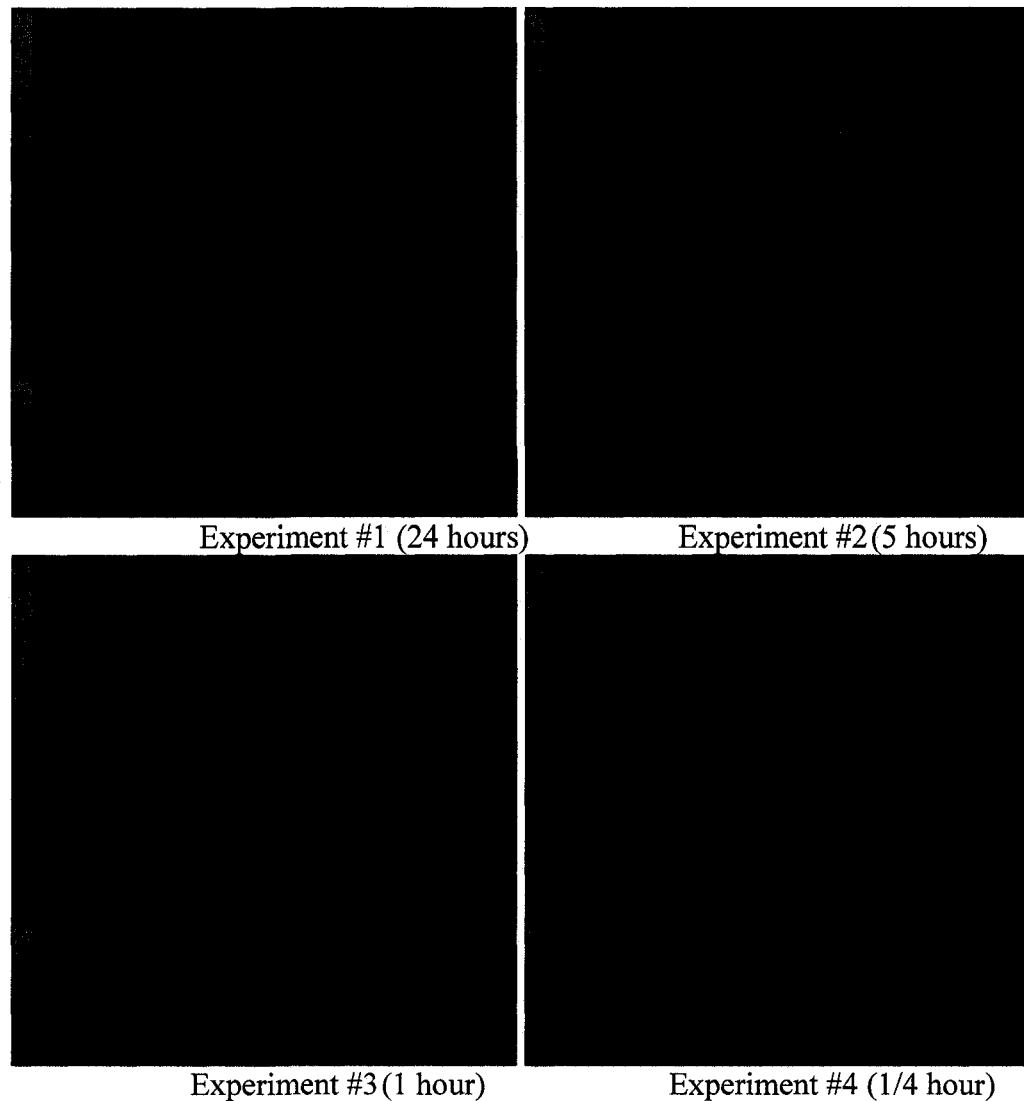


Fig. 3.12 Reconstructed images of SPECT scans of the snake phantom using different imaging parameters.

As the results indicated, long term SPECT imaging presented the best reconstructed image quality owing to better statistics. The reconstructed result of one hour imaging was less accurate and real-time (1/4 hour) imaging was the poorest in quality mainly due to low statistics. However, one may note that a relatively low total dose of 20 μCi was used in these studies. A potential solution to achieve high-quality

imaging using short-term or possibly real-time would be to compensate the statistics by applying a relatively high dose of radioisotope.

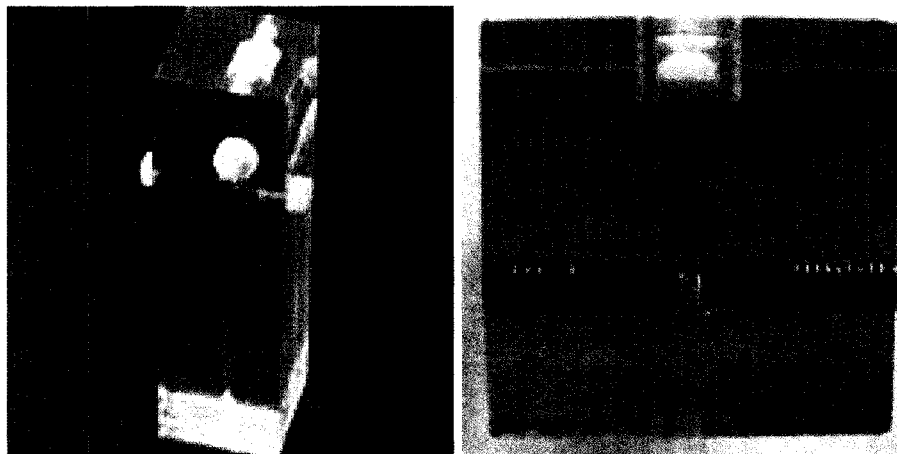


Fig. 3.13. Photographs of the plastic phantom simulating the thyroid and submaxillary glands of a mouse. The three voids, each containing $\sim 2 \mu\text{Ci Na}^{125}\text{I}$ solution, were spaced 2.5 mm from one another [118].

3.2.5.2 Experiment II – thyroid phantom

The thyroid is an important biological system in a mouse. The size of the mouse thyroid and the spacing between thyroid and submaxillary glands provides an excellent test of SPECT imaging. Therefore, the experiment described here was to evaluate the performance of parallel-hole SPECT using a phantom simulating the structure of the mouse thyroid and submaxillary glands. The overall and end views of the thyroid phantom are presented in Fig. 3.13. In the phantom, three small cylindrical voids were drilled with their axes in the same plane and spaced 2.5 mm from one another. Each void was about 50 mm^3 in volume and sealed with nylon screws after being filled with $\sim 2 \mu\text{Ci Na}^{125}\text{I}$ solution.

The thyroid phantom was placed on the AOR of the imaging system with the plane containing three voids perpendicular to the AOR. SPECT imaging of the phantom was accomplished with an angular increment of 3° for 120 projections and 5 minutes imaging time at each angular position using the parallel-hole detector. Six reconstructed images are presented in Fig. 3.14 based on the data from this SPECT scan. The six images are consecutive along the AOR and present the tomographic information in the section of the phantom containing the three hot voids. Each slice is 1.2 mm thick and vertical to the AOR.

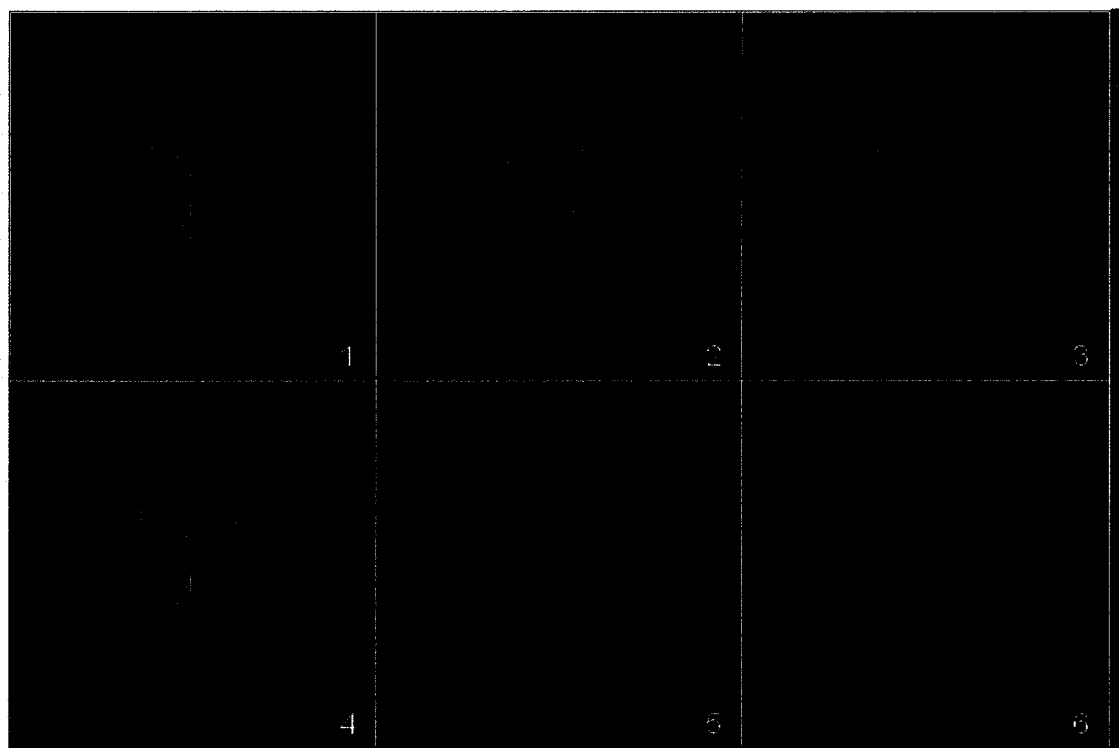


Fig. 3.14. Six consecutive reconstructed images of the thyroid phantom. The parallel-hole SPECT scan was carried out with 3° increments and 5 minutes at each angular position .

One may note that the central slices 3 and 4 clearly resolve the three voids separated by 2.5 mm (edge to edge), suggesting the reconstructed spatial resolution of the parallel-hole SPECT could be better than 2.5 mm. Moreover, the reconstructed voids

presented a structure consistent with their physical volumes. Particularly, the reconstructed image indicates that there has been some leakage of radiotracer along the threads of the nylon screw of the top void, which can also be visually observed in the end view of the phantom in Fig. 3.13.

3.2.6 Single-pinhole SPECT imaging – phantom study

A preliminary experiment has also been carried out using a three-capillary phantom to test the validity of single-pinhole SPECT. The three capillaries, each with about 16 μCi in 8 cm, were parallel in three dimensions. One capillary was positioned on the intersectional line of two perpendicular planes containing the other two capillaries. Those two capillaries were 4 mm and 8 mm away from the first capillary, respectively. Single-pinhole SPECT scan was accomplished with an angular increment of 3° for 120 projections and 3 minutes in duration. Presented in Fig. 3.15 are a planar image of the phantom and a transaxial image reconstructed from the SPECT data.

Consistent with their physical spatial distribution, the three capillaries were properly reconstructed as demonstrated in Fig. 3.15. The three hot spots in the reconstructed image formed a right angled triangle. The perpendicular sides determined from the reconstructed image were about 4 mm and 8 mm, respectively.



Fig. 3.15 (Left) a projection of the 48 μCi three-capillary phantom. (Right) a transaxial image of the phantom reconstructed from the data of a single-pinhole SPECT scan with 3° increments for 120 projections and 3 minutes in duration.

Further characterization of pinhole SPECT was accomplished later when we developed multipinhole circular/helical SPECT. Details are described in Chapters 4 and 5.

3.2.7 Simultaneous parallel-hole/pinhole SPECT– animal study

Encouraged by the phantom studies, a preliminary proof-of-concept study of an animal was carried out using simultaneous SPECT imaging with parallel-hole and pinhole collimation. A mouse was injected with about 10 μCi of ^{125}I tagged insulin. One hour later the mouse was sacrificed and imaged with both detectors. The SPECT scan was 3° increments and 3 minutes of imaging at each of the 120 positions. The pinhole detector was focused on the stomach region of the mouse.

Presented in Fig. 3.16 are reconstructed images of parallel-hole SPECT. The left two images in Fig. 3.16 are planar views at 0° and 180° , respectively. The three hot spots in those images are fiducial marks. The top and bottom image in the right panel of Fig.

3.16 are transaxial and sagittal reconstructed images, respectively. Both images indicated accumulation of ^{125}I -tagged insulin in the stomach region as can be expected.

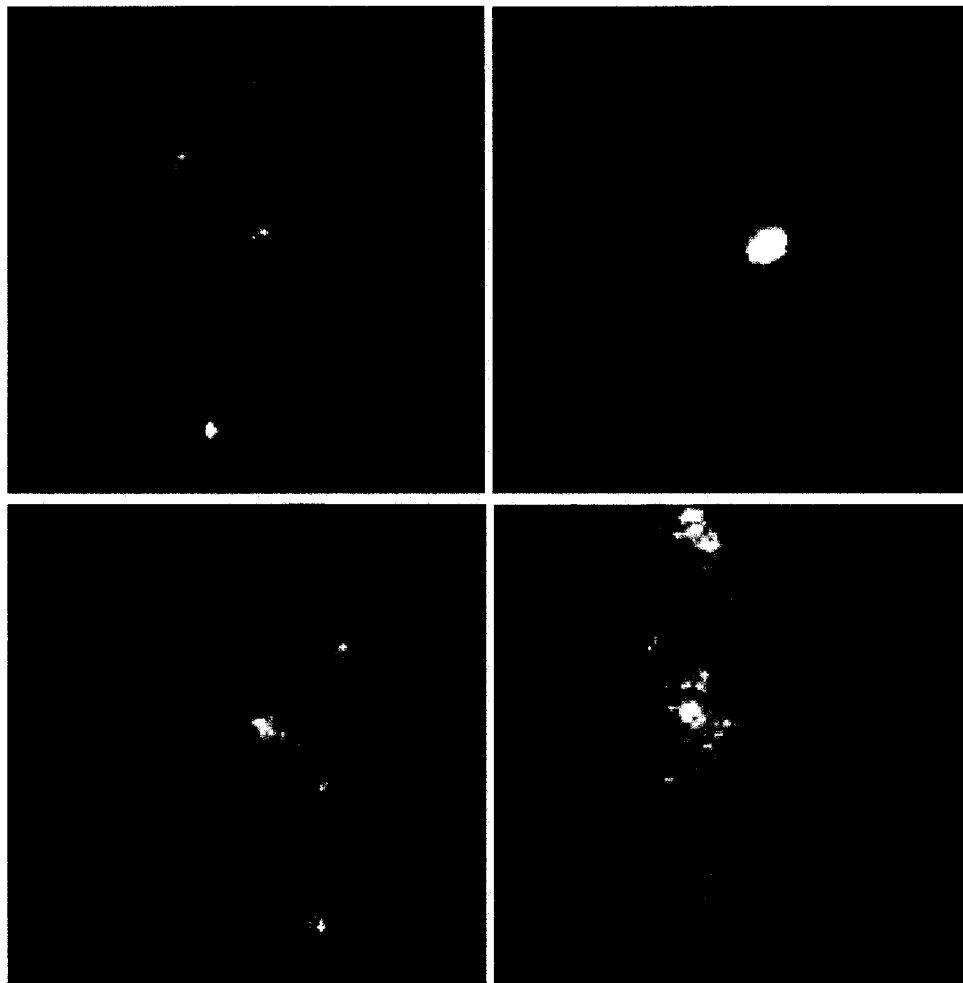


Fig. 3.16. (Left two images) parallel-hole projections of the mouse injected with 10 μCi at 0° and 180° , respectively. (Top-right) transaxial image of the mouse stomach region. (Bottom-right) sagittal image of the mouse reconstructed from the parallel-hole SPECT scan with 3° increments for 120 projections and 3 minutes of imaging at each angular position [118].

In contrast with parallel-hole SPECT, reconstructed results of single-pinhole SPECT scan presented poor image quality owing to low statistics. As previously noted, the mouse was injected with a relatively low dose of 10 μCi radiotracer. The accumulated

radioactivity probably is less than 1 μCi in the mouse stomach. To obtain useful reconstructed images, a higher dose of radioisotope may be required, especially for short term imaging to monitor relatively rapid biological processes.

3.2.8 Discussion and conclusion

We have developed a versatile imaging system capable of simultaneous gamma imaging with parallel-hole and single-pinhole collimation. Preliminary planar imaging studies suggest the potential utility of this system in biological research for simultaneous investigation of the entire small animal and regions of interest of the animal. Further preliminary studies indicated that this imaging system is also promising for SPECT imaging of small animals. Reasonably high resolution (better than 2.5 mm) has been achieved with a dedicated parallel-hole collimator. However, the dose of radioactive ligands employed in the biological study needs to be optimized to achieve the balance between high imaging quality and short imaging time. One possible solution for parallel-hole SPECT may be to employ an array of three or four detectors so that each detector only need rotate 120° or 90° to obtain the data set of a full 360° . In particular, due to the low sensitivity for pinhole imaging, a reasonably high level of radioactivity may be required in order to obtain high-quality image reconstruction for *in vivo*, real-time SPECT of animals. An alternative method to improve the sensitivity for pinhole SPECT while keeping its high resolution is to employ multiple pinholes, which will be described later in Chapters 4 and 5.

This gantry setup also expresses great flexibility for future system development. The small fluoroscopic X-ray apparatus was readily installed onto the gantry to enable

dual-modality imaging. The mouse-sized compact gamma cameras we developed recently were easily incorporated as demonstrated in the following section.

3.3 Development of compact gamma cameras for biological imaging

As noted previously, an array of three or four detectors could substantially reduce imaging duration for SPECT while allowing a reduced dose of radioactivity to be utilized. However, detectors based on the 110 mm diameter circular R3292 PSPMT modules may be not suitable for this setup. Though this type of detector has proved to be an excellent choice for large field-of-view imaging, it will not be cost-effective to incorporate several such detectors for parallel-hole SPECT imaging. The large diameter of these detectors will prevent them from providing a compact array in proximity to the subject animal or the AOR. For parallel-hole imaging, the spatial resolution of the detector at the AOR degrades with increased distance from the detector to the AOR. This will consequentially cause diminution of reconstructed spatial resolution of parallel-hole SPECT. Considering the high cost of a detector based on the Hamamatsu R3292 module and the difficulty to place several such detectors close to the subject animal simultaneously, we sought to develop a compact, economical detector suitable for imaging an entire mouse or specific organs with high performance. In comparison with the 110 mm diameter circular detector, this detector should be compact enough and must readily facilitate simultaneous use of three or four such detectors arranged in close proximity to the subject mouse for parallel-hole SPECT imaging [1].

As indicated by the reviews in Chapter 2, the Hamamatsu H8500, a new 2 inch square PSPMT, has become generally available with promising performance [125].

Building upon the reported research based on the H8500 PSPMT, we sought to develop a “mouse-size” compact gamma camera suitable for imaging an entire mouse, which also can facilitate parallel-hole SPECT imaging with small radius of rotation and permit use of several such detectors simultaneously [1]. My contribution in this work has been to calibrate and characterize the detectors, to design a new and more effective parallel-hole collimator and to evaluate the performance of the detectors based upon proof-of-concept studies.

Two such compact detectors have been developed to date. The difference between them lies in the readout circuit and the collimator. The following sections describe in detail the calibration and performance evaluation of the first “mouse-sized” detector. Based on the results of the first detector, a new parallel-hole collimator providing better resolution with acceptable efficiency has been designed and manufactured for a second detector. The efficiency and resolution of the new collimator is compared with those of the initial collimator based on the second detector.

3.3.1 Development of the first novel “mouse-sized” gamma camera

Details concerning the design of this detector can be found in a report presented previously [1]. Parameters of this detector will be briefly described here.

3.3.1.1 Summary of the first “mouse-sized” gamma camera

This novel gamma camera was developed based on a pair of Hamamatsu H8500 flat-panel PSPMTs. Each H8500 module measured $52 \times 52 \times 34 \text{ mm}^3$ with a sensitive area about $49 \times 49 \text{ mm}^2$. The two tubes were placed side by side and optically coupled to a 36×80 array of NaI(Tl) scintillators. Each crystal element measured $1 \times 1 \times 5 \text{ mm}^3$

with 0.2 mm reflective walls in between the scintillators. The outermost row of pixels was made 2 mm wide to add strength in the fabrication of the scintillator. The scintillator array was encapsulated with a 50 μm aluminum cover causing about 15% attenuation for ~ 35 keV (^{125}I) photons and included a 3 mm glass window faced to the PSPMT tubes. A 5 mm thick CuBe parallel-hole collimator suitable for ^{125}I imaging was employed with 0.55 mm square openings and 0.11 mm septa. The active area of this collimator was 52 mm x 105 mm. All the components of this detector including electronic readouts were assembled and contained in an aluminum box measuring 140 x 82 x 107 mm³. The assembled gamma camera is presented in Fig. 3.17 along with a sample collimator for such detector.

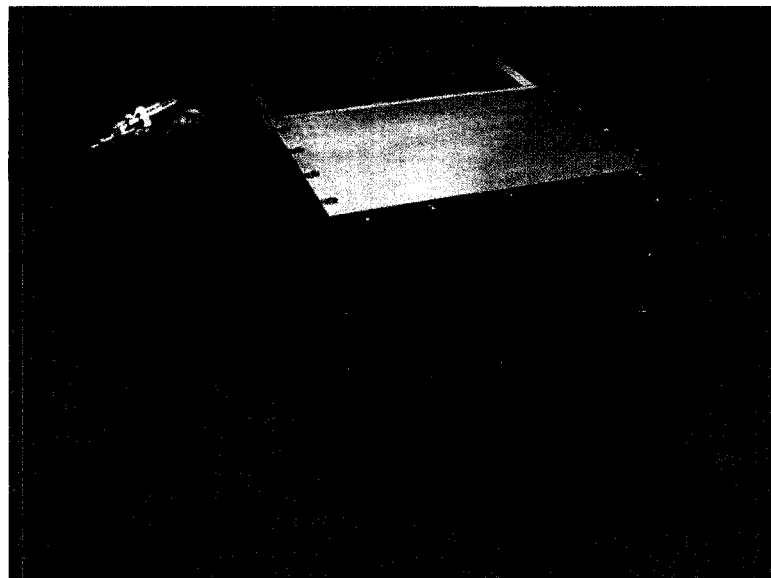


Fig. 3.17. Photograph of the detector and a collimator identical to the one used in the detector. [1]

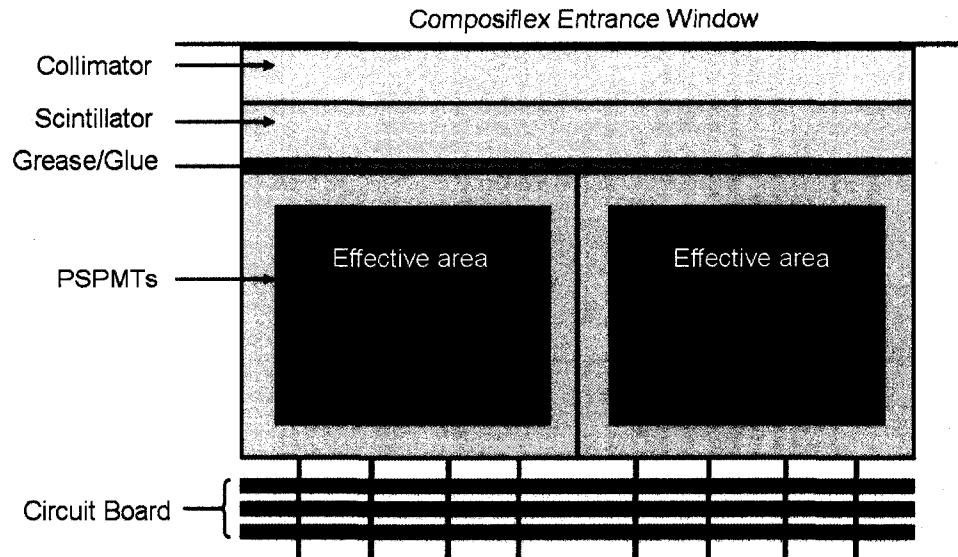


Fig. 3.18. The diagram of the inside view of the compact gamma camera

3.3.1.2 Calibration of the compact gamma camera

A diagram of a side view of the detector is presented in Fig. 3.18. One may note that an insensitive region (~ 3 mm width) exists in between the two H8500 PSPMTs, where there were no anode pads but only glass walls. However, the position information of a gamma photon entering the gap region could still be determined by referring to a crystal lookup table, which represented the geometric response region of the individual crystal elements [1]. In order to do that, a raw crystal map of the scintillator array was obtained using a high energy (662 keV gamma rays) point source ^{137}Cs placed 150 mm above the detector. As shown in the left panel of Fig. 3.18, each crystal element could be clearly identified even including the crystal elements located in the insensitive gap region. A crystal lookup table (see the middle panel of Fig. 3.18) for the scintillator array was then generated using a special Kmax program. In a manner similar to the calibration of the 110 mm diameter circular detector described earlier in subsection 3.2.1, energy

calibration of individual scintillator pixels was carried out followed by correction of the non-uniformity of the detector in efficiency using a flood-correction table. This table was obtained with a planar, uniform liquid ^{125}I source ($\sim 40 \mu\text{Ci}$) sufficient to cover the entire sensitive area of the detector. All the tables for detector calibration were implemented in the data acquisition program developed with Kmax software. The calibration was automatically executed by this program when acquiring data. The energy window for imaging in this work included photons with energy between 22 keV and 40 keV.

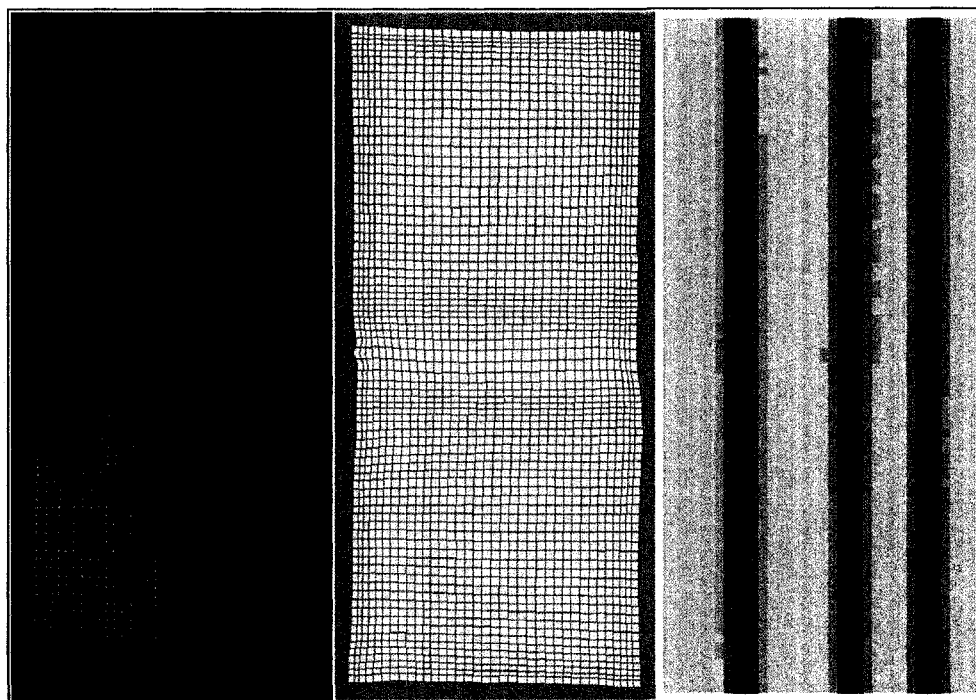


Fig. 3.19. (Left) raw crystal map using $\sim 15 \mu\text{Ci}$ ^{137}Cs . (Central) crystal lookup table built upon the left image. (Right) a three-capillary image with uniformity corrected [1].

A three-capillary phantom was used to demonstrate the efficacy of the detector calibration. Each capillary contained about $10 \mu\text{Ci}$ Na^{125}I in 11 cm. As is evident in the right panel of Fig. 3.19, the planar image of the three-capillary phantom indicated neither

sensitivity loss nor visible deterioration of performance in the transition region between the two PSPMTs [1]. Shown in Fig. 3.20 is a profile image of the three capillaries. The similar peak values of the capillaries further suggested uniform sensitivity of the detector after calibration.

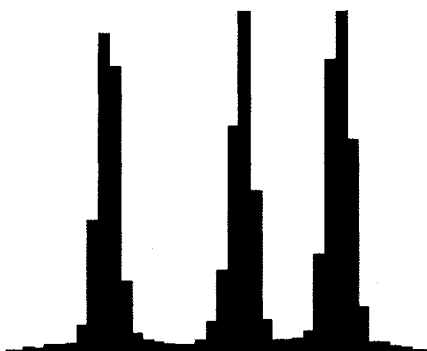


Fig. 3.20. A profile image of the three capillaries suggesting uniform sensitivity of the detector after calibration. [1]

3.3.1.3 Characterization – efficiency and resolution

A capillary with 0.3 mm inner diameter loaded with 10 μCi of Na^{125}I was used to determine the sensitivity of this compact gamma camera. The measured sensitivity was 1840 cpm/ μCi with the capillary positioned about 4 mm from the surface of the collimator.

For measurement of the spatial resolution of this detector, individual planar images were achieved with the capillary positioned at a variety of distances from the surface of the collimator, i.e., 4 mm, 17 mm, 32 mm, 47 mm and 62 mm. Three one-pixel-width profiles of each image were obtained in top, bottom and gap region of the detector, respectively. After these profiles were fitted with Gaussian curves three full-width-at-half-maximum (FWHM) spatial resolutions were then determined and averaged

to provide the spatial resolution of the detector at that distance. Presented in Fig. 3.21 is the mean spatial resolution (FWHM) of the compact detector as a function of the distance between the source and detector. A theoretical resolution curve determined by the formulae of Keller [62] and Smith *et al.* [63] is also presented in Fig. 3.21 in comparison with the experimental measurement. One may note the measured resolutions of this detector had an overall FWHM difference of about 0.6 mm from the ideal theoretical resolutions.

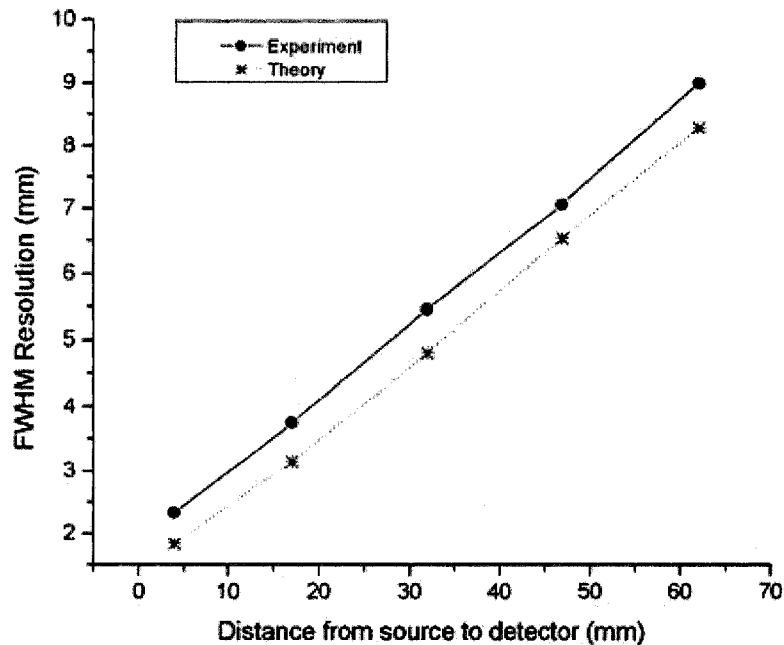


Fig. 3.21 Theoretical prediction and experimental measurement of the resolution as a function of the distance between source and detector. [1]

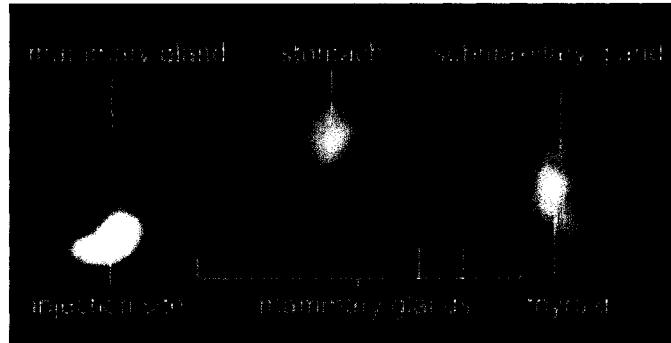


Fig. 3.22 One-hour parallel-hole planar image of the lactating mouse injected with 10 μCi Na^{125}I . The detector clearly delineates the accumulation of radioiodine in lactating mammary glands as expected. [1]

3.3.1.4 Planar and SPECT imaging – animal studies

In order to further verify the efficacy of this detector in biological studies, we have carried out animal studies including planar and SPECT imaging. The first study was planar imaging of a lactating mouse. Iodine is a significant element for a lactating mouse to produce milk in its mammary glands. Since iodine was transported into the mammary glands via the sodium iodide symporter (NIS), a well-known protein which is also expressed in other tissues such as thyroid glands and stomach [126], imaging of the lactating mouse injected with Na^{125}I can delineate its lactating mammary glands expressing NIS. Presented in Fig. 3.22 is a 60-min gamma image obtained immediately after an anesthetized lactating mouse was injected with 10 μCi of Na^{125}I . This image indicates the injection site in the left rear leg. As expected, high uptake of ^{125}I is evident in the stomach region and thyroid and submaxillary glands. As in the salivary glands, individual lactating mammary glands of this mouse showed substantial accumulation of radioiodine and were clearly distinguished in the gamma image. In addition, the heart and lung region presented some level of accumulation of ^{125}I owing to blood flow in

comparison with background tissues. The performance of the detector clearly demonstrated its utility in imaging ^{125}I -tagged ligands used in biological studies.

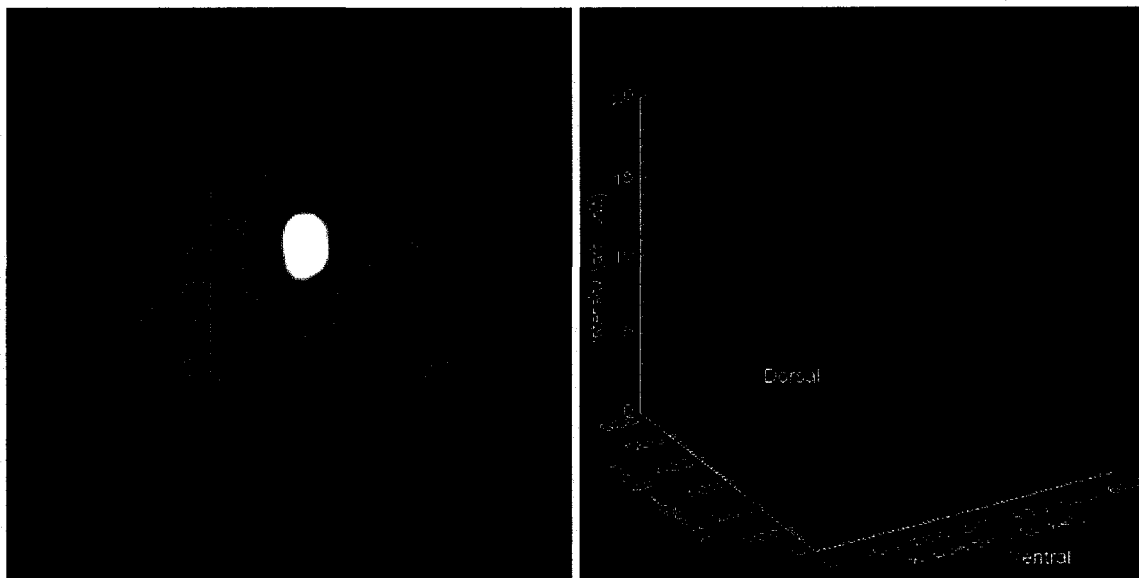


Fig. 3.23. A transaxial image (left) and its surface plot (right) of the thyroid region of a mouse injected with $14\ \mu\text{Ci}\ \text{Na}^{125}\text{I}$. Both reconstructed images presenting dramatic difference in uptake of ^{125}I in the thyroid gland from in the submaxillary glands. [1]

Experiments were also carried out in order to evaluate the performance of this detector for SPECT imaging. In the first test, a mouse was euthanized 65 minutes post injection of $14\ \mu\text{Ci}\ \text{Na}^{125}\text{I}$. A SPECT scan of the mouse was accomplished with 3° intervals and 3 minutes for each of the 120 projections. Presented in Fig. 3.23 are a reconstructed image and its surface plot in the region containing both thyroid and submaxillary glands. The transaxial image clearly demonstrates the accumulation of ^{125}I in the thyroid gland and the two submaxillary glands adjacent to the thyroid [1]. The surface plot of the same transaxial image further indicates the dramatic difference in uptake of ^{125}I in the thyroid gland from in the submaxillary glands. These results were

entirely consistent with what is expected for active iodine accumulation in these two structures [1].

The data from a second SPECT scan were obtained with another female mouse that bore a mammary tumor. The animal was euthanized 65 minutes after injection of 14 $\mu\text{Ci Na}^{125}\text{I}$. Again, the 120 3-min projection images were taken with 3° spacing around the mouse. The reconstructed results are presented in Fig. 3.24 and Fig. 3.25. Shown in Fig. 3.24 are the reconstructed transaxial images of the mouse in the region containing the axillary mammary tumor, the thyroid and submaxillary glands [1]. As is evident from those images, NIS activity in this mammary tumor was substantial and higher than in the submaxillary glands but lower than the thyroid gland. The coronal views of the reconstructed results in Fig. 3.25 represent the distribution of radioiodine in the body region containing the thyroid, stomach and tumor. Those images also indicate the high level of NIS activity in both the stomach and thyroid gland as expected. In addition to the clear NIS activity in the tumor, there was also clear accumulation of ^{125}I in the salivary glands [1].

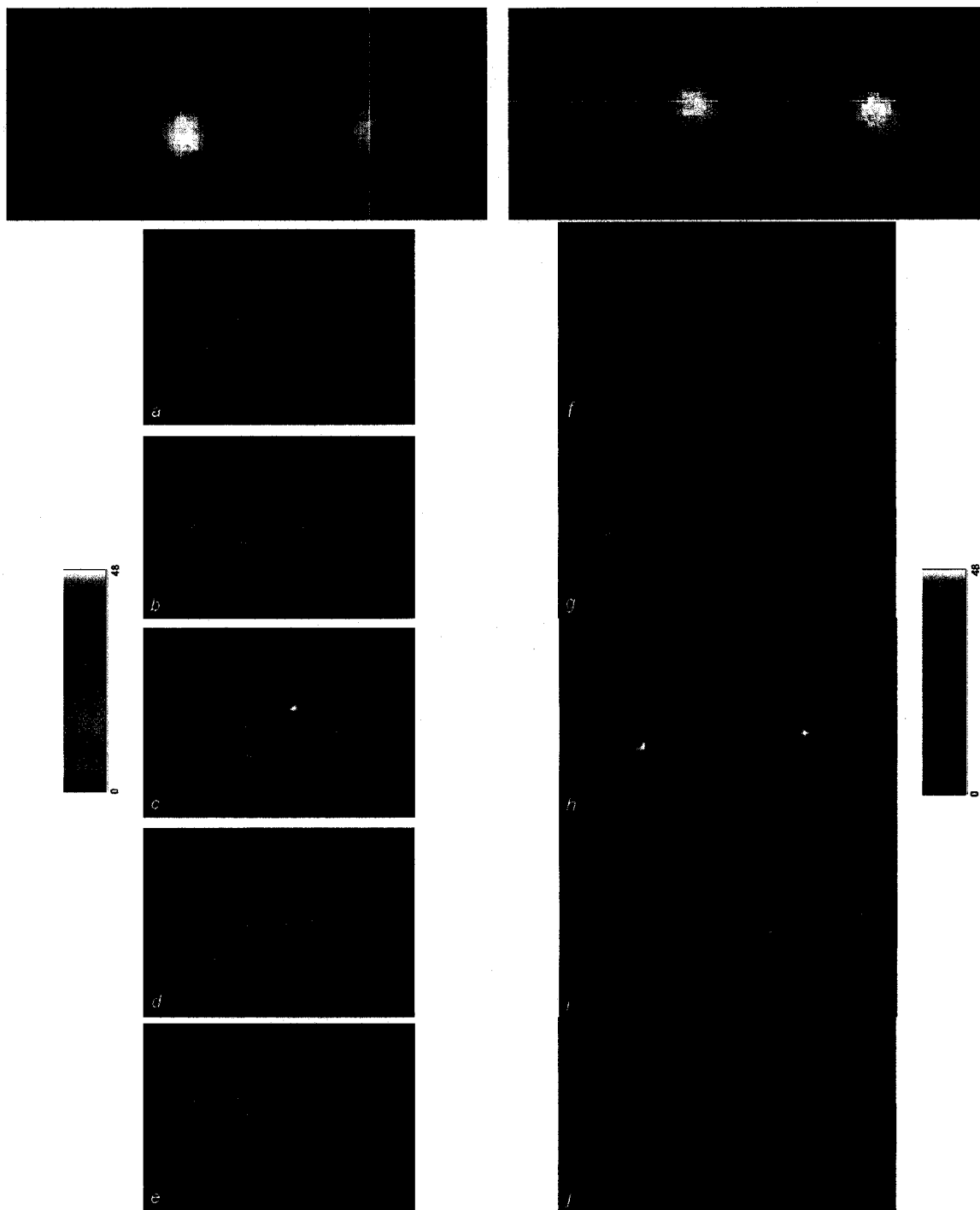


Fig. 3.24 Top image is a projection of a mouse bearing a mammary tumor at 0° , followed by five consecutive transaxial images (a-e, from tail to head) in the region containing both the thyroid and tumor. [1]

Fig. 3.25 Top image is a projection of a mouse bearing a mammary tumor at 90° , followed by five consecutive coronal images (f-j, from ventral to dorsal side) of the entire mouse.[1]

3.3.2 Development of the second “mouse-sized” gamma camera

The results of the first compact gamma camera equipped with a 5 mm thick collimator (collimator #1) demonstrated the suitability of this detector for biological imaging of an entire mouse. However, it would be valuable to facilitate practical SPECT imaging of a mouse with such a detector using a shorter period such as 1 or 2 hours and a relatively low dose of radioisotope. One may also note from Fig. 3.20 that the resolution of this detector decreased substantially over a range of source-to-detector distance from 4 mm to 47 mm. This range of distance is critical for SPECT imaging and the resolution degradation over this range may diminish the reconstructed resolution of SPECT. In order to achieve better resolution and to reduce imaging time, a second compact gamma camera containing a newly designed CuBe parallel-hole collimator has been built and installed on the gantry to form a dual-detector array with the newly designed parallel-hole collimator.

The new CuBe collimator (Collimator #2) measures 6 mm thick with 0.3×0.3 mm² openings and 0.05 mm septa. Collimator dimensions including its thickness, the hole size and septal thickness were determined based on the formulae of Keller [62] and Smith *et al.* [63]. The efficiency and spatial resolution of the new compact gamma camera were measured with a single capillary phantom with an inner diameter of 0.3 mm containing an activity of 10 μ Ci in 8 cm length. The capillary phantom was imaged for 10 min at distances of 4 mm, 17 mm, 32 mm, 47 mm and 62 mm from the detector. The spatial resolution was obtained from the average of a Gaussian fit to three different one-pixel-wide slices across the line source. The theoretical resolution (R_s) was calculated based on the geometric resolution (R_g) of the collimator and the intrinsic resolution (R_i)

of the detector, i.e. $R_s^2 = R_g^2 + R_i^2$. Spatial resolution of collimators #1 and #2 was compared based on this new detector.

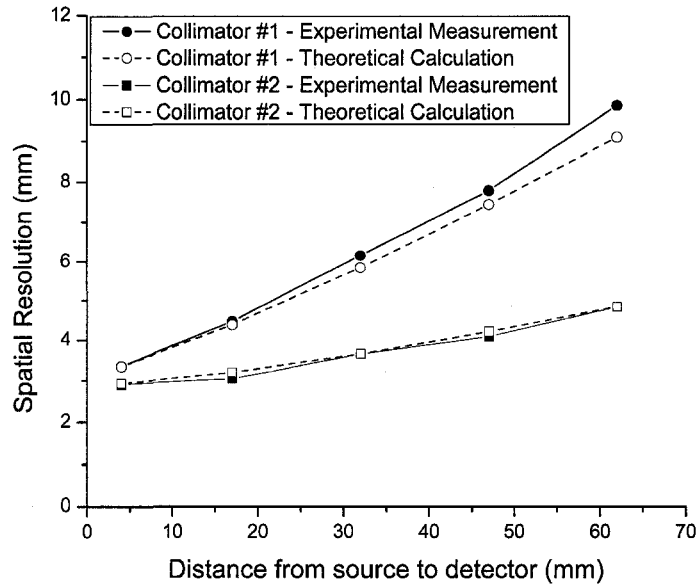


Fig. 3.26. Comparison of spatial resolution with the newly constructed detector equipped with 5 mm thick high-sensitivity collimator #1 and 6 mm thick high-resolution collimator #2 respectively. Relatively high resolution was preserved over a useful range with the 6 mm thick collimator while the efficiency was lessened by a factor about 6 [119].

The measured efficiency of compact detector #2 is 1538 cpm/ μ Ci and 268 cpm/ μ Ci at 4 mm away from the detector for 5 mm thick collimator #1 and 6 mm thick collimator #2 respectively. A plot is presented in Fig. 3.25 of measured detector spatial resolution (FWHM) vs. source-collimator separation. This result is in good general agreement with theoretical predictions fitted with an intrinsic resolution 2.8 mm which takes into account the 3 mm thick optical glass windows of the scintillation array, the 2 mm thick PSPMT windows and an air gap of 3.2 mm between the collimator and scintillator. The difference between theoretical and experimental resolutions at a large distance from the detector for collimator #1 results from the 0.3 mm inner-diameter

capillary used for resolution measurement positioned at an angle with respect to the collimator having 0.55-mm square openings. As one may notice in Fig. 3.26, the advantage of collimator #2 is that it provides an acceptable resolution of 2.9 – 4.1 mm FWHM over a long range 4 – 47 mm of the distance between the object and the detector. This is significant for SPECT scans because such a range in distance typically exists when imaging mice.

3.3.3 Conclusion

We have developed novel compact gamma cameras particularly suitable for imaging an entire mouse either with planar scintigraphy or SPECT imaging. High performance has been demonstrated based on the evaluation of sensitivity, resolution and on preliminary animal studies. A collimator has been designed and manufactured in order to provide useful resolution with acceptable trade-off in sensitivity over a long range (4 - 47 mm) of source-to-detector distance, suggesting the potential for better results of SPECT imaging. In addition, the size of this detector makes it possible to employ an array of three or four such detectors simultaneously for short-period SPECT imaging of a mouse injected with a dose of radioactive ligands at a physiologically safe level.

Chapter 4

Development of multipinhole helical SPECT

As mentioned earlier, pinhole collimation in SPECT has a definite advantage in achieving high spatial resolution, however, with a significant trade-off in sensitivity and sampling completeness. New multipinhole or helical SPECT imaging systems (see review in section 2.4) have been proposed to overcome the disadvantages of single-pinhole SPECT in low-sensitivity and sampling completeness while keeping its advantage of high spatial resolution. In this work, we have sought to further enhance our imaging system by combining multipinhole circular SPECT with a helical orbit. Our principle goal has been to achieve enlarged FOV and enhanced resolution and sensitivity by taking advantage of that combination to facilitate high-quality imaging of specific organs such as the thyroid region of a mouse while retaining the potential of imaging the entire body. Shown in Fig. 4.1 is the current system incorporating multipinhole helical/circular SPECT in addition to parallel-hole SPECT.

Described in this chapter are the system design, development, characterization comparison including field of view, sensitivity and resolution among various modes of pinhole circular or helical SPECT. Phantom studies were also carried out to validate the performance improvement.

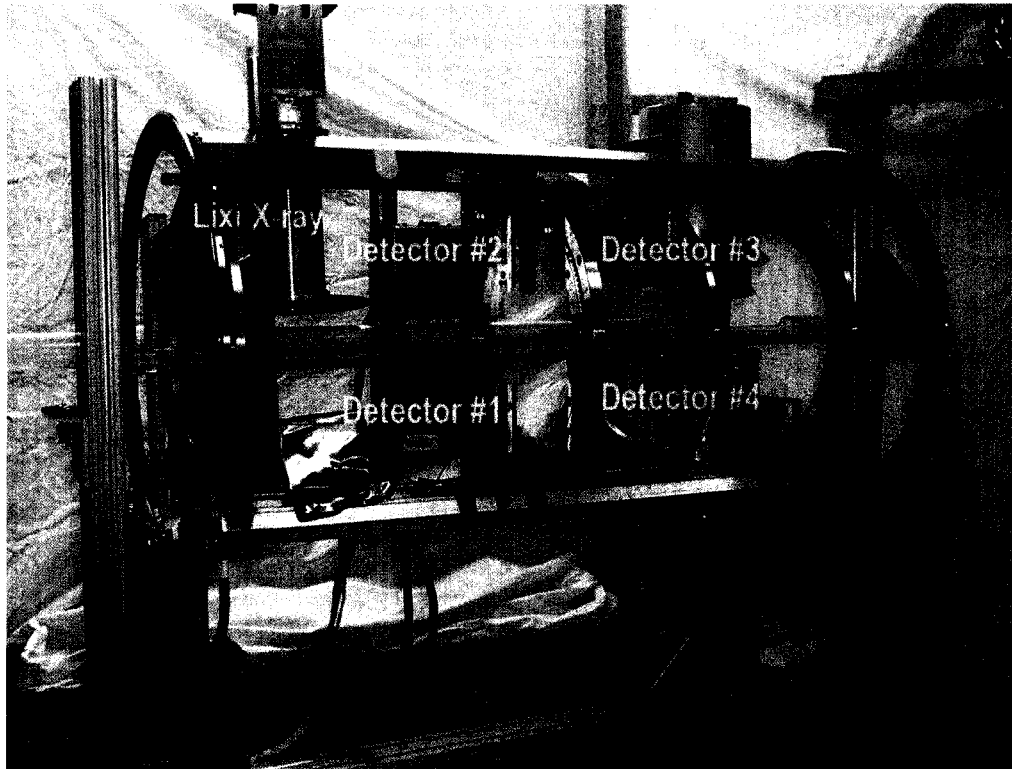


Fig. 4.1. Photograph of the compact parallel-hole and pinhole circular/helical SPECT imaging system. Signal processing and storage instruments are not shown in this picture. All detectors are incorporated in a cylindrical gantry capable of rotating 360°. Detectors #1-2 are “mouse-sized” compact gamma cameras and detectors #3-4 are 110 mm diameter circular detectors.

4.1 System design

A 110 mm diameter circular detector (#4 in Fig. 4.1) was employed with pinhole collimation. Depending on the effective view area of the detectors and the requirements for acceptable spatial resolution, researchers have designed multipinhole collimation both with and without multiplexing of the image. The experimental results of Meikle *et al.* [65] indicate that the resolution of multipinhole circular SPECT achieved with multiplex effects is not appreciably different from that of single-pinhole SPECT. Therefore, we

have designed a collimator for multiplexed imaging based on the effective view area of this 110 mm diameter circular detector.

To resolve the sampling incompleteness of single-pinhole SPECT resulting from a circular orbit and to enlarge the FOV of the detector, we have implemented a translation rack supporting the mouse bed along the axis of rotation (AOR) of the system so that a helical trajectory is employed. Such a combination of multipinhole and helical SPECT not only provides improved sampling completeness but also increases the field of view in both transaxial and longitudinal direction and hence enables large field-of-view imaging especially when a large magnification factor is involved.

4.2 Gamma-ray detector for pinhole collimation

The 110 mm diameter circular detector for pinhole imaging was described in section 3.2.1. A five-pinhole brass collimator as shown in Fig. 4.2 was employed for multipinhole collimation. The collimator was 25 mm from the AOR of the gantry with a magnifying factor of 3 used in this work.

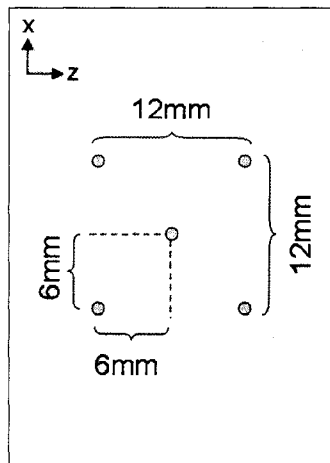


Fig. 4.2. Diagram of the 5-pinhole collimator.

4.3 Design of a five-pinhole collimator

A typical pinhole collimator has the knife-edge shape as shown in Fig. 4.3a. For a knife-edge pinhole collimator, the analytic formulae of geometric sensitivity P_s , resolution R_a and effective diameter d_e have been previously expressed as equations (2.1-2.3) in section 2.4.2.

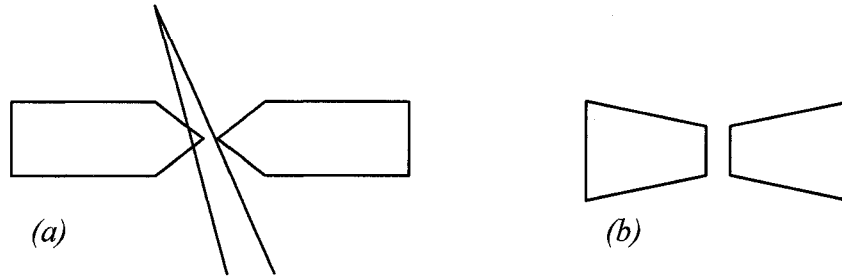


Fig. 4.3 (a) Knife-edge pinhole and the penetration effect; (b) Pinhole with channel edge

As one may note, the effective diameter d_e actually takes into account the penetration effect at the edge of the pinhole. As indicated by the formula 2.3, the opening angle of the pinhole and linear absorption coefficient of the collimator material are the two factors affecting the effective diameter, which may degrade the resolution. To reduce the penetration effect at the edge of the pinhole, Smith *et al.* employed a pinhole channel (see Fig. 4.3b) in design of a pinhole aperture instead of the usual knife edge [63].

The criteria for designing a multipinhole collimator have been proposed by Schramm *et al.* [66]. The projections from the multiple pinholes should be closely packed but with reduced multiplexing (especially multiple superposition) in order to take advantage of the effective detector area as much as possible and to minimize the uncertainty of the origin of a detected gamma ray. The object should also be sampled homogeneously with large incident angle avoided [66].

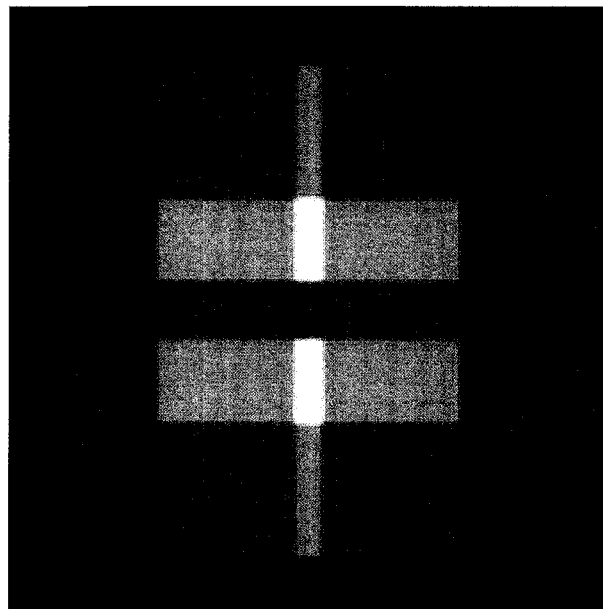
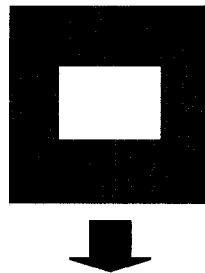
The multipinhole collimator desired in our study serves the purpose of SPECT imaging of specific mouse tissues, particularly the thyroid, with the potential for whole mouse imaging. Therefore, the parameters of this multipinhole collimator have been determined accordingly based upon the formulae 2.1-2.3 in section 2.4.2 and criteria.

Considering the effective detector area (~ 106 mm diameter sensitive region of the scintillator), a magnifying factor 3 was employed in order to achieve high-resolution (near 1 mm) imaging. This setting allows the detector to image a ~ 35 mm diameter view area in the object plane containing the axis of rotation, which is sufficient to cover the mouse thyroid region. To achieve a good balance between resolution and sensitivity, the pinhole used in the collimator is 1 mm diameter. Since the geometric sensitivity also dramatically decreases with the increased distance between the object and collimator, the detector has to be placed as close as possible to the mouse, in this case, 25 mm. An opening angle of 90° was determined and employed for the pinhole. This acceptance angle is large enough for the detector to accept the incident photons from the effective view area in the objective plane. A channel edge was also employed for the pinhole to reduce penetration effects at the edge of the pinhole. The material used for the collimator is brass which has a linear attenuation coefficient about 60/cm for ~ 35 keV photons from ^{125}I . A pinhole channel height of 0.2 mm can thus effectively reduce penetration effects at the edge region of the pinhole.

Shown in the Fig. 4.2 is the diagram of a five-pinhole collimator chosen for imaging specific organs of small animals such as the mouse thyroid based on the sensitive area of the 110 mm diameter circular detector. The projection pattern of this multipinhole collimator was simulated using a 17.6×12.8 mm² rectangular object (see Fig. 4.4) whose

area is sufficient to cover the thyroid region of a mouse. Image multiplexing percentages were calculated based on this simulation. Multiplexing percentages are defined as the overlap area divided by the detector plane area. For the current five-pinhole collimator shown in Fig. 4.2, about 85% of the detector area is used to image the simulated object which includes a multiplexing area of $\sim 20\%$ of the detector area. The area of multiple superposition (an order of overlap more than 2) is less than 2%.

Object ($17.6 \times 12.8 \text{ mm}^2$)



**Five-pinhole projection on the
detector with an amplifying factor of 3**

Fig. 4.4. The simulated object (top) and projection (bottom) images using the five-pinhole collimator with a magnifying factor of 3.

In summary, a five-pinhole collimator has been designed and fabricated. The actual collimator is shown in Fig. 4.5. Each pinhole in the 5 mm thick brass collimator is 1 mm in diameter with an 0.2 mm (in height) pinhole channel and an opening angle of 90° . A collimator of 1 to 4 pinholes can readily be effected by shielding the unused pinhole(s) with 0.5 mm lead sheet sufficient to block the 35 keV photons from ^{125}I . This collimator has met our needs in multipinhole imaging studies.

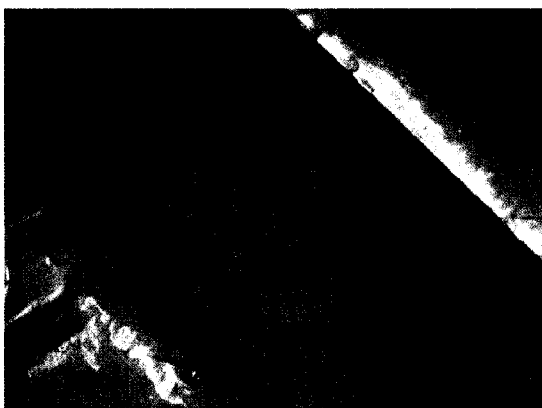


Fig. 4.5. Photograph of the five-pinhole collimator

4.4 Step-and-shoot helical orbit

A circular orbit for imaging was effected by a stepping motor (Fig. 4.6, Motor 1) which controlled rotation of the gantry around the axis of rotation. By adding a second SLO-SYN stepping motor (Fig. 4.6, Motor 2, 200 steps per revolution, Superior Electric Inc.) to control the displacement of the mouse bed along the AOR, a helical orbit was accomplished for step-and-shoot imaging. The second motor drove a steel rack, on one end of which the mouse bed was fixed, through a spur gear as seen in Fig. 4.6. This combination of the three components resulted in a stepping increment 1 mm per 10 steps along the AOR.

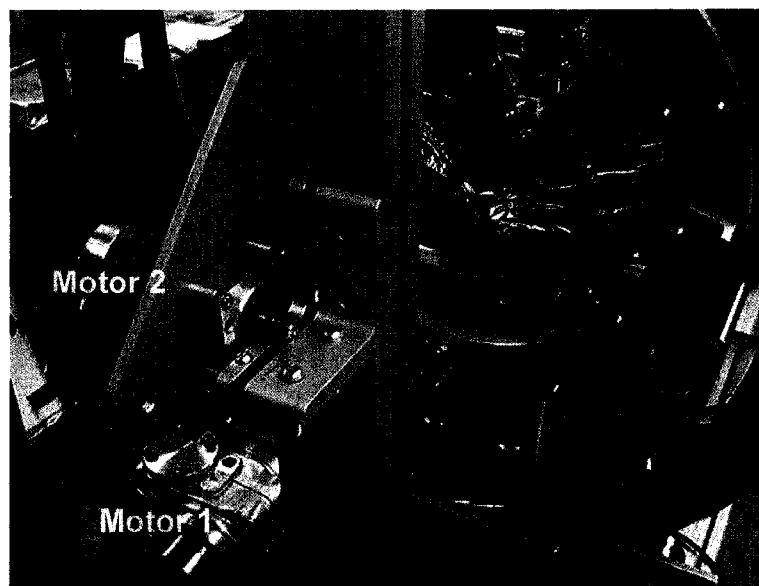


Fig. 4.6. Photograph of the setup to accomplish step-and-shoot helical orbit. Motor 1 controls the rotation of the cylindrical gantry round the AOR. Motor 2 controls the displacement along the AOR of the rack with a mouse bed fixed to one end.

4.5 Image reconstruction program and validation

Image reconstruction programs were developed for multipinhole circular and helical SPECT based on an iterative ML-EM algorithm. The ML-EM algorithm was implemented using a method extended from that described by Li *et al.* [88] with Siddon's ray tracing technique [89] applied. No attenuation correction was applied. The image reconstruction programs were written in IDL language. Part of the program was adapted from Steven Meikle's image reconstruction program for pinhole circular SPECT. The reconstruction used cubic voxels with edge length 0.4 mm for pinhole collimation. In order to ensure that the image reconstruction programs work properly, they were validated by both simulation and phantom studies.

4.5.1 Simulation test

As the core routine of image reconstruction is the same for pinhole circular or helical SPECT, it was sufficient to test the code using the simple case of single-pinhole circular SPECT. A set of projection images of a single capillary was simulated using a “perfectly” centered pinhole on the detector. To simplify the test, the simulated tube was positioned on the axis of rotation longitudinally. The projected tube in a pinhole image (Fig. 4.7a) is set to be uniform with a width of 2 pixels (1.2 mm/pixel). The length of the tube is 38 pixels with detected activity 10 counts for each pixel. Because the geometric sensitivity for a pinhole is proportional to $\cos^3\phi$ (where ϕ is the incident angle of the photon) when this fine capillary is parallel to the axis of rotation, radioactivity in the actual digital tube should not be uniform. A total of 120 slices of such projection images was simulated with a magnifying factor of 3 used. Shown in Figs. 4.7b and 7c are transaxial and coronal images after image reconstruction with the programs. The transaxial image shows a reconstructed dot with a diameter of about 2 pixels (0.4 mm/pixel). The coronal image indicates that the activity in both end regions of the digital tube is hotter than the central region. Both reconstructed images present exactly the results expected.

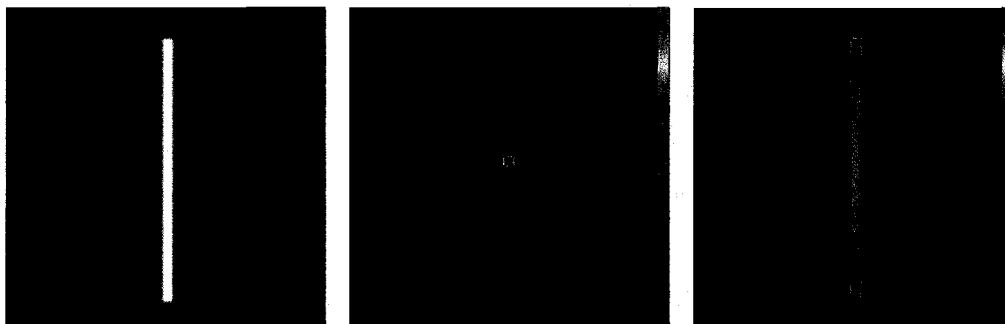


Fig. 4.7. (a) simulated uniform projection of a digital tube; (b) transverse and (c) coronal images of the reconstructed non-uniform digital tube

To further verify that the program reconstructed the digital tube correctly, the longitudinal activity profile of the reconstructed tube was used to predict the activity profile of the tube in a pinhole projection image. The presumption is that if the program did the reconstruction properly, the predicted profile should be consistent with our initial simulation, in other words, that the longitudinal activity profile of the tube should present a plateau shape. Shown in Fig. 4.8 is a longitudinal profile of the activity in the reconstructed digital tube. Again, because the geometric sensitivity for a pinhole is proportional to $\cos^3\phi$ when the tube is parallel to the axis of rotation, the activity profile of the tube in a projection image can be predicted by multiplying the value at each pixel in Fig. 4.8 by a factor of $\cos^3\phi$ corresponding to that pixel. Shown in Fig. 4.9, the predicted profile is flat and consistent with the uniform projection of the tube as initially simulated, which validates our image reconstruction.

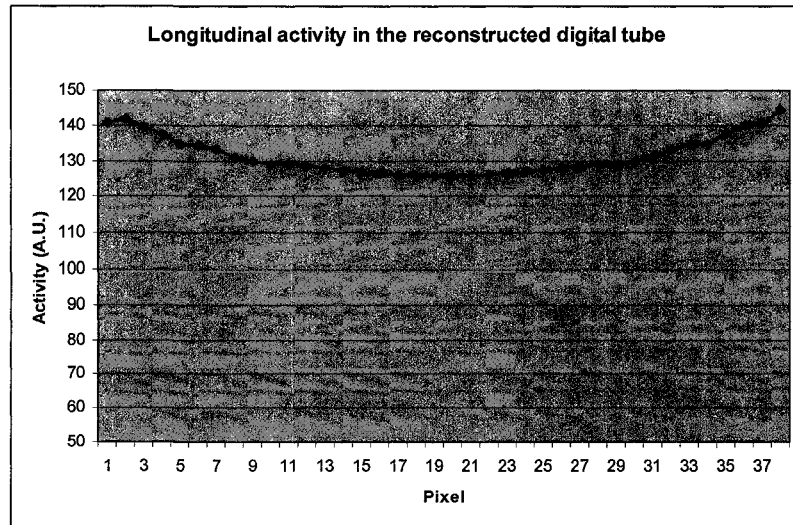


Fig. 4.8 longitudinal profile of the activity in the reconstructed digital tube

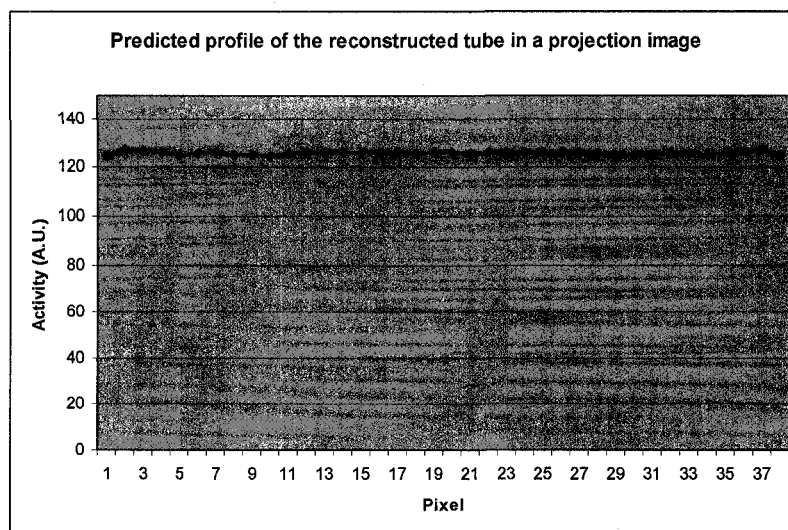


Fig. 4.9 Predicted profile in a projection image of the reconstructed digital tube using the values in Fig. 4.8. This predicted profile is consistent with the uniform projection as initially simulated.

4.5.2 Phantom tests

The image reconstruction program of Steve Meikle is accompanied by a sample set of projection images from a single-pinhole circular SPECT scan of a five-capillary phantom. The 18 projection images in the data set were obtained at angular positions separated by 20° increments. Each projection image is 64×64 pixels, in which the effective area of the detector takes 47×47 pixels. A magnifying factor of 2 was employed for this phantom test with 45 mm between the axis of rotation and the pinhole collimator. The single pinhole is located at the center with respect to the detector. The results after image reconstruction using my program are compared with those of Meikle's program as a standard. Compared are both reconstructed images and the total counts in the reconstructed volume after each iteration. The reconstructed images from both programs are presented in Fig. 4.10. As one may note, these two reconstructed images are almost identical and consistent in detail.



Fig. 4.10. Reconstructed images after five iterations using Meikle's program (left) and my program (right), respectively.

Listed in Table 4.1 are the total counts in the reconstructed volume after each iteration (up to five iterations in this comparison). The results show that the total counts and their trend with the iteration number are consistent within errors using both image reconstruction programs.

Iteration number	Steven Meikle' Program	My Program
1	84872	81035
2	83622	80077
3	83165	79860
4	83122	79860
5	83307	79957

Table 4.1. Total counts in the reconstructed images

A further quantification test of the image reconstruction program for multipinhole helical SPECT was carried out with a phantom containing three ^{125}I sources simulating the thyroid region of a mouse. Details can be found in section 5.2.3.3. Briefly, using image analysis programs, we compared the ratio among the region of interests (ROIs) of the three sources in a planar gamma-ray image with the ratio based on the reconstructed results of a two-pinhole helical SPECT scan of the phantom. Excellent agreement has

been achieved between those two ratios, which further trends to verify the efficacy of the image reconstruction program I developed.

4.6 SPECT scans

Unless stated otherwise, every SPECT run in the following set of experiments was taken in 3° increments and with a 3 minute dwell time at each angular position for a total of 120 projections. The step increment along the axis of rotation is 0.5 mm for the helical orbit. A magnifying factor of 3 was used in each scan with the radius of rotation for SPECT imaging set to 2.5 cm. The energy window set for gamma-ray imaging was from 22 to 40 keV, which was suitable for the photons emitted from ^{125}I .

4.7 Characterization comparison

Characterization comparison was carried out among single-, three-, and five-pinhole circular and helical SPECT. The central pinhole and the three pinholes on the diagonal of the five-pinhole collimator were employed respectively for single- and three-pinhole collimations by shielding the unused pinholes.

4.7.1 Field of view

In order to simplify the comparison of FOV for the multipinhole case, we compared the effective view area (EVA) in the plane passing through the AOR. The FOV of the corresponding collimation is simply the volume by rotation of the EVA around the AOR. The EVA of pinhole collimation was calculated based on the geometry of the pinholes with a magnifying factor of 3. The EVAs of three- and five-pinhole collimation were compared with single-pinhole collimation as reference. A $17.6 \times 12.8 \text{ mm}^2$

rectangular object big enough to cover the thyroid region of a mouse was simulated to calculate the multiplexing percentage which is the overlap area divided by the overall area of detector plane.

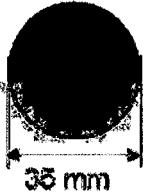
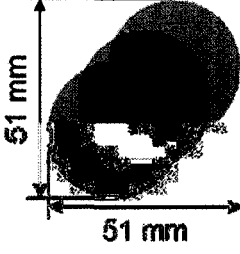
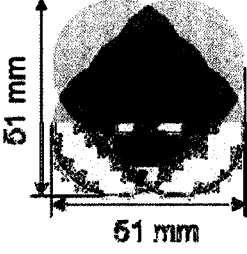
Collimator	Single-pinhole	3-pinhole	5-pinhole
Effective view area in the plane passing the AOR with magnifying factor 3			
View area increase	/	81%	138%
Multiplexing percentage	/	9.5%	20%
SPECT efficiency (counts/min/ μCi)	237	572	927
HSPECT efficiency (counts/min/ μCi)	240	562	893

Table 4.2. Characterization comparison among various modes of SPECT. One may note view area increase is over the single-pinhole case. Multiplexing percentage is the overlap area divided by total detector area with a simulated $17.6 \times 12.8 \text{ mm}^2$ rectangular object whose area is large enough to cover the thyroid region of a mouse.

As shown in Table 4.2, EVAs of three- and five-pinhole collimation have been enlarged by 81% and 138% respectively compared to single-pinhole collimation. For a conventional circular orbit, however, one may readily show that the overall FOV is the same for both three- and five-pinhole case. The FOV of the helical mode is extended

from its corresponding circular mode which eventually depends on the displacement of the detector along the AOR. By choosing a suitable step increment along the AOR, one expects the FOV of a helical mode to cover a specific region of interest or the entire body of the animal.

The enlarged EVA of multipinhole collimation indicates increased sampling area and efficiency for a single projection of the object. However, the five-pinhole collimation causes multiple-fold (up to 5-fold) multiplexing though it has about the same total multiplexing percentage as the three-pinhole collimation. Such a high-fold multiplexing image results in more uncertainty in photon origin and may affect the reconstructed resolution adversely.

4.7.2 Efficiency

The efficiency of different modes of SPECT/HSPECT was determined by a phantom simulating the thyroid region of a mouse. The phantom measures 15.9 x 15.9 x 15.9 mm³ and contains three small voids. Each small void holds a hot source. Small pellets fitting exactly in the void served as isotope media after being immersed in radioisotope solution for homogeneous accumulation of the isotope ¹²⁵I. The pellets were taken out after a few days, allowed to dry naturally in a safety hood and then firmly sealed in the void. Such a method minimizes possible radioactive leakage. The bottom two voids were separated by 3 mm representing the salivary glands of a mouse while the top one simulating the thyroid is spaced 2 mm away from them. The thyroid phantom contains a total of 15 µCi with 5 µCi at each void. For each mode of SPECT/HSPECT, the phantom was imaged at 120 positions with 3° increment and 3 min at each position.

The step increment of helical SPECT along the AOR is 0.1 mm with a total of 12 mm displacement for the entire imaging. The total counts of all the 120 planar images were then collected and averaged over time to obtain the efficiency.

As expected, the efficiency of pinhole circular SPECT is almost identical to that of short-range helical SPECT. Moreover, the efficiency of five-pinhole collimation is increased significantly to the level near that of parallel-hole collimation with the 5 mm thick high-sensitivity collimator #1, i.e. 1538 cpm/ μ Ci, while the single-pinhole collimation shows relatively poor sensitivity.

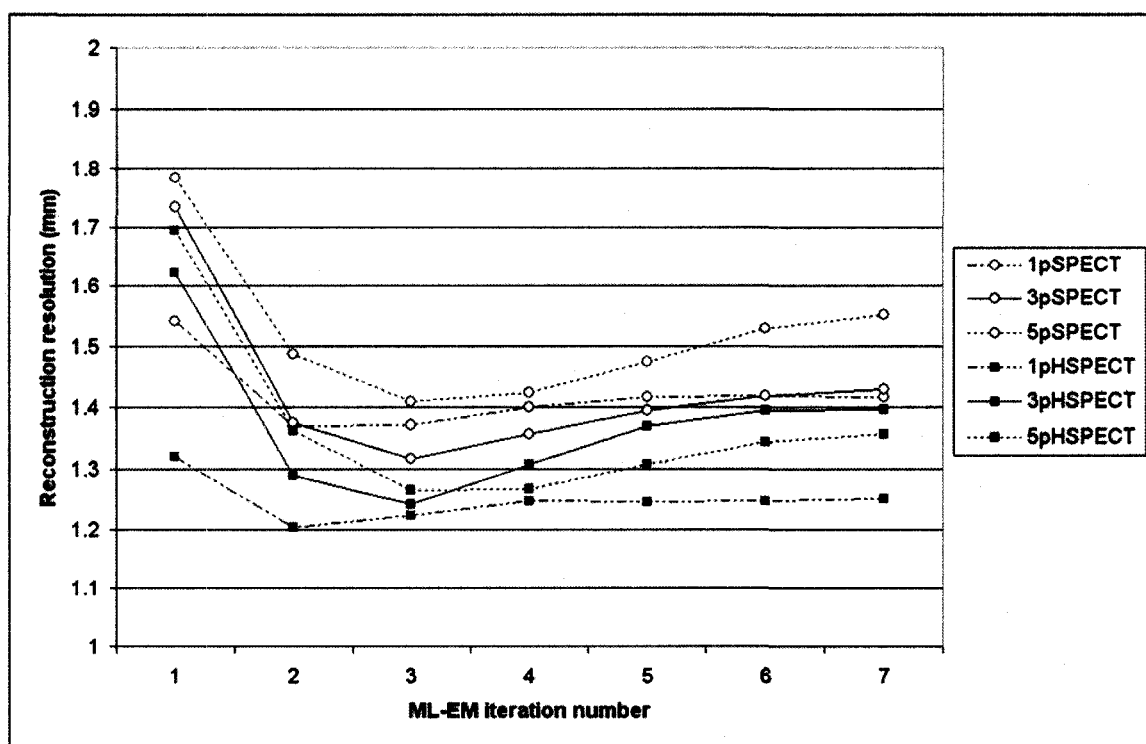


Fig. 4.11 Reconstruction resolution (FWHM) as a function of ML-EM iteration number for various modes of pinhole circular or helical SPECT

4.7.3 Resolution

Test scans of different modes of pinhole SPECT/HSPECT were carried out using the three-capillary phantom shown in Fig. 4.13(a). One of the capillaries was located 5.6 mm off the AOR and used to determine the reconstruction resolution (FWHM) of each mode of pinhole circular or helical SPECT. Each FWHM was obtained through Gaussian fit. The step increment along the AOR was 0.5 mm for each 3° rotation of helical SPECT. Five transaxial images were reconstructed at different positions of the capillary for each scan. The intensity profiles along the line across the center of the reconstructed capillary region were then analyzed and fitted to Gaussian curves. Each FWHM was then calculated and the group corresponding to each SPECT mode was averaged to obtain the resolution of the mode. The relationship was determined between the reconstruction resolution and iteration number.

Presented in Fig. 4.11 is the plot of the overall reconstruction resolution as a function of ML-EM iteration number for various modes of pinhole circular/helical SPECT. Six sample profiles of the capillary in the transverse reconstructed slices after 13 iterations are presented in Fig. 4.12 corresponding to 1-, 3- 5-pinhole circular/helical SPECT respectively. Each profile was normalized to its peak value.

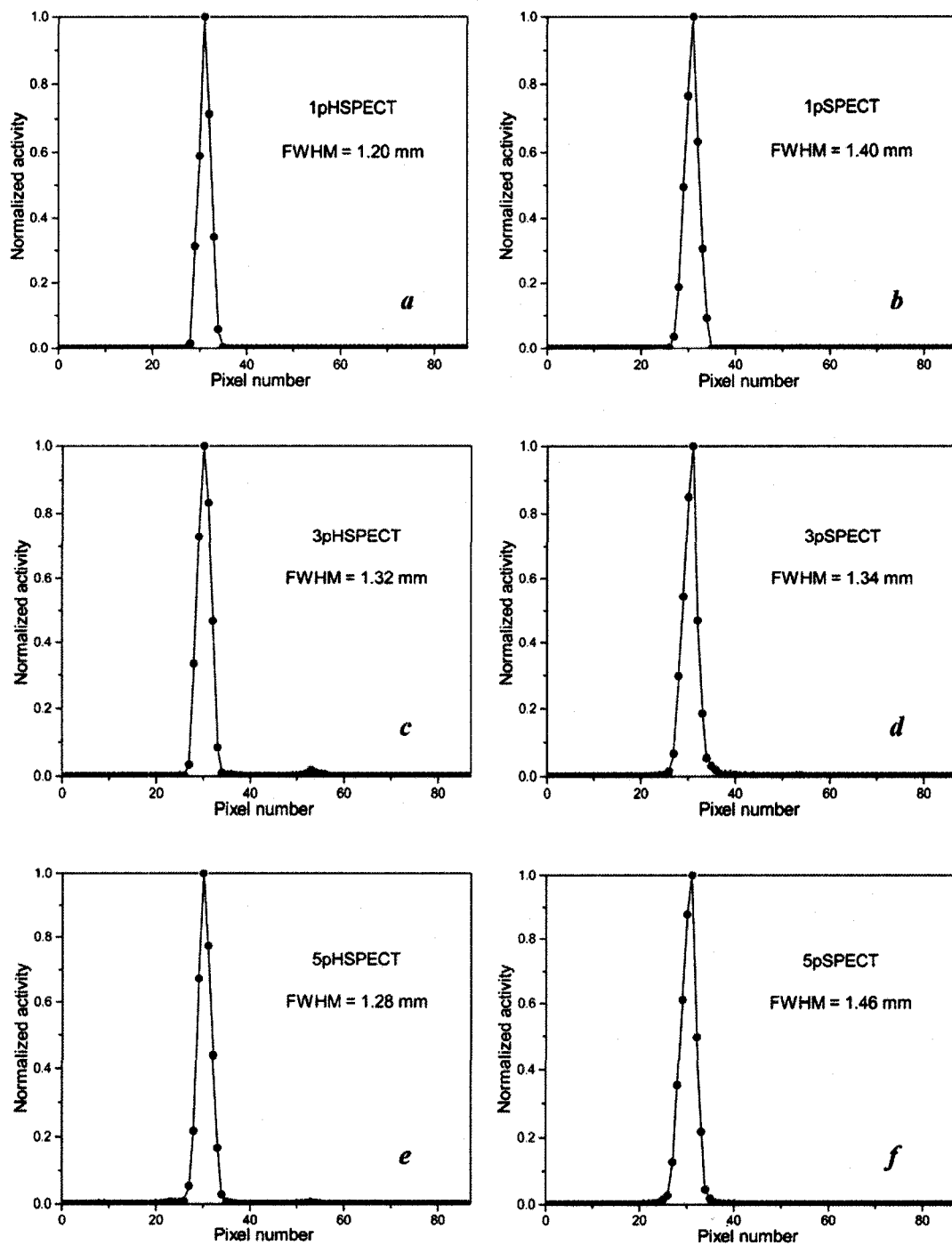


Fig. 4.12. Six profiles (a) – (f) of the capillary in the transverse reconstructed slices after 13 iterations for 1-, 3- 5-pinhole helical SPECT (a, c, e) and circular SPECT (b, d, f)

4.8 SPECT imaging – phantom studies

We have made preliminary performance evaluations based on phantom studies. An experiment was carried out to demonstrate the extended field of view. Shown in Figure 13(a) is the phantom set up with three capillary tubes, each of which was 0.3 mm in inner diameter and contained 18 μCi Na^{125}I in 8 cm length. One capillary was put on the intersecting line of two perpendicular planes. A second capillary in one of the planes

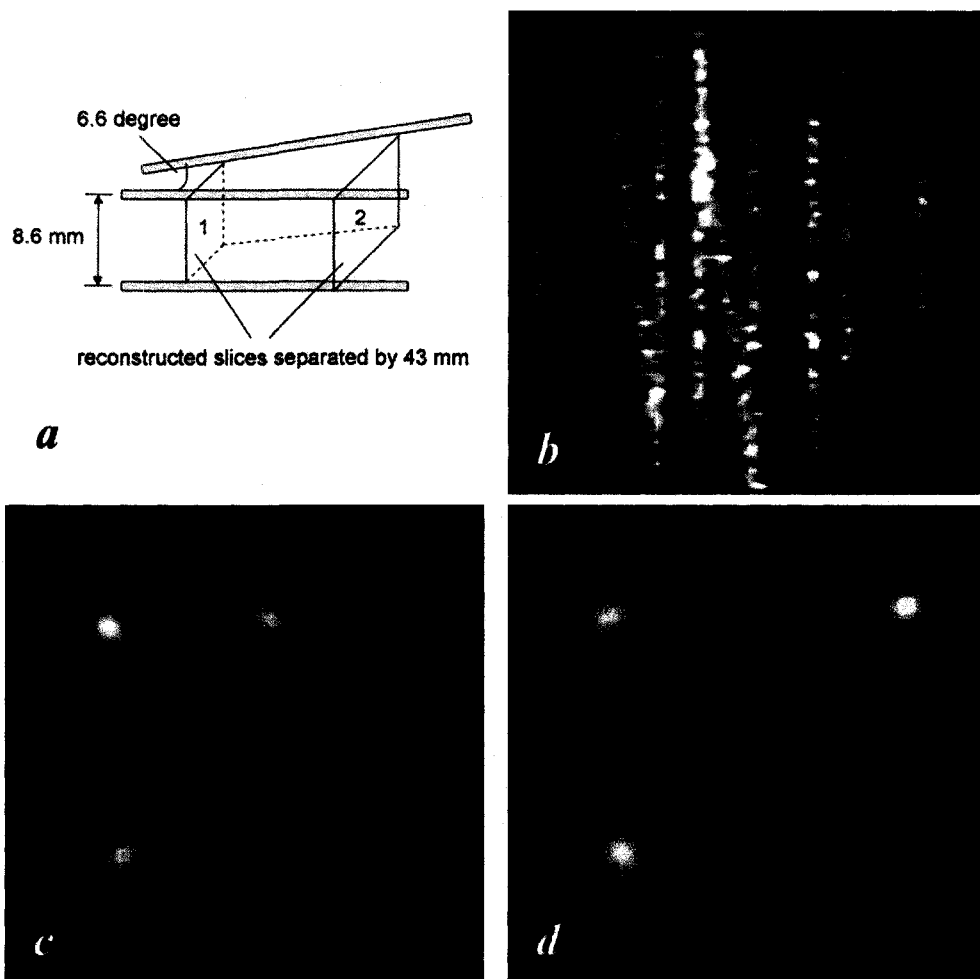


Fig. 4.13. A 54 μCi three-capillary phantom study of 3-pinhole helical SPECT. (a) Phantom setup. (b) A 3-min projection (c) Reconstructed slice 1 (d) Reconstructed slice 2.

was parallel to it with 8.6 mm separation and a third one was in the other plane at an angle of 6.6° . A 3-pinhole collimator was employed and helical SPECT was performed with an object translation step increment of 0.5 mm (the total movement along the AOR was 60 mm). Shown in Fig. 4.13(b) is a typical 3-min projection of the phantom. Two transverse reconstructed slices are presented in figures 13(c)-(d). They were taken at positions separated by about 43 mm, which was larger than the 35 mm diameter of the EVA of the detector with a single pinhole.

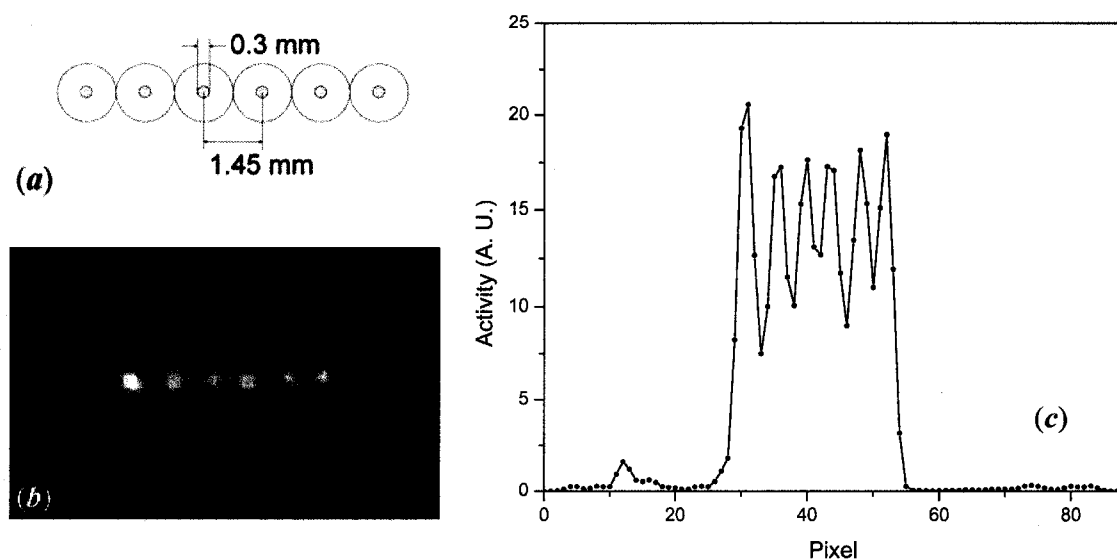


Fig. 4.14. (a) A transaxial view of the phantom made with 6 capillary tubes placed side by side. Each tube contained $\sim 10 \mu\text{Ci}$ Na^{125}I in 8 cm length. (b) A transaxial image of a 3-pinhole helical SPECT scan of the phantom. The step increment along AOR is 0.5 mm. (c) The profile of the six capillaries in the reconstructed image (b).

To demonstrate that the calculated reconstruction resolution is reasonable, we did three-pinhole helical SPECT of the capillary phantom shown in Figure 14(a), which was made with six glass capillary tubes placed side by side. The helical increment along the AOR was 0.5 mm per step. Each capillary contained $\sim 10 \mu\text{Ci}$ Na^{125}I in 8 cm length. The diameter of each capillary was identical to that used for resolution measurement, namely,

0.3 mm in inner diameter and 1.45 mm in outer diameter. Therefore, the center-to-center distance of two adjacent tubes was 1.45 mm. The phantom of six capillaries placed side by side is shown in Fig. 4.14(a), followed by the reconstructed image presented in Fig. 4.14(b). Shown in Fig. 4.14(c) is the profile of the capillaries in the reconstructed image of a 3-pinhole helical SPECT scan. Each capillary can be resolved consistent with the calculated resolution.

Performance of the imaging system was further evaluated using an ultra-micro hot spot phantom (Data Spectrum Co.) filled with $\sim 270 \mu\text{Ci Na}^{125}\text{I}$, which had a radioactivity concentration of $54 \mu\text{Ci/ml}$. The phantom is 3.50 cm in outer diameter and about 5.5 cm in height. The rod insert is 2.7 cm in diameter with a height of 0.99 cm. The hot rod diameters of the six wedge-shaped regions in the insert are 0.75, 1.0, 1.35, 1.7, 2.0, and 2.4 mm, respectively. The center-to-center spacing of the rods in each wedge is two times the rod diameter. An additional ~ 1.3 cm thick plastic disk insert was used to reduce the total volume of solution required to fill the phantom. Helical SPECT scans using this hot-rod phantom were carried out with one or three pinholes with planar projections at 3° increments and 3 min/projection. The step increment was set to 0.1 mm considering the thickness (~ 10 mm) of the rod insert. Out of the 120 projections obtained in each scan, sixty projections with angular positions at 6° intervals were used to represent a three-hour helical SPECT scan with a step increment of 0.2 mm along the AOR. Images were reconstructed using 30 and 60 iterations for 1- and 3-pinhole helical SPECT, respectively. Reconstructed images with 4.4 mm total thickness are presented in Fig. 4.15.

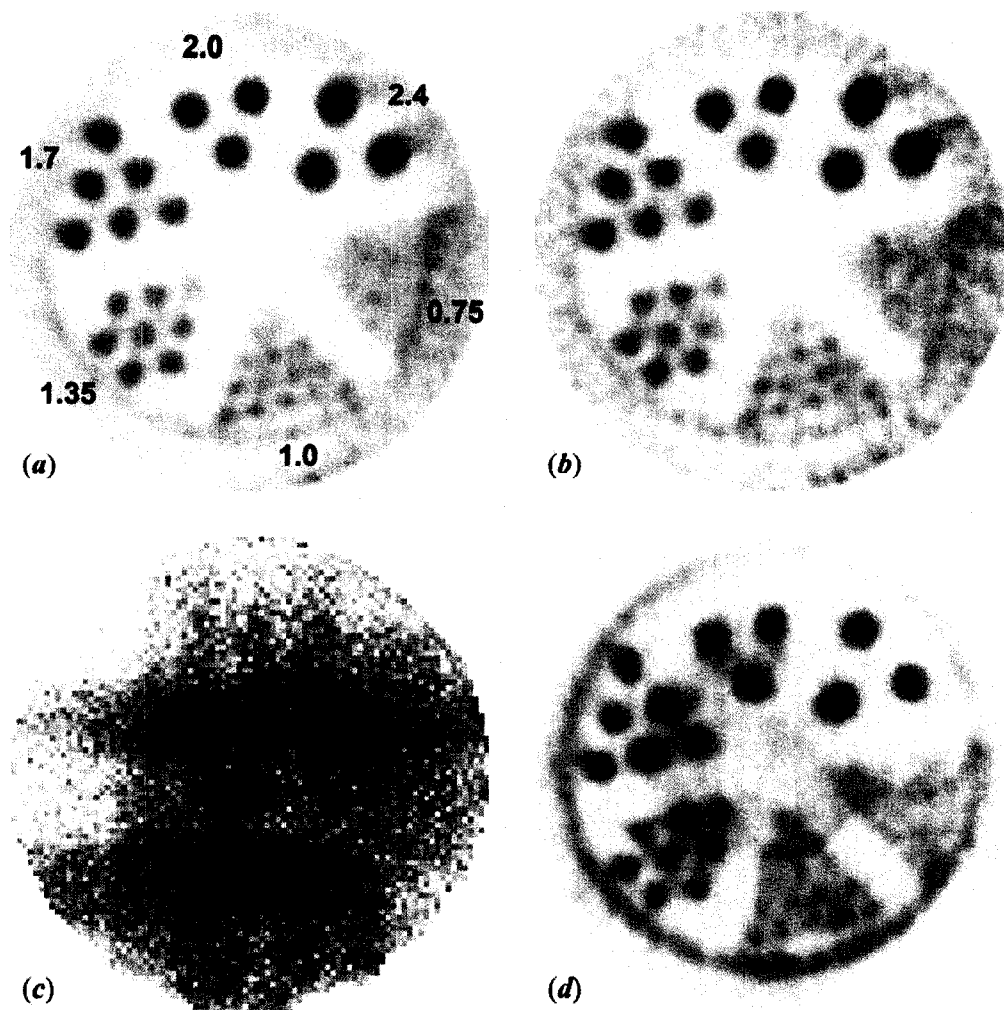


Fig. 4.15. (a) A transaxial view of the hot-rod phantom using single-pinhole helical SPECT with 3° angular increments and 0.1 mm step increments along the AOR. Each of the 120 projections was 3 min/projection. The hot-rod phantom contained $270 \mu\text{Ci } ^{125}\text{I}$ with a concentration of $54 \mu\text{Ci/ml}$. The hot rod diameters of the six wedge-shaped regions in the phantom are 0.75, 1.0, 1.35, 1.7, 2.0, and 2.4 mm, respectively. (b) An image reconstructed from 60 slices out of those 120 projections to represent three-hour 1pHSPECT (c) One 3-min projection of the hot-rod phantom of a three-pinhole helical SPECT scan with the same imaging parameters as the 1pHSPECT scan. (d) A transverse image reconstructed from the 120 projections of the 3pHSPECT scan.

The reconstructed images of the hot-rod phantom are shown in Fig. 4.15 for single- and three-pinhole helical SPECT (1pHSPECT or 3pHSPECT). The image from six-hour 1pHSPECT can resolve the 1 mm diameter rods well and a few of the 0.75 mm rods. The image reconstructed from 60 out of the 120 projections of the six-hour

1pHSPECT scan reflects some noise owing to reduced statistics but still resolves the 1 mm rods.

Similarly, as shown in Fig. 4.15(d), the reconstructed image of six-hour 3pHSPECT can also resolve 1 mm rods well and some of the 0.75 mm rods. The enlarged field of view using three pinholes facilitates reconstruction of the circular gap region in the phantom between the rod insert disk and the inner wall of the container. This hot circular region is only partially shown in single-pinhole cases. Some artifacts appear in the 3-pinhole cases mainly owing to the fact that there are always parts of the phantom truncated in projections through each pinhole as evidenced by a three-pinhole projection, Fig. 4.15(c). This results from the relatively large scale of the phantom contrasting somewhat with the main focus of the system design on imaging small organs of a mouse such as the thyroid with a magnifying factor 3. Multiplexing effects can be another factor contributing to artifacts. Results of both the single- and three-pinhole helical SPECT clearly demonstrate that the resolution we measured based upon fine capillaries containing high radioactivity concentration are also valid for a more conventional case in which a radioactivity concentration of a few $\mu\text{Ci/ml}$ of radioactivity is used in the hot rod phantom.

4.9 Discussion and conclusion

We have described the development of a compact gamma-ray imaging system incorporating multipinhole helical/circular SPECT in addition to parallel-hole SPECT. The characterization of various modes of pinhole SPECT has been investigated using radioactive phantoms. As shown in Table 4.2, the diameter of the FOV of 3- or 5-pinhole

circular SPECT is increased by a factor of ~ 1.5 compared with the single-pinhole case. The FOV is further increased in the longitudinal direction for multipinhole helical SPECT depending on the step increment along the AOR.

The resolution comparison among pinhole SPECT/HSPECT shows that a reconstructed spatial resolution of 1.2 - 1.5 mm can be achieved with this system. Both the profiles in Fig. 4.12 and the result of 3-pinhole helical SPECT of the six-capillary phantom in Fig. 4.14 demonstrate that the calculated FWHM resolution is reasonable. The results in Fig. 4.11 indicate that there is no appreciable difference in the reconstruction resolution among one-, three- and five-pinhole SPECT using both circular and helical orbits. Referring to Table 4.2, the results further indicate that acceptable reconstruction resolution can be achieved with this system while the efficiency is enhanced substantially with an increase in the number of pinholes from one to five. On the other hand, we observed slower convergence of the ML-EM algorithm for multiple pinhole data than for a single pinhole in either the circular or helical case. There is also slight loss of reconstruction resolution with increasing iteration number. Both these results are consistent with the report of Meikle *et al.*, whose simulation result of mean squared error versus iteration number indicated both slower convergence of the ML-EM algorithm for multipinhole SPECT and increased noise with increasing number of iterations [65].

The measured resolutions are further demonstrated by experiments using hot-rod phantoms. Results from both single- and 3-pinhole helical SPECT can resolve hot rods as small as 1 mm in diameter. The reconstructed images of the 3-pinhole case show some artifacts in that phantom as explained above. Small organs in the mouse, such as the

thyroid, can be fully projected on the detector through two or more pinholes simultaneously with little or no multiplexing area, which can substantially improve the image quality. The system design is also intended for a relatively low injection dose of radioactivity in biological studies. The results here demonstrate that our system has the potential for high-resolution SPECT imaging using a radioactivity concentration as small as 54 $\mu\text{Ci/ml}$, which is of the same order as in the thyroid of a mouse injected with tens of μCi of ^{125}I .

Our system is constructed in an economical, compact and, especially, expandable manner. An additional small fluoroscopic X-ray apparatus (Lixi, Inc.) installed on the gantry is available to provide dual-modality imaging [117] as described in section 3.1. More “mouse-sized” parallel-hole detectors may be incorporated to facilitate faster three- or four-head SPECT of a small animal. The pixellated NaI scintillators for both parallel-hole and pinhole detector are 5 mm in depth, which is adequate for imaging various higher energy isotopes such as $^{99\text{m}}\text{Tc}$ if a suitable collimator is implemented.

In conclusion, a compact SPECT system has been built and tested incorporating multipinhole helical/circular SPECT in addition to parallel-hole SPECT. The variety of imaging modes in this system can readily meet the requirements for a range of small animal applications. Our phantom studies have demonstrated the feasibility of employing multipinhole helical SPECT for small animal imaging. The results indicate that the resolution of our system is virtually identical for one, three and five-pinhole SPECT, while the efficiency is enhanced by the presence of the additional pinholes. The accomplishment of enlarged field of view, very good resolution and improved sensitivity with multipinhole circular or helical SPECT suggests the potential for high-resolution

imaging of small tissues or entire animals with good sensitivity. Additional work is planned with realistic animal phantoms, followed by studies with anesthetized mice.

Chapter 5

***In vivo* gamma imaging in studies of the mouse thyroid**

Among mouse tissues and organs of interest to investigators, the thyroid is particularly useful for imaging studies in biological research as either target tissue or a system for proof-of-concept tests. Radionuclide imaging of the thyroid is practicable considering the underlying molecular biology of the expression of the sodium iodide symporter (NIS), an intrinsic membrane protein facilitating transport of active iodide into the thyroid gland. The thyroid is thus particularly suitable for such imaging given that NIS-expressing follicular cells take up several radioisotopes, for example, ^{125}I , $^{99\text{m}}\text{Tc}$ and ^{188}Re [127]. The thyroid has a relationship to a number of diseases and thyroid imaging has potential implications for pathophysiology and therapeutics in those diseases in addition to providing a better understanding of thyroid physiology [128, 129].

This chapter describes the application and potential of our imaging system in thyroid studies. The first section of this chapter briefly describes the application of planar gamma imaging in re-evaluation of the use of KI in blocking the uptake of radioiodine in the thyroid of living mice. In this discussion the emphasis is on gamma imaging and results rather than biological investigation. The remainder of this chapter presents in detail the *in vivo* study of visualizing NIS in the mouse thyroid using the multipinhole helical SPECT system (see detail in Chapter 4) with a relatively low dose of ^{125}I .

Complementary results from molecular biology assays including immunohistochemistry and reverse transcriptase polymerase chain reaction are also presented to verify that radioiodine incorporation in the thyroid gland reflects NIS expression, validating the SPECT imaging of the mouse thyroid at the molecular level.

5.1 *In vivo* study of KI blocking efficiency in mice

As mentioned previously, low emission energy and the reasonably long half-life of ^{125}I make it an efficient tool for imaging a small animal over more extended periods of time. However, radioiodine administered into the mouse body usually is transported into the thyroid and “trapped” there in the form of thyroid hormones. This can prolong thyroid exposure to radiation and could eventually result in thyroid malfunction [2]. To protect the mouse thyroid from such potential damage in biological studies, we orally administered potassium iodide in order to block the thyroid from taking up radioiodine in these studies. Initially we employed the FDA-recommended human blockade dose of KI scaled to the body weight of the subject mice. However, we found that the blockade efficacy was incomplete. It is worth noting that hundreds of radio-iodinated compounds are widely used in biomedicine both with animal and human subjects. In addition, there can be a need to protect humans from the potential accidental release of radioiodine fission fragments, especially ^{131}I and ^{129}I associated with nuclear power [2]. Therefore, we have recently carried out a study to re-evaluate KI-blocking efficiency in both thyroid and extrathyroidal tissues including stomach, thorax, and leg using the mouse model and our imaging system.

To achieve these aims, we have designed a set of experiments for the re-evaluation of KI blocking efficacy and applied *in vivo* gamma imaging using a 110 mm diameter circular detector and image analysis into these experiments. My principle contribution in this work was to carry out data acquisition of gamma imaging and image processing required by the designed experiments, to determine the relationship between whole body clearance and KI dose administered into the mice, and to provide support for data analysis including improving ROI programs written in IDL.

5.1.1 Gamma-ray detector and imaging

The detector employed in this study has been described in detail in previous publications [68, 117] and also briefly in Section 3.3.1. To confirm the accuracy of gamma-ray imaging using this detector and its applicability as a tool for *in vivo* biological studies, we compared the ROI data of a mouse thyroid obtained from gamma images with the counts of the alternative method, i.e. liquid scintillation (LS) counting of the dissected thyroid tissue[2]. A significant correlation ($r^2 = 0.9842$, $p < 0.05$) was found between the results of these two independent methods, which validate the efficacy of this gamma camera for imaging application in biological studies.

Planar gamma imaging of the mice was carried out *in vivo* in this study. Each anesthetized mouse was imaged immediately after a dose of $\sim 14 \mu\text{Ci Na}^{125}\text{I}$ was administered into the mouse body. The data from one full-hour imaging of each mouse included information on each individual gamma-ray count, its spatial position and time, were collected using a Macintosh G3 computer. The mouse was kept anesthetized and

alive during the imaging period. After data collection, the data files were transferred to a Macintosh G4 computer for data analysis.

5.1.2 Data analysis

Using computer programs written in IDL language (ITT Corporation), the data files were grouped into several 5-min interval blocks. Each block is stored in a file (called a “timecut”) representing the two-dimensional distribution of radioiodine in the mouse body accumulated in the corresponding five-minute interval. Therefore, the set of timecuts can “re-display” the 2D distribution of radioiodine and its change in the mouse body over the full-hour imaging period. By placing a region of interest on an image and collecting the total counts, one can quantitatively evaluate the level of cumulative radioiodine in target tissues such as the thyroid *in vivo* and its change over time. The ROI size used for analysis of the mouse thyroid gland has been set to 4 x 4 pixels (1.2 x 1.2 mm² per pixel). In addition, ROIs with a size of 8 x 8 pixels were used for analyzing other tissues including thorax, stomach, left leg and injection site. For easy comparison among those tissues, all the ROI results were normalized as the percentage of the total injection dose (%ID) determined by the total counts of the whole-mouse ROI with a size of 30 x 80 pixels.

5.1.3 Experiments and results

In this subsection, the purposes and results of the experiments designed to evaluate the blocking efficiency of KI in the thyroid and extrathyroidal tissues are described. Those results have been published recently in Health Physics [2]. The figures

presented in this subsection except Fig. 5.5 and Fig. 5.6 are reproduced from that publication with permission granted by the publisher Lippincott Williams & Wilkins.

These experiments studied the dynamic change of the radioiodine accumulated in the target tissues at different time periods (0 to 1 hour, 1 hour to 24 hours, 1 hour to 7 days, respectively) after injection of Na^{125}I into the mouse body. A variety of KI blockade dosage employed, no KI, 1X, 3X, 5X and 10X KI doses, where 1X was equivalent to the dose scaled from human dose to mouse by body weight. The dynamic change of radioiodine level during the first hour after injection was compared among the thyroid, stomach and injection site with thorax and left leg as references for background (see Fig. 5.1). The KI blocking dose was fed to the mouse orally 60 minutes prior to injection of the radioiodine. The results in Fig. 5.1 indicate that, although a 1X KI dose effectively blocks the radioiodine accumulation in the thyroid, a higher KI dose such as 5X or 10X can substantially increase the blocking efficiency when administered prior to exposure to radioactive iodine [2]. As to other tissues, the KI blocking effects are similar for the different KI doses. Presented in Fig. 5.2 is a set of five images of mice administered a variety of KI blocking dose prior to injection of radioiodine. These images, taken in the time period 50-55 minutes after injection of radioactive iodine, show mice administered blocking doses of 0, 1, 3, 5 and 10X the scaled human KI dose prior to injection of ^{125}I .

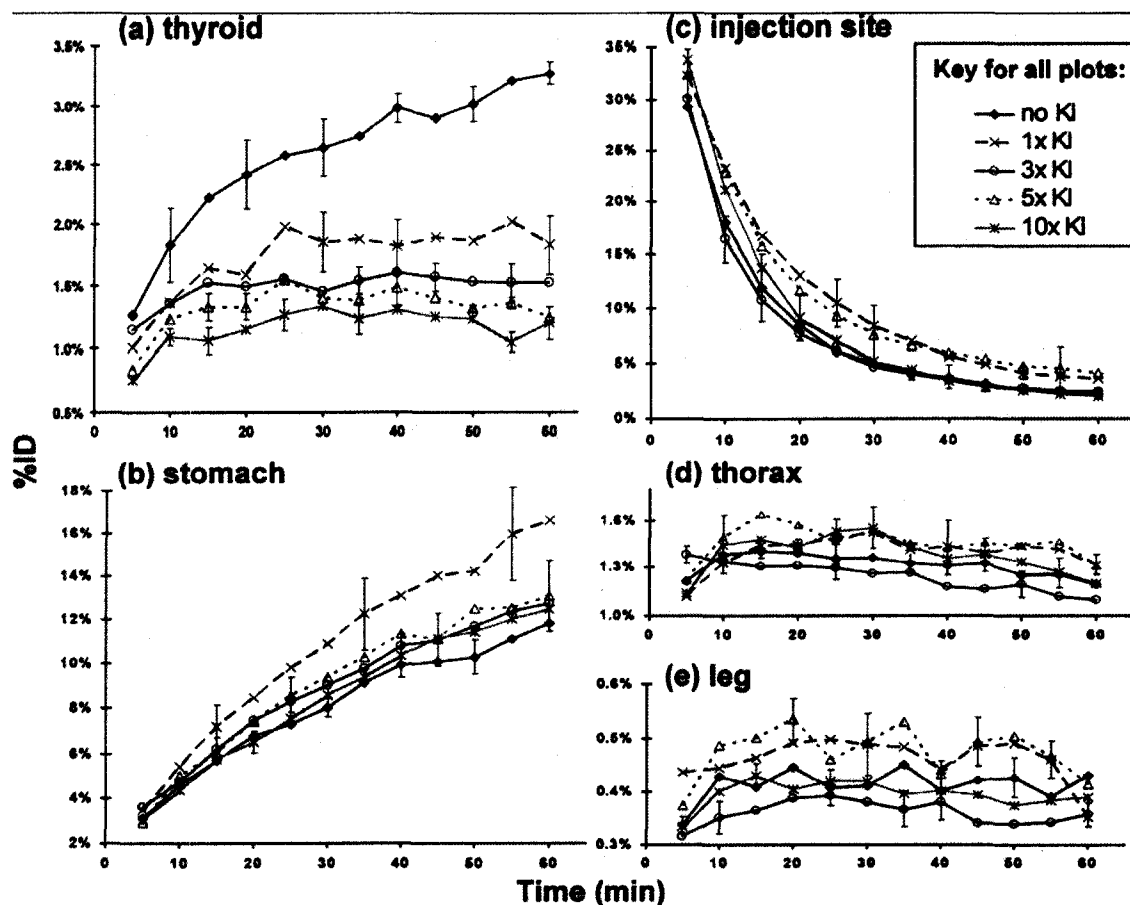


Fig. 5.1. The dynamic change of radioiodine uptake during the first hour after injection in thyroid, stomach, injection site, thorax and left leg. A variety of KI blockade dosage was employed including no KI, 1X, 3X, 5X and 10X KI doses, where 1X was equivalent to the dose scaled from human dosage to mouse based on body weight [2].

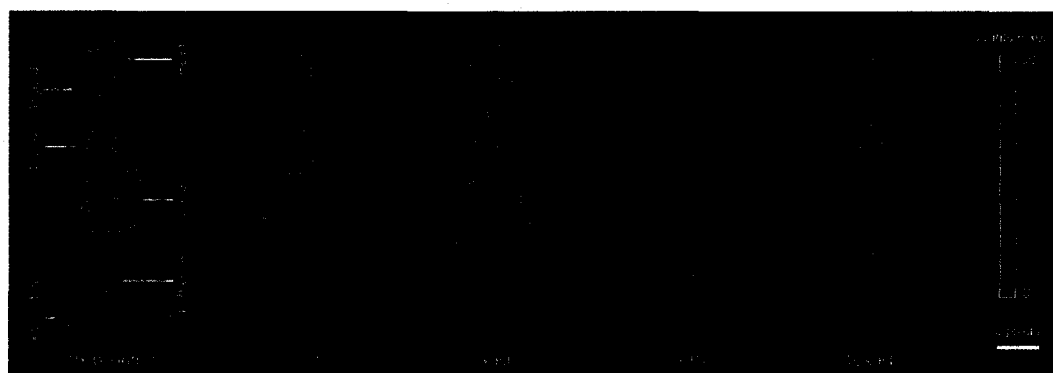


Fig. 5.2. Images which reflect KI blocking effects in different target tissues for five mice receiving KI blocking doses of 0, 1X, 3X, 5X, 10X the scaled human blocking dose. The images were taken during the period 50-55 minutes after injection of radioactive iodine [2]. The KI doses were administered orally 60 minutes prior to ^{125}I injection.

For comparison to the evaluation of immediate blocking efficiency in Experiment I, a second experiment was carried out to examine the retention of the KI blocking over a longer time period at 1 hour, 1 day and 7 days following exposure to radioiodine. In this experiment, 1X and 5X KI human doses were used with unblocked mice as control animals. Consistent with Experiment I, the results presented in Fig. 5.3 show 5X KI human dose, administered 60 minutes before injection of ^{125}I , continues to provide a higher level of protection than the 1X KI dose 7 days after radioiodine injection [2].

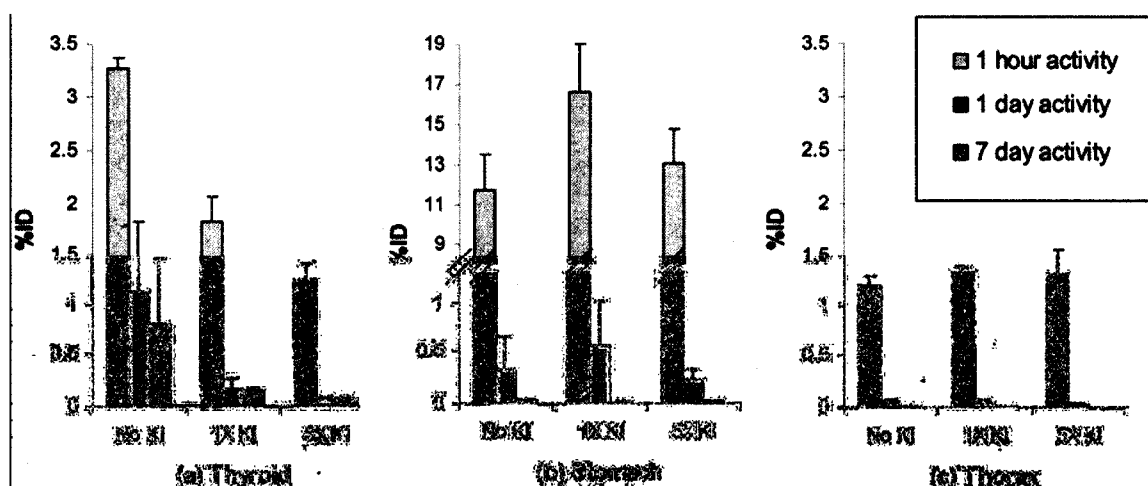


Fig. 5.3. Evaluation of the retention of the 1X and 5X KI blocking efficiency at times 1 hour, 1 day and 7 days following blocking dose and exposure to radioiodine with unblocked mice as control animals [2].

A third experiment was designed to learn whether the significant drop in activity between 1 hour and 1 day as shown in Fig. 5.3 happened in a precipitous or a more gradual manner. This experiment examined the ^{125}I retention in thyroid, stomach and thorax at 1, 6, 12 and 24 hours after administration of the blocking dose followed 60 minutes later by injection of the ^{125}I dose. The blockade dose administered to mice was 1X KI human dose [2]. The results in Fig. 5.4 indicate that thyroid radioiodine content

declined gradually over the first 24 hours after injection while, surprisingly, the radioactivity in the stomach increased between hours 1 and 6 [2].

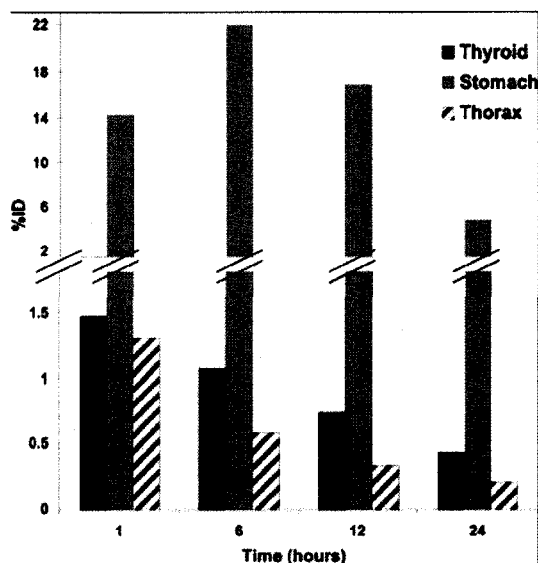


Fig. 5.4. Evaluation of ^{125}I retention in thyroid, stomach and thorax at 1, 6, 12 and 24 hours after injection using 1X KI human dose which was administered orally 60 minutes prior to ^{125}I injection [2].

In an attempt to determine the relationship between urine or whole body clearance and KI dose, we carried out Experiment IV using a small sample of mice ($n = 2$ for each group orally administered 0X, 1X and 5X human KI dose, respectively). Again, KI dose was administered 60 minutes prior to radioiodine injection. After injection, each mouse was put back in an individual cage, inside which there was an absorbent paper entirely covering the bottom area of that cage in order to collect the urine and feces of that mouse. Twenty four hours following radioiodine injection, each mouse was *in vivo* imaged for 5 minutes and the image was saved as a timecut. The mouse was then sacrificed immediately after imaging. The feces, the paper containing mouse urine and the mouse body were collected and imaged separately followed by data analysis. For normalization purpose, the sum of the counts of all the three subjects was considered as the total

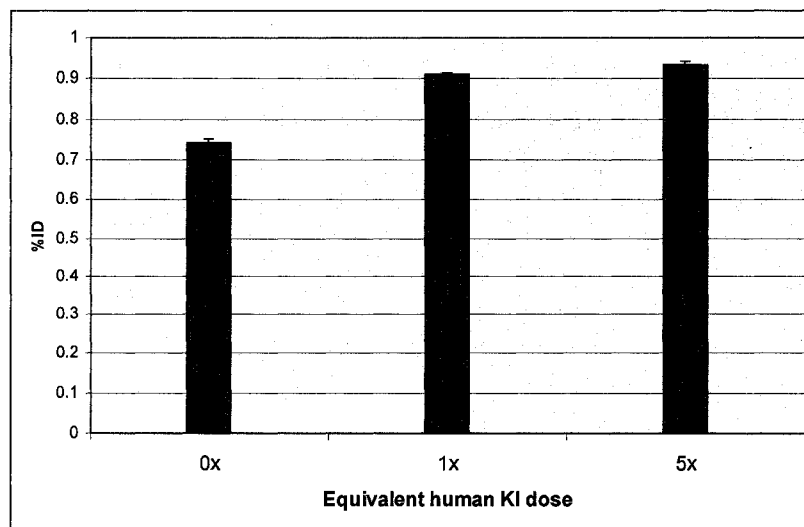


Fig. 5.5 Urinary clearance as a function of equivalent human KI dose 24 hours after radioiodine injection. A variety of KI doses (0X, 1X and 5X) was orally administered into the mouse 25 hours prior to gamma imaging.

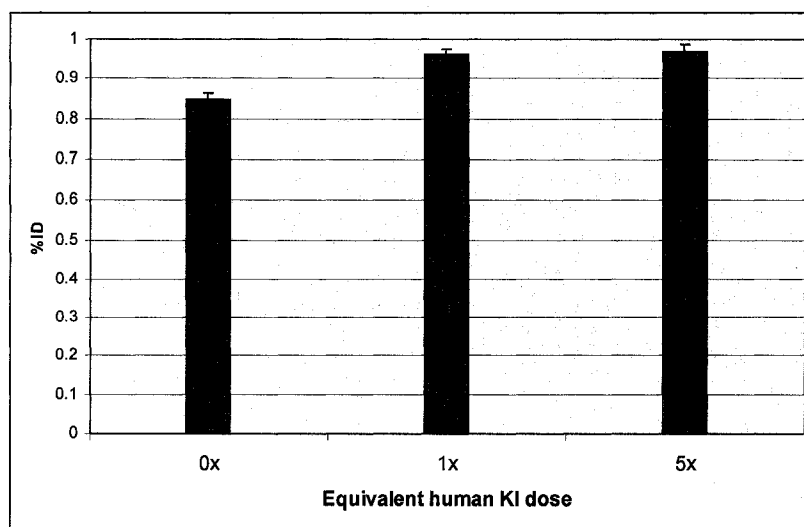


Fig. 5.6 Whole body clearance as a function of equivalent human KI dose 24 hours after radioiodine injection. A variety of KI doses (0X, 1X and 5X) was orally administered into the mouse 25 hours prior to gamma imaging.

injection dose in this case. My analysis showed that over 96% of radioiodine in the mouse body had been cleared through urine and feces during the first 24 hours after injection (see Fig. 5.6). Both urinary clearance (see Fig. 5.5) and whole body clearance (see Fig. 5.6) for blocked animals were substantially higher than unblocked animals 24

hours after radioiodine injection, which was consistent with our previous results. The data also indicated no statistically significant differences between either urinary or whole body clearance using 1X and 5X human KI doses.

5.1.4 Discussion and conclusion

The results of this study re-evaluating the blocking efficiency of KI suggest that the KI human dose equivalent provides much less effective protection for the mouse thyroid than a higher KI dose. The dose effects are also interesting in extrathyroidal tissues, in particular the stomach, and could be important for those tissues-related studies. In particular, this study demonstrated the utility and advantages of our imaging system as a promising tool in a range of similar biological studies.

This system allows *in vivo* gamma imaging of the mice. This significant feature facilitates evaluation of the KI-blocking effects on the same animal repetitively over a chosen time period. A small number of mice was required in this study as a consequence. The real-time feature of the imaging system makes it possible for us to examine the distribution of radioiodine content in target tissues in both dynamic and static manners. Moreover, owing to the relatively high spatial resolution (~ 2 mm), good sensitivity and a field-of-view sufficient for whole-mouse imaging, we are able to obtain high-quality gamma images using a relatively low dose of radioiodine (~ 14 μ Ci). Those gamma images enable us to distinguish the target tissues easily with good detail. Hence, more accurate ROI analysis can be carried out as well as comparison among either different mice or different tissues in the same mouse. In particular, statistical variation in the study

arising from the inter-animal differences is reduced since each animal could serve as its own control.

In conclusion, this study, based on a mouse model, suggests the potential value of reconsidering KI dosage or alternative thyroid blockade pharmaceuticals for emergency protection of human thyroid [2]. On the other hand, since mice have been extensively used in preclinical research to study tumor therapy through radioiodine uptake, this study may also prove of value in determining the effective and appropriate dosages for mouse thyroid protection.

5.2 *In vivo* multipinhole helical SPECT imaging of a mouse thyroid

The study described in Section 5.1 suggested the need for further evaluation of KI blocking efficiency while simultaneously indicating the need of novel, non-invasive technologies for further addressing this health issue [2]. Such *in vivo* study on the mouse thyroid may also benefit from higher resolution that can yield data on the three-dimensional biodistribution of the thyroid's saturation. This information can be provided by data obtained through SPECT techniques. Several clinical studies have demonstrated the advantages of SPECT in effectively detecting thyroid carcinoma, evaluating tracheal compression, finding the extension of multinodular goiter and determining the thyroid volume and mass for dosimetry of radioiodine therapy [130-133]. However, the requirements of both high resolution and sensitivity and the difficulty in localizing radiotracers have limited the utility of SPECT in work with small organs such as brain or thyroid using mouse models [134, 135].

This situation has been improved by a SPECT system incorporating high-performance detectors and/or high-resolution pinhole collimation [1, 111, 116, 136]. As demonstrated in section 3.3.1.4, *ex vivo* parallel-hole SPECT based on a compact gamma camera illustrated considerable difference between the uptake of ^{125}I in the thyroid region and in the salivary glands. The first successful *in vivo* ^{125}I SPECT image was achieved by McElroy *et al.* [136] using a single-pinhole A-SPECT system and 1 mCi Na^{125}I , and clearly delineated both lobes of the thyroid in the reconstructed image. Using a 100 μm diameter gold alloy pinhole constructed by electron discharge machining, Beekman *et al.* successfully achieved a spatial resolution of 200 μm for planar imaging of the thyroid of a mouse injected with 250 μCi Na^{125}I [116]. That work suggested the potential for ultra-high-resolution SPECT of small organs such as the mouse thyroid. Hong *et al.* reported the *ex vivo* ^{125}I imaging of the thyroid of a rat using a compact SPECT/CT system and 1 mCi to localize the isotope [111].

The major drawback of high-resolution single-pinhole SPECT is low sensitivity [137]. A high dose can compensate for the low sensitivity of single-pinhole SPECT. That dose, however, may be a factor affecting physiology and leading to invalid results [138]. The use of large amounts of radiotracer brings the potential for pharmacologic effect risk and increases radiation burden which can cause tissue damage [139]. The high dose may further change the result of imaging studies repeated over time and prevent longitudinal studies using the same animal [139, 140]. Cao *et al.* reported that a dose below 1 mCi is suggested for mouse studies using $^{99\text{m}}\text{Tc}$ -tagged ligands based upon preliminary unpublished dosimetry data [137]. The high-dose effect in thyroid imaging using radioiodine is a significant issue needing consideration. After being administered into the

body, the radioiodine transported into the thyroid is incorporated into the hormones triiodothyronine and thyroxine. This prolongs thyroid exposure to radiation and could eventually result in thyroid malfunction [2]. Low emission energy ($\sim 35\text{keV}$) and the reasonably long half-life (59.4 days) of ^{125}I make it a useful tool for imaging a small animal over more extended periods of time, which, however, also requires the applicable dose be kept as small as possible.

As the review in Chapter 2 indicates, recent advances of pinhole SPECT have provided a potential path to solve these issues with regard to both resolution and sensitivity of mouse thyroid imaging. In Chapter 4, I have described the details of development and phantom tests of multipinhole circular/helical SPECT. Herein we demonstrate the applicability of multipinhole helical SPECT to *in vivo* molecular imaging by presenting results of a study of visualizing NIS activity in the mouse thyroid. This work has employed a low-level dose of ^{125}I ranging as small as $12\text{ }\mu\text{Ci}$ for phantoms to $130\text{-}200\text{ }\mu\text{Ci}$ for subject mice in SPECT imaging. This is significantly lower than the order of millicuries used in previously reported ^{125}I SPECT imaging of mouse thyroid [111, 136]. In addition, we verify that multipinhole helical SPECT is a valid tool for monitoring biological activity at the molecular level such as NIS expression in the thyroid through molecular biology assays. Collaborators Eric Blue and Stephen Schworer of Biology have carried out immunohistochemistry and RT-PCR, respectively. Correlative results from both imaging and molecular assays can thus validate multipinhole helical SPECT for *in vivo* molecular imaging of biological processes.

5.2.1 Multipinhole helical SPECT system and scans

The multipinhole helical SPECT system has been described in detail in Chapter 4 and will be briefly mentioned here. In this work, two pinholes (the central and lower left pinholes) are used with no overlapping area of the projections of the mouse thyroid from both pinholes. Other unused pinholes were shielded with 0.5 mm lead sheet sufficient to block $\sim 35\text{keV}$ photons from ^{125}I . The radius of rotation was 25 mm from the collimator with a magnifying factor of 3 employed in these studies. This setup resulted in a total effective view area from using two pinholes of 13.6 cm^2 at the axis of rotation. The energy window set for gamma imaging was from 22 to 40 keV.

SPECT scans in this work have been acquired at 3° increments around the AOR for a total of 360° . Both the dwell time at each angular position and the step increment along the AOR may be variable and thus are stated in each specific case. We used 10 iterations for image reconstruction in all the following studies except the hot-rod phantom study in which 50 iterations were used. The reconstructed images were smoothed with a Hann filter. No attenuation correction was applied in this work. The reconstruction used 0.4-mm cubic voxels.

5.2.2 Parallel-hole gamma-ray imaging

As a reference tool, one compact gamma-ray camera described in section 3.3 was used for planar imaging of the phantoms. A 5 mm thick parallel-hole CuBe collimator with 0.55-mm square holes separated by 0.11 septa was employed in this detector. This collimation provides a spatial resolution about 2.5 mm FWHM on contact with the

collimator with an effective area of about $46 \times 96 \text{ mm}^2$. As with the circular gamma camera, the energy window for gamma rays was from 22 to 40 keV.

5.2.3 Phantom studies

Phantom studies were carried out to evaluate the performance of two-pinhole helical SPECT. Each SPECT scan in the phantom studies used a dwell time of 3 minutes at each angular position.

5.2.3.1 Resolution

The same phantom and method described in section 4.7.3 were employed to determine the relationship between the reconstruction resolution and the number of ML-EM iterations for two-pinhole helical SPECT. This relationship as presented in Fig. 5.7 indicates that the overall resolution after about 10 iterations of image reconstruction is around 1.3 mm which is adequate for imaging the bilobal structure of the thyroid of a C57-derived mouse. A typical separation between the two lobes of the thyroid is about 1.8-2.5 mm.

To demonstrate that this measurement of resolution is reasonable, a test was carried out with a phantom of two parallel capillaries separated by 2 mm. The step increment along the AOR was 0.1 mm which was also used in the following helical SPECT scans of the thyroid phantom and mouse thyroid.

As shown in Fig. 5.8, a reconstructed image from a further test demonstrates that two capillaries separated by 2 mm can clearly be resolved, confirming the feasibility of multipinhole helical SPECT imaging of the mouse thyroid.

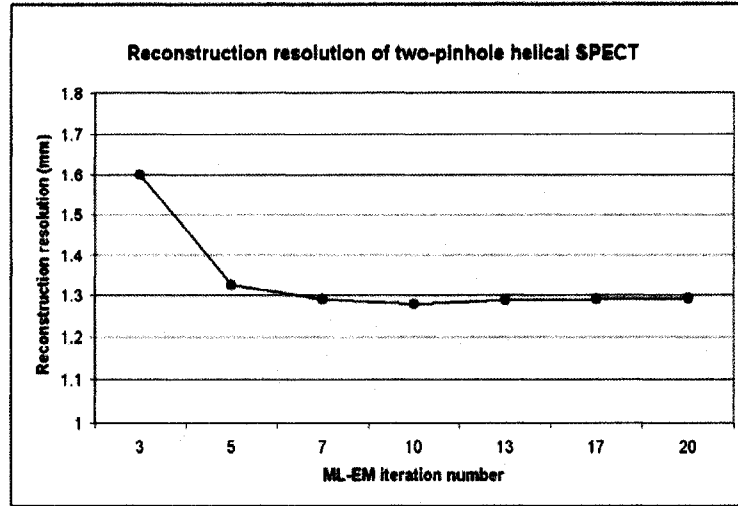


Fig. 5.7. Relationship between the reconstruction resolution (FWHM) and number of ML-EM iterations for two-pinhole helical SPECT

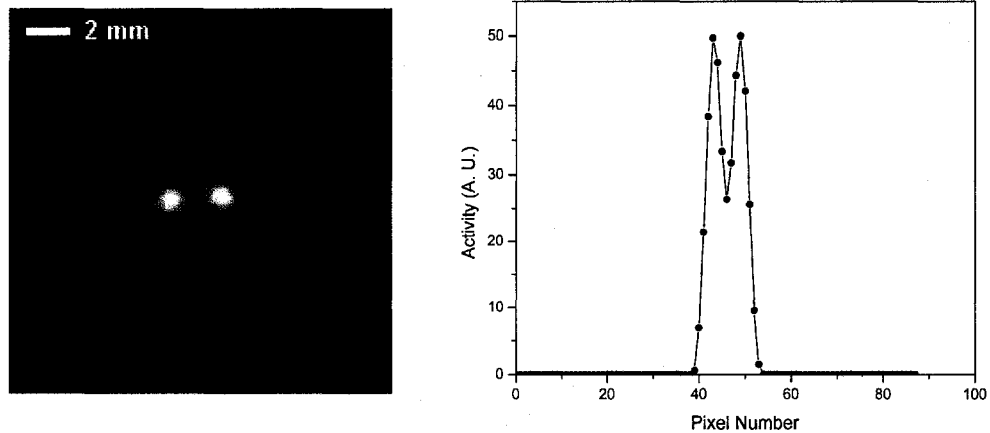


Fig. 5.8. (Left) A reconstructed transaxial slice (0.4 mm thickness) of the 2-capillary phantom. (Right) A profile along the line across the centers of the reconstructed capillaries in the reconstructed image of a two-pinhole helical SPECT scan. The step increment along the AOR is 0.1 mm.

A further test similar to the one described in section 4.8 was carried out using the same ultra-micro hot rod phantom to investigate the potential of two-pinhole helical SPECT for resolving a more sophisticated structure with a relatively low radioactivity

concentration. The phantom contained a solution of 270 μCi ^{125}I . A two-pinhole helical SPECT scan was obtained with step increments of 0.1 mm along the AOR.

Even with the collimator designed for imaging small tissues such as the mouse thyroid and a low radioactivity concentration employed, two-pinhole helical SPECT of the relatively large-scale hot-rod phantom still properly resolves the wedges with rods as small as 1 mm in diameter and many of the 0.75 mm diameter rods can be visualized as well (Fig. 5.9, right). Some artifacts appear in the figure owing to multiplexing effects and the truncation of the phantom in projections as shown in the left panel of Fig. 5.9.

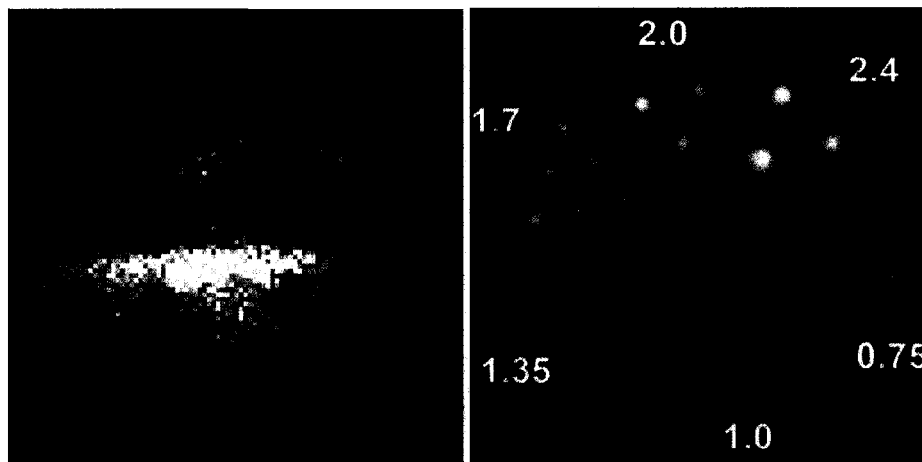


Fig. 5.9 (left) A 3 min two-pinhole projection of the hot rod phantom. (right) A 4 mm thick reconstructed image of two-pinhole helical SPECT of the phantom with 3° increments and 3 minutes at each angular position. The step increment along the AOR was 0.1 mm. The phantom contained a total radioactivity of 270 μCi ^{125}I with a concentration of 54 $\mu\text{Ci}/\text{ml}$.

5.2.3.2 Sensitivity

Single (central pinhole) and two-pinhole helical SPECT were carried out for the purpose of sensitivity comparison using a phantom similar to the one described in section

5.2.3.2. For the phantom used in this work (see Fig. 5.10), the bottom two voids are separated by ~ 2 mm representing the salivary glands of a mouse while the top one simulating the thyroid is spaced 3 mm away from them. The phantom measures $14 \times 13 \times 17$ mm³. Each void contains a ~ 4 μ Ci pellet (~ 12 μ Ci in total in the phantom). This thyroid phantom was placed in the central region of FOV with the plane of the voids perpendicular to the AOR.

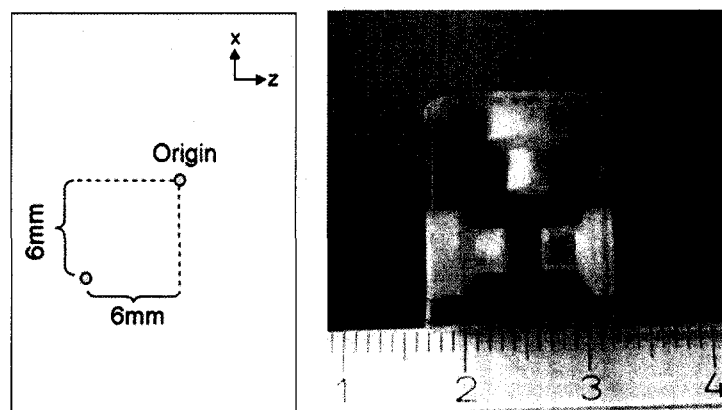


Fig. 5.10. (Left) Diagram of the two-pinhole collimator. The central and bottom-left pinholes were employed in this work. (Right) An example of a three-position thyroid-salivary gland phantom used in this work

The measured efficiency with the thyroid phantom is 221 cpm/ μ Ci and 398 cpm/ μ Ci for one and two-pinhole helical SPECT respectively. We note that the efficiency is not exactly doubled for two-pinhole case owing to the fact that the sensitivity is proportional to $(\cos^3\theta/d^2)$ for each pinhole, where θ is the gamma-ray incident angle and d is the perpendicular distance from the object point to the collimator [89].

5.2.3.3 Quantification

After the two-pinhole SPECT scan, a parallel-hole projection of the thyroid phantom was acquired for 30 minutes. A sum of 14 reconstructed slices (a total of 5.6

mm thickness) from the two-pinhole helical SPECT scan covering the pellets region of the phantom was compared with the 30-min parallel-hole projection. The region of interest (ROI) of each pellet was analyzed with the ROI analysis program written in IDL language. The ROI counts of the pellets from the parallel-hole projection were compared with the data from the sum reconstructed image. A 25-pixel ROI ($1.2 \times 1.2 \text{ mm}^2/\text{pixel}$) was obtained for each pellet in the parallel-hole projection while a 225-pixel ROI ($0.4 \times 0.4 \text{ mm}^2/\text{pixel}$) was used in the reconstructed SPECT image.

The 30-min parallel-hole projection of the $\sim 12 \text{ } \mu\text{Ci}$ thyroid phantom is shown in the left panel of Fig. 5.11. The ROI ratio of the pellets in clockwise order starting from the bottom-right one is 1: 0.92: 0.94 while it is 1: 0.90: 0.99 for the reconstructed case as shown in the right panel of Fig. 5.11. The ratios are consistent when one takes into account the statistical errors arising from the low level of the isotope in the phantom. Both ratios show that the bottom-left pellet is the least hot indicating some inhomogeneous absorption of isotope. The 5.6 mm thick sum image of 14 slices of images covering the pellets region in the thyroid phantom indicates that the top void was not ideally drilled but is slightly off the median of the bottom two pellets as can be observed in the left planar image. The reconstructed image also shows that each $\sim 4 \text{ mm}$ long pellet is less hot in center than at both ends presumably because the pellet inhomogeneously absorbed radioiodine in the solution of Na^{125}I due to its smooth side surface and rough cut ends.

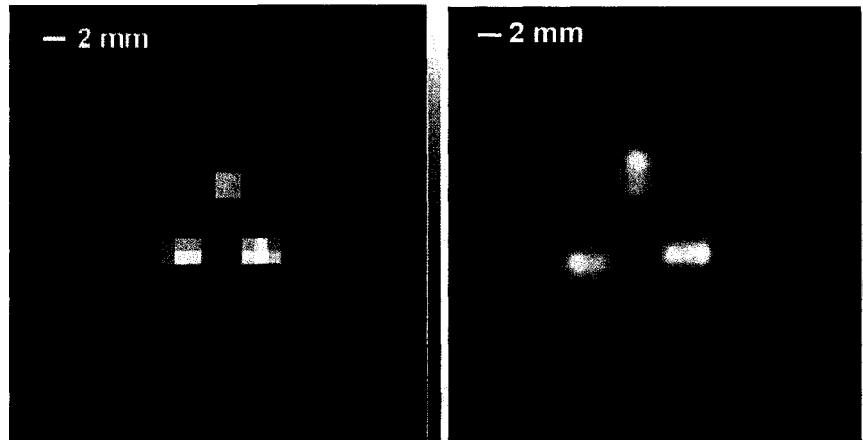


Fig. 5.11. The experiment shown in this figure was carried out with a thyroid phantom that had $\sim 4 \mu\text{Ci}$ in each void (a total dose of $\sim 12 \mu\text{Ci}$). (Left) a 30-min parallel-hole projection of the thyroid phantom. (Right) the 5.6 mm thick sum image of 14 reconstructed images from a two-pinhole helical SPECT scan covering the pellets region in the phantom for comparison with the left projection image. The step increment along the AOR is 0.1 mm.

5.2.4 Mouse studies

5.2.4.1 *In vivo* multipinhole helical SPECT

With two-pinhole helical SPECT, we have imaged to date two mice with a moderate-level injection dose of ^{125}I and 0.1 mm step increments along the AOR. The first mouse was injected with $130 \mu\text{Ci Na}^{125}\text{I}$ and 24 hours later anesthetized and imaged with 2 minute dwell time at each angular position (a total of 4 hours). That mouse died in the 3rd hour, apparently due to the anesthesia. After the final fourth hour of imaging, the mouse was dissected and the thyroid tissue was measured to determine the dose level of the isotope and then to verify the presence of NIS protein and mRNA with the whole-mount immunohistochemistry and RT-PCR, respectively.

The second mouse was injected with $200 \mu\text{Ci Na}^{125}\text{I}$. That mouse was anesthetized and imaged *in vivo* 24 hours later. One-minute acquisitions (a total of 2

hours) were obtained at each of 120 angular positions. The mouse was returned to its cage after the imaging to confirm that there were no effects due to the anesthetic or iodine dose. We compared the sum of 12 reconstructed slices (a total of 4.8 mm thickness) of the thyroid region with one of the 1-min projections from the two-pinhole helical SPECT, in which the thyroid is near the central pinhole.

The bilobal structure of a mouse thyroid is shown in the left panel of Fig. 5.12. As shown, the two lobes of the thyroid are separated by the trachea by about 1.8-2.5 mm depending upon their shape. The thyroid anatomical structure is well resolved by a 1.2 mm thick coronal slice reconstructed from the 4-hour two-pinhole helical SPECT scan of a mouse shown in the right panel of Fig. 5.12. Measurement of the dissected mouse thyroid showed that about 10 μCi remained in the thyroid tissue after imaging.

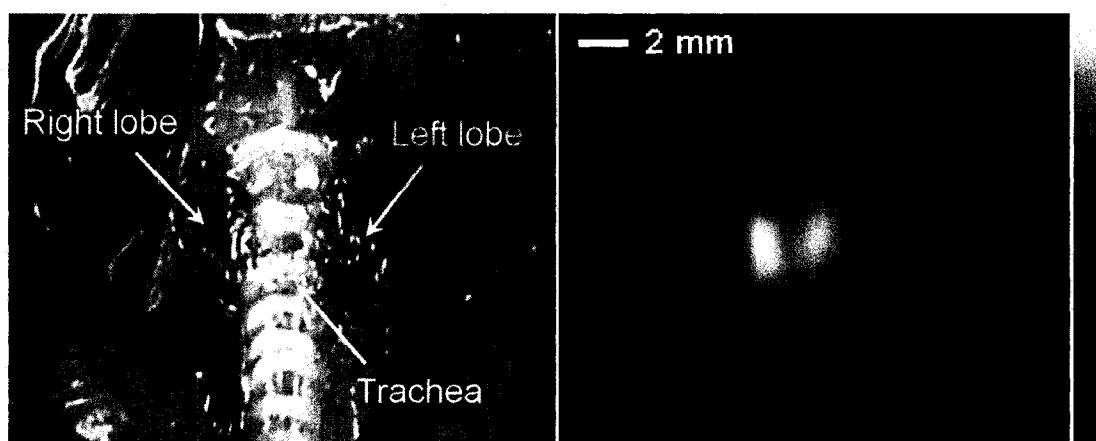


Fig. 5.12. (Left) Anatomical display of the thyroid region of a mouse. (Right) A mouse was injected with 130 μCi Na^{125}I and 24 hours later anesthetized and imaged with 2-pinhole helical SPECT for 4 hours. Although this mouse died in the third hour of imaging, it was possible to accumulate SPECT data throughout a four-hour period. A 1.2 mm thick reconstructed image on the right presents the coronal view of the mouse thyroid, resolving its two lobes separated about 2 mm. The physical measurement of the dissected thyroid tissue indicated the accumulated dose in the two thyroid lobes was $\sim 10\mu\text{Ci}$ in total.

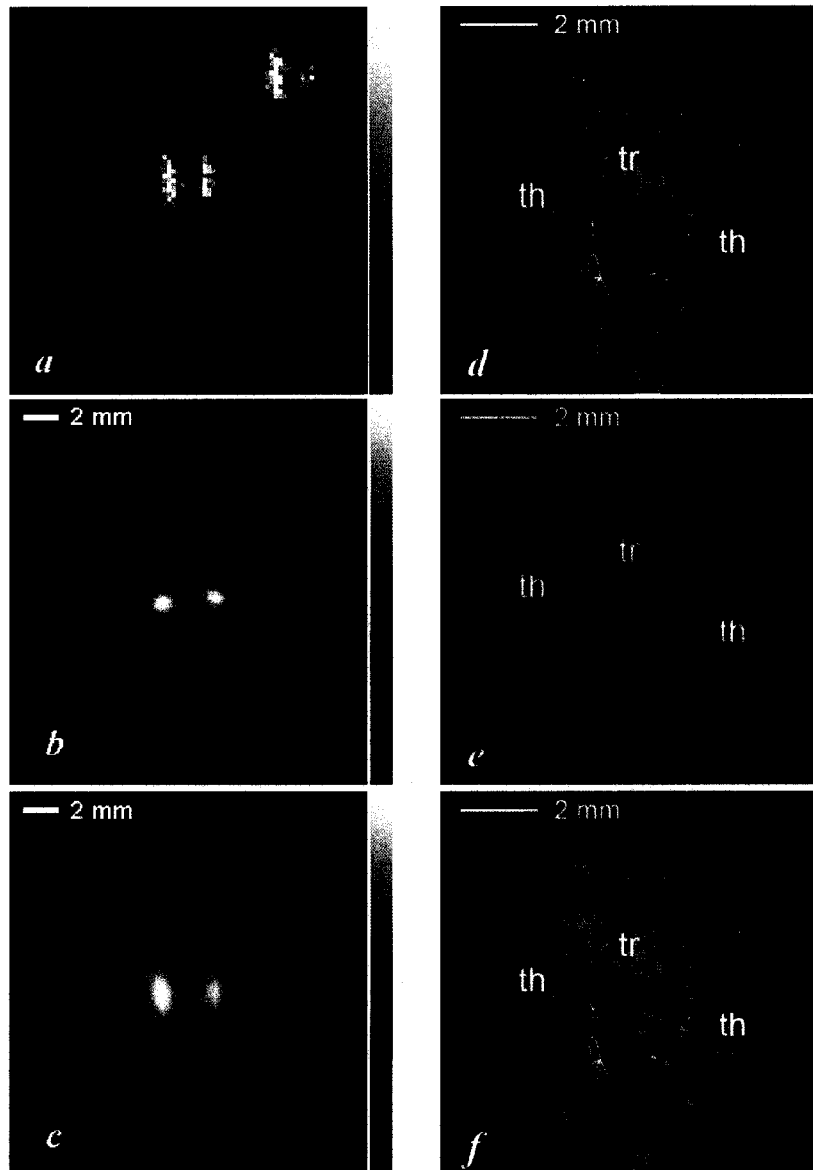


Fig. 5.13. (a)-(c): A C57-derived mouse was injected with 200 μ Ci Na¹²⁵I and imaged *in vivo* after 24 hours for a 2-hour 2-pinhole helical SPECT scan with step increments 0.1 mm along the AOR and 3 $^{\circ}$ increments around the AOR. A 1-min projection image from the scan is shown in (a) with the central pinhole near the thyroid region of the mouse. Presented in (b) is a transaxial image of the thyroid region. A 4.8 mm thick sum image (c) of 12 coronal images fully covering the mouse thyroid region shows agreement in the thyroid structure with the projection image (a). Both images (b) and (c) clearly delineate the two lobes of the thyroid, which are separated \sim 2 mm. The physical measurement after imaging indicated a total of \sim 20 μ Ci remained in the thyroid region. (d)-(f): An overlay (f) of the fluorescent image (e) from NIS immunohistochemistry on the bright field (d) of a dissected mouse thyroid, in which the green signal indicates NIS localization in the thyroid lobes based on indirect staining of the anti-NIS antibody.

Shown in Fig. 5.13(a) is a 1-min two-pinhole projection of the thyroid region of a mouse injected with 200 μCi and imaged 24 hours later *in vivo*. A single transaxial image from the two-hour, two-pinhole helical SPECT scan in Fig. 5.13(b) clearly delineates the bilobal structure of the mouse thyroid. Fully covering the whole thyroid region of the mouse, the 4.8 mm thick sum image Fig. 5.13(c) of 12 reconstructed coronal slices from the same helical SPECT scan indicates the consistent shape and separation of the lobes with the projection image in Fig. 5.13(a). Measurement after imaging shows that approximately 20 μCi was still present in the thyroid of this mouse.

5.2.4.2 Whole-mount immunohistochemistry and RT-PCR

Whole-mount immunohistochemistry was used to localize the NIS protein in the thyroid. As shown in Fig. 5.13(d)-(f), immunohistostaining was used to verify the presence of NIS protein in the mouse thyroid. The bright field of the dissected mouse thyroid is shown in Fig. 5.13(d) while the fluorescent image is in Fig. 5.13(e), in which green signal indicates localization of the NIS protein by indirect staining of the anti-NIS antibody. A composite thyroid image Fig. 5.13(f) of both the fluorescent image Fig. 5.13(e) and bright field Fig. 5.13(d) shows the green signal appears only in the lobar region, consistent with NIS protein expression that facilitates iodine uptake and metabolism. The NIS immunohistochemistry results were further supported by RT-PCR outcomes (data not shown), which also corresponded to ^{125}I uptake measured by the gamma camera.

5.2.5 Discussion and Conclusion

In vivo molecular imaging of some tissues such as the thyroid using mice has significant physiological and pathological meanings. However, *in vivo* imaging of the mouse thyroid has the simultaneous requirements of high resolution and low radioactivity. Using phantoms, we have demonstrated in this work the capability of a multipinhole helical SPECT system we developed recently to meet the imaging needs in resolution, sensitivity and image quality for such studies. Our further animal studies have demonstrated that we have achieved *in vivo* functional imaging of the mouse thyroid with high performance using a relatively low level of radioactivity and two-pinhole helical SPECT. The efficacy of the imaging results has been validated by molecular biology data from both immunohistochemistry and RT-PCR.

Our “proof-of-concept” phantom studies show that two-pinhole helical SPECT provides reconstructed resolution of about 1.3 mm which can accurately resolve the position of three voids containing a total of ~ 12 μCi in a phantom simulating the thyroid region. The ROI analysis of the reconstructed images shows an excellent agreement between the 2-D projective image and 3-D reconstructed images of the thyroid phantom. The test with a relatively large-scale hot-rod phantom further demonstrates that our system is capable of high-resolution imaging of a more sophisticated structure containing a low ^{125}I radioconcentration of 54 $\mu\text{Ci}/\text{ml}$, which is typical for actual biological studies.

The reconstructed image from a two-pinhole helical SPECT scan of a mouse clearly delineates the structure of the two lobes of the mouse thyroid which are separated by about 2 mm. *In vivo* two-pinhole helical SPECT of the thyroid of an anesthetized mouse was successfully carried out using a relatively low dose of ^{125}I (200 μCi), and an

imaging period of 2 hours. The summed image sufficient to cover the whole thyroid region shows good correlation with the pinhole projection of the mouse thyroid. The bilobal structure of the mouse thyroid has been further examined with *ex vivo* whole-mount immunohistochemistry and the fluorescent anti-NIS indirectly localized the NIS protein in the dissected thyroid lobes in the same locations as the pattern of ^{125}I distribution. An additional study using RT-PCR verified the correlation between the immunohistochemistry results and NIS mRNA expression. The molecular biology data have validated the *in vivo* multipinhole helical SPECT imaging of the mouse thyroid and have further strengthened its potential for studies of other NIS-expressing tissues.

Recently, studies have been reported in which NIS gene expression has been utilized for purposes of imaging or therapy of diseases such as hyperthyroidism or tumors [141, 142]. These studies usually require *in vivo* measurements of the volume and mass of the tissues such as the thyroid in Grave's disease for appropriate planning of radioiodine therapy [131, 132] or imaging the recurrent or metastatic tumors post treatment [127, 143]. The work we presented here suggests the potential of multipinhole helical SPECT in accomplishing those goals in *in vivo* studies using mouse models.

In conclusion, multipinhole helical SPECT has provided the capability of *in vivo* imaging of the mouse thyroid at the molecular level using a dose of 200 μCi of ^{125}I and an imaging period of about 2 hours. This work has been verified as an NIS-dependent process by molecular biology techniques, i.e. immunohistochemistry and RT-PCR. Combining planar scintigraphy to allow quantifying and distinguishing tissue-mass voids and tomography for visualizing *in situ* living tissues, our imaging system has potential

application to molecular imaging in a variety of *in vivo* studies of the mouse thyroid or of other NIS-expressing tissues such as the stomach or mammary tumors.

Chapter 6

***In vivo* gamma imaging in a study of mammary tumors**

Described in this chapter is the application of *in vivo* gamma-ray imaging in a study of mammary tumors using endogenous NIS expression in a mouse model and the novel compact gamma camera (see section 3.3) dedicated for mouse studies. The role and development of gamma-ray imaging in breast cancer are first introduced followed by the goals of this work. The methods of data acquisition and analysis are then detailed and the results as well. The final section includes discussion and preliminary conclusions from this study.

6.1 Background

Breast cancer is one of the most common cancers in women. There are increasing requirements of high-performance breast cancer imaging in current studies of this significant human health issue. Despite screening and diagnosis of tumors, modern breast cancer studies require the imaging technique to detect a tumor at its earliest stage, to characterize the heterogeneity of the tumor and to monitor the tumor development over time. The overall death rate for breast cancer has steadily declined since the early 1990s mainly owing to a combination of screening, improved treatment and better awareness [144]. Imaging techniques including mammography, MRI, ultrasonography, optical

imaging, and radionuclide imaging (PET and scintimammography) play a key role in this achievement. Each imaging technique has made its own contribution to address this health issue in different aspects. Mammography is the most established breast cancer imaging technique and the primary tool for screening and diagnosis of breast cancer. However, mammography has lower sensitivity in those with dense breasts [145]. Ultrasonography works as an adjunct to screening and diagnostic mammography. This technique is painless and relatively inexpensive but is highly dependent on the operator and has a high false-positive rate [146]. The other imaging modality as an adjunct to mammography is breast MRI. New breast MR imaging techniques using molecular markers of malignancy may help to improve tumor characterization. The limitation of breast MRI in specificity may lead to additional work-ups and biopsies [146]. Optical imaging such as near-infrared (NIR) tomography has been intensively investigated to detect and characterize breast cancer [147]. However, optical mammography has a major disadvantage of poor spatial resolution. Moreover, the *in vivo* optical characteristics of common lesions and healthy breast tissues are not yet fully known [148].

Radionuclide imaging including PET and scintimammography (planar scintigraphy or SPECT) has also been a significant method contributing to breast cancer studies. The following review indicates that radionuclide imaging has been widely applied in a number of studies on breast tumors and its application is usually accompanied with molecular techniques such as immunohistochemistry or other anatomical imaging modalities such as CT and MRI, etc. Both PET and scintimammography have presented advantages in meeting current needs for breast cancer research.

6.1.1 PET and breast cancer imaging

Several studies have proven the accuracy of PET in detection of the primary tumor and axillary staging [149, 150]. F-18 fluorodeoxyglucose (^{18}F FDG), a glucose analog, is a standard PET radiotracer used in clinical PET imaging. The property of ^{18}F FDG enables the analysis of the glucose metabolism and blood flow in the cancers [151, 152]. The increased glucose metabolism of malignant breast cancer cells facilitates accurate differentiation of cancer from benign tissues [153]. A review shows that ^{18}F FDG-PET presents a sensitivity value ranging between 80% and 90% and a specificity value between 71% and 95% in breast cancer diagnosis [154]. PET imaging has also been employed to make correlations between imaging and tumor parameters (lesion size, proliferative activity, vascularity, multidrug resistance) [155-157] or predictive and prognostic factors such as the estrogen receptor [158]. However, since PET images do not delineate fine details like a CT or MRI, the most important clinical application of PET currently is to determine the presence and extent of metastatic or recurrent breast cancer [159, 160], to evaluate multi-drug resistance [161] and to monitor response to therapy [162, 163].

Despite the obvious utility of ^{18}F FDG, additional innovative radiotracers are under development. Many radiotracers are aimed at more specific cellular processes in addition to glucose metabolism [164]. A number of studies have been carried out to investigate a multitude of radiotracers such as [^{18}F]Xeloda for specific imaging of enzymes [165], [^{18}F]FES for hormone receptor expression [166], [^{11}C]methionine for protein synthesis [167], [^{18}F]FLT for proliferation rate [167], [^{18}F]fluoride for bone mineralization [167], [^{18}F]fluoroetanidazole for hypoxia [168], etc.

In addition to new tracers, PET technology is also rapidly evolving. A chief advance is the dual-modality PET/CT scanner. Initial studies have shown the advantages of PET/CT over either single modality and its particular usefulness in pre-radiation therapy planning [164, 169, 170]. A series of recent studies have demonstrated the advantages of PET/CT in detecting multiple metastases or small tumors, monitoring the tumor response to chemotherapy, and accurately localizing lymph node metastasis [171-173]. PET-MRI has been used to improve the specificity of primary breast cancer detection [174]. A few single-case reports indicate that PET/CT or PET/MRI may reveal heterogeneity of breast cancer [175, 176].

To improve both the sensitivity and specificity, PET dedicated to breast cancer or positron emission mammography (PEM) has been developed and employed as a cost-effective alternative [177]. Several groups have proposed and evaluated the performance of PEM systems [178-180] and the PEM detectors based on PSPMT [177, 181-184], PSAPD [185-188], and CZT [186] with promising results for breast cancer imaging. Comparative studies have demonstrated that the clinical impact of PEM is superior to that of conventional gamma camera or CT [189, 190]. Studies on detection of primary cancer [191, 192] have shown excellent sensitivity and specificity. In particular, the PEM Flex system developed by Weinberg [177] and commercialized by Naviscan PET Systems, Inc. has achieved a high resolution 1.5-2 mm and demonstrated superior performance to other modalities, i.e. PET/CT, MRI and gamma camera [193]. The high accuracy of this system in primary cancer detection suggests its potential in depiction of primary breast cancer [194].

With the advent of preclinical PET systems such as microPET and NIH Atlas PET, researchers are able to evaluate preclinical models of breast cancers using small animals with improved performance [195]. Several studies have employed MicroPET to image integrin, peptide nucleic acid, and multidrug resistance in addition to FDG [196-200]. A recent report also indicates that small animal FDG-PET is a useful tool to monitor mammary tumor development and treatment response through longitudinal imaging [201]. Recent progress in developing multi-modality scanners for small animals has shown their potential in preclinical studies of breast cancer [202, 203].

As this review indicates, PET has presented its advantages in many aspects of breast cancer imaging. However, this technique is limited by a low sensitivity to detect lobular carcinoma and small tumors [151, 154]. The underlying biochemical mechanisms have not been fully clarified for enhanced glucose metabolism in FDG studies [204]. Owing to the lack of correlation with significant prognostic markers such as the tumor size, FDG uptake might not be used as a prognostic criterion for breast cancer studies [167]. Moreover, preparing the radiotracers for PET imaging may require a nearby cyclotron and sophisticated radiochemistry techniques [205].

6.1.2 Scintimammography and breast cancer imaging

Similar to PET, scintimammography including planar scintigraphy and SPECT is well known as an adjunct to mammography and is effective in reducing the rates of negative biopsies [206]. In recent years, ^{99m}Tc -sestamibi scintimammography has shown a high sensitivity between 84% and 94% and specificity between 69% and 94% in the diagnosis of breast cancer [207]. Though scintimammography cannot substitute the

current primary imaging techniques for breast cancers mainly due to its low sensitivity in detecting breast tumors < 10 mm, it is recommended for patients with equivocal mammograms as well as women with dense breasts or implants. These advantages dwell on the fact that breast density and implants have much less effect on scintimammography owing to the properties of gamma rays [206, 207]. Not only for diagnosis of breast cancer, scintimammography plays a significant role in evaluating lymph node status and breast cancer metastases [208-210], predicting multidrug resistance [211, 212], assessing tumor response to chemotherapy [213, 214], monitoring recurrence of breast cancer [215], and potentially developing drugs for tumor therapy [216].

To date the most common tracers used in scintimammography are ^{99m}Tc -sestamibi and ^{99m}Tc -tetrofosmin and a large body of studies have been carried out with these radiotracers [206]. Considerable effort has also been put on finding new radiotracers targeting antibodies or receptors on tumor cells which are suitable for scintimammography and potential tumor therapy [217, 218]. These radioligands include new EGFR inhibitors [219], Fab [220], somatostatin [221], ^{99m}Tc -NC100692 [222], anti-HER2 affibody [223], trastuzumab [224], ^{67}Ga -radiopharmaceutical [199], ^{99m}Tc -EDDA/HYNIC-TOC [225], ^{201}Tl -thallium-chloride [226], peptide [227], tamoxifen [228], endoglin [229], as well as others. Researchers recently have shown interest in developing molecular imaging agents that are dual labeled with nuclear and optical reporters [230-232]. These ligands can provide unique opportunities for breast cancer imaging with SPECT (or PET) agents and for the following intraoperative guidance with near-infrared (NIR) fluorophores [231].

With the advances in imaging techniques, multi-modality imaging, especially SPECT/CT has been recently applied in breast cancer with the attempts to further improve the performance of scintimammography. A significant advantage of SPECT-CT in breast cancer is that it helps improve sentinel node identification, leading to a better plan of therapy [233, 234]. SPECT-CT has also shown improved sensitivity over planar scintigraphy [235] and has been found to be more accurate in diagnosing breast tumor metastases [236]. A study on breast cancer metastasis using a mouse model with bioluminescent imaging and SPECT/CT also indicates that multimodality imaging techniques can be very helpful for monitoring bone metastasis [237]. A pilot study demonstrated that MRI/scintimammography seems to be more accurate in measuring the size of breast cancer than other methods (clinical exam, mammography, MRI alone) [238].

As several reviews indicate, gamma cameras dedicated to breast cancer imaging may improve the accuracy of scintimammography in small breast cancer detection. Several groups have developed and evaluated dedicated gamma cameras based on CZT detectors with better visualization of objects smaller than 10 mm, suggesting the potential for early tumor detection [239-241]. Similar attempts have also been made with scintillation detectors using PSPMTs and pixellated CsI(Tl), NaI(Tl), or continuous LaBr₃(Ce) scintillators with high spatial resolution [242-244]. Clinical systems dedicated for breast cancer imaging are available commercially now such as Dilon 6800 gamma camera for Breast-Specific Gamma Imaging (BSGI) [245] or LumaGEM digital system for molecular breast imaging [246]. Different collimation has been employed including pinhole collimator [210, 247], rotating multisegment slant-hole collimator [248], and

slant hole collimator [249] with improved visualization of breast lesions. Improved accuracy of dedicated gamma cameras in breast cancer detection has been verified in several reports [250-252].

As with PET, a variety of SPECT systems dedicated for small animals have been developed and some of them are available commercially such as nanoSPECT (BioScan Inc.), X-SPECT (Gamma Medica Inc.) and U-SPECT II (Molecular Imaging Laboratories). These dedicated imaging systems are being introduced into preclinical studies of breast cancer with promising results [211, 253]. Particularly in these attempts, using a high-resolution SPECT/CT system (X-SPECT), Kim *et al.* were able to achieve detailed distribution information of a ^{99m}Tc -labeled antibody within breast tumor xenografts *in vivo*, which is consistent with *ex vivo* bioluminescence imaging or histology [253].

6.1.3 NIS and breast cancer imaging

Despite the development of new ligands for breast cancer studies, researchers recently have shown a growing interest in the sodium iodide symporter (NIS) gene both as a molecular imaging reporter gene and as a therapeutic gene [142]. NIS is a transmembrane ion channel responsible for iodine metabolism. Endogenous NIS expression in breast tissues such as mammary glands or tumors has been confirmed by many groups [126, 254]. As a potential way of imaging and therapy of breast cancers, researchers have sought different stimulators to enhance the NIS expression in breast tissues [255, 256]. A multitude of agents such as, oxytocin, prolactin and tRA have been found to significantly induce iodide uptake, NIS mRNA or NIS protein production in

various cancer cell lines or *in vivo*. Several studies using either PET or scintimammography have suggested NIS is a promising molecule for *in vivo* radionuclide imaging of breast cancer [142, 257]. In those studies, radionuclide imaging has been used to verify the presence of NIS expression, to locate the NIS-expressing sites, and to qualitatively or quantitatively determine NIS gene expression. However, the NIS expression in early-stage tumors and its role for early tumor detection remains unclear. Moreover, NIS gene expression may also deliver detailed information such as tumor size and pattern in gamma images that could benefit breast cancer study for better understanding of breast cancer and eventually better treatment.

6.2 Hypothesis and goals

As Mankoff pointed out, to better detect early-stage breast cancer, we will need equally the development of improved instrumentation for radionuclide breast imaging and the development of radiotracers “designed to match the biology of early breast cancer” [258]. The previous studies of NIS in breast cancer and gamma-ray imaging technology leads us to hypothesize that the patterns of metabolic ^{125}I uptake presented in gamma images correlate with the molecular patterns of tumors as evidenced by functional NIS expression. This correlation would facilitate detecting the tumor at its early stage, investigating the parameters of the tumor, and learning the tumor progression by *in vivo* gamma-ray imaging.

By combining a novel gamma camera dedicated to biological imaging and the unique signatures of endogenous NIS gene expression, the goals of this work are not only an attempt to evaluate the potential of NIS as the reporter gene for early breast tumor

detection using mouse models, but also an effort to characterize breast tumors and to monitor tumor development *in vivo* using NIS. Specifically, these goals include:

1. To demonstrate the efficacy of the gamma camera in imaging MMTV mammary tumors by correlating the gamma images with immunohistochemical signals representing NIS indirectly.
2. To demonstrate the capability of the gamma camera in detecting small tumors (<10 mm) and monitoring mammary glands bearing no tumors.
3. Based upon the underlying functional NIS expression in mammary tumors, to define the extent of known breast cancer by tumor sizes and patterns and investigate their correlations.
4. To investigate the kinetic characteristics of tumors by dynamic patterns and trends of radiotracer uptake and evaluate their potential correlation with other tumor parameters
5. To study tumor progression through *in vivo*, non-invasive imaging of the same tumor of the same animal over time (which consequentially requires a low dose of radioisotope).

Our careful analysis has confirmed that the sodium iodide symporter molecular biology data substantiate the ^{125}I imaging data and demonstrate the validity of *in vivo* radionuclide imaging for mammary tumor study. We have shown the feasibility of gamma-ray imaging in a morphological study of MMTV mammary tumors. Using a low-level dose of 14 μCi and confirmed by immunohistochemistry, we have demonstrated that sodium iodide may also potentially be a promising radiotracer for detecting non-palpable tumors at the earliest stage (as small as 3 mm). We have identified three patterns of iodine distribution in MMTV tumors and found static correlations among the patterns, iodine uptake, and tumor size based upon a population of 40 MMTV mice exhibiting 59

tumors in total for a total of 69 gamma-ray imaging cases. This preclinical study has also shown that radionuclide scintigraphy using Na¹²⁵I provides a promising method for *in vivo* study of morphological changes such as size and distribution pattern associated with tumor development, implying significant therapeutic value such as monitoring tumor response to pharmaceuticals over time or at different stages of development. Details about this study are described in the following sections.

6.3 Animals and tumor distribution

Animal studies were carried out with protocols approved by the WM animal research committee. C57BL/6J derived, MMTV-infected mice were employed for this study. Tumors appeared randomly and were imaged when monitored visually.

To date, 40 MMTV mice with a total of 59 tumors have been imaged. A tumor was visually determined *in vivo* or *ex vivo*. As shown in the left panel of Fig. 6.1, this population revealed that most MMTV mice developed one (n=23, 57%) or two tumors (n=15, 38%). MMTV mice rarely develop more than three tumors (n=1, 5%). The possibilities of developing left (n=19) and right (n=20) thoracic tumors in MMTV mice were found to be approximately the same, 32% and 34% respectively (Fig. 6.1, right). A few mice developed left (n=2) or right (n=1) cervical tumors. Statistical analysis indicates the possibility of developing thoracic tumors (n=39, 66%) is significantly ($p < 0.05$) higher than that of inguinal tumors (n= 17, 29%).

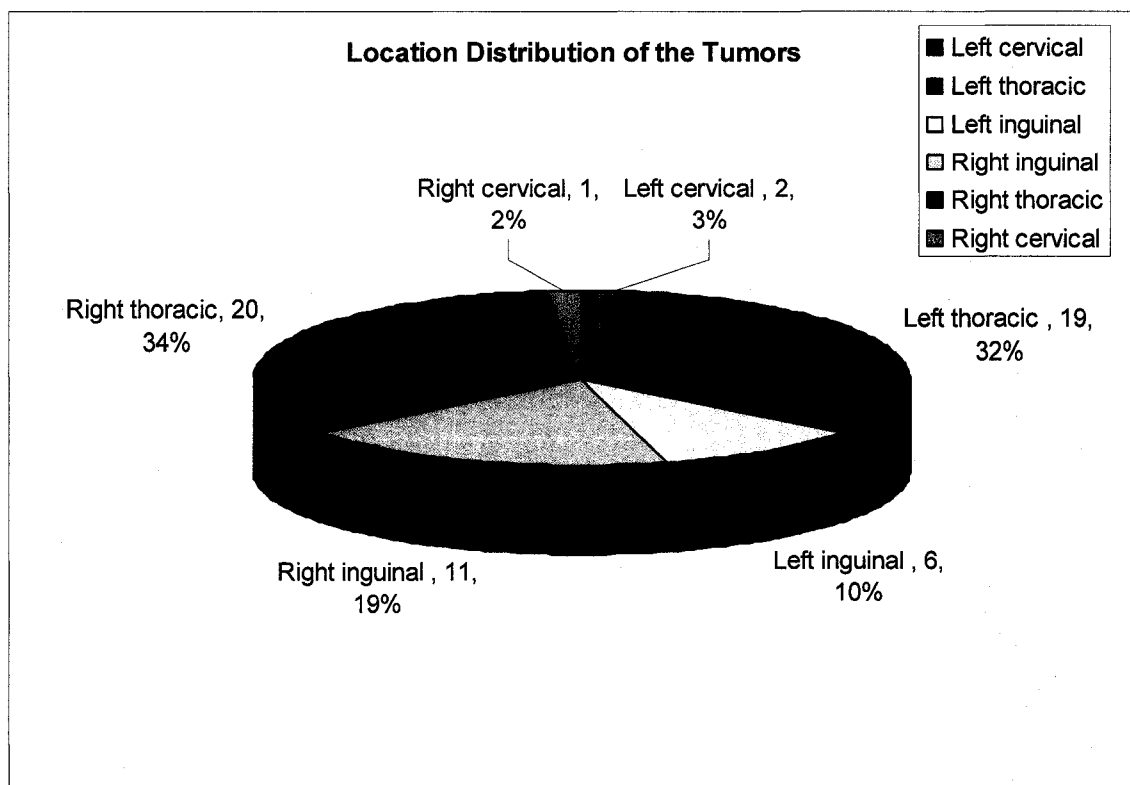
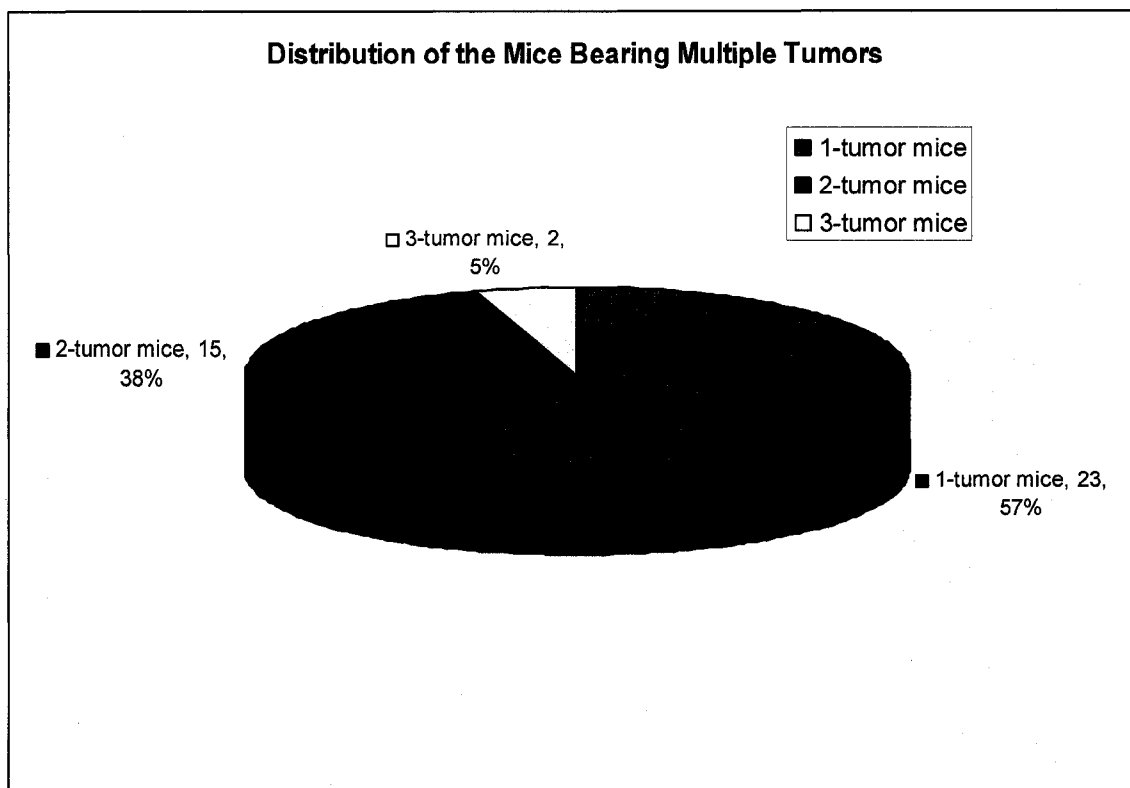


Fig. 6.1 tumor distribution in the MMTV mice

These mice were divided into three groups. The first group (n=24) were *in vivo* imaged only once with the gamma camera. A second group (n=11) were randomly selected and repeatedly imaged twice (n = 9) or three times (n=2). A third group (n=5) were randomly selected, imaged once and then euthanatized. Tumors and also mammary glands with no visual tumors were collected and studied, followed by immunohistochemistry for comparison with the gamma-ray images. Two sets of C57BL/6J female mice with no tumors served as control animals. Each set (n=3) includes a nulliparous, a previously lactating and a lactating mouse. After gamma-ray imaging, each animal was euthanatized and their mammary glands were collected for immunohistochemistry.

6.4 Whole-mount immunofluorescence methodology

Whole-mount immunofluorescence methodology was used to confirm the presence of NIS protein in the tissues. The whole-mount immunohistochemistry protocol was slightly modified from Johnstone *et al.* [259]. After the processing according to the protocol, normal glands, control glands and tumors were visualized under a dissecting scope in both bright and fluorescein filtered fields. An overlay image was created using Adobe Photoshop 7.0.

6.5 *In vivo* gamma-ray imaging of MMTV tumors

6.5.1 Data acquisition

We obtained all the gamma-ray images and data with the compact gamma camera briefly described in section 3.3. The 5 mm thick CuBe parallel-hole collimator with 0.55-

mm square holes separated by 0.11 mm septal walls was employed in this study. This collimation provides an effective area of about $46 \times 96 \text{ mm}^2$ and a spatial resolution (FWHM) about 2.5 mm on contact with the detector surface.

Five minutes prior to gamma-ray imaging, sodium pentobarbital was administered IP (intraperitoneally) as anesthetic to the animals. Each animal was then injected with 14 $\mu\text{Ci Na}^{125}\text{I}$ in NaOH in the femoral biceps followed immediately by one-hour imaging with the gamma camera. The animal was monitored and kept stable over the imaging period.

The detector and related data acquisition instruments were interfaced to a Macintosh G3 computer via a SCSI port. Each photon detected by the gamma camera was referred to as an “event”. A program developed with the data acquisition software Kmax (Sparrow, Inc.) recorded the time, energy and computationally determined coordinates of every event sorted into the data files. These were later transferred to a Macintosh G4 for further processing.

6.5.2 Data analysis

An analysis program developed with data processing and visualization language IDL (Research Systems, Inc, Boulder, Co) was used to group event files into 5-min time interval blocks recorded as two-dimensional matrices (referred to as “timecuts”). Each matrix represents a 5-min digitized gamma-ray image of that mouse. The coordinates of each pixel correspond to the planar position where the isotope decay is visualized in the mouse by the detector. The total counts stored at each pixel represent the radioactivity detected at that location over the 5-min interval. Another IDL-based program was used to

visualize the gamma-ray images and sum the total events in a designated region of interest (ROI) in the images. This treatment allowed time-dependent distribution analysis of any chosen pathological or physiological region such as tumors or mammary glands.

Mammary glands

We chose a square ROI with an area of 9 pixels (each pixel is 1.2 x 1.2 mm²) to analyze the mammary glands. In order to compare the radioactivity contained in the mammary glands, we normalized the values by expressing the data as a percentage of the total injected dose (%ID) defined by an ROI with 2880 pixels covering the entire body of the mouse. In evaluating the relationship between immunohistochemistry and gamma-ray imaging, the radioactivity accumulated from the mammary gland over the 50-55 min time interval was compared and correlated visually with the intensity of the NIS green signal in the overlay image from immunohistochemistry.

Tumor size, radioiodine uptake and pattern

Each tumor was analyzed with a rectangular or square ROI with variable size so as to fully contain the tumor without including nearby organs such as heart or salivary glands. In order to present the actual size and morphology of the tumor, each pixel in the tumor ROI was corrected by subtracting a threshold value to exclude the major background of radioiodine uptake due to blood flow. A threshold is the mean value per pixel of all the four-pixel ROIs in the same abdominal or thoracic region of the mouse in each gamma-ray image. The usage of this threshold for blood flow correction was justified by the statistics indicating that the value of the threshold was in the same range as the radioiodine activity in the heart region 55 minutes post injection. We determined

the tumor size over each 5-min time interval as the total number of non-zero pixels in the corresponding tumor ROI with threshold subtracted and with any negative values set to zero. We defined the size over 50-55 min time interval as the actual size (in pixels) of the tumor. We regarded the total counts in the corrected tumor ROI as the net uptake of radioiodine in the tumor excluding the major effect of blood flow. For the purpose of comparing the radioactivity contained in the tumors, we again normalized these values to the total injected dose.

Static correlation between the tumor size and radioactivity in the tumor over the 50-55 min time interval was evaluated. A 13-level contour map of the corrected ROI was used to reveal the patterns of radioiodine distribution in the tumor over each 5-min time interval. We identified the radioiodine distribution pattern of each tumor and then associate the patterns with tumor size.

In order to evaluate the potential correlation or association among tumor size, pattern, and dynamic trend of radioactivity (over the imaging period of one hour) in the tumor, we group the tumor size into three types: small (1-75 pixels), medium (75-150 pixels) and large (above 150 pixels). For each type, we associated the mean dynamic trends of radioactivity with tumor patterns. We then correlated the trends of each pattern with the types.

Difference plots

As with the tumor pattern contour, we used contour plots of the difference between raw tumor ROIs without threshold deduction to reveal the regions where radioactivity changes occurred over time. Differences were analyzed with three sets of

raw tumor ROIs between different time intervals: 0-5 min vs. 5-10 min, 25-30 min vs. 30-35 min, and 50-55 min vs. 55-60 min. The difference between each set of tumor ROIs was calculated by subtracting the earlier raw tumor ROI from the later ROI. The total difference values were obtained and compared. The consequent positive and negative values (absolute values) distributed in the “difference ROIs” were then visualized as both a positive plot (counts increase over time) and a negative plot (counts decrease over time) respectively. A hot region in a positive difference plot therefore implies radioiodine uptake while a negative plot means loss of radioactivity over that period. We divided the regions representing radioactivity change into central regions and edge regions. Central regions represent central or near-central areas within a tumor while edge regions are at the edge or out of the tumor area defined by the tumor ROI with threshold deducted. Potential trends of the change of the difference over time were analyzed and related with tumor pattern and/or size.

Statistical analysis

Linear regression analysis is used to evaluate possible correlations between selected data sets. When appropriate, Spearman’s correlation coefficients are used to test for significance between some of the measured parameters. $P < 0.05$ is considered statistically significant.

6.5.3 Correlation between gamma-ray imaging and immunohistochemistry

The prerequisite to apply our imager to this study is that we must first demonstrate the validity of *in vivo* radionuclide imaging of NIS expression in mammary tumors. For this purpose, we have evaluated the correlation between the data of gamma-

ray imaging and immunohistochemistry with normal mammary glands (NMGs, n=6) of non-tumor-bearing C57Bl/6J mice, mammary glands bearing no visual tumors (n=5) and mammary tumors (n=5) of MMTV mice. Current literature suggests that NIS should only be expressed during lactation. A comparative study with an unrelated strain of C57 mice was imaged and stained for NIS to test current literature. For each set of C57 NMGs at different stages, we first compared their immunohistochemical result visually and then their ROI data from gamma-ray imaging quantitatively, followed by correlation between immunohistochemistry and gamma-ray imaging. For the purpose of evaluating the potential effect of MMTV on normal mammary glands, we semi-quantitatively compared the radioactivity difference between the C57 NMGs and MMTV MGs bearing no visual tumors. The immunohistochemical results of both the MMTV tumors and MGs with no visual tumors were visually correlated with their gamma-ray images.

The results have demonstrated that the data of gamma imaging correlates precisely with molecular biology data from immunohistochemistry. For the strain of C57 mice, nulliparous mice (n=2) did not incorporate ^{125}I in their mammary glands nor did they stain for NIS. Conversely, lactating C57 mice (n=2) strongly incorporated ^{125}I into lactating glands and stained highly for NIS that reflected the gamma camera image. Multiparous C57 mice (n=2) did not incorporate ^{125}I into previously lactating mammary glands, but when staining for the NIS one multiparous animal did have very low localization of the NIS and the other did not. The immunohistochemical results are well

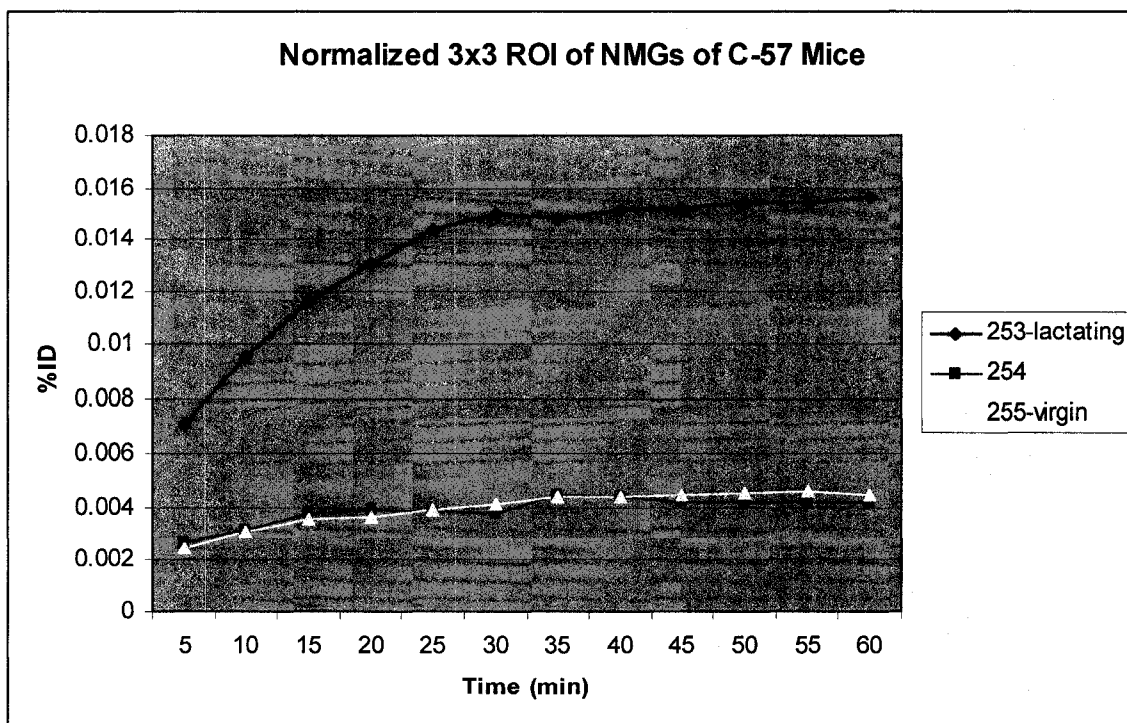
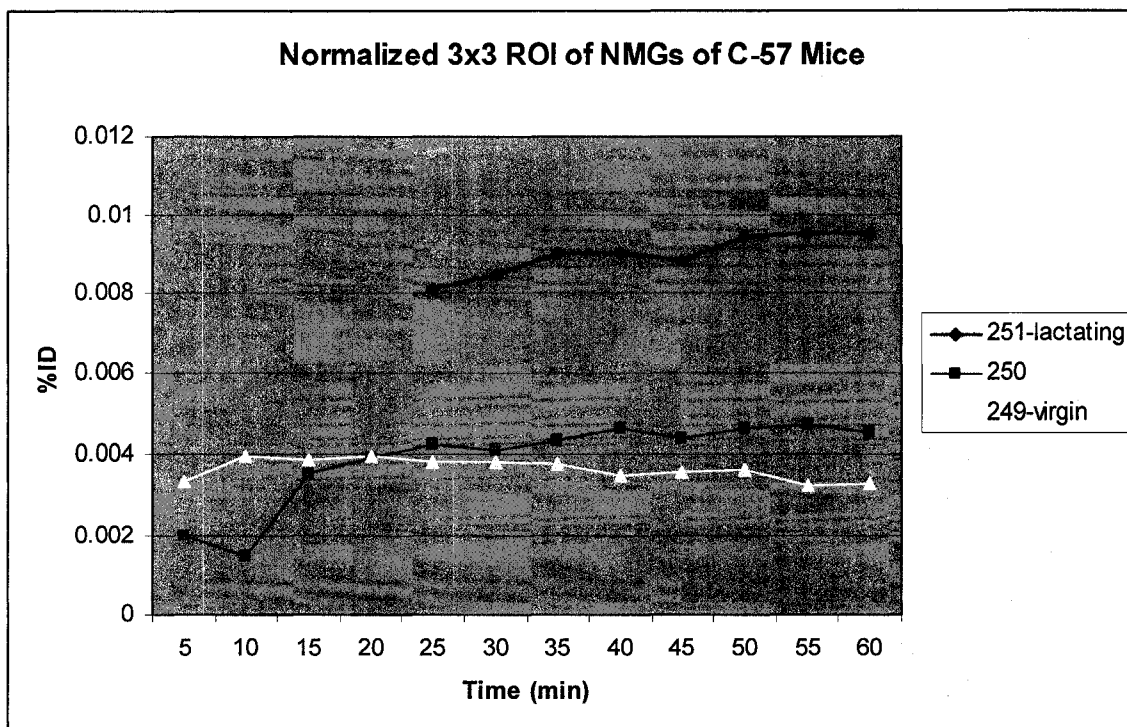


Fig. 6.2. The ROIs of NMGs of two groups of C-57 mice bearing no tumors. Each group includes a lactating, a previously lactating and a virgin mouse.

correlated with the ROI results (Fig. 6.2) from gamma-ray imaging. Based on this comparative study the C57 mice strain supports the literature findings that NIS is primarily expressed and present during lactation.

ROI data from gamma-ray imaging indicated that associative mammary glands (n=5) of MMTV tumor bearing mice on occasion incorporated ^{125}I at higher rates than the NMG of C57 mice. Localization of ^{125}I in those mammary glands can even be visually observed in gamma-ray images (Fig. 6.3), which was further confirmed by immunohistochemistry demonstrating NIS expression. Moreover, the patterning of green signal produced by indirect antibody staining against the NIS in MMTV tumors (n=5) appears highly parallel to the patterning of ^{125}I incorporation visualized by the gamma camera for each tumor size. Shown in Fig. 6.3 is an example of this correlation. Two tumors have been confirmed in this mouse through dissection. One was a large tumor dissected into four pieces with the alignment as shown in the gamma image. The other was a non-palpable tumor with 3 mm diameter. The top-right image in Fig. 6.3 shows the immunohistochemical result of the dissected large tumor. That pattern of NIS expression correlates precisely with the pattern shown in the gamma image. The bottom-right image shows the correlation between gamma image and immunohistochemistry even for a tumor as small as 3 mm in diameter. Hence, the correlations have been verified between immunohistochemistry and scintigraphy of C57 NMGs, associative MGs and tumors of MMTV mice, leading to the assumption that the usage of radionuclide imaging is valid in studying molecular activities associated with NIS-expressing MMTV tumors.

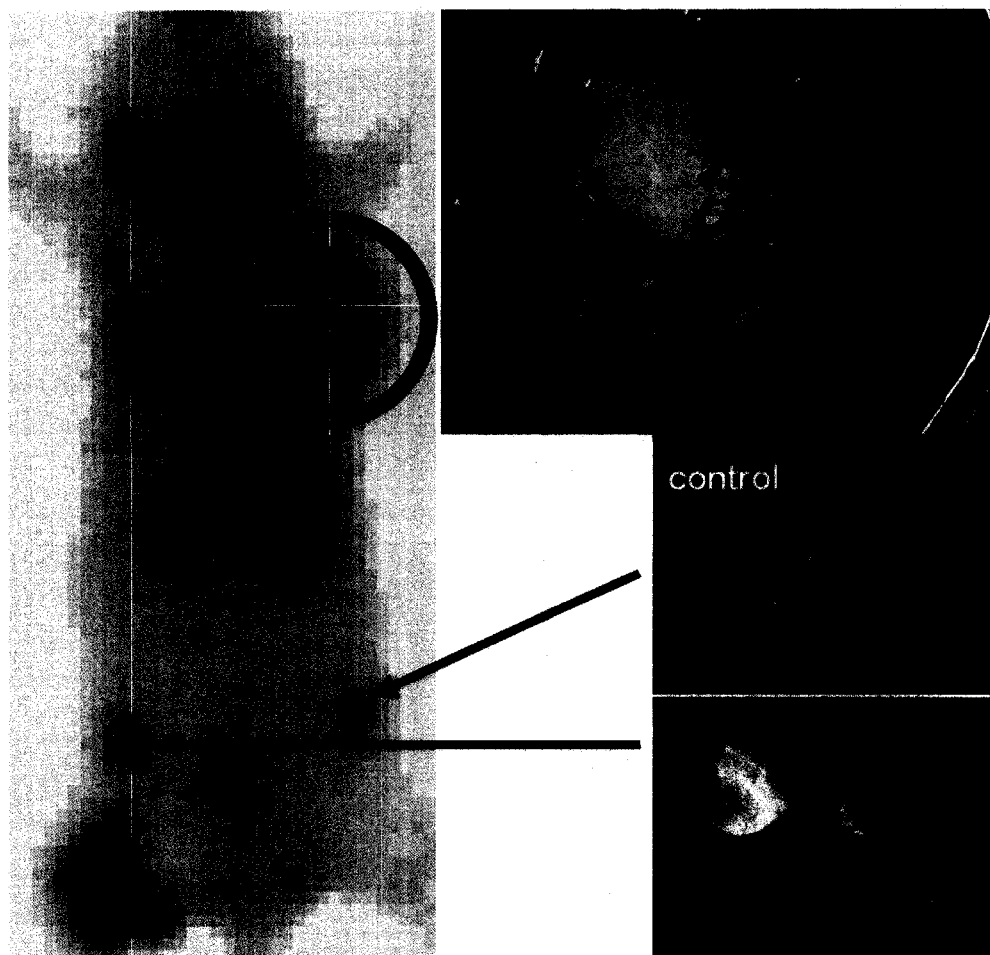


Fig. 6.3. Correlation between gamma image and immunohistochemistry. (Left panel) gamma planar image of a MMTV-infected mouse bearing one large thoracic tumor in the left and one small non-palpable inguinal tumor in the right. The large tumor was dissected according to the alignment in the gamma image. (Right panel) top, immunohistochemical data of the dissected large tumor; middle, the right inguinal mammary gland bearing no visual tumors as the control; bottom, immunohistochemical data of the small tumor measuring 3 mm in diameter. The green signal produced by indirect antibody staining against the NIS demonstrates the presence and pattern of NIS expression in the mammary tumors.

6.5.4 Results of gamma-ray imaging

Following the validation of efficacy of our system for gamma-ray imaging of MMTV tumors, we have analyzed the data of all applicable imaging cases and evaluated the performance of gamma-ray imaging in studying mammary tumors. Accordingly, the

significant parameters of interest have been investigated including radiotracer distribution in a tumor, tumor size and pattern, and potential association/correlation among those parameters.

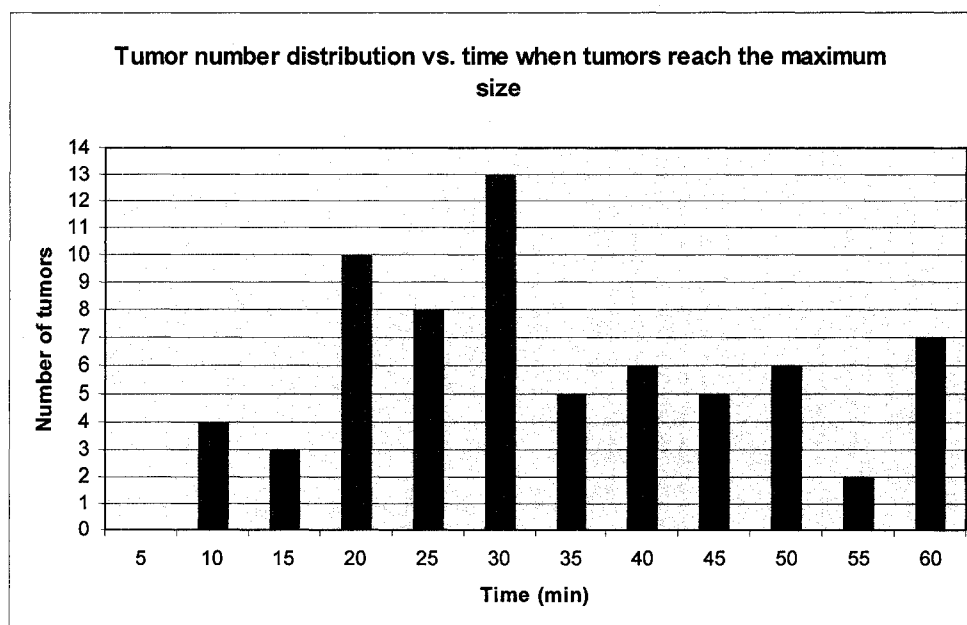
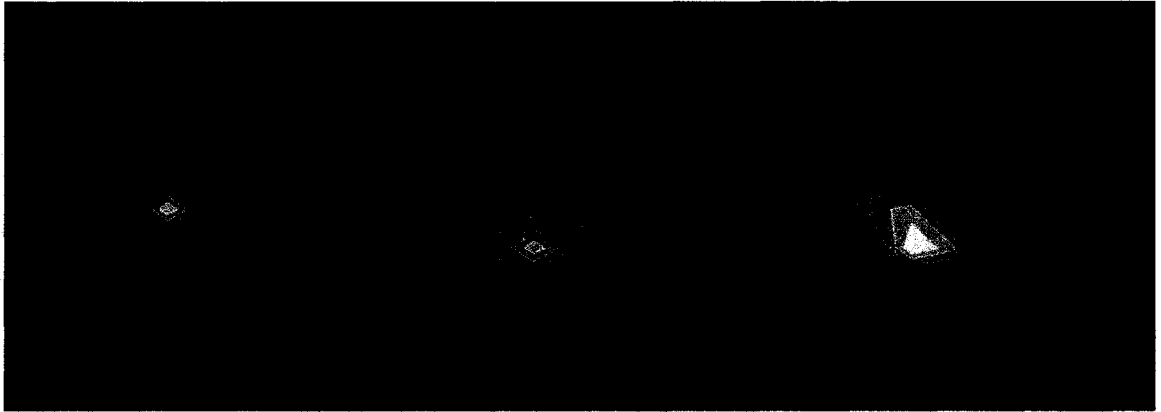


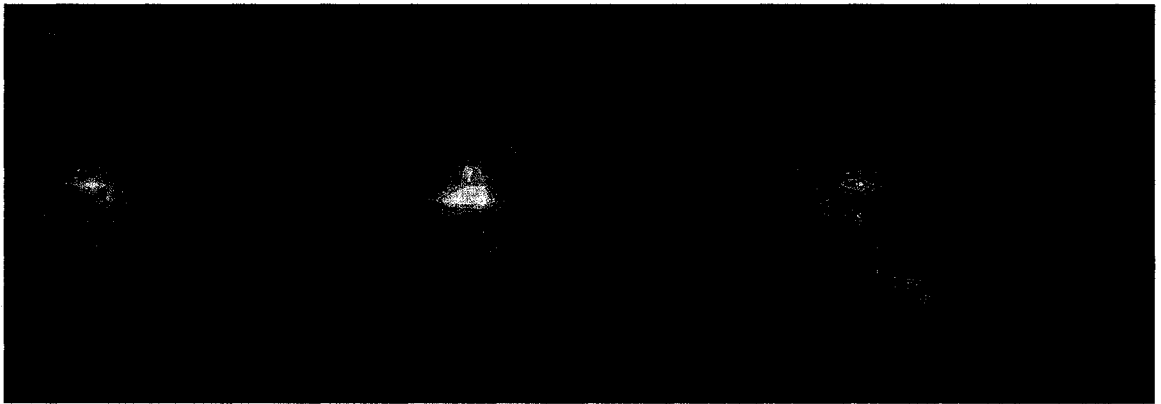
Fig. 6.4. Distribution of times for ^{125}I to reach the maximum tumor size within one hour

6.5.4.1 Time for full-size distribution of iodine in MMTV tumors

ROI analysis shows that ^{125}I reaches maximum distribution in MMTV tumors at a variety of times after the injection of radioactivity. Shown in Fig. 6.4 is the statistical diversity of time for ^{125}I to distribute everywhere (maximum tumor size) in a MMTV tumor though about 45% of the tumors ($n=31$) present full tumor-size distribution during the period of 20-30 minutes post injection. The distribution of radioiodine in seven tumors was relatively slow and continued even during the period of 55-60 minutes post injection. After analyzing all time cuts for imaged tumors the 50-55 minute range reflected well maximum tumor dispersal and thus tumor size.



(a) Center-to-edge pattern



(b) Multi-spot pattern



(c) Ring pattern

Fig. 6.5. Three typical patterns of ^{125}I distribution in MMTV tumors

6.5.4.2 Three patterns of ^{125}I distribution in MMTV tumors

We have identified three patterns of ^{125}I distribution in the tumors from the 69 imaging cases: center-to-edge (n=24), multi-spot (n=31) and ring (n=4). The center-to-edge pattern as shown in Fig. 6.5a initially presents localization of radioiodine in one region. With that region as the center, radioiodine distribution expands nearby and then to farther regions until the whole tumor is fully distributed with ^{125}I . For the multi-spot pattern presented in Fig. 6.5b, tumors initially present localization of radioiodine at one or more spots and then at other spots and/or their nearby regions. The ring pattern (Fig. 6.5c) is a special case of multi-spot pattern when the multi spots form a ring shape. We treat ring-pattern tumors as multi-spot tumors in the following analysis because of the small number of samples and similar behaviors as the latter.

6.5.4.3 Relationship among tumor patterns, size, and ^{125}I uptake

Results also indicate that there is an association/correlation among tumor patterns, size and uptake of ^{125}I over the 50-55 min interval. Revealed in Fig. 6.6 is that center-to-edge pattern associated with the tumors with small size (< 75 pixels in area where one pixel is 1.2 mm x 1.2 mm) while medium (76-150 pixels in area) and large tumors (> 150 pixels in area) are all multi-spot pattern. The overall accumulation of ^{125}I in a tumor increases as the tumor size increases. Further analysis shows that ^{125}I level in the small-size tumors during the period of 50-55 min post injection demonstrates a significant correlation between ^{125}I uptake and tumor size (Fig. 6.7, left; $r^2 = 0.553$, $p < 0.05$). The moderate-size tumors present a correlation with the size, but not significant (Fig. 6.7, middle; $r^2 = 0.3392$, $p > 0.05$). No correlation is found between uptake in the large tumors and size (Fig. 6.7, right; $r^2 = 0.0406$).

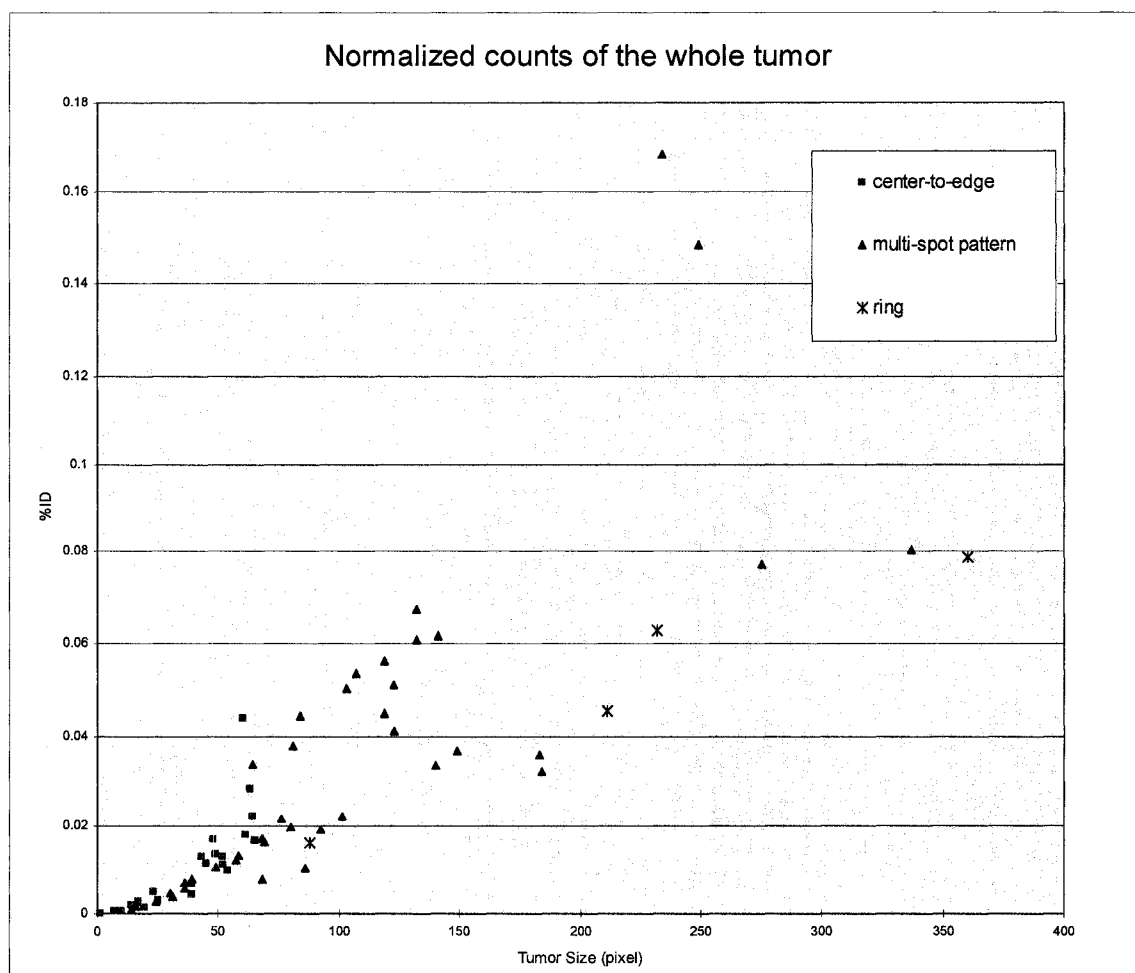


Fig. 6.6 Correlation among tumor patterns, size and ^{125}I uptake during 50-55 minutes

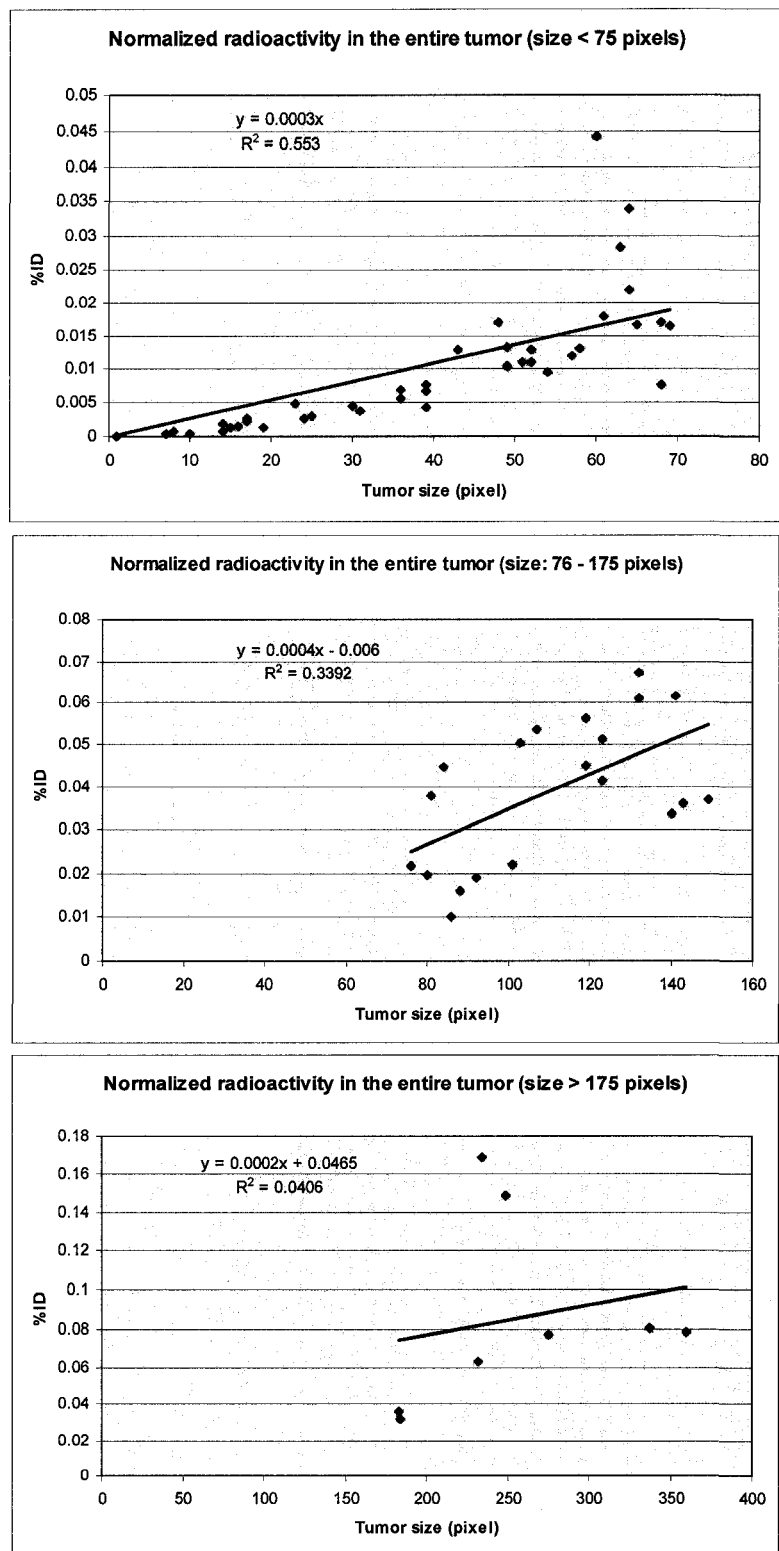


Fig. 6.7 Correlations between the ^{125}I uptake and tumor size: (left) small; (middle) moderate; (right) large

We find no overall association of tumor patterns with the mean dynamic trends of ^{125}I uptake ($n = 9$ for each catalog of tumor size). However, for the small-size tumors, mean iodine uptake ($n= 9$, Fig. 6.8, top) is much higher for the center-to-edge pattern than for the multi-spot pattern even though the tumors in these two catalogs have approximately the same mean size (Fig. 6.8, bottom).

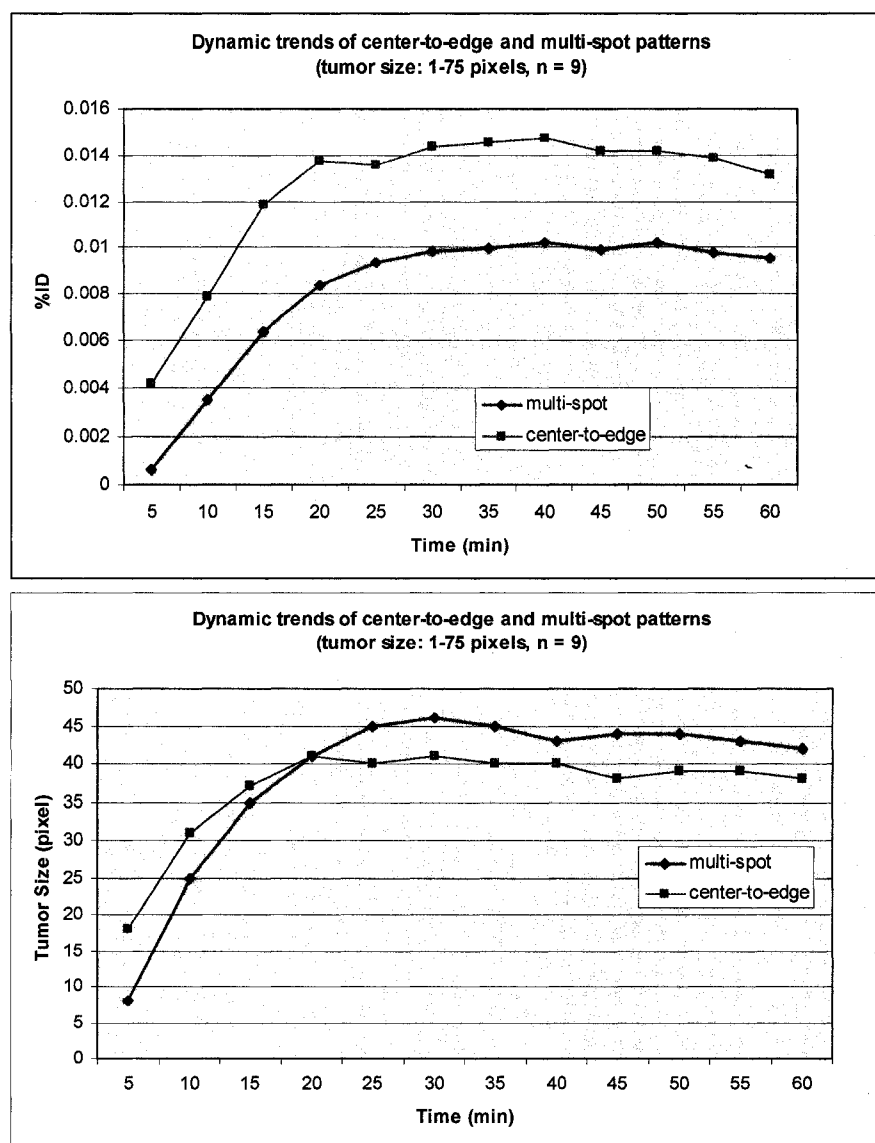


Fig. 6.8. Respective comparison of dynamic ^{125}I uptake (top) and size (bottom) between center-to-edge and multi-spot patterns.

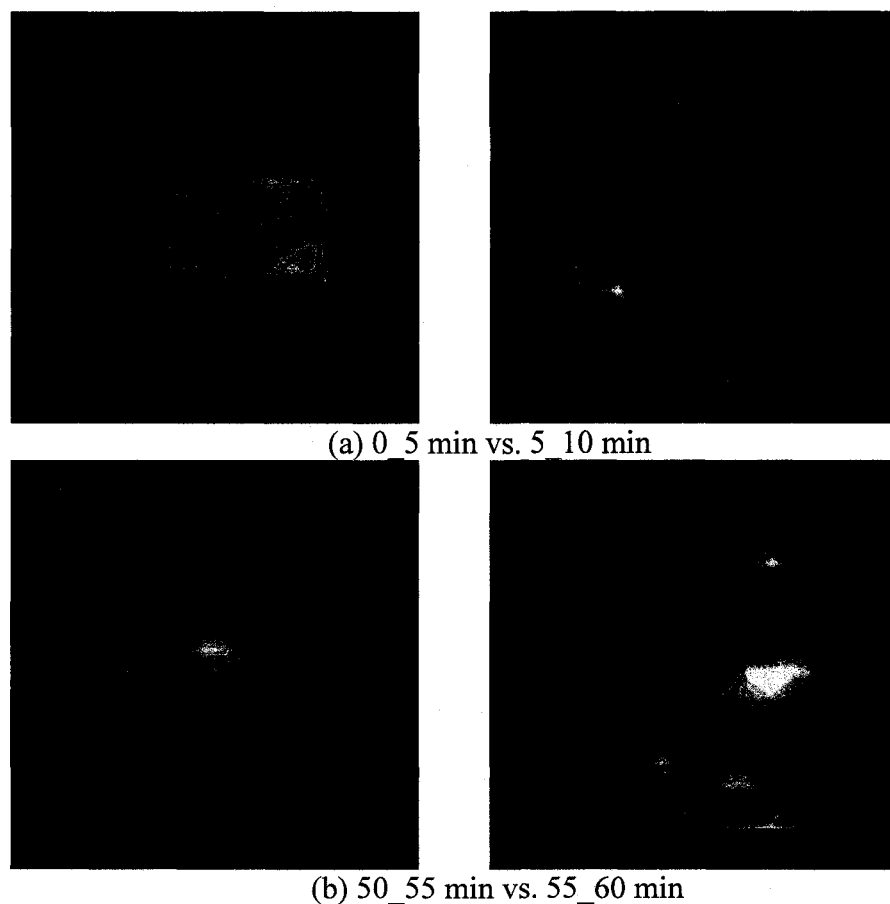


Fig. 6.9. Difference plots at beginning and ending periods of imaging

6.5.4.4 Difference plots

The difference plots revealed that the most activity change, usually ^{125}I accumulation, appeared in the first ten minutes post injection as shown in Fig. 6.9a. The regions in the difference plots presenting the greatest local change of ^{125}I activity usually happen at or very near the regions that initially were very active in ^{125}I uptake. This change may also appear at the regions or their vicinity that previously had the locally greatest activity change. Negative plots indicate that significant loss of ^{125}I from some regions of the tumor usually appears during the last period of imaging (30-60 minutes, Fig. 6.9b). The dynamic trend of positive/negative area corresponding to radioiodine

uptake/loss in that period was correlated with the trend of net counts difference. A variety of trends during the same period of time (30-60 minutes) indicated the diversity of the appearance of local positive/negative regions presenting the uptake/loss of radioiodine. However, no association/correlation of these trends was found with tumor patterns or sizes. The analysis results indicate that the regions eventually losing ^{125}I in most tumors (n=48 out of 67) were in both central and edge area of the tumor.

6.5.5 *In vivo* gamma-ray imaging and tumor development

In vivo imaging facilitates repetitive study of the same tumor in the same animal. Therefore, we employed gamma-ray imaging to monitor the tumor development over time. The MMTV mice (n=11) in the second group were imaged repeatedly with time intervals from four to 27 days. We evaluated the change of tumor size over time and correlated it with the change of total radioactivity in the entire tumor and the change of mean counts per pixel of the tumor respectively. The size change owing to tumor development was further associated with the possible pattern change. Moreover, we investigated the potential relationship of the tumor location with tumor development.

Two MMTV tumors had no detectable size change for time intervals from six to 27 days while the rest of the tumors (n = 9) increased their size by 45-185% after four to 21 days with tumor development. These changes are positively associated with the changes of radioactivity of ^{125}I in the entire tumors (Table. 6.1). The tumors with no detectable change of size had no substantial change of total radioactivity while those developing their size increased the total uptake of ^{125}I . However, we found no clear

correlation between the change of tumor size and the change of mean counts per pixel of a tumor representing the average level of the NIS expression in the tumor.

Imaging date post injection (days)	Tumor Pattern	Tumor size (pixels)	¹²⁵ I uptake in the entire tumor
0	Center-to-edge	24	0.00477
14	Center-to-edge	52	0.01284
35	Multi-spot	107	0.01918

Table 6.1. Repeated imaging of a right thoracic tumor

The results based on the limited samples (n = 11) show no relationship between the speed of tumor development and the initial size or pattern of the tumor. Both initially small and large tumors can develop their size rapidly. Pattern change (n=2) was observed from center-to-edge to multi-spot for initial tumors with a small size. Tumor location was not found to be related to these conclusions. In summary, radionuclide scintigraphy is a promising method for *in vivo* study of morphological changes such as size and distribution pattern associated with tumor development.

6.6 Discussion and conclusion

In an attempt to address the needs of high-performance breast cancer imaging, we have investigated in this study the application of *in vivo* gamma ray imaging for breast cancer study using a novel gamma camera and endogenous NIS expression in a mouse model. We have validated in this work the efficacy of *in vivo* gamma imaging of MMTV tumors with NIS as the reporter gene through molecular biology assay immunohistochemistry. We have demonstrated the capability of the dedicated gamma camera in detecting tumors as small as 3 mm and monitoring mammary glands bearing no visual tumors. Based upon analyzing the gamma images of endogenous NIS

expression in the mammary tumors of MMTV-infected mice, we have determined the sizes, patterns and radioactivity of the known tumors and the correlations among those parameters. We have also investigated the dynamic patterns and trends of radioactivity of the tumors over the one-hour imaging period and their relationship with other tumor parameters. We have finally shown the feasibility of *in vivo* gamma imaging for the study of tumor development over time through the same tumor of the same animal using a relatively low dose (14 μ Ci) of ^{125}I . The results suggest that the combination of a dedicated gamma camera and endogenous NIS expression has great promise to meet current imaging requirements for breast cancer studies.

Our results show that gamma images correlate with immunohistochemistry data not only for moderate tumors but also tumors as small as 3 mm. This is a significant achievement because small tumors usually have less NIS expression than larger tumors and thus may take up only a small amount of radioactivity for gamma imaging. As shown in Fig. 6.3, our dedicated gamma camera clearly shows localization of ^{125}I in both the large and small tumors. The 3 mm diameter small tumor (Fig. 6.3) was actually non-palpable until we confirmed it after the mouse dissection. Interestingly, we also notice that the mammary glands bearing no palpable tumors of over 50% MMTV-infected mice presented localization of radioiodine. Owing to the limited opportunity of dissection for confirmation, it remains unclear whether these mammary glands contain tiny tumors or not. Whether this phenomenon results from underlying biological issues related to MMTV is also of interest for further studies. However, these results have strongly suggested the advantage of our dedicated gamma camera for detecting a breast tumor at its earliest stage using NIS as the reporter gene.

We have evaluated the relationship among the tumor parameters such as sizes, patterns and radioactivity. As many other studies have done, we have correlated the tumor size with the total radioactivity in the tumor. We have found a similar general relationship that larger tumors accumulate more radioactivity. In addition to that, we learned that the small tumors present a relatively stronger correlation with their sizes while larger tumors have little or no significant relationship with tumor sizes. These results imply that the role of biological parameters beyond size is becoming more important in affecting the uptake of radioactivity in tumors with increasing size. Our study further reveals tumor patterns and the association with tumor sizes. We have identified three patterns of MMTV tumors with tumor size, i.e. center-to-edge (type I), multi-spot and ring (type II). These two types of tumors are associated with tumor size below and above 75 pixels, respectively. Though the manner in which these types of tumors are related to their biological properties requires further investigation, these results clearly suggests the feasibility of characterization of such tumors using *in vivo* gamma imaging.

Our study also indicates a possible way to reveal radioiodine transfer in the tumor by referring to the positive and negative difference plots. Presented in Fig. 6.10 is a presumed pathway for iodine transfer in a tumor with center-to-edge pattern:

1. Initial uptake of ^{125}I via NIS expression of the active tumor tissues;
2. Adjacent tumor tissues become hot with ^{125}I transferred from central regions;
3. ^{125}I transfer continues from the near-central regions to edge regions

Our preliminary study of tumor progression shows a possible association between the development of a small tumor and the change of tumor pattern. We have also found

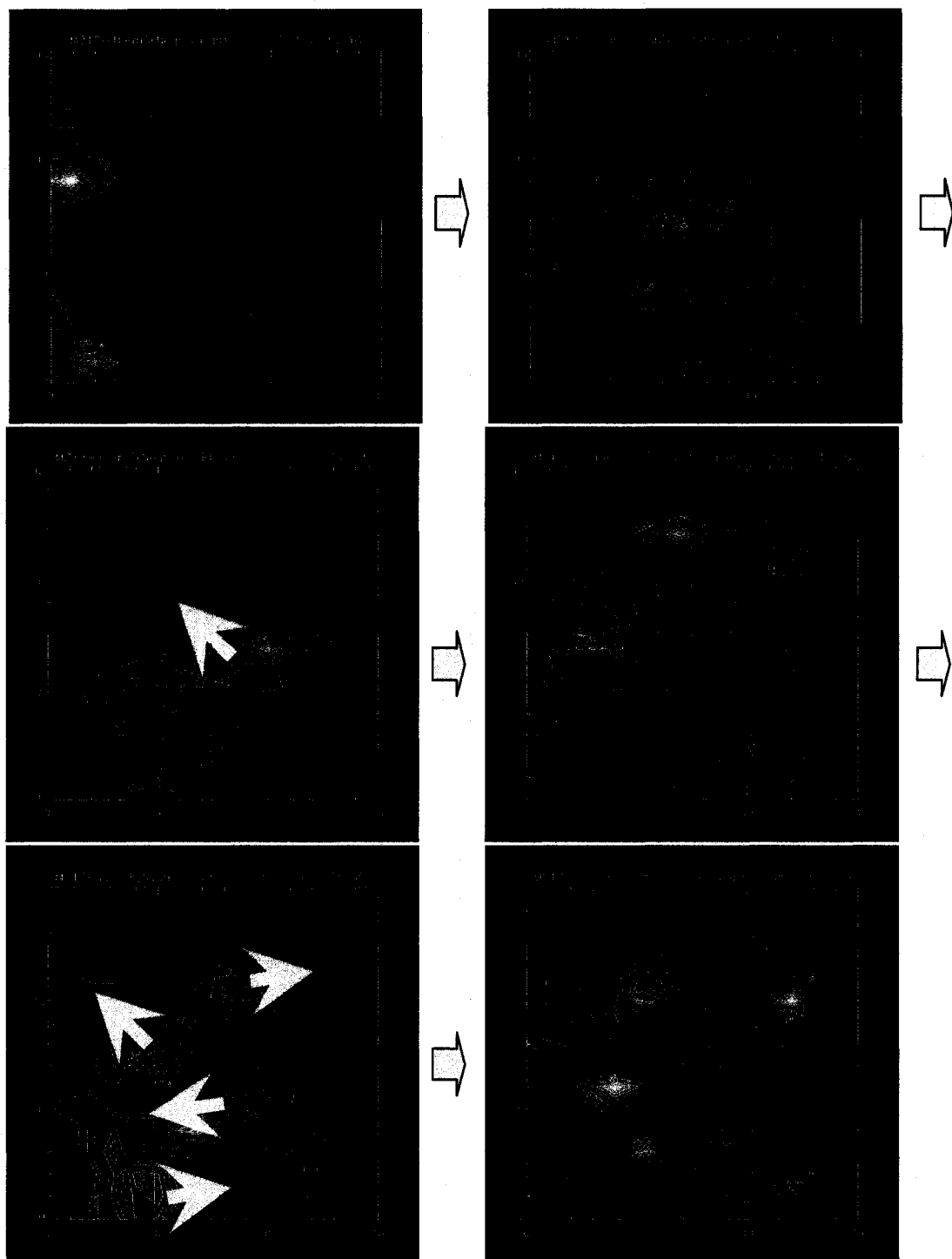


Fig. 6.10. Presumed pathway for iodine transfer in a tumor. (Top row:) Uptake of ^{125}I via NIS expression of the active tumor tissues in the first ten minutes post injection of radiotracers; (Middle row:) adjacent tumor tissues become hot with ^{125}I transferred from central regions in the period of 25-35 minutes post injection; (Bottom row:) ^{125}I transfer continues from the near-central regions to edge regions in the period of 50-60 minutes.

that the diversity of the speed of tumor development has no clear relationship with the initial size of the tumor. Though this study was limited by the sample size and a large sample size may provide more comprehensive results, the results indicate that gamma imaging with a dedicated gamma camera is a promising *in vivo* method of monitoring the morphological changes associated with tumor development.

In conclusion, we have demonstrated that *in vivo* gamma imaging using a dedicated gamma camera with NIS as the reporter gene is very promising for breast cancer studies based upon mouse models. Specifically, we have confirmed the efficacy of gamma imaging of mammary tumors by correlating the distribution of ^{125}I observed in gamma images with the data of immunohistochemistry. We have found that NIS is an effective reporter gene for detecting a tumor at its earliest stage. Based on this reporter gene, we have identified three patterns of ^{125}I distribution in tumors, i.e. center-to-edge, multi-spot and ring, which are associated with tumor sizes. Our study particularly shows that the total ^{125}I uptake in a tumor has little or no significant correlation with increasing tumor size. The dynamic changes of pattern and trends of ^{125}I uptake in a tumor suggest a possible way to reveal the pathway of ^{125}I transfer in the tumor. Our preliminary results also indicate that the imaging method we proposed here has the potential for a range of studies of tumor development.

Chapter 7

Future directions and conclusion

7.1 Future directions

We have developed a versatile imaging system suitable for biological studies using small animals. Our collaboration is pursuing further extension of the capabilities of this system in three directions: development of a relatively large field-of-view detector interchangeable for parallel-hole or pinhole imaging, incorporation of a mouse monitoring system, development of computer-aided pattern recognition program for image analysis of mammary tumors.

7.1.1 Development of a novel LaBr₃ detector

One major improvement we are achieving is the development of a novel high-performance detector readily adaptable to parallel-hole and pinhole SPECT thus meeting the different requirements of a variety of biological studies using small animals such as mice or rats. The new flat-panel PSPMT, Hamamatsu H9500, has become available recently. The H9500 PSPMT has an external size of 52 mm x 52 mm x 33.3 mm with an effective view area 49 mm x 49 mm and a 1.5 mm glass window, which results in only a small dead space between adjacent tubes. A matrix of 16 x 16 anode pads is utilized in this module with anode pitch of 3 mm in both directions. Therefore, H9500 PSPMTs

provide better spatial resolution than the earlier H8500 modules from the same manufacturer. The quantum efficiency of the H9500 is also good, i.e. 24% at 420 nm. These properties make the H9500 PSPMT an excellent choice for developing a new detector for small animal imaging. This new tube has demonstrated its applicability to gamma-ray imaging [72, 260-263]. Several research groups have carried out studies on this tube and have reported on its suitability and feasibility for nuclear medicine imaging applications. Inadama *et al.* [262] and Imrek *et al.* [261] have demonstrated the suitability of this PSPMT when applied to PET imaging of small animals. The simulations and preliminary measurements reported by Garibaldi *et al.* suggest the feasibility of high-performance gamma-ray detectors for early diagnosis and therapy monitoring of breast cancer built from arrays of smaller anode pixel size PSPMTs such as H9500 using their new multi-channel electronics [260]. Our collaborators, Popov *et al.* and Proffitt *et al.* have developed high-performance readout electronics and high-rate USB data acquisition system suitable for the application of H9500 PSPMTs in PET and SPECT imaging, respectively [72, 263]. These studies indicated that it was promising to design a high-performance detector based on the H9500. As to scintillators, lanthanum bromide (LaBr_3) has shown very promising characteristics as a gamma-ray imager and spectrometer. The excellent energy resolution of LaBr_3 (6% at 140 keV and ~3% FWHM at 662 keV) makes it the major competitor of semiconductor detectors working at room temperature. LaBr_3 scintillator also has high light yield (63000 photons/MeV), flat response as a function of incident gamma energy and short scintillation decay time (16ns). These features satisfy the principal requirements for gamma-ray imaging such as high light output, high photo-fraction and excellent energy resolution [264, 265]. Several groups

have proposed LaBr_3 detectors for gamma-ray imaging [74, 264, 266]. The report on recent advances and future perspectives of gamma imagers for scintimammography by Pani *et al.* [264] indicated that a $\text{LaBr}_3(\text{Ce})$ gamma camera showed superior spatial and energy resolution compared with a previous camera based on a $\text{NaI}(\text{Tl})$ scintillator array. Despres *et al.* investigated a PSAPD-based gamma camera using continuous crystals including $\text{LaBr}_3(\text{Ce})$ [74]. Their results suggest that the continuous crystal configuration is especially well suited for a small-animal imaging system. A study by Yamamoto *et al.* confirmed that $\text{LaBr}_3(\text{Ce})$ is promising for low-energy gamma-ray imaging [266].

Building upon those reported results, we have designed a novel detector that is suitable for either parallel-hole or multipinhole SPECT. Shown in Fig. 7.1 is a photograph of the integrated detector including scintillator, PSPMTs and electronics. This detector incorporates a single piece of 3 mm thick continuous $\text{LaBr}_3(\text{Ce})$ scintillator and an array of 2 x 2 Hamamatsu H9500 PSPMT modules. High-performance readout electronics and high-rate USB data acquisition system have been employed for this detector [72, 263]. The preliminary test shows that the intrinsic resolution of the detector is around 0.7 mm for 166 keV gamma rays. Owing to the relatively large sensitive area of $100 \times 100 \text{ mm}^2$, the detector (if equipped with parallel-hole collimator) will allow us to image a pair of mice simultaneously for immediate comparison of their response to radiotracers. Multipinhole collimators can also be easily employed in this detector to enable relatively large field-of-view multipinhole circular or helical SPECT with a goal of improved performance.

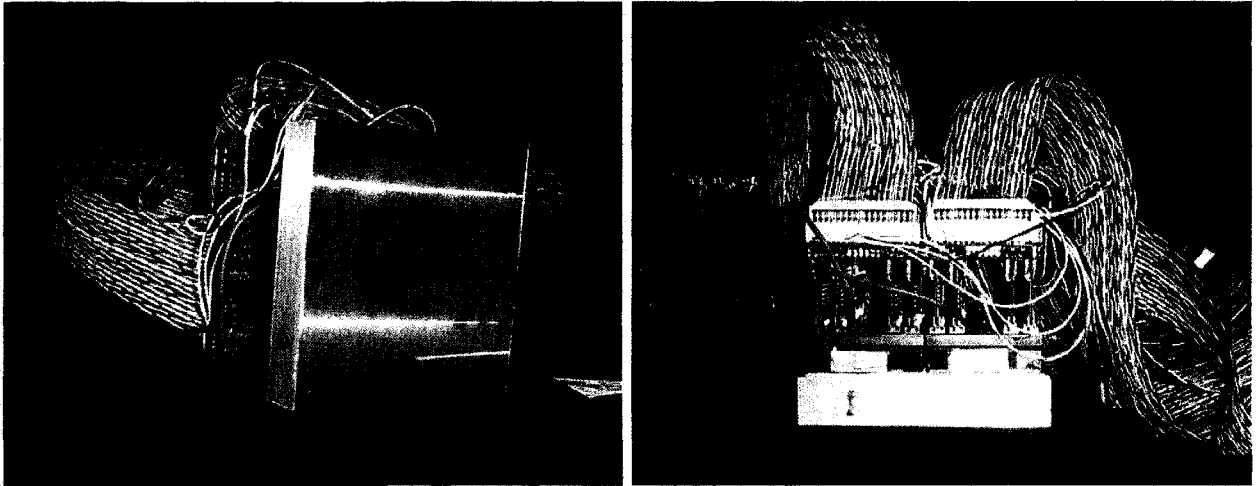


Fig. 7.1 Photographs of the prototype $\text{LaBr}_3(\text{Ce})$ detector

Currently we can achieve spatial resolution of 1.2-1.5 mm for multipinhole (up to five 1 mm diameter pinholes) circular/helical SPECT using a 110 mm diameter circular detector. However, submillimeter resolution would allow us to resolve better the fine structure of the tissues we are studying. The novel LaBr_3 detector will make it easier to further improve the resolution of our multipinhole circular/helical SPECT system. An effective way to improve the resolution is to reduce the diameter of the pinhole, which consequently reduces the sensitivity of the detector. The relatively large sensitive area of the LaBr_3 detector enables us to use more pinholes to compensate for the loss of sensitivity due to the reduced pinhole diameter.

7.1.2 Mouse anesthesia vital sign monitoring system improvement

To optimize imaging conditions for animal subjects, several changes in current procedures can be envisioned. They could involve the use of gas anesthesia and continuous vital sign monitoring. Future development of this capability is expected as we

modify a veterinary monitoring system (Arc 2000, Silogic International Ltd.) and a heated anesthetizing gas flow system. The improvement is called in progress in our lab.

7.1.3 Computer-aided pattern recognition for tumor studies

In the ongoing study of mammary tumors using MMTV-infected mice, we have concluded that it is important to determine the pattern of each individual tumor and to correlate that pattern with other parameters such as size or stage of development in order to produce an illustrative relationship which may imply biological information for researchers. In the imaging study of MMTV tumors as described in Chapter 6, we determined tumor patterns visually. With the advances in computer science, a variety of computer-aided methods of image analysis have been developed for different imaging modalities. Segmentation of ROI (in mammography) [267] or volume of interest (VOI in PET and SPECT) [201, 268] are significant to determine the morphological characteristics for pattern recognition and for quantitative, objective analysis of the target tissues. The segmentation method in dynamic scintigraphy [269] producing a functional image representing regions with temporal dynamics, seems interesting though it has been proposed for dynamic cardiac imaging. Researchers use a combination of observers such as radiologists and physicians for visual pattern determination and semi-quantitative methods such as standardized uptake value (SUV) to classify patterns in PET imaging data [270]. An alternative approach to evaluate the heterogeneity of tissues in images is to use the quantitative output scores of image analysis techniques, i.e. automated quantitative analysis (AQUA) score [271], fractal dimension [272], or artificial neural

networks (ANNs) output [273]. It is likely, therefore, that there is potential in applying some of these pattern recognition techniques to image analysis of MMTV tumors.

7.2 Conclusion

A compact imaging system equipped with novel detectors suitable for biological imaging of small animals has been developed. This versatile apparatus is capable of dual-modality (gamma ray/X-ray) planar imaging, parallel-hole SPECT, and multipinhole circular/helical SPECT. In particular, we have developed compact gamma cameras for biological imaging based upon newly available PSPMT modules. We have recently extended this system to be capable of multipinhole helical SPECT based on a 110 mm diameter circular detector. The efficacy of this effort has been verified with a number of phantom and mouse studies. This imaging system has further been applied to several biological studies including mouse thyroid and mammary tumors. Results demonstrate that this work can readily meet a number of different requirements for a variety of small animal imaging applications. This compact, high-performance imaging system is not only suitable for *in vivo* small animal research as evidenced by the applications described here but its modular construction will allow expansion and further development as new needs and new opportunities arise.

Bibliography

- [1] E. L. Bradley, J. Cella, S. Majewski, V. Popov, J. Qian, M. S. Saha, M. F. Smith, A. G. Weisenberger, and R. E. Welsh, "A compact gamma camera for biological imaging," *Nuclear Science, IEEE Transactions on*, vol. 53, pp. 59-65, 2006.
- [2] W. T. Hammond, E. L. Bradley, R. E. Welsh, J. Qian, A. G. Weisenberger, M. F. Smith, S. Majewski, and M. S. Saha, "A gamma camera re-evaluation of potassium iodide blocking efficiency in mice," *Health Phys*, vol. 92, pp. 396-406, Apr 2007.
- [3] J. Qian, R. E. Blue, E. L. Bradley, S. Majewski, M. S. Saha, S. Schworer, M. F. Smith, A. G. Weisenberger, and R. E. Welsh, "In vivo multipinhole helical SPECT applied to visualization of sodium iodide symporter activity in the mouse thyroid," (to be submitted).
- [4] H. R. Herschman, "Molecular imaging: looking at problems, seeing solutions," *Science*, vol. 302, pp. 605-8, Oct 24 2003.
- [5] M. G. Pomper, "Can small animal imaging accelerate drug development?," *J Cell Biochem Suppl*, vol. 39, pp. 211-20, 2002.
- [6] A. F. Chatziioannou, "Molecular imaging of small animals with dedicated PET tomographs," *Eur J Nucl Med Mol Imaging*, vol. 29, pp. 98-114, Jan 2002.
- [7] D. A. Weber and M. Ivanovic, "Ultra-high-resolution imaging of small animals: implications for preclinical and research studies," *J Nucl Cardiol*, vol. 6, pp. 332-44, May-Jun 1999.
- [8] S. R. Cherry, "In vivo molecular and genomic imaging: new challenges for imaging physics," *Phys Med Biol*, vol. 49, pp. R13-48, Feb 7 2004.
- [9] V. Sharma, G. D. Luker, and D. Piwnica-Worms, "Molecular imaging of gene expression and protein function in vivo with PET and SPECT," *J Magn Reson Imaging*, vol. 16, pp. 336-51, Oct 2002.
- [10] S. R. Cherry, "Multimodality in vivo imaging systems: twice the power or double the trouble?," *Annu Rev Biomed Eng*, vol. 8, pp. 35-62, 2006.
- [11] A. Fenster, "A Trends guide to imaging technologies," *Trends in Biotechnology*, vol. 20, pp. S1-S2, 2002.
- [12] R. G. Blasberg and J. Gelovani-Tjuvajev, "In vivo molecular-genetic imaging," *Journal of Cellular Biochemistry*, vol. 87, pp. 172-183, 2002.
- [13] A. Bogdanov and R. Weissleder, "In vivo imaging of gene delivery and expression," *Trends in Biotechnology*, vol. 20, pp. S11-S18, 2002.
- [14] S. P. Hume and R. Myers, "Dedicated small animal scanners: a new tool for drug development?," *Curr Pharm Des*, vol. 8, pp. 1497-511, 2002.
- [15] N. Beckmann, R. Kneuer, H. U. Gremlich, H. Karmouty-Quintana, F. X. Ble, and M. Muller, "In Vivo mouse imaging and spectroscopy in drug discovery," *NMR in Biomedicine*, vol. 20, pp. 154-185, 2007.
- [16] T. F. Budinger, D. A. Benaron, and A. P. Koretsky, "Imaging Transgenic Animals," *Annual Review of Biomedical Engineering*, vol. 1, pp. 611-648, 1999.
- [17] D. C. Sullivan and J. M. Hoffman, "In vivo imaging of gene expression," *Semin Radiat Oncol*, vol. 11, pp. 37-46, Jan 2001.
- [18] M. N. Wernick and J. N. Aarsvold, *Emission tomography: the fundamentals of PET and SPECT*. Elsevier Academic Press, 2004.
- [19] A. Van der Linden, N. Van Camp, P. Ramos-Cabrera, and M. Hoehn, "Current status of functional MRI on small animals: application to physiology, pathophysiology, and cognition," *NMR Biomed*, vol. 20, pp. 522-45, Aug 2007.
- [20] R. G. Blasberg, "In vivo molecular-genetic imaging: multi-modality nuclear and optical combinations," *Nucl Med Biol*, vol. 30, pp. 879-88, Nov 2003.
- [21] M. Doubrovina, I. Serganova, P. Mayer-Kuckuk, V. Ponomarev, and R. G. Blasberg, "Multimodality in vivo molecular-genetic imaging," *Bioconjug Chem*, vol. 15, pp. 1376-88, Nov-Dec 2004.
- [22] I. Serganova and R. G. Blasberg, "Multi-modality molecular imaging of tumors," *Hematol Oncol Clin North Am*, vol. 20, pp. 1215-48, Dec 2006.
- [23] C. S. Levin, "Primer on molecular imaging technology," *Eur J Nucl Med Mol Imaging*, vol. 32 Suppl 2, pp. S325-45, Dec 2005.

- [24] <http://en.wikipedia.org/wiki/Image:PET-schema.png>.
- [25] L. Eriksson, D. Townsend, M. Eriksson, C. Melcher, M. Schmand, B. Bendriem, and R. Nutt, "Experience with scintillators for PET: towards the fifth generation of PET scanners," *Nuclear Instruments and Methods in Physics Research Section A: Accelerators, Spectrometers, Detectors and Associated Equipment*, vol. 525, pp. 242-248, 2004.
- [26] C. W. E. van Eijk, "Inorganic scintillators in medical imaging detectors," *Nuclear Instruments and Methods in Physics Research Section A: Accelerators, Spectrometers, Detectors and Associated Equipment*, vol. 509, pp. 17-25, 2003.
- [27] F. Bauer, M. Aykac, M. Loope, C. W. Williams, L. Eriksson, and M. Schmand, "Performance Study of the New Hamamatsu R9779 and Photonis XP20D0 Fast 2" Photomultipliers," *Nuclear Science, IEEE Transactions on*, vol. 54, pp. 422-426, 2007.
- [28] I. Britvitch, E. Lorenz, A. Olshevski, D. Renker, Z. Sadygov, R. Scheuermann, A. Stoykov, A. Werner, and I. Zheleznykh, "Development of scintillation detectors based on avalanche microchannel photodiodes," *Nuclear Instruments and Methods in Physics Research Section A: Accelerators, Spectrometers, Detectors and Associated Equipment*, vol. 571, pp. 317-320, 2007.
- [29] Zecotek Photonics, Inc.
- [30] Radiation Monitoring Devices, Inc.
- [31] M. E. Casey and R. Nutt, "A Multicrystal Two Dimensional BGO Detector System for Positron Emission Tomography," *Nuclear Science, IEEE Transactions on*, vol. 33, pp. 460-463, 1986.
- [32] S. R. Cherry, J. A. Sorenson, and M. E. Phelps, *Physics in Nuclear Medicine*: Elsevier Science, 2003.
- [33] G. Di Domenico, G. Zavattini, N. Cesca, N. Auricchio, R. Andritschke, F. Schopper, and G. Kanbach, "SiliPET: An ultra-high resolution design of a small animal PET scanner based on stacks of double-sided silicon strip detector," *Nuclear Instruments and Methods in Physics Research Section A: Accelerators, Spectrometers, Detectors and Associated Equipment*, vol. 571, pp. 22-25, 2007.
- [34] A. E. Spinelli, D. D'Ambrosio, C. Pettinato, S. Trespidi, C. Nanni, V. Ambrosini, G. Baldazzi, C. Bergamini, and M. Marengo, "Performance evaluation of a small animal PET scanner. Spatial resolution characterization using 18F and 11C," *Nuclear Instruments and Methods in Physics Research Section A: Accelerators, Spectrometers, Detectors and Associated Equipment*, vol. 571, pp. 215-218, 2007.
- [35] K. Ishii, Y. Kikuchi, S. Matsuyama, Y. Kanai, K. Kotani, T. Ito, H. Yamazaki, Y. Funaki, R. Iwata, M. Itoh, K. Yanai, J. Hatazawa, N. Itoh, N. Tanizaki, D. Amano, M. Yamada, and T. Yamaguchi, "First achievement of less than 1 mm FWHM resolution in practical semiconductor animal PET scanner," *Nuclear Instruments and Methods in Physics Research Section A: Accelerators, Spectrometers, Detectors and Associated Equipment*, vol. 576, pp. 435-440, 2007.
- [36] A. Drezet, O. Monnet, F. Mathy, G. Montemont, and L. Verger, "CdZnTe detectors for small field of view positron emission tomographic imaging," *Nuclear Instruments and Methods in Physics Research Section A: Accelerators, Spectrometers, Detectors and Associated Equipment*, vol. 571, pp. 465-470, 2007.
- [37] A. Alessio and P. Kinahan, "PET Image Reconstruction," in *Nuclear Medicine* 2nd ed, R. E. Henkin, Ed.: Mosby, 2006.
- [38] J. M. Ollinger, "Model-based scatter correction for fully 3D PET," *Physics in Medicine and Biology*, pp. 153-176, 1996.
- [39] S. D. Wollenweber, "Parameterization of a model-based 3-D PET scatter correction," *Nuclear Science, IEEE Transactions on*, vol. 49, pp. 722-727, 2002.
- [40] P. Razifar, M. Lubberink, H. Schneider, B. Langstrom, E. Bengtsson, and M. Bergstrom, "Non-isotropic noise correlation in PET data reconstructed by FBP but not by OSEM demonstrated using auto-correlation function," *BMC Med Imaging*, vol. 5, p. 3, May 13 2005.
- [41] P. E. Kinahan and J. G. Rogers, "Analytic 3D image reconstruction using all detected events," *Nuclear Science, IEEE Transactions on*, vol. 36, pp. 964-968, 1989.
- [42] A. Dempster, N. Laird, and D. Rubin, "Maximum likelihood from incomplete data via the EM algorithm," *Journal of the Royal Statistical Society*, vol. 39, pp. 1-38, 1977.
- [43] C. A. Johnson, J. Seidel, R. E. Carson, W. R. Gandler, A. Sofer, M. V. Green, and M. E. Daube-Witherspoon, "Evaluation of 3D reconstruction algorithms for a small animal PET camera," *Nuclear Science, IEEE Transactions on*, vol. 44, pp. 1303-1308, 1997.

- [44] C. Comtat, P. E. Kinahan, M. Defrise, C. A. M. C. Michel, and D. W. A. T. D. W. Townsend, "Fast reconstruction of 3D PET data with accurate statistical modeling," *Nuclear Science, IEEE Transactions on*, vol. 45, pp. 1083-1089, 1998.
- [45] Philips Co.
- [46] www.raytest.de.
- [47] P. M. Bloomfield, S. Rajeswaran, T. J. Spinks, S. P. Hume, R. Myers, S. Ashworth, K. M. Clifford, W. F. Jones, L. G. Byars, J. Young, and et al., "The design and physical characteristics of a small animal positron emission tomograph," *Phys Med Biol*, vol. 40, pp. 1105-26, Jun 1995.
- [48] J. A. Correia, C. A. Burnham, D. Kaufman, A. L. Brownell, and A. J. Fischman, "Performance evaluation of MMP-II: A second-generation small animal PET," *Nuclear Science, IEEE Transactions on*, vol. 51, pp. 21-26, 2004.
- [49] A. Del Guerra, G. Di Domenico, M. Scandola, and G. Zavattini, "YAP-PET: first results of a small animal positron emission tomograph based on YAP:Ce finger crystals," *Nuclear Science, IEEE Transactions on*, vol. 45, pp. 3105-3108, 1998.
- [50] R. Laforest, L. Desmond, S. Stefan, F. N. A. D. F. N. Danny, and A. J. Y. Jeffrey Yap, "Performance Evaluation of the microPET®—FOCUS-F120," *Nuclear Science, IEEE Transactions on*, vol. 54, pp. 42-49, 2007.
- [51] R. Lecomte, J. Cadorette, P. Richard, S. A. R. S. Rodrigue, and D. A. R. D. Rouleau, "Design and engineering aspects of a high resolution positron tomograph for small animal imaging," *Nuclear Science, IEEE Transactions on*, vol. 41, pp. 1446-1452, 1994.
- [52] D. P. McElroy, W. Pimpl, B. J. Pichler, M. Rafecas, T. Schuler, and S. I. Ziegler, "Characterization and readout of MADPET-II detector modules: validation of a unique design concept for high resolution small animal PET," *Nuclear Science, IEEE Transactions on*, vol. 52, pp. 199-204, 2005.
- [53] J. Missimer, Z. Madi, M. Honer, C. Keller, A. Schubiger, and S. M. Ametamey, "Performance evaluation of the 16-module quad-HIDAC small animal PET camera," *Phys Med Biol*, vol. 49, pp. 2069-81, May 21 2004.
- [54] J. Seidel, J. J. Vaquero, and M. V. Green, "Resolution uniformity and sensitivity of the NIH ATLAS small animal PET scanner: Comparison to simulated LSO scanners without depth-of-interaction capability," *Nuclear Science, IEEE Transactions on*, vol. 50, pp. 1347-1350, 2003.
- [55] Y. C. Tai, A. F. Chatziioannou, Y. Yang, R. W. Silverman, K. Meadors, S. Siegel, D. F. Newport, J. R. Stickel, and S. R. Cherry, "MicroPET II: design, development and initial performance of an improved microPET scanner for small-animal imaging," *Physics in Medicine and Biology*, vol. 48, pp. 1519-1537, 2003.
- [56] S. Weber, A. Terstegge, H. Herzog, R. Reinartz, P. Reinhart, F. Rongen, H. W. Muller-Garmer, and H. Halling, "The design of an animal PET: flexible geometry for achieving optimal spatial resolution or high sensitivity," *Medical Imaging, IEEE Transactions on*, vol. 16, pp. 684-689, 1997.
- [57] A. L. Goertzen, A. K. Meadors, R. W. Silverman, and S. R. Cherry, "Simultaneous molecular and anatomical imaging of the mouse in vivo," *Physics in Medicine and Biology*, vol. 47, pp. 4315-4328, 2002.
- [58] A. Del Guerra, C. Damiani, G. Di Domenico, A. A. M. A. Motta, M. A. G. M. Giganti, R. A. M. R. Marchesini, A. A. P. A. Piffanelli, N. A. S. N. Sabba, L. A. S. L. Sartori, and G. A. Z. G. Zavattini, "An integrated PET-SPECT small animal imager: preliminary results," *Nuclear Science, IEEE Transactions on*, vol. 47, pp. 1537-1540, 2000.
- [59] Y. Shao, S. R. Cherry, K. Farahani, R. A. S. R. Slates, R. W. A. S. R. W. Silverman, K. A. M. K. Meadors, A. A. B. A. Bowery, S. A. S. S. Siegel, P. K. A. M. P. K. Marsden, and P. B. A. G. P. B. Garlick, "Development of a PET detector system compatible with MRI/NMR systems," *Nuclear Science, IEEE Transactions on*, vol. 44, pp. 1167-1171, 1997.
- [60] J. R. Mercer, "Molecular imaging agents for clinical positron emission tomography in oncology other than fluorodeoxyglucose (FDG): applications, limitations and potential," *J Pharm Pharm Sci*, vol. 10, pp. 180-202, 2007.
- [61] H. O. Anger, "Scintillation camera," *Rev. Sci. Instr.*, vol. 29, pp. 27-33, 1958.
- [62] E. L. Keller, "Optimum dimensions of parallel-hole, multi-aperture collimators for gamma-ray cameras," *J Nucl Med*, vol. 9, pp. 233-5, Jun 1968.

- [63] M. F. Smith, S. Majewski, and A. G. Weisenberger, "Optimizing pinhole and parallel hole collimation for scintimammography with compact pixellated detectors," *IEEE Trans. Nucl. Sci.*, vol. 50, pp. 321-326, 2003.
- [64] F. J. Beekman, F. van der Have, B. Vastenhouw, A. J. van der Linden, P. P. van Rijk, J. P. Burbach, and M. P. Smidt, "U-SPECT-I: a novel system for submillimeter-resolution tomography with radiolabeled molecules in mice," *J Nucl Med*, vol. 46, pp. 1194-200, Jul 2005.
- [65] S. R. Meikle, P. Kench, R. Wojcik, M. F. Smith, A. G. Weisenberger, S. Majewski, M. Lerch, and A. B. Rosenfeld, "Performance evaluation of a multipinhole small animal SPECT system," *Conf. Rec. 2003 Nuclear Science Symp. Medical Imaging Conf.*, vol. 3, pp. 1988-1992 Vol.3, 2003.
- [66] N. U. Schramm, G. Ebel, U. Engeland, T. Schurrat, M. Behe, and T. M. Behr, "High-resolution SPECT using multipinhole collimation," *IEEE Trans. Nucl. Sci.*, vol. 50, pp. 315-320, 2003.
- [67] S. D. Metzler, K. L. Greer, and R. J. Jaszczak, "Helical pinhole SPECT for small-animal imaging: a method for addressing sampling completeness," *Nuclear Science, IEEE Transactions on*, vol. 50, pp. 1575-1583, 2003.
- [68] A. G. Weisenberger, R. Wojcik, E. L. Bradley, P. Brewer, S. Majewski, J. Qian, A. Ranck, M. S. Saha, K. Smith, M. F. Smith, and R. E. Welsh, "SPECT-CT system for small animal imaging," *Nuclear Science, IEEE Transactions on*, vol. 50, pp. 74-79, 2003.
- [69] A. G. Weisenberger, B. Kross, S. Majewski, R. Wojcik, E. L. Bradley, and M. S. Saha, "Design features and performance of a CsI(Na) array based gamma camera for small animal gene research," *Nuclear Science, IEEE Transactions on*, vol. 45, pp. 3053-3058, 1998.
- [70] A. G. Weisenberger, E. L. Bradley, S. Majewski, and M. S. Saha, "Development of a novel radiation imaging detector system for in vivo gene imaging in small animal studies," *Nuclear Science, IEEE Transactions on*, vol. 45, pp. 1743-1749, 1998.
- [71] R. Pani, R. Pellegrini, M. N. Cinti, C. Trotta, G. Trotta, F. Garibaldi, R. Scafe, and A. Del Guerra, "Flat Panel PMT for photon emission imaging," *Nuclear Instruments and Methods in Physics Research Section A: Accelerators, Spectrometers, Detectors and Associated Equipment*, vol. 505, pp. 590-594, 2003.
- [72] V. Popov and S. Majewski, "A Compact High Performance Readout Electronics Solution for H9500 Hamamatsu 256 Multianode Photomultiplier Tube for Application in Gamma Cameras," in *Nuclear Science Symposium Conference Record, 2006. IEEE*, 2006, pp. 2981-2985.
- [73] W. C. Barber, T. Funk, M. McClish, K. S. Shah, and B. H. Hasegawa, "PSAPD gamma camera for SPECT imaging," in *Nuclear Science Symposium Conference Record, 2004 IEEE*, 2004, pp. 2815-2817 Vol. 5.
- [74] P. Despres, W. C. Barber, T. Funk, M. McClish, K. S. Shah, and B. H. Hasegawa, "Investigation of a continuous crystal PSAPD-based gamma camera," *Nuclear Science, IEEE Transactions on*, vol. 53, pp. 1643-1649, 2006.
- [75] G. A. de Vree, A. H. Westra, I. Moody, F. van der Have, K. M. Ligtoet, and F. J. Beekman, "Photon-counting gamma camera based on an electron-multiplying CCD," *Nuclear Science, IEEE Transactions on*, vol. 52, pp. 580-588, 2005.
- [76] E. Richer, M. A. Lewis, B. Smith, X. Li, S. Seliounine, R. P. Mason, and P. P. Antich, "Comparison of CsI(Tl) and scintillating plastic in a multi-pinhole/CCD-based gamma camera for small-animal low-energy SPECT," in *Small-animal SPECT imaging*, M. A. Kupinski and H. H. Barrett, Eds.: Springer, 2005, pp. 189-194.
- [77] M. T. Madsen, "Recent Advances in SPECT Imaging," *The Journal of Nuclear Medicine*, vol. 48, pp. 661-673, 2007.
- [78] R. Pani, M. N. Cinti, R. Pellegrini, P. Bennati, M. Betti, F. Vittorini, M. Mattioli, G. Trotta, V. Orsolini Cencelli, R. Scaf, F. Navarra, D. Bollini, G. Baldazzi, G. Moschini, and F. de Notaristefani, "LaBr₃:Ce scintillation gamma camera prototype for X and gamma ray imaging," *Nuclear Instruments and Methods in Physics Research Section A: Accelerators, Spectrometers, Detectors and Associated Equipment*, vol. 576, pp. 15-18, 2007.
- [79] J. Qian, E. L. Bradley, S. Majewski, J. McKisson, V. Popov, J. Proffitt, M. S. Saha, J. Sutton, A. G. Weisenberger, R. E. Welsh, and A. Yazdi, "Preliminary tests of a high performance LaBr₃ gamma imager for small animals (abstract)," *Bulletin of the American Physical Society*, vol. 52, p. 31, 2007.
- [80] D. G. Darambara and A. Todd-Pokropek, "Solid state detectors in nuclear medicine," *Q J Nucl Med*, vol. 46, pp. 3-7, Mar 2002.

- [81] E. W. Izaguirre, S. Mingshan, T. Vandehei, P. Despres, Y. Huang, T. Funk, J. Li, K. Parnham, B. E. Pratt, and B. H. Hasegawa, "Evaluation of a Large Pixellated Cadmium Zinc Telluride Detector for Small Animal Radionuclide Imaging," in *Nuclear Science Symposium Conference Record, 2006. IEEE*, 2006, pp. 3817-3820.
- [82] J. B. Habraken, K. de Bruin, M. Shehata, J. Booij, R. Bennink, B. L. van Eck Smit, and E. Busemann Sokole, "Evaluation of high-resolution pinhole SPECT using a small rotating animal," *J Nucl Med*, vol. 42, pp. 1863-9, Dec 2001.
- [83] C. Lackas, N. U. Schramm, J. W. Hoppin, U. Engeland, A. Wirrwar, and H. Halling, "T-SPECT: a novel imaging technique for small animal research," *Nuclear Science, IEEE Transactions on*, vol. 52, pp. 181-187, 2005.
- [84] A. L. Goertzen, D. W. Jones, J. Seidel, K. Li, and M. V. Green, "First results from the high-resolution mouseSPECT annular scintillation camera," *IEEE Trans Med Imaging*, vol. 24, pp. 863-7, Jul 2005.
- [85] L. R. Furenlid, D. W. Wilson, C. Yi-chun, A. H. K. Hyunki Kim, P. J. A. P. J. Pietraski, M. J. A. C. M. J. Crawford, and H. H. A. B. H. H. Barrett, "FastSPECT II: a second-generation high-resolution dynamic SPECT imager," *Nuclear Science, IEEE Transactions on*, vol. 51, pp. 631-635, 2004.
- [86] S. R. Meikle, P. Kench, M. Kassiou, and R. B. Banati, "Small animal SPECT and its place in the matrix of molecular imaging technologies," *Phys Med Biol*, vol. 50, pp. R45-61, Nov 21 2005.
- [87] H. M. Hudson and R. S. Larkin, "Accelerated image reconstruction using ordered subsets of projection data," *Medical Imaging, IEEE Transactions on*, vol. 13, pp. 601-609, 1994.
- [88] J. Li, R. J. Jaszcak, and R. E. Coleman, "Maximum likelihood reconstruction for pinhole SPECT with a displaced center-of-rotation," *IEEE Trans. Med. Imag.*, vol. 14, pp. 407-409, 1995.
- [89] R. L. Siddon, "Fast calculation of the exact radiological path for a three-dimensional CT array," *Med Phys*, vol. 12, pp. 252-255, 1985.
- [90] N. Kubo, S. Zhao, Y. Fujiki, A. Kinda, N. Motomura, C. Katoh, T. Shiga, H. Kawashima, Y. Kuge, and N. Tamaki, "Evaluating performance of a pixel array semiconductor SPECT system for small animal imaging," *Ann Nucl Med*, vol. 19, pp. 633-9, Oct 2005.
- [91] Y. Qi, B. M. W. Tsui, Y. Wang, B. Yoder, R. Wojcik, S. Majewski, and A. G. Weisenberger, "Development and characterization of a high-resolution microSPECT system for small-animal imaging," in *Small-animal SPECT imaging*, M. A. Kupinski and H. H. Barrett, Eds.: Springer, 2005, pp. 189-194.
- [92] Y.-J. Qi, "High-resolution SPECT for small-animal imaging," *Nuclear Science and Techniques*, vol. 17, pp. 164-169, 2006.
- [93] N. U. Schramm, C. Lackas, J. Hoppin, T. Schurrat, M. Behe, U. Engeland, and T. M. Behr, "On the performance of two multi-pinhole SPECT systems for small animal research," *Nuclear Science Symposium Conference Record, 2004 IEEE*, vol. 5, pp. 2823-2824, 2004.
- [94] C. Lackas, N. U. Schramm, J. W. Hoppin, and H. Halling, "On the development of a high-resolution multi-pinhole SPECT/CT," *Nuclear Science Symposium Conference Record, 2004 IEEE*, vol. 6, pp. 3893-3895, 2004.
- [95] S. R. Meikle, P. Kench, A. G. Weisenberger, R. Wojcik, M. F. Smith, S. Majewski, S. Eberl, R. R. Fulton, A. B. Rosenfeld, and M. J. Fulham, "A prototype coded aperture detector for small animal SPECT," *Nuclear Science, IEEE Transactions on*, vol. 49, pp. 2167-2171, 2002.
- [96] F. J. Beekman and B. Vastenhouw, "Design and simulation of U-SPECT, an ultra-high resolution molecular imaging system," in *Nuclear Science Symposium Conference Record, 2002 IEEE*, 2002, pp. 792-796 vol.2.
- [97] T. E. Peterson, S. Shokouhi, L. R. Furenlid, and D. W. Wilson, "Multi-pinhole SPECT imaging with silicon strip detectors," in *Nuclear Science Symposium Conference Record, 2005 IEEE*, 2005, pp. 2752-2756.
- [98] S. P. Mok, Y. Wang, and B. M. W. Tsui, "Design of a novel pinhole collimator system for SPECT imaging of small animals with different sizes," in *Nuclear Science Symposium Conference Record, 2005 IEEE*, 2005, pp. 2649-2652.
- [99] J. Y. Hesterman, M. A. Kupinski, L. R. Furenlid, D. W. Wilson, and H. H. Barrett, "The multi-module, multi-resolution system (M3R): a novel small-animal SPECT system," *Med Phys*, vol. 34, pp. 987-93, Mar 2007.

- [100] H. Kim, L. R. Furenlid, M. J. Crawford, D. W. Wilson, H. B. Barber, T. E. Peterson, W. C. Hunter, Z. Liu, J. M. Woolfenden, and H. H. Barrett, "SemiSPECT: a small-animal single-photon emission computed tomography (SPECT) imager based on eight cadmium zinc telluride (CZT) detector arrays," *Med Phys*, vol. 33, pp. 465-74, Feb 2006.
- [101] T. Funk, P. Despres, W. C. Barber, K. S. Shah, and B. H. Hasegawa, "A multipinhole small animal SPECT system with submillimeter spatial resolution," *Med Phys*, vol. 33, pp. 1259-1268, 2006.
- [102] S. D. Metzler, K. L. Greer, K. Bobkov, and R. J. Jaszcak, "Laser alignment system for helical pinhole SPECT," *Nuclear Science, IEEE Transactions on*, vol. 51, pp. 603-610, 2004.
- [103] S. D. Metzler, K. L. Greer, and R. J. Jaszcak, "Determination of mechanical and electronic shifts for pinhole SPECT using a single point source," *IEEE Trans Med Imaging*, vol. 24, pp. 361-70, Mar 2005.
- [104] S. D. Metzler, R. J. Jaszcak, K. L. Greer, and J. E. Bowsher, "Angular-Dependent Axial-Shift Correction for Pinhole SPECT," *Nuclear Science, IEEE Transactions on*, vol. 54, pp. 124-129, 2007.
- [105] S. D. Metzler, R. J. Jaszcak, N. H. Patil, S. Vemulapalli, G. Akabani, and B. B. Chin, "Molecular imaging of small animals with a triple-head SPECT system using pinhole collimation," *IEEE Trans Med Imaging*, vol. 24, pp. 853-62, Jul 2005.
- [106] N. H. Patil and S. D. Metzler, "Step-and-shoot versus continuous helical pinhole SPECT for improved axial resolution," in *Nuclear Science Symposium Conference Record, 2004 IEEE*, 2004, pp. 2422-2426 Vol. 4.
- [107] M. Sun, E. W. Izaguirre, T. Funk, A. B. Hwang, J. Carver, S. Thompson, B. E. Patt, K. B. Parnham, T. Vandehei, L. Junqiang, and B. H. Hasegawa, "A small animal helical SPECT scanner," *Conf. Rec. 2005 Nuclear Science Symp. Medical Imaging Conf.*, vol. 4, pp. 2066-2069, 2005.
- [108] G. L. Zeng and D. Gagnon, "CdZnTe strip detector SPECT imaging with a slit collimator," *Phys Med Biol*, vol. 49, pp. 2257-71, Jun 7 2004.
- [109] S. D. Metzler, R. Accorsi, J. R. Novak, A. S. Ayan, and R. J. Jaszcak, "On-axis sensitivity and resolution of a slit-slat collimator," *J Nucl Med*, vol. 47, pp. 1884-90, Nov 2006.
- [110] A. B. Hwang, K. Iwata, A. E. Sakdinawat, M. C. A. W. M. C. Wu, and B. H. A. H. B. H. Hasegawa, "Gantry specifications for a dual modality imaging system for small animals," in *Nuclear Science Symposium Conference Record, 2002 IEEE*, 2002, pp. 1303-1307 vol.2.
- [111] K. J. Hong, Y. Choi, S. C. Lee, S. Y. Lee, T. Y. Song, B. J. Min, J. H. Jung, Y. S. Choe, K. H. Lee, and B. T. Kim, "A Compact SPECT/CT System for Small Animal Imaging," *IEEE Trans. Nucl. Sci.*, vol. 53, pp. 2601-2604, 2006.
- [112] C. Goetz, E. Breton, P. Choquet, V. Israel-Jost, and A. Constantinesco, "SPECT Low-Field MRI System for Small-Animal Imaging," *J Nucl Med*, vol. 12, p. 12, Dec 12 2007.
- [113] S. Nikolaus, A. Wirrwar, C. Antke, S. Arkian, N. Schramm, H.-W. Müller, and R. Larisch, "Quantitation of dopamine transporter blockade by methylphenidate: first in vivo investigation using [123I]FP-CIT and a dedicated small animal SPECT," *European Journal of Nuclear Medicine and Molecular Imaging*, vol. 32, pp. 308-313, 2005.
- [114] M. C. Wu, B. H. Hasegawa, and M. W. Dae, "Performance evaluation of a pinhole SPECT system for myocardial perfusion imaging of mice," *Med Phys*, vol. 29, pp. 2830-9, Dec 2002.
- [115] F. Forrer, R. Valkema, B. Bernard, N. U. Schramm, J. W. Hoppin, E. Rolleman, E. P. Krenning, and M. de Jong, "In vivo radionuclide uptake quantification using a multi-pinhole SPECT system to predict renal function in small animals," *Eur J Nucl Med Mol Imaging*, vol. 33, pp. 1214-7, Oct 2006.
- [116] F. J. Beekman, D. P. McElroy, F. Berger, S. S. Gambhir, E. J. Hoffman, and S. R. Cherry, "Towards in vivo nuclear microscopy: iodine-125 imaging in mice using micro-pinholes," *Eur J Nucl Med Mol Imaging*, vol. 29, pp. 933-8, Jul 2002.
- [117] M. S. Saha, E. L. Bradley, P. Brewer, K. K. Gleason, B. Kross, S. Majewski, V. Popov, J. Qian, A. Ranck, K. Smith, M. F. Smith, A. G. Weisenberger, R. Wojcik, and R. E. Welsh, "Incorporation of a fluoroscopic X-ray modality in a small animal imaging system," *Nuclear Science, IEEE Transactions on*, vol. 50, pp. 333-338, 2003.
- [118] R. E. Welsh, E. L. Bradley, J. Cella, B. Kross, S. Majewski, V. Popov, J. Qian, M. S. Saha, K. Smith, M. F. Smith, A. G. Weisenberger, and R. Wojcik, "Simultaneous /sup 125/I SPECT imaging of small animals with pinhole and parallel collimation," *Nuclear Science Symposium Conference Record, 2003 IEEE*, vol. 4, pp. 2300-2304, 2003.

- [119] J. Qian, E. L. Bradley, S. Majewski, V. Popov, M. S. Saha, M. F. Smith, A. G. Weisenberger, and R. E. Welsh, "A Multi-Function Compact Small-Animal Imaging System Incorporating Multipinhole Standard and Helical SPECT and Parallel-Hole SPECT," *Nuclear Science Symposium Conference Record*, 2006. *IEEE*, vol. 4, pp. 2430-2438, 2006.
- [120] I. Lixi, Downers Grove, IL.
- [121] J. L. Noteboom, W. A. Hummel, J. J. Broerse, J. J. de Vijlder, T. Vulsma, and D. W. van Bakkum, "Protection of the infant thyroid from radioactive contamination by the administration of stable iodide. An experimental evaluation in chimpanzees.," *Radiat Res*, vol. 147, pp. 698-703, 1997.
- [122] K. M. Saxena, E. M. Chapman, and C. V. Pryles, "Minimal dosage of iodide required to suppress uptake of iodine-131 by normal thyroid," *Science*, vol. 138, pp. 430-431, 1962.
- [123] N. Takamura, Y. Nakamura, K. Ishigaki, J. Ishigaki, M. Mine, K. Aoyagi, and S. Yamashita, "Thyroid blockade during a radiation emergency in iodine-rich areas: effect of a stable-iodine dosage," *J Radiat Res*, vol. 45, pp. 201-204, 2004.
- [124] P. J. Green, "Bayesian reconstructions from emission tomography data using a modified EM algorithm," *Medical Imaging, IEEE Transactions on*, vol. 9, pp. 84-93, 1990.
- [125] I. Hamamatsu, Hamamatsu City, Japan.
- [126] U. H. Tazebay, I. L. Wapnir, O. Levy, O. Dohan, L. S. Zuckier, Q. H. Zhao, H. F. Deng, P. S. Amenta, S. Fineberg, R. G. Pestell, and N. Carrasco, "The mammary gland iodide transporter is expressed during lactation and in breast cancer," *Nat Med*, vol. 6, pp. 871-8, Aug 2000.
- [127] D. K. Marsee, D. H. Shen, L. R. MacDonald, D. D. Vadysirisack, X. Lin, G. Hinkle, R. T. Kloos, and S. M. Jhiang, "Imaging of metastatic pulmonary tumors following NIS gene transfer using single photon emission computed tomography," *Cancer Gene Ther*, vol. 11, pp. 121-7, Feb 2004.
- [128] D. H. Shen, R. T. Kloos, E. L. Mazzaferri, and S. M. Jhian, "Sodium iodide symporter in health and disease," *Thyroid*, vol. 11, pp. 415-25, May 2001.
- [129] P. P. Smyth and R. M. Dwyer, "The sodium iodide symporter and thyroid disease," *Clin Endocrinol*, vol. 56, pp. 427-9, Apr 2002.
- [130] Y. Krausz, M. Wilk, F. Saliman, and R. Chisin, "Role of high-resolution pinhole tomography in the evaluation of thyroid abnormalities," *Thyroid*, vol. 7, pp. 847-52, Dec 1997.
- [131] G. S. Pant, R. Kumar, A. K. Gupta, S. K. Sharma, and A. K. Pandey, "Estimation of thyroid mass in Graves' disease by a scintigraphic method," *Nucl Med Commun*, vol. 24, pp. 743-748, 2003 2003.
- [132] J. W. van Isselt, J. M. de Klerk, P. P. van Rijk, A. P. van Gils, L. J. Polman, C. Kamphuis, R. Meijer, and F. J. Beekman, "Comparison of methods for thyroid volume estimation in patients with Graves' disease," *Eur J Nucl Med Mol Imaging*, vol. 30, pp. 525-31, Apr 2003.
- [133] P. M. Wanet, A. Sand, and J. Abramovici, "Physical and clinical evaluation of high-resolution thyroid pinhole tomography," *J Nucl Med*, vol. 37, pp. 2017-20, Dec 1996.
- [134] F. J. Beekman, A. P. Colijn, B. Vastenhouw, V. M. Wiegant, and M. A. F. M. Gerrits, "High-resolution emission tomography of small laboratory animals: physics and gamma-astronomy meet molecular biology," *Nuclear Instruments and Methods in Physics Research Section A: Accelerators, Spectrometers, Detectors and Associated Equipment*, vol. 509, pp. 229-234, 2003.
- [135] D. A. Weber, M. Ivanovic, D. Franceschi, S. E. Strand, K. Erlandsson, M. Franceschi, H. L. Atkins, J. A. Coderre, H. Susskind, T. Button, and et al., "Pinhole SPECT: an approach to in vivo high resolution SPECT imaging in small laboratory animals," *J Nucl Med*, vol. 35, pp. 342-8, Feb 1994.
- [136] D. P. McElroy, L. R. MacDonald, F. J. Beekman, W. Yuchuan, B. E. Patt, J. S. Iwanczyk, B. M. W. Tsui, and E. J. Hoffman, "Performance evaluation of A-SPECT: a high resolution desktop pinhole SPECT system for imaging small animals," *IEEE Trans. Nucl. Sci.*, vol. 49, pp. 2139-2147, 2002.
- [137] Z. Cao, G. Bal, R. Accorsi, and P. D. Acton, "Optimal number of pinholes in multi-pinhole SPECT for mouse brain imaging--a simulation study," *Phys Med Biol*, vol. 50, pp. 4609-24, Oct 7 2005.
- [138] M. P. Kung and H. F. Kung, "Mass effect of injected dose in small rodent imaging by SPECT and PET," *Nucl Med Biol*, vol. 32, pp. 673-8, Oct 2005.
- [139] K. Peremans, B. Cornelissen, B. Van Den Bossche, K. Audenaert, and C. Van de Wiele, "A review of small animal imaging planar and pinhole spect Gamma camera imaging," *Vet Radiol Ultrasound*, vol. 46, pp. 162-70, Mar-Apr 2005.
- [140] T. Funk, M. Sun, and B. H. Hasegawa, "Radiation dose estimate in small animal SPECT and PET," *Med Phys*, vol. 31, pp. 2680-6, Sep 2004.

- [141] E. Dadachova and N. Carrasco, "The Na/I symporter (NIS): imaging and therapeutic applications," *Semin Nucl Med*, vol. 34, pp. 23-31, Jan 2004.
- [142] M. L. Schipper, C. G. Riese, S. Seitz, A. Weber, M. Behe, T. Schurrat, N. Schramm, B. Keil, H. Alfke, and T. M. Behr, "Efficacy of ^{99m}Tc pertechnetate and ¹³¹I radioisotope therapy in sodium/iodide symporter (NIS)-expressing neuroendocrine tumors in vivo," *Eur J Nucl Med Mol Imaging*, vol. 34, pp. 638-50, May 2007.
- [143] H. R. Maxon, "Detection of residual and recurrent thyroid cancer by radionuclide imaging," *Thyroid*, vol. 9, pp. 443-6, May 1999.
- [144] F. Bray, P. McCarron, and D. M. Parkin, "The changing global patterns of female breast cancer incidence and mortality," *Breast Cancer Res*, vol. 6, pp. 229-39, 2004.
- [145] D. Knutson and E. Steiner, "Screening for breast cancer: current recommendations and future directions," *Am Fam Physician*, vol. 75, pp. 1660-6, Jun 1 2007.
- [146] S. Pruthi, K. R. Brandt, A. C. Degnim, M. P. Goetz, E. A. Perez, C. A. Reynolds, P. J. Schomberg, G. K. Dy, and J. N. Ingle, "A multidisciplinary approach to the management of breast cancer, part 1: prevention and diagnosis," *Mayo Clin Proc*, vol. 82, pp. 999-1012, Aug 2007.
- [147] S. G. Demos, A. J. Vogel, and A. H. Gandjbakhche, "Advances in optical spectroscopy and imaging of breast lesions," *J Mammary Gland Biol Neoplasia*, vol. 11, pp. 165-81, Apr 2006.
- [148] A. P. Gibson, J. C. Hebden, and S. R. Arridge, "Recent advances in diffuse optical imaging," *Phys Med Biol*, vol. 50, pp. R1-43, Feb 21 2005.
- [149] N. Avril and L. P. Adler, "F-18 fluorodeoxyglucose-positron emission tomography imaging for primary breast cancer and loco-regional staging," *Radiol Clin North Am*, vol. 45, pp. 645-57, vi, Jul 2007.
- [150] B. Klaeser, O. Wiederkehr, D. Koeberle, A. Mueller, B. Bubeck, and B. Thuerlimann, "Therapeutic impact of 2-[fluorine-18]fluoro-2-deoxy-D-glucose positron emission tomography in the pre- and postoperative staging of patients with clinically intermediate or high-risk breast cancer," *Ann Oncol*, vol. 18, pp. 1329-34, Aug 2007.
- [151] N. Avril, M. Menzel, J. Dose, M. Schelling, W. Weber, F. Janicke, W. Nathrath, and M. Schwaiger, "Glucose metabolism of breast cancer assessed by 18F-FDG PET: histologic and immunohistochemical tissue analysis," *J Nucl Med*, vol. 42, pp. 9-16, Jan 2001.
- [152] M. Hentschel, T. Paulus, M. Mix, E. Moser, E. U. Nitzsche, and I. Brink, "Analysis of blood flow and glucose metabolism in mammary carcinomas and normal breast: a H2(15)O PET and 18F-FDG PET study," *Nucl Med Commun*, vol. 28, pp. 789-97, Oct 2007.
- [153] S. S. Gambhir, "Molecular imaging of cancer with positron emission tomography," *Nat Rev Cancer*, vol. 2, pp. 683-93, Sep 2002.
- [154] F. Benard and E. Turcotte, "Imaging in breast cancer: Single-photon computed tomography and positron-emission tomography," *Breast Cancer Res*, vol. 7, pp. 153-62, 2005.
- [155] A. Buck, H. Schirrmester, T. Kuhn, C. Shen, T. Kalker, J. Kotzerke, A. Dankerl, G. Glatting, S. Reske, and T. Mattfeldt, "FDG uptake in breast cancer: correlation with biological and clinical prognostic parameters," *Eur J Nucl Med Mol Imaging*, vol. 29, pp. 1317-23, Oct 2002.
- [156] L. M. Kenny, D. M. Vigushin, A. Al-Nahhas, S. Osman, S. K. Luthra, S. Shousha, R. C. Coombes, and E. O. Aboagye, "Quantification of cellular proliferation in tumor and normal tissues of patients with breast cancer by [18F]fluorothymidine-positron emission tomography imaging: evaluation of analytical methods," *Cancer Res*, vol. 65, pp. 10104-12, Nov 1 2005.
- [157] B. S. Pio, C. K. Park, R. Pietras, W. A. Hsueh, N. Satyamurthy, M. D. Pegram, J. Czernin, M. E. Phelps, and D. H. Silverman, "Usefulness of 3'-[F-18]fluoro-3'-deoxythymidine with positron emission tomography in predicting breast cancer response to therapy," *Mol Imaging Biol*, vol. 8, pp. 36-42, Jan-Feb 2006.
- [158] A. Mavi, T. F. Cermik, M. Urhan, H. Puskulcu, S. Basu, J. Q. Yu, H. Zhuang, B. Czerniecki, and A. Alavi, "The effects of estrogen, progesterone, and C-erbB-2 receptor states on 18F-FDG uptake of primary breast cancer lesions," *J Nucl Med*, vol. 48, pp. 1266-72, Aug 2007.
- [159] W. B. Eubank, "Diagnosis of recurrent and metastatic disease using f-18 fluorodeoxyglucose-positron emission tomography in breast cancer," *Radiol Clin North Am*, vol. 45, pp. 659-67, vi, Jul 2007.
- [160] H. Schirrmester, "Detection of bone metastases in breast cancer by positron emission tomography," *Radiol Clin North Am*, vol. 45, pp. 669-76, vi, Jul 2007.

- [161] K. A. Kurdziel, J. D. Kalen, J. I. Hirsch, J. D. Wilson, R. Agarwal, D. Barrett, H. D. Bear, and J. F. McCumiskey, "Imaging multidrug resistance with 4-[18F]fluoropaclitaxel," *Nucl Med Biol*, vol. 34, pp. 823-31, Oct 2007.
- [162] T. F. Cermik, A. Mavi, S. Basu, and A. Alavi, "Impact of FDG PET on the preoperative staging of newly diagnosed breast cancer," *Eur J Nucl Med Mol Imaging*, Oct 24 2007.
- [163] R. K. Doot, L. K. Dunnwald, E. K. Schubert, M. Muzi, L. M. Peterson, P. E. Kinahan, B. F. Kurland, and D. A. Mankoff, "Dynamic and static approaches to quantifying 18F-FDG uptake for measuring cancer response to therapy, including the effect of granulocyte CSF," *J Nucl Med*, vol. 48, pp. 920-5, Jun 2007.
- [164] A. Quon and S. S. Gambhir, "FDG-PET and beyond: molecular breast cancer imaging," *J Clin Oncol*, vol. 23, pp. 1664-73, Mar 10 2005.
- [165] X. Fei, J. Q. Wang, K. D. Miller, G. W. Sledge, G. D. Hutchins, and Q. H. Zheng, "Synthesis of [18F]Xeloda as a novel potential PET radiotracer for imaging enzymes in cancers," *Nucl Med Biol*, vol. 31, pp. 1033-41, Nov 2004.
- [166] L. Sundararajan, H. M. Linden, J. M. Link, K. A. Krohn, and D. A. Mankoff, "18F-Fluoroestradiol," *Semin Nucl Med*, vol. 37, pp. 470-6, Nov 2007.
- [167] A. K. Buck, H. Schirrmester, T. Mattfeldt, and S. N. Reske, "Biological characterisation of breast cancer by means of PET," *Eur J Nucl Med Mol Imaging*, vol. 31 Suppl 1, pp. S80-7, Jun 2004.
- [168] H. Barthel, H. Wilson, D. R. Collingridge, G. Brown, S. Osman, S. K. Luthra, F. Brady, P. Workman, P. M. Price, and E. O. Aboagye, "In vivo evaluation of [18F]fluoroetanidazole as a new marker for imaging tumour hypoxia with positron emission tomography," *Br J Cancer*, vol. 90, pp. 2232-42, Jun 1 2004.
- [169] E. Pelosi, C. Messa, S. Sironi, M. Picchio, C. Landoni, V. Bettinardi, L. Gianolli, A. Del Maschio, M. C. Gilardi, and F. Fazio, "Value of integrated PET/CT for lesion localisation in cancer patients: a comparative study," *Eur J Nucl Med Mol Imaging*, vol. 31, pp. 932-9, Jul 2004.
- [170] B. Zangheri, C. Messa, M. Picchio, L. Gianolli, C. Landoni, and F. Fazio, "PET/CT and breast cancer," *Eur J Nucl Med Mol Imaging*, vol. 31 Suppl 1, pp. S135-42, Jun 2004.
- [171] M. Beresford, I. Lyburn, B. Sanghera, A. Makris, and W. L. Wong, "Serial integrated (18)F-fluorodeoxythymidine PET/CT monitoring neoadjuvant chemotherapeutic response in invasive ductal carcinoma," *Breast J*, vol. 13, pp. 424-5, Jul-Aug 2007.
- [172] S. K. Yang, N. Cho, and W. K. Moon, "The role of PET/CT for evaluating breast cancer," *Korean J Radiol*, vol. 8, pp. 429-37, Sep-Oct 2007.
- [173] W. T. Yang, H. T. Le-Petross, H. Macapinlac, S. Carkaci, A. M. Gonzalez-Angulo, S. Dawood, E. Resetskova, G. N. Hortobagyi, and M. Cristofanilli, "Inflammatory breast cancer: PET/CT, MRI, mammography, and sonography findings," *Breast Cancer Res Treat*, Jul 26 2007.
- [174] L. Moy, F. Ponzio, M. E. Noz, G. Q. Maguire, Jr., A. D. Murphy-Walcott, A. E. Deans, M. T. Kitazono, L. Travascio, and E. L. Kramer, "Improving specificity of breast MRI using prone PET and fused MRI and PET 3D volume datasets," *J Nucl Med*, vol. 48, pp. 528-37, Apr 2007.
- [175] M. Beresford, B. Sanghera, W. L. Wong, and A. Makris, "Imaging of primary breast cancer with 18F-fluorodeoxythymidine PET-CT reveals heterogeneity of proliferation throughout the tumour," *Eur J Nucl Med Mol Imaging*, vol. 33, p. 624, May 2006.
- [176] S. I. Semple, F. J. Gilbert, T. W. Redpath, T. S. Ahearn, A. E. Welch, A. W. Hutcheon, S. D. Heys, E. H. Smyth, I. D. Miller, and I. C. Smith, "Correlation of MRI/PET rim enhancement in breast cancer: a delivery related phenomenon with therapy implications?," *Lancet Oncol*, vol. 4, p. 759, Dec 2003.
- [177] I. Weinberg, D. Beylin, S. Yarnall, E. Anashkin, P. Stepanov, S. Dolinsky, V. Zavarzin, W. Peter, K. Lauckner, K. Morton, R. Freimanis, N. Lesko, E. Levine, N. Perrier, J. Lovelace, K. Geisinger, R. Williams, S. Wollenweber, D. Narayanan, M. Doss, J. Hummel, E. Sigurdson, K. Evers, M. Torosian, and L. Adler, "Applications of a PET device with 1.5 mm FWHM intrinsic spatial resolution to breast cancer imaging," in *Biomedical Imaging: Nano to Macro, 2004. IEEE International Symposium on*, 2004, pp. 1396-1399 Vol. 2.
- [178] M. C. Abreu, P. Almeida, F. Balau, N. C. Ferreira, S. Fetal, F. Fraga, M. Martins, N. Matela, R. Moura, C. Ortigao, L. Peralta, P. Rato, R. Ribeiro, P. Rodrigues, A. I. Santos, A. Trindade, and J. Varela, "Clear-PEM: a dedicated PET camera for improved breast cancer detection," *Radiat Prot Dosimetry*, vol. 116, pp. 208-10, 2005.

- [179] E. A. Levine, R. I. Freimanis, N. D. Perrier, K. Morton, N. M. Lesko, S. Bergman, K. R. Geisinger, R. C. Williams, C. Sharpe, V. Zavarzin, I. N. Weinberg, P. Y. Stepanov, D. Beylin, K. Lauckner, M. Doss, J. Lovelace, and L. P. Adler, "Positron emission mammography: initial clinical results," *Ann Surg Oncol*, vol. 10, pp. 86-91, Jan-Feb 2003.
- [180] M. F. Smith, R. R. Raylman, S. Majewski, and A. G. Weisenberger, "Positron emission mammography with tomographic acquisition using dual planar detectors: initial evaluations," *Phys Med Biol*, vol. 49, pp. 2437-52, Jun 7 2004.
- [181] M. Camarda, N. Belcari, A. D. Guerra, S. Galeotti, F. Morsani, D. J. Herbert, and A. Vaiano, "Development of the YAP-PEM scanner for breast cancer imaging," *Phys Med*, vol. 21 Suppl 1, pp. 114-6, 2006.
- [182] N. K. Doshi, Y. Shao, R. W. Silverman, and S. R. Cherry, "Design and evaluation of an LSO PET detector for breast cancer imaging," *Med Phys*, vol. 27, pp. 1535-43, Jul 2000.
- [183] R. R. Raylman, S. Majewski, and M. R. Mayhugh, "Light sharing in multi-flat-panel-PMT PEM detectors," *Phys Med*, vol. 21 Suppl 1, pp. 83-6, 2006.
- [184] R. R. Raylman and M. F. Smith, "A task-based evaluation of PEM detector element size," *Phys Med*, vol. 21 Suppl 1, pp. 80-2, 2006.
- [185] A. M. Foudray, F. Habte, G. Chinn, J. Zhang, and C. S. Levin, "Count rate studies of a box-shaped PET breast imaging system comprised of position sensitive avalanche photodiodes utilizing monte carlo simulation," *Phys Med*, vol. 21 Suppl 1, pp. 64-7, 2006.
- [186] C. S. Levin, A. M. Foudray, and F. Habte, "Impact of high energy resolution detectors on the performance of a PET system dedicated to breast cancer imaging," *Phys Med*, vol. 21 Suppl 1, pp. 28-34, 2006.
- [187] J. Zhang, G. Chinn, A. M. Foudray, F. Habte, P. Olcott, and C. S. Levin, "Evaluation of a dual-panel PET camera design to breast cancer imaging," *Phys Med*, vol. 21 Suppl 1, pp. 94-8, 2006.
- [188] J. Zhang, P. D. Olcott, G. Chinn, A. M. Foudray, and C. S. Levin, "Study of the performance of a novel 1 mm resolution dual-panel PET camera design dedicated to breast cancer imaging using Monte Carlo simulation," *Med Phys*, vol. 34, pp. 689-702, Feb 2007.
- [189] A. Andrieux, O. Switsers, M. H. Chajari, J. H. Jacob, T. Delozier, R. Gervais, N. Allouache, V. Laurencon, M. Henry-Amar, and S. Bardet, "Clinical impact of fluorine-18 fluorodeoxyglucose positron emission tomography in cancer patients. A comparative study between dedicated camera and dual-head coincidence gamma camera," *Q J Nucl Med Mol Imaging*, vol. 50, pp. 68-77, Mar 2006.
- [190] E. Even-Sapir, B. Yuzefovich, E. Miller, J. P. Bouhnik, O. Zak, H. Lerman, G. Lievshitz, and C. Levin, "Coincidence imaging using 2 dual-head gamma-camera systems, with and without attenuation correction," *J Nucl Med Technol*, vol. 32, pp. 190-7, Dec 2004.
- [191] E. L. Rosen, T. G. Turkington, M. S. Soo, J. A. Baker, and R. E. Coleman, "Detection of primary breast carcinoma with a dedicated, large-field-of-view FDG PET mammography device: initial experience," *Radiology*, vol. 234, pp. 527-34, Feb 2005.
- [192] I. N. Weinberg, D. Beylin, V. Zavarzin, S. Yarnall, P. Y. Stepanov, E. Anashkin, D. Narayanan, S. Dolinsky, K. Lauckner, and L. P. Adler, "Positron emission mammography: high-resolution biochemical breast imaging," *Technol Cancer Res Treat*, vol. 4, pp. 55-60, Feb 2005.
- [193] www.naviscanpet.com.
- [194] W. A. Berg, I. N. Weinberg, D. Narayanan, M. E. Lobrano, E. Ross, L. Amodei, L. Tafra, L. P. Adler, J. Uddo, W. Stein, 3rd, and E. A. Levine, "High-resolution fluorodeoxyglucose positron emission tomography with compression ("positron emission mammography") is highly accurate in depicting primary breast cancer," *Breast J*, vol. 12, pp. 309-23, Jul-Aug 2006.
- [195] Y. C. Tai and R. Laforest, "Instrumentation aspects of animal PET," *Annu Rev Biomed Eng*, vol. 7, pp. 255-85, 2005.
- [196] A. Aliaga, J. A. Rousseau, J. Cadorette, E. Croteau, J. E. van Lier, R. Lecomte, and F. Benard, "A small animal positron emission tomography study of the effect of chemotherapy and hormonal therapy on the uptake of 2-deoxy-2-[F-18]fluoro-D-glucose in murine models of breast cancer," *Mol Imaging Biol*, vol. 9, pp. 144-50, May-Jun 2007.
- [197] X. Chen, R. Park, M. Tohme, A. H. Shahinian, J. R. Bading, and P. S. Conti, "MicroPET and autoradiographic imaging of breast cancer alpha v-integrin expression using 18F- and 64Cu-labeled RGD peptide," *Bioconjug Chem*, vol. 15, pp. 41-9, Jan-Feb 2004.

- [198] A. L. Kesner, W. A. Hsueh, N. L. Htet, B. S. Pio, J. Czernin, M. D. Pegram, M. E. Phelps, and D. H. Silverman, "Biodistribution and Predictive Value of ^{18}F -Fluorocyclophosphamide in Mice Bearing Human Breast Cancer Xenografts," *J Nucl Med*, Nov 15 2007.
- [199] V. Sharma, J. L. Prior, M. G. Belinsky, G. D. Kruh, and D. Piwnica-Worms, "Characterization of a $^{67}\text{Ga}/^{68}\text{Ga}$ radiopharmaceutical for SPECT and PET of MDR1 P-glycoprotein transport activity in vivo: validation in multidrug-resistant tumors and at the blood-brain barrier," *J Nucl Med*, vol. 46, pp. 354-64, Feb 2005.
- [200] X. Sun, H. Fang, X. Li, R. Rossin, M. J. Welch, and J. S. Taylor, "MicroPET imaging of MCF-7 tumors in mice via unr mRNA-targeted peptide nucleic acids," *Bioconjug Chem*, vol. 16, pp. 294-305, Mar-Apr 2005.
- [201] C. K. Abbey, A. D. Borowsky, J. P. Gregg, R. D. Cardiff, and S. R. Cherry, "Preclinical imaging of mammary intraepithelial neoplasia with positron emission tomography," *J Mammary Gland Biol Neoplasia*, vol. 11, pp. 137-49, Apr 2006.
- [202] A. L. Goertzen, A. K. Meadors, R. W. Silverman, and S. R. Cherry, "Simultaneous molecular and anatomical imaging of the mouse in vivo," *Phys Med Biol*, vol. 47, pp. 4315-28, Dec 21 2002.
- [203] R. R. Raylman, S. Majewski, S. S. Velan, S. Lemieux, B. Kross, V. Popov, M. F. Smith, and A. G. Weisenberger, "Simultaneous acquisition of magnetic resonance spectroscopy (MRS) data and positron emission tomography (PET) images with a prototype MR-compatible, small animal PET imager," *J Magn Reson*, vol. 186, pp. 305-10, Jun 2007.
- [204] W. B. Eubank and D. A. Mankoff, "Evolving role of positron emission tomography in breast cancer imaging," *Semin Nucl Med*, vol. 35, pp. 84-99, Apr 2005.
- [205] D. Dingli, S. J. Russell, and J. C. Morris, 3rd, "In vivo imaging and tumor therapy with the sodium iodide symporter," *J Cell Biochem*, vol. 90, pp. 1079-86, Dec 15 2003.
- [206] O. Schillaci, R. Danieli, P. Romano, R. Santoni, and G. Simonetti, "Scintimammography for the detection of breast cancer," *Expert Rev Med Devices*, vol. 2, pp. 191-6, Mar 2005.
- [207] G. M. Gommans, F. M. van der Zant, A. van Dongen, R. O. Boer, G. J. Teule, and J. W. de Waard, "(^{99}m)Technetium-sestamibi scintimammography in non-palpable breast lesions found on screening X-ray mammography," *Eur J Surg Oncol*, vol. 33, pp. 23-7, Feb 2007.
- [208] T. Hamaoka, J. E. Madewell, D. A. Podoloff, G. N. Hortobagyi, and N. T. Ueno, "Bone imaging in metastatic breast cancer," *J Clin Oncol*, vol. 22, pp. 2942-53, Jul 15 2004.
- [209] G. Madeddu and A. Spanu, "Use of tomographic nuclear medicine procedures, SPECT and pinhole SPECT, with cationic lipophilic radiotracers for the evaluation of axillary lymph node status in breast cancer patients," *Eur J Nucl Med Mol Imaging*, vol. 31 Suppl 1, pp. S23-34, Jun 2004.
- [210] A. Spanu, F. Tanda, G. Dettori, A. Manca, F. Chessa, A. Porcu, A. Falchi, S. Nuvoli, and G. Madeddu, "The role of (^{99}m)Tc-tetrofosmin pinhole-SPECT in breast cancer non palpable axillary lymph node metastases detection," *Q J Nucl Med*, vol. 47, pp. 116-28, Jun 2003.
- [211] Z. Liu, G. D. Stevenson, H. H. Barrett, G. A. Kastis, M. Bettan, L. R. Furenlid, D. W. Wilson, J. M. Woolfenden, and K. Y. Pak, " ^{99}mTc glucarate high-resolution imaging of drug sensitive and drug resistant human breast cancer xenografts in SCID mice," *Nucl Med Commun*, vol. 25, pp. 711-20, Jul 2004.
- [212] S. B. Sergieva, K. V. Timcheva, and N. D. Hadjiolov, " ^{99}mTc -MIBI scintigraphy as a functional method for the evaluation of multidrug resistance in breast cancer patients," *J Buon*, vol. 11, pp. 61-8, Jan-Mar 2006.
- [213] H. Jacobsson, B. Wilczek, J. Bergh, E. von Schoultz, E. Eriksson, and S. A. Larsson, "Different methods for the detection of small changes in uptake between single-photon emission computed tomography (SPECT) examinations: ^{99}mTc -sestamibi in chemotherapy for breast tumours," *Nucl Med Commun*, vol. 27, pp. 347-52, Apr 2006.
- [214] B. Wilczek, E. von Schoultz, J. Bergh, E. Eriksson, S. A. Larsson, and H. Jacobsson, "Early assessment of neoadjuvant chemotherapy by FEC-courses of locally advanced breast cancer using ^{99}mTc -MIBI," *Acta Radiol*, vol. 44, pp. 284-7, May 2003.
- [215] S. Usmani, K. Niaz, Z. Maseeh Uz, K. Niyaz, H. A. Khan, S. Habib, and S. Kamal, "Chest wall recurrence of breast cancer demonstrated on ^{99}mTc -MIBI scintimammography," *Nucl Med Commun*, vol. 28, pp. 842-6, Nov 2007.

- [216] E. F. de Vries, M. G. Rots, and G. A. Hospers, "Nuclear imaging of hormonal receptor status in breast cancer: a tool for guiding endocrine treatment and drug development," *Curr Cancer Drug Targets*, vol. 7, pp. 510-9, Sep 2007.
- [217] F. Berger and S. S. Gambhir, "Recent advances in imaging endogenous or transferred gene expression utilizing radionuclide technologies in living subjects: applications to breast cancer," *Breast Cancer Res*, vol. 3, pp. 28-35, 2001.
- [218] D. A. Mankoff, "Radiotracer breast cancer imaging: Beyond FDG and MIBI," *Phys Med*, vol. 21 Suppl 1, pp. 12-6, 2006.
- [219] C. Fernandes, C. Oliveira, L. Gano, A. Bourkoulas, I. Pirmettis, and I. Santos, "Radioiodination of new EGFR inhibitors as potential SPECT agents for molecular imaging of breast cancer," *Bioorg Med Chem*, vol. 15, pp. 3974-80, Jun 15 2007.
- [220] M. S. Dennis, H. Jin, D. Dugger, R. Yang, L. McFarland, A. Ogasawara, S. Williams, M. J. Cole, S. Ross, and R. Schwall, "Imaging tumors with an albumin-binding Fab, a novel tumor-targeting agent," *Cancer Res*, vol. 67, pp. 254-61, Jan 1 2007.
- [221] S. Panareo, P. Carcoforo, S. Lanzara, S. Corcione, E. Bagatin, M. Casali, A. Costanzo, E. Basaglia, and L. M. Feggi, "Radiolabelled somatostatin analogs for diagnosis and radio-guided surgery of neuroendocrine breast cancer undetectable with conventional imaging procedures," *Breast*, Sep 12 2007.
- [222] T. Bach-Gansmo, R. Danielsson, A. Saracco, B. Wilczek, T. V. Bogsrud, A. Fangberget, A. Tangerud, and D. Tobin, "Integrin receptor imaging of breast cancer: a proof-of-concept study to evaluate ^{99m}Tc -NC100692," *J Nucl Med*, vol. 47, pp. 1434-9, Sep 2006.
- [223] A. Orlova, F. Y. Nilsson, M. Wikman, C. Widstrom, S. Stahl, J. Carlsson, and V. Tolmachev, "Comparative in vivo evaluation of technetium and iodine labels on an anti-HER2 affibody for single-photon imaging of HER2 expression in tumors," *J Nucl Med*, vol. 47, pp. 512-9, Mar 2006.
- [224] P. J. Perik, M. N. Lub-De Hooze, J. A. Gietema, W. T. van der Graaf, M. A. de Korte, S. Jonkman, J. G. Kosterink, D. J. van Veldhuisen, D. T. Sleijfer, P. L. Jager, and E. G. de Vries, "Indium-111-labeled trastuzumab scintigraphy in patients with human epidermal growth factor receptor 2-positive metastatic breast cancer," *J Clin Oncol*, vol. 24, pp. 2276-82, May 20 2006.
- [225] A. Plachcinska, R. Mikolajczak, H. Maecke, E. Mlodkowska, J. Kunert-Radek, A. Michalski, K. Rzeszutek, J. Kozak, and J. Kusmirek, "Clinical usefulness of ^{99m}Tc -EDDA/HYNIC-TOC scintigraphy in oncological diagnostics: a pilot study," *Cancer Biother Radiopharm*, vol. 19, pp. 261-70, Apr 2004.
- [226] D. R. Chen, L. B. Jeng, A. Kao, C. C. Lin, and C. C. Lee, "Comparing thallium-201 spect mammoscintigraphy and ultrasonography to detect breast cancer in mammographical dense breasts," *Neoplasma*, vol. 50, pp. 222-6, 2003.
- [227] M. L. Janssen, W. J. Oyen, I. Dijkgraaf, L. F. Massuger, C. Frielink, D. S. Edwards, M. Rajopadhye, H. Boonstra, F. H. Corstens, and O. C. Boerman, "Tumor targeting with radiolabeled $\alpha(v)\beta(3)$ integrin binding peptides in a nude mouse model," *Cancer Res*, vol. 62, pp. 6146-51, Nov 1 2002.
- [228] C. Van de Wiele, V. Cocquyt, R. VandenBroecke, F. De Vos, S. Van Belle, K. Dhaene, G. Slegers, and R. A. Dierckx, "Iodine-labeled tamoxifen uptake in primary human breast carcinoma," *J Nucl Med*, vol. 42, pp. 1818-20, Dec 2001.
- [229] E. Fonsatti, A. P. Jekunen, K. J. Kairemo, S. Coral, M. Snellman, M. R. Nicotra, P. G. Natali, M. Altomonte, and M. Maio, "Endoglin is a suitable target for efficient imaging of solid tumors: in vivo evidence in a canine mammary carcinoma model," *Clin Cancer Res*, vol. 6, pp. 2037-43, May 2000.
- [230] J. P. Houston, S. Ke, W. Wang, C. Li, and E. M. Sevick-Muraca, "Quality analysis of in vivo near-infrared fluorescence and conventional gamma images acquired using a dual-labeled tumor-targeting probe," *J Biomed Opt*, vol. 10, p. 054010, Sep-Oct 2005.
- [231] L. Sampath, S. Kwon, S. Ke, W. Wang, R. Schiff, M. E. Mawad, and E. M. Sevick-Muraca, "Dual-labeled trastuzumab-based imaging agent for the detection of human epidermal growth factor receptor 2 overexpression in breast cancer," *J Nucl Med*, vol. 48, pp. 1501-10, Sep 2007.
- [232] W. Wang, S. Ke, S. Kwon, S. Yallampalli, A. G. Cameron, K. E. Adams, M. E. Mawad, and E. M. Sevick-Muraca, "A new optical and nuclear dual-labeled imaging agent targeting interleukin 11 receptor α -chain," *Bioconjug Chem*, vol. 18, pp. 397-402, Mar-Apr 2007.

- [233] D. B. Husarik and H. C. Steinert, "Single-photon emission computed tomography/computed tomography for sentinel node mapping in breast cancer," *Semin Nucl Med*, vol. 37, pp. 29-33, Jan 2007.
- [234] I. M. van der Ploeg, R. A. Valdes Olmos, O. E. Nieweg, E. J. Rutgers, B. B. Kroon, and C. A. Hoefnagel, "The additional value of SPECT/CT in lymphatic mapping in breast cancer and melanoma," *J Nucl Med*, vol. 48, pp. 1756-60, Nov 2007.
- [235] O. Schillaci, R. Danieli, L. Filippi, P. Romano, E. Cossu, C. Manni, and G. Simonetti, "Scintimammography with a hybrid SPECT/CT imaging system," *Anticancer Res*, vol. 27, pp. 557-62, Jan-Feb 2007.
- [236] C. W. Dumcke and J. L. Madsen, "Usefulness of SPECT/CT in the diagnosis of intrathoracic goiter versus metastases from cancer of the breast," *Clin Nucl Med*, vol. 32, pp. 156-9, Feb 2007.
- [237] S. Cowey, A. A. Szafran, J. Kappes, K. R. Zinn, G. P. Siegal, R. A. Desmond, H. Kim, L. Evans, and R. W. Hardy, "Breast cancer metastasis to bone: evaluation of bioluminescent imaging and microSPECT/CT for detecting bone metastasis in immunodeficient mice," *Clin Exp Metastasis*, vol. 24, pp. 389-401, 2007.
- [238] G. M. Duarte, C. Cabello, R. Z. Torresan, M. Alvarenga, G. H. Telles, S. T. Bianchessi, N. Caserta, S. R. Segala, C. de Lima Mda, E. C. Etchebehere, E. E. Camargo, and E. Tinois, "Fusion of magnetic resonance and scintimammography images for breast cancer evaluation: a pilot study," *Ann Surg Oncol*, vol. 14, pp. 2903-10, Oct 2007.
- [239] C. N. Brzymialkiewicz, M. P. Tornai, R. L. McKinley, and J. E. Bowsher, "Evaluation of fully 3-D emission mammotomography with a compact cadmium zinc telluride detector," *IEEE Trans Med Imaging*, vol. 24, pp. 868-77, Jul 2005.
- [240] C. B. Hruska, M. K. O'Connor, and D. A. Collins, "Comparison of small field of view gamma camera systems for scintimammography," *Nucl Med Commun*, vol. 26, pp. 441-5, May 2005.
- [241] B. Mueller, M. K. O'Connor, I. Blevis, D. J. Rhodes, R. Smith, D. A. Collins, and S. W. Phillips, "Evaluation of a small cadmium zinc telluride detector for scintimammography," *J Nucl Med*, vol. 44, pp. 602-9, Apr 2003.
- [242] F. Garibaldi, E. Cisbani, S. Colilli, F. Cusanno, R. Fratoni, F. Giuliani, M. Gricia, M. Lucentini, R. Fratoni, S. Lo Meo, M. L. Magliozzi, F. Santanvenere, M. N. Cinti, R. Pani, R. Pellegrini, G. Simonetti, O. Schillaci, S. Del Vecchio, M. Salvatore, S. Majewski, R. C. Lanza, G. De Vincentis, and F. Scopinaro, "Molecular imaging: High-resolution detectors for early diagnosis and therapy monitoring of breast cancer," *Nuclear Instruments and Methods in Physics Research Section A: Accelerators, Spectrometers, Detectors and Associated Equipment*, vol. 569, pp. 286-290, 2006.
- [243] N. D. Giokaris, G. K. Loudos, D. Maintas, D. Papapanagiotou, K. S. Nikita, N. K. Uzunoglu, A. Karabarbounis, C. N. Papanicolas, E. Stiliaris, S. C. Archimandritis, A. D. Varvarigou, C. N. Stefanis, S. Majewski, A. Weisen-berger, R. Pani, and F. Scopinaro, "Imaging of breast phantoms using a high-resolution position sensitive photomultiplier tube," *Nuclear Instruments and Methods in Physics Research Section A: Accelerators, Spectrometers, Detectors and Associated Equipment*, vol. 497, pp. 141-149, 2003.
- [244] R. Pani, R. Pellegrini, M. N. Cinti, P. Bennati, M. Betti, V. Casali, O. Schillaci, M. Mattioli, V. Orsolini Cencelli, F. Navarra, D. Bollini, G. Moschini, F. Garibaldi, F. Cusanno, G. Iurlaro, L. Montani, R. Scafe, and F. de Notaristefani, "Recent advances and future perspectives of gamma imagers for scintimammography," *Nuclear Instruments and Methods in Physics Research Section A: Accelerators, Spectrometers, Detectors and Associated Equipment*, vol. 569, pp. 296-300, 2006.
- [245] www.dilon.com.
- [246] www.gm-ideas.com.
- [247] M. P. Tornai, J. E. Bowsher, R. J. Jaszczak, B. C. Pieper, K. L. Greer, P. H. Hardenbergh, and R. E. Coleman, "Mammotomography with pinhole incomplete circular orbit SPECT," *J Nucl Med*, vol. 44, pp. 583-93, Apr 2003.
- [248] J. Xu, C. Liu, Y. Wang, E. C. Frey, and B. M. Tsui, "Quantitative rotating multisegment slant-hole SPECT mammography with attenuation and collimator-detector response compensation," *IEEE Trans Med Imaging*, vol. 26, pp. 906-16, Jul 2007.
- [249] I. Stark and H. Seywerd, "An analysis of an alternative scintimammography system," *Phys Med*, vol. 21 Suppl 1, pp. 128-31, 2006.

- [250] R. F. Brem, K. H. Michener, and G. Zawistowski, "Approaches to improving breast cancer diagnosis using a high resolution, breast specific gamma camera," *Phys Med*, vol. 21 Suppl 1, pp. 17-9, 2006.
- [251] M. K. O'Connor, S. W. Phillips, C. B. Hruska, D. J. Rhodes, and D. A. Collins, "Molecular breast imaging: advantages and limitations of a scintimammographic technique in patients with small breast tumors," *Breast J*, vol. 13, pp. 3-11, Jan-Feb 2007.
- [252] A. Spanu, P. Cottu, A. Manca, F. Chessa, D. Sanna, and G. Madeddu, "Scintimammography with dedicated breast camera in unifocal and multifocal/multicentric primary breast cancer detection: a comparative study with SPECT," *Int J Oncol*, vol. 31, pp. 369-77, Aug 2007.
- [253] H. Kim, T. R. Chaudhuri, D. J. Buchsbaum, D. Wang, and K. R. Zinn, "High-resolution single-photon emission computed tomography and X-ray computed tomography imaging of Tc-99m-labeled anti-DR5 antibody in breast tumor xenografts," *Mol Cancer Ther*, vol. 6, pp. 866-75, Mar 2007.
- [254] F. Berger, S. Unterholzner, J. Diebold, P. Knesewitsch, K. Hahn, and C. Spitzweg, "Mammary radioiodine accumulation due to functional sodium iodide symporter expression in a benign fibroadenoma," *Biochem Biophys Res Commun*, vol. 349, pp. 1258-63, Nov 3 2006.
- [255] T. Kogai, K. Taki, and G. A. Brent, "Enhancement of sodium/iodide symporter expression in thyroid and breast cancer," *Endocr Relat Cancer*, vol. 13, pp. 797-826, Sep 2006.
- [256] M. J. Willhauck, B. Sharif-Samani, R. Senekowitsch-Schmidtke, N. Wunderlich, B. Goke, J. C. Morris, and C. Spitzweg, "Functional sodium iodide symporter expression in breast cancer xenografts in vivo after systemic treatment with retinoic acid and dexamethasone," *Breast Cancer Res Treat*, Jul 18 2007.
- [257] T. Groot-Wassink, E. O. Aboagye, Y. Wang, N. R. Lemoine, A. J. Reader, and G. Vassaux, "Quantitative imaging of Na/I symporter transgene expression using positron emission tomography in the living animal," *Mol Ther*, vol. 9, pp. 436-42, Mar 2004.
- [258] D. A. Mankoff, L. K. Dunnwald, and P. Kinahan, "Are we ready for dedicated breast imaging approaches?," *J Nucl Med*, vol. 44, pp. 594-5, Apr 2003.
- [259] C. N. Johnstone, N. C. Tebbutt, H. E. Abud, S. J. White, K. L. Stenvers, N. E. Hall, S. H. Cody, R. H. Whitehead, B. Catimel, E. C. Nice, A. W. Burgess, and J. K. Heath, "Characterization of mouse A33 antigen, a definitive marker for basolateral surfaces of intestinal epithelial cells," *Am J Physiol Gastrointest Liver Physiol*, vol. 279, pp. G500-10, Sep 2000.
- [260] F. Garibaldi, E. Cisbani, S. Colilli, F. Cusanno, R. Fratoni, F. Giuliani, M. Gricia, M. Lucentini, S. Lo Meo, M. L. Magliozzi, F. Santanvenere, M. N. Cinti, R. Pani, R. Pellegrini, G. Simonetti, O. Schillaci, S. Del Vecchio, M. Salvatore, S. Majewski, R. C. Lanza, G. De Vincentis, and F. Scopinaro, "Molecular imaging: High-resolution detectors for early diagnosis and therapy monitoring of breast cancer," *Nuclear Instruments and Methods in Physics Research Section A: Accelerators, Spectrometers, Detectors and Associated Equipment*, vol. 569, pp. 286-290, 2006.
- [261] J. Imrek, G. Hegyesi, G. Kalinka, J. Molnar, D. Novak, I. Valastyan, J. Vegh, L. Balkay, M. Emri, S. Kis, L. Tron, T. Biikki, Z. Szabo, and A. Kerek, "Development of an Improved Detector Module for miniPET-II," in *Nuclear Science Symposium Conference Record, 2006. IEEE, 2006*, pp. 3037-3040.
- [262] N. Inadama, H. Murayama, T. Yamaya, K. Kitamura, T. Yamashita, H. Kawai, T. Tsuda, M. Sato, Y. Ono, and M. Hamamoto, "Preliminary evaluation of four-layer BGO DOI-detector for PET," *Nuclear Science, IEEE Transactions on*, vol. 53, pp. 30-34, 2006.
- [263] J. Proffitt, W. Hammond, S. Majewski, V. Popov, R. R. Raylman, and A. G. Weisenberger, "Implementation of a High-Rate USB Data Acquisition System for PET and SPECT Imaging," in *Nuclear Science Symposium Conference Record, 2006. IEEE, 2006*, pp. 3063-3067.
- [264] R. Pani, R. Pellegrini, M. N. Cinti, P. Bennati, M. Betti, V. Casali, O. Schillaci, M. Mattioli, V. Orsolini Cencelli, F. Navarra, D. Bollini, G. Moschini, F. Garibaldi, F. Cusanno, G. Iurlaro, L. Montani, R. Scaf, and F. de Notaristefani, "Recent advances and future perspectives of gamma imagers for scintimammography," *Nuclear Instruments and Methods in Physics Research Section A: Accelerators, Spectrometers, Detectors and Associated Equipment*, vol. 569, pp. 296-300, 2006.
- [265] E. V. D. van Loef, P. Dorenbos, C. W. E. van Eijk, K. Kramer, and H. U. Gudel, "High-energy-resolution scintillator: Ce[^{sup}3+] activated LaBr[_{sub}3]," *Applied Physics Letters*, vol. 79, pp. 1573-1575, 2001.

- [266] S. Yamamoto and J. Hatazawa, "Development of a small field-of-view LaBr₃(Ce) gamma camera for low energy single photon imaging," *J NUCL MED MEETING ABSTRACTS*, vol. 48, pp. 94P-, May 1, 2007 2007.
- [267] D. Betal, N. Roberts, and G. H. Whitehouse, "Segmentation and numerical analysis of microcalcifications on mammograms using mathematical morphology," *Br J Radiol*, vol. 70, pp. 903-17, Sep 1997.
- [268] T. Eckert, K. Van Laere, C. Tang, D. E. Lewis, C. Edwards, P. Santens, and D. Eidelberg, "Quantification of Parkinson's disease-related network expression with ECD SPECT," *Eur J Nucl Med Mol Imaging*, vol. 34, pp. 496-501, Apr 2007.
- [269] A. O. Boudraa, J. C. Cexus, and H. Zaidi, "Functional segmentation of dynamic nuclear images by cross-psi B-energy operator," *Comput Methods Programs Biomed*, vol. 84, pp. 146-52, Dec 2006.
- [270] H. Koga, M. Sasaki, Y. Kuwabara, K. Hiraka, M. Nakagawa, K. Abe, K. Kaneko, K. Hayashi, and H. Honda, "An analysis of the physiological FDG uptake pattern in the stomach," *Ann Nucl Med*, vol. 17, pp. 733-8, Dec 2003.
- [271] G. G. Chung, M. P. Zerkowski, S. Ghosh, R. L. Camp, and D. L. Rimm, "Quantitative analysis of estrogen receptor heterogeneity in breast cancer," *Lab Invest*, vol. 87, pp. 662-9, Jul 2007.
- [272] T. Yoshikawa, K. Murase, N. Oku, K. Kitagawa, M. Imaizumi, M. Takasawa, T. Nishikawa, M. Matsumoto, J. Hatazawa, and M. Hori, "Statistical image analysis of cerebral blood flow in vascular dementia with small-vessel disease," *J Nucl Med*, vol. 44, pp. 505-11, Apr 2003.
- [273] P. D. Acton and A. Newberg, "Artificial neural network classifier for the diagnosis of Parkinson's disease using [^{99m}Tc]TRODAT-1 and SPECT," *Phys Med Biol*, vol. 51, pp. 3057-66, Jun 21 2006.

VITA

Jianguo Qian

Jianguo Qian was born in Yizheng, Jiangsu Province, China on August 7, 1974. Jianguo Qian received his B.S. in Physical Electronics at Fudan University in 1997. He received his M.S. degree at Shanghai Jiao Tong University in 2000, with a concentration in Microelectronics and Solid State Electronics.

In June 2000, the author entered the College of William and Mary as a graduate assistant in the Department of Applied Science. With the completion of the thesis and satisfaction in all other degree requirements, the author received his Ph. D degree in Medical Imaging in August 2008.